Dynamic Neural Network-Based Feedback Linearization of Electrohydraulic Suspension Systems

Name: Muhammed.Dangor
Student Number: 304976
Supervisor: Prof. J.O. Pedro

A dissertation submitted to the Faculty of Engineering and the Built Environment, University of the Witwatersrand, Johannesburg, in fulfilment of the requirements for the degree of Master of Science in Engineering.

Johannesburg, May 2014

Declaration

I declare that this dissertation is my own, unaided work, except where otherwise acknowledged. It is being submitted for the degree of Master of Science in Engineering in the University of the Witwatersrand, Johannesburg. It has not been submitted before for any degree or examination at any other university.

Signed this 27th day of May 2014

Name: Muhammed.Dangor
Student Number: 304976
Supervisor: Prof. J.O. Pedro

Acknowledgements

I would like to extend a hand of gratitude to the following people:

1. My dear parents and siblings for providing me with support to achieve my goals.
2. Prof. J.O. Pedro for his assitance throughtout this project.
3. Dr. O.A. Dahunsi for excellent mentorship.
4. Prof. M.M. Ali for providing me with groundbreaking and unexplored novel ideas.
5. And most importantly, to almighty Allah be the glory for the successful completion of this work.

Abstract

Resolving the trade-offs between suspension travel, ride comfort, road holding, vehicle handling and power consumptions is the primary challenge in designing Active-Vehicle-Suspension-Systems (AVSS). Controller tuning with global optimization techniques is proposed to realise the best compromise between these conflicting criteria. Optimization methods adapted include Controlled-Random-Search (CRS), Differential-Evolution (DE), Genetic-Algorithm (GA), Particle-Swarm-Optimization (PSO) and Pattern-Search (PS). Quarter-car and full-car nonlinear AVSS models that incorporate electrohydraulic actuator dynamics are designed. Two control schemes are proposed for this investigation. The first is the conventional Proportional-Integral-Derivative (PID) control, which is applied in a multi-loop architecture to stabilise the actuator and manipulate the primary control variables. Global optimization-based tuning achieved enhanced responses in each aspect of PID-based AVSS performance and a better resolve in conflicting criteria, with DE performing the best. The full-car PID-based AVSS was analysed for DE as well as modified variants of the PSO and CRS. These modified methods surpassed its predecessors with a better performance index and this was anticipated as they were augmented to permit for efficient exploration of the search space with enhanced flexibility in the algorithms. However, DE still maintained the best outcome in this aspect. The second method is indirect adaptive dynamic-neural-network-based-feedback-linearization (DNNFBL), where neural networks were trained with optimization algorithms and later feedback linearization control was applied to it. PSO generated the most desirable results, followed by DE. The remaining approaches exhibited significantly weaker results for this control method. Such outcomes were accredited to the nature of the DE and PSO algorithms and their superior search characteristics as well as the nature of the problem, which now had more variables. The adaptive nature and ability to cancel system nonlinearities saw the full-car PSO-based DNNFBL controller outperform its PID counterpart. It achieved a better resolve between performance criteria, minimal chatter, superior parameter sensitivity, and improved suspension travel, roll acceleration and control force response.

Scope and Contribution

- Implementation of global optimization methods including novel ground breaking ideas to select controller gains with the aim of improving suspension performance and resolving conflicting design trade-offs.
- Applying heurestic global optimizaition approaches to train neural networks as opposed to the function based methods that are commonly used.
- Conducting research on complex systems such as quarter-car and full-car nonlinear electrohydraulic active vehicle suspension systems.
- Learning the dynamics of the 11 Degrees-of-Freedom coupled nonlinear system through the use of dynamic neural networks.
- Developing an intelligent controller that performs feedback linearization of the trained dynamic neural network which in its entirety aims to cancel the effect of nonlinear dynamics with the system.
- Generation of a hybrid linear and intelligent controller which is tuned using heurestic optimization approahces to augment system performance.

Published Work

Journals

1. **Pedro, J.O., Dangor, M., Dahunsi, O.A. and Ali, M.M.(2013). "Differential Evolution-Based PID Control of Nonlinear Full-car Electrohydraulic Suspensions", *Mathematical Problems in Engineering*, vol. 2013, pp. 1-13.**

2. **Pedro, J.O., Dangor, M., Dahunsi, O.A. and Ali, M.M.(2013). "Intelligent Feedback Linearisation Control of Nonlinear Electrohydraulic Suspension Systems Using Particle Swarm Optimisation", *Applied Soft Computing*.**

Conferences

1. **Pedro, J.O., Dangor, M., Dahunsi, O.A. and Ali, M.M.(2013). "CRS and PS-Optimised PID Controller for Nonlinear, Electrohydraulic Suspension Systems", *Proceedings of the* 9^{th} *Asian Control Conference (ASCC2013)*, Istanbul, Turkey, 23-26 June 2013, pp. 1-6.**

2. **Pedro, J.O., Dangor, M., Dahunsi, O.A. and Ali, M.M.(2013). "DE-Based PID Control of Full-Car Nonlinear, Servo-Hydraulic Suspension Systems", *Proceedings of the* 11^{th} *IEEE Africon Conference (Africon2013)*, Mauritius, 7-12 September 2013, pp. 1-6.**

3. **Dangor, M., Dahunsi, O.A., Pedro, J.O., and Ali, M.M.(2014). "PSO-based DNN Feedback Linearization of a Full-Car Electrohydraulic Suspension Systems" *International Federation of Automatic Control (IFAC)*, South Africa, Cape Town, 24-29 August 2014.**

Journal Papers in Development

1. **Dangor, M., Dahunsi, O.A., Pedro, J.O., and Ali, M.M.(2014). "Evolutionary Algorithm Enhanced PID Control of Nonlinear Electrohydraulic Vehicle Suspensions", *Nonlinear Dynamics*. Under Review.**

2. **Dangor, M., Dahunsi, O.A., Pedro, J.O., and Ali, M.M.(2014). "PSO-based DNN Feedback Linearization Control of Full-Car Nonlinear Electrohydraulic Suspension Systems" *International Journal of Applied Mathematics and Computer Science*.**

Contents

Declaration i

Acknowledgements ii

Abstract iii

Scope and Contribution iv

Published Work v

Contents vii

List of Figures xii

List of Tables xx

Nomenclature xxii

1 Introduction 1

1.1 Background 1

1.2 Types of Suspension Systems 1

1.3 Challenges Associated with AVSS 3

1.4 Literature Review 4
1.4.1 Classification of Mathematical Models 4
1.4.2 Selection of Design Specifications 8
1.4.3 Analysis of Current AVSS Controllers in Literature and Associated Shortcomings 9
1.4.3.1 Linear Control 11
1.4.3.2 Nonlinear Control 15
1.4.3.3 Intelligent Control 17
1.4.4 Gaps in Literature 22
1.5 Proposed Controller Architecture 23
1.6 Research Objectives 24
1.7 Design Assumptions 25
1.8 Research Questions 25
1.9 Research Strategy and Methodology 25
1.10 Contributions to Knowledge 26
1.11 Layout of Dissertation 28

2 System Description and Mathematical Modelling 29

2.1 Description of the Quarter-Car Model 29
2.2 Development of the Full-Car Model 35
2.3 Model of Realistic Road Disturbances 46

3 PID Benchmark Controller Design and Optimization 49

3.1 Quarter-Car PID-Based Control 49

3.1.1 Introduction 49

3.1.2 Controller Design of Quarter-Car AVSS 49

3.1.3 Design Specifications of Quarter-Car AVSS 51

3.1.4 Comparative Study between Passive and PID-Based AVSS Response 53

3.1.5 Application of Global Optimization Methods to Controller Tuning of Quarter-Car AVSS 57

3.1.5.1 DE Global Optimization Method 58

3.1.5.2 GA Global Optimization Method 61

3.1.5.3 PSO Global Optimization Method 63

3.1.5.4 CRS Global Optimization Method 67

3.1.5.5 PS Global Optimization Method 69

3.1.5.6 Optimization Set Up and Initialization 71

3.1.6 Examination of System Response Attained through the use of Global Optimization Methods 72

3.1.7 Sensitivity to Parameter Variations and Frequency-Domain Analysis for PID-Based AVSS 82

3.1.8 Summary 86

3.2 PID-Controlled Full-Car System 87

3.2.1 Introduction 87

3.2.2 Controller Design 87

3.2.3 Performance Criteria and Design Specifications 89

3.2.4 Global Optimization Tuning Methods Applied for Gain Selection 90

3.2.4.1 Modified Particle Swarm Optimization (MPSO) . . 91

3.2.4.2 Modified Controlled Random Search (MCRS) 93

3.2.4.3 Analysis of the Convergence of the Various Routines 95

3.2.5 Simulation Results and Discussion 98

3.2.6 Sensitivity to Parameter Variations and Frequency-Domain Analysis 107

3.2.7 Summary 112

4 Dynamic Neural Network-Based Feedback Linearization Control of a Nonlinear Quarter-Car Electrohydraulic Vehicle Suspension System 114

4.1 Introduction 114

4.2 Stability Analysis 115

4.3 Proposed Control Structure 119

4.4 System Identification 120

4.5 Control Law Formulation 129

4.6 Controller Tuning Approaches 132

4.7 Simulation Results and Comparative Examination of Tuning Approaches 134

4.8 System Robustness to Parameter Variations and Frequency-Domain Analysis 141

4.9 Comparison Study on PID and Intelligent Controllers 144

4.10 Summary 145

5 Dynamic Neural Network-Based Feedback Linearization Control of a Nonlinear Full-Car Electrohydraulic Vehicle Suspension System 146

5.1 Input-output Linearization of Full-car AVSS 147

5.2 System Identification 154

5.3 Controller Development and Tuning 167

5.4 Simulation Results 174

5.5 Sensitivity to Parameter Variations and Frequency-Domain Analysis 184

5.6 Assessment in Relation to Benchmark PID Design 188

5.7 Summary 190

6 Conclusions and Recommendations 191

6.1 Conclusions 191

6.2 PID Control through Global Optimization-Based Tuning 192

6.3 Intelligent Control 193

6.4 Recommendations 194

List of Figures

1.1 Trade-offs associated with suspension systems [Pedro et al. (2013a)] 2

1.2 Graphical representation of the quarter-car suspension system model 5

1.3 Illustration of the half-car configuration [Ekoru and Pedro (2013)] . 5

1.4 Schematic of the full-car model [Pedro et al. (2013a)] 6

1.5 Graph summarising ride comfort as per ISO standards (Griffin (2007)) 9

1.6 Basic AVSS control structure 10

1.7 Schematic of multi-loop AVSS controller 10

1.8 Proposed network architecture 24

1.9 Road map to be followed in this research investigation 27

2.1 Graphical representation of the quarter-car configuration [Pedro et al. (2011)] 30

2.2 Free-body-diagram describing the forces acting on the chassis 30

2.3 Free-body-diagram describing the forces acting on the chassis 30

2.4 Depiction of the fluid flows and pressures within the hydraulic actuator [Pedro et al. (2011)] 32

2.5 Schematic describing the full-car model 36

2.6 Free-body-diagram depicting the forces acting on the full-car chassis 37

2.7 Free-body-diagram showing the forces acting on each wheel 38

2.8 Road disturbance input for the quarter-car suspension system study 47

2.9 Road disturbance input for the full-car suspension system study . . 48

3.1 Schematic describing the PID-based AVSS for quarter-car model . . 50

3.2 Suspension travel response for both PVSS and manually-tuned PID-controlled AVSS 54

3.3 Sprung mass acceleration response for both PVSS and manually-tuned PID-controlled AVSS 54

3.4 Road holding characteristics of PVSS and manually-tuned PID-controlled AVSS 55

3.5 Actuator force supplied for manually-tuned PID-controlled AVSS . . 55

3.6 Control input voltage supplied for manually-tuned PID-controlled AVSS 56

3.7 Closed-loop diagram for optimal PID controller design 57

3.8 Schematic illustrating the search capabilities of DE-based optimization 60

3.9 Vector plot showing the process of reproduction 63

3.10 Vector plot demonstrating the process of Particle Swarm Optimization 66

3.11 Impact of the centre of gravity on the Controlled Random Search algorithm 68

3.12 Demonstration of the Pattern Search local optimization technique . 70

3.13 Performance index convergence history of the DE, GA and PSO algorithms 72

3.14 Convergence history of performance index when applying CRS-based controller tuning 73

3.15 Bar graphs depicting the variation in suspension travel for each control law 75

3.16 Bar graphs illustrating the difference in heave acceleration for the proposed controllers 75

3.17 Bar graphs summarizing the road holding data for each control case 77

3.18 Bar graphs summarizing the results obtained for global optimization for the case of actuator force 77

3.19 Quantitative information pertaining to the control input voltage response 78

3.20 Suspension travel response for optimized PID-based AVSS 80

3.21 Sprung mass acceleration response for optimized PID-based AVSS . 80

3.22 Road holding characteristics for optimized PID-based AVSS 81

3.23 Actuator force supplied for the optimized PID-based AVSS 81

3.24 Control input voltage supplied for optimized PID-based AVSS 82

3.25 System response for a -20% variation in some selected system parameters 83

3.26 System response for a +20% variation in some selected system parameters 83

3.27 Frequency response for body-heave acceleration of the passive system and the proposed control schemes 85

3.28 Road holding frequency response for passive, PID-controlled and DE-controlled cases 86

3.29 Schematic of the PID control architecture for full-car AVSS 88

3.30 Schematic illustrating the effect of the proposed modified PSO . . . 91

3.31 Illustration of the contributing effect of the modified CRS routine . . 94

3.32 Evolution of performance index using the suggested evolutionary algorithms 95

3.33 Comparative plot depicting the variation in performance index between the CRS and MCRS routines 96

3.34 Bar graphs depicting the variation in suspension travel for each control law 98

3.35 Bar graphs illustrating the difference in control input voltage for the proposed controllers 99

3.36 Bar graphs summarizing the road holding aspect for each control case 99

3.37 Quantitative information pertaining to vehicle handling, ride comfort and actuator force supplied 100

3.38 Illustration of the variation in suspension travel response using the proposed tuning methods 100

3.39 Variation in the tyre dynamic load experienced at the rear left suspension system for the various tuning policies 101

3.40 Difference in control input voltage produced using the suggested tuning approaches 101

3.41 Vehicle body pitch acceleration for each of the tuning routines . . . 102

3.42 Vehicle body roll acceleration for the various tuning policies 102

3.43 Ride comfort experienced for each of the proposed tuning methods . 103

3.44 Effective hydraulic force applied to the vehicle chassis for the various tuning algorithms 103

3.45 Suspension travel response of the DE+PID case for a -20% variation in selected parameters 108

3.46 Suspension travel response of the DE+PID case for a +20% variation in selected parameters 108

3.47 Frequency response comparative plot for the body-heave acceleration 109

3.48 Comparative plot of frequency response pertaining to body pitch acceleration 110

3.49 Roll acceleration frequency response comparative plot for relevant cases 110

3.50 Frequency response for road holding 111

4.1 General structure of FBL control scheme 116

4.2 Controller architecture of the DNNFBL-based AVSS 120

4.3 Schematic describing the operation of a DNN 121

4.4 Method explaining the process of system identification [Dahunsi and Pedro (2010)] 122

4.5 Quarter-car AVSS control input voltage supplied for system identification 123

4.6 Quarter-car model suspension travel output for the training phase of system identification 124

4.7 Quarter-car suspension travel output for different hidden layer sizes 124

4.8 Convergence history of the various training algorithms used in system identification of the quarter-car AVSS 126

4.9 Convergence history of the MSE value when incorporating CRS-based system identification 127

4.10 DNN identification results for quarter-car intelligent controller using proposed global optimization methods 128

4.11 DNN validation results for quarter-car intelligent controller using proposed global optimization methods 128

4.12 Convergence history of evolutionary algorithms used for intelligent controller tuning of the quarter-car AVSS 133

4.13 Comparison of suspension travel response for the proposed intelligent controllers 135

4.14 Comparison between the various controllers on the basis of ride comfort 135

4.15 Wheel deflection characteristics obtained through the various control methodologies 136

4.16 Comparison of actuation force applied between the chassis and the wheel for each case 136

4.17 Variation of control input for each control methodology 137

4.18 Bar graphs depicting the variation in suspension travel for each control law 137

4.19 Bar graphs illustrating the difference in body-heave acceleration for the proposed controllers 138

4.20 Bar graphs summarizing the road holding data for each control case 138

4.21 Actuator force bar graphs summarizing the results obtained for the various control schemes 139

4.22 Quantitative information pertaining to the control input voltage response 139

4.23 Suspension travel response for a +20% variation in selected parameters 142

4.24 Suspension travel response to -20% variation in selected parameters 142

4.25 Ride comfort frequency response of the proposed intelligent controllers 143

4.26 Road holding frequency response of the proposed intelligent controllers 144

5.1 Schematic of the proposed full-car indirect adaptive intelligent controller 147

5.2 Front right actuator input data used for system identification 155

5.3 Front left actuator input data used for system identification 156

5.4 Rear right actuator input data used for system identification 156

5.5 Rear left actuator input data used for system identification 157

5.6 Front right suspension travel output data used for system identification 157

5.7 Front left suspension travel output data used for system identification 158

5.8 Rear right suspension travel output data used for system identification 158

5.9 Rear left suspension travel output data used for system identification 159

5.10 Schematic of the applied MIMO DNN 160

5.11 Network output data for various DNN configurations 161

5.12 DNN training results obtained through PSO learning 162

5.13 Identification results obtained for the front right suspension system . 163

5.14 Identification results obtained for the front left suspension system . . 163

5.15 Identification results obtained for the rear right suspension system . 164

5.16 Identification results obtained for the rear left suspension system . . 164

5.17 DNN validation results for the front right suspension system 165

5.18 DNN validation results for the front left suspension system 165

5.19 DNN validation results for the rear right suspension system 166

5.20 DNN validation results for the rear left suspension system 166

5.21 Convergence of performance index through PSO-based optimization for full-car intelligent controller 173

5.22 Bar graphs depicting the variation in suspension travel for each control law 174

5.23 Bar graphs illustrating the difference in control input voltage for the proposed controllers 175

5.24 Bar graphs summarizing the road holding aspect for each control case 175

5.25 Quantitative information pertaining to the vehicle handling, ride comfort and actuator force 176

5.26 Suspension travel response through the implementation of intelligent control 176

5.27 Comparative plot of the tyre dynamic load response for the proposed intelligent control schemes 177

5.28 Ride comfort observed through the use of intelligent control and optimized intelligent control 177

5.29 Cumulative actuator force produced in the employment of intelligent control 182

5.30 Ride comfort observed through the use of intelligent control and optimized intelligent control 182

5.31 Vehicle handling characteristics as captured by pitch acceleration for the intelligent control scheme 183

5.32 Vehicle handling features observed through roll acceleration for the intelligent control techniques 184

5.33 Suspension travel response for +20% variations in selected parameter 185

5.34 Suspension travel response for −20% variations in selected parameters 185

5.35 Frequency response of ride comfort for the full-car intelligent system in the region of anticipated sensitive frequencies 186

5.36 Frequency-domain analyses of vehicle handling for the full-car intelligent system with respect to pitch acceleration 187

5.37 Examination of frequency response for roll acceleration for the full-car intelligent system 187

5.38 Road holding frequency-domain analyses 188

List of Tables

2.1 System parameters for the quarter-car model 34

2.2 Values of the system parameters for the full-car AVSS 40

2.3 Parameter values for the deterministic road bumps 48

3.1 PID gains obtained using manual tuning for the quarter-car AVSS . 53

3.2 Performance characteristics of PVSS and manually-tuned PID-controlled AVSS 56

3.3 Global optimization parameter settings for the suggested routines . . 71

3.4 PID gains computed using the various global optimization schemes . 74

3.5 Summary of selected suspension performance incorporating the various optimization routines 76

3.6 PSD configuration settings for frequency-domain study 84

3.7 Optimization parameter settings for full-car PID-based AVSS optimal polices 95

3.8 Gains computed through the various optimization algorithms for full-car PID controller 97

3.9 Summary of selected suspension performance incorporating the various optimization routines 104

3.10 Summary of selected suspension performance incorporating the various optimization routines 105

3.11 Configuration settings used to obtain frequency response 111

4.1 Configuration of applied dynamic neural networks for the quarter-car system 125

4.2 Optimization parameters used in each optimal policy for system identification of the quarter-car system 126

4.3 Optimization parameters used in the selected optimization algorithms for controller tuning of the quarter-car DNNFBL controller 132

4.4 Controller gains acquired for the proposed DNNFBL controllers . . . 134

4.5 Summary of selected suspension performance incorporating the various optimization routines 140

5.1 Configuration setting of input data for system identification for the full-car model 155

5.2 PSO settings for the full-car system identification 162

5.3 Optimization parameters for the PSO routine for the full-car intelligent controller 173

5.4 List of controller gains selected for full-car intelligent control 178

5.5 Summary of selected suspension performance incorporating the proposed intelligent controller 179

5.6 Summary of selected suspension performance incorporating the proposed intelligent controller 180

5.7 PSD frequency configuration for full-car intelligent controllers 186

Nomenclature

List of Acronyms

Acronym	Definition
2D	2 Dimensional
ANN	Artificial Neural Networks
AVSS	Active Vehicle Suspension Systems
BIBO	Bounded-Input-Bounded-Output
CRS	Controlled Random Search
DE	Differential Evolution
DNN	Dynamic Neural Network
DNNFBL	Dynamic Neural Network Based Feedback Linearization
DOF	Degrees of Freedom
ELV	Maximum Exposure Limit
FBL	Feedback Linearization
FLC	Fuzzy Logic Control
GA	Genetic Algorithm
LQG	Linear Quadratic Gaussian
LQR	Linear Quadratic Regulator
MCRS	Modified Controlled Random Search
MPSO	Modified Particle Swarm Optimization
PID	Proportional Intergral Derivative
PS	Pattern Search
PSD	Power Spectral Density
PSO	Particle Swarm Optimization
PVSS	Passive Vehicle Suspension Systems
SAVSS	Semi-Active Vehicle Suspension Systems
SLMC	Sliding Mode Control
WBL	White Band Limited Noise
WBV	Whole Body Vibration

List of Symbols

Symbol	Definition	SI Units
	Quarter-Car Mathematical Model	
m_s	Chassis or sprung mass	kg
m_u	Wheel or unsprung mass	kg
k_s	Spring stiffness coefficient	N/m
b_s	Damping coefficient	Ns/m
F_a	Actuator force	N
F_k	Suspension spring force	N
F_b	Suspension damping force	N
F_t	Tyre force	
F_w	Disturbance transmitted by the road profile	N
k_s^l	Linear suspension spring constant	N/m
k_s^{nl}	Nonlinear suspension spring constant	N/m^3
b_s^l	Linear damping constant of suspension system	Ns/m
b_s^{nl}	Nonlinear suspension damping constant	$Ns^{1/2}/m^{1/2}$
b_s^{sym}	Symmetric suspension damping constant	Ns/m
w	Road profile	m
x_w	Wheel vertical deflection	m
x_c	Chassis vertical deflection	m
$\dot{x}_c$	Chassis vertical velocity	m/s
$\dot{x}_w$	Wheel vertical velocity	m/s
k_t	Tyre stiffness	N/m
$\ddot{x}_c$	Chassis vertical acceleration in quarter-car model	m/s^2
$\ddot{x}_w$	Wheel vertical acceleration in quarter-car model	m/s^2
	Quater-Car Hydraulic Parameters	
x_v	Spool-valve displacement	m
P_L	Load pressure in hydraulic actuator	Pa
u	Control input voltage	V
$\dot{m}$	Mass flow rate of working fluid	kg/s
ρ	Density of hydraulic fluid	kg/m^3
v	Velocity of hydraulic fluid	m/s

A_{hyd}	Cross-sectional area of hydraulic cylinder	m^2
V	Volume of hydraulic cylinder	m^3
P_s	Supply pressure	Pa
β	Bulk modulus of hydraulic fluid	Pa
Q_{piston}	Volumetric flow rate created by piston	m^3/s
$Q_{leakage}$	Volumetric flow rate of leaked fluid	m^3/s
C_{tp}	Coefficient of losses	$--$
Ω	Area gradient of spool valve	m
C_d	Coefficient of discharge	$--$
Q_l	Flow generated by the motion of the spool valve	m^3/s
$\dot{P}_L$	Rate of change of hydraulic pressure	Pa
Θ	Hydraulic parameter	$--$
K_v	Servo-valve gain	$--$
τ	Time constant	$--$

Full-Car Model Parameters

z	Displacement of centre of gravity of chassis	m
$\ddot{x}$	Body-heave acceleration	m/s^2
z_{fr}	Vertical displacement of the front right corner of the chassis	m
z_{fl}	Vertical displacement of the front left corner of the chassis	m
z_{rr}	Vertical displacement of the rear right corner of the chassis	m
z_{rl}	Vertical displacement of the rear left corner of the chassis	m
z_{tfr}	Vertical displacement of the front right wheel	m
z_{tfl}	Vertical displacement of the rear left wheel	m
z_{trr}	Vertical displacement of the rear right wheel	m
z_{trl}	Vertical displacement of the rear left wheel	m
θ	Pitch angular displacement of the chassis	rad
α	Roll angular displacement of the chassis	rad
$\ddot{\theta}$	Pitch acceleration	rad/s^2
$\ddot{\alpha}$	Roll acceleration	rad/s^2
F_{kfr}	Front right suspension spring force	N
F_{kfl}	Front left suspension spring force	N
F_{krr}	Rear right suspension spring force	N
F_{krl}	Rear left suspension spring force	N
F_{bfr}	Front right damping spring force	N
F_{bfl}	Front left suspension damping force	N
F_{brr}	Rear right suspension damping force	N
F_{brl}	Rear left suspension damping force	N

F_{afr}	Front right suspension actuator force	N
F_{afl}	Front left suspension actuator force	N
F_{arr}	Rear right suspension actuator force	N
F_{arl}	Rear left suspension actuator force	N
M_s	Chassis mass	kg
m_w	Wheel mass	kg
w_{fr}	Road profile at front right wheel	m
w_{fl}	Road profile at front left wheel	m
w_{rr}	Road profile at rear right wheel	m
w_{rl}	Road profile at rear left wheel	m
l_f	Lateral distance of the front suspensions	
	from the centre of gravity	m
l_r	Lateral distance of the rear suspensions	
	from the centre of gravity	m
a_f	Longitudinal length of the vehicle	m
I_θ	Pitch moment of inertia	$kg.m^2$
I_α	Roll moment of inertia	$kg.m^2$
k_{tfr}	Front right tyre stiffness	N/m
k_{tfl}	Front left tyre stiffness	N/m
k_{trr}	Rear right tyre stiffness	N/m
k_{trl}	Rear left suspension tire stiffness	N/m
b_{tfr}	Front right tyre damping coefficient	Ns/m
b_{tfl}	Front left tyre damping coefficient	Ns/m
b_{trr}	Rear right tyre damping coefficient	Ns/m
b_{trl}	Rear left suspension tyre damping coefficient	Ns/m
k^l_{sfr}	Front right suspension linear spring constant	N/m
k^l_{sfl}	Front left suspension linear spring constant	N/m
k^l_{srr}	Rear right suspension linear spring constant	N/m
k^l_{srl}	Rear left suspension linear spring constant	N/m
k^{nl}_{sfr}	Front right suspension nonlinear spring constant	N/m^3
k^{nl}_{sfl}	Front left suspension nonlinear spring constant	N/m^3
k^{nl}_{srr}	Rear right suspension nonlinear spring constant	N/m^3
k^{nl}_{srl}	Rear left suspension linear spring constant	N/m^3
b^l_{sfr}	Front right suspension linear damping coefficient	Ns/m
b^l_{sfl}	Front left suspension linear damping coefficient	Ns/m
b^l_{srr}	Rear right suspension linear damping coefficient	Ns/m
b^l_{srl}	Rear left suspension linear damping coefficient	Ns/m
b^{nl}_{sfr}	Front right suspension nonlinear damping coefficient	$Ns^{1/2}/m^{1/2}$
b^{nl}_{sfl}	Front left suspension nonlinear damping coefficient	$Ns^{1/2}/m^{1/2}$
b^{nl}_{srr}	Rear right suspension nonlinear damping coefficient	$Ns^{1/2}/m^{1/2}$
b^{nl}_{srl}	Rear left suspension nonlinear damping coefficient	$Ns^{1/2}/m^{1/2}$

b_{sfr}^{sym}	Front right suspension symmetric damping coefficient	Ns/m
b_{sfl}^{sym}	Front left suspension symmetric damping coefficient	Ns/m
b_{srr}^{sym}	Rear right suspension symmetric damping coefficient	Ns/m
b_{srl}^{sym}	Rear left suspension symmetric damping coefficient	Ns/m

Quarter-Car PID control

J	Performance index	$--$
y	Suspension travel	m
y_{max}	Maximum suspension travel	m
$\ddot{x}_{cmax}$	Maximum allowable heave acceleration	m/s^2
u_{max}	Input voltage limit	V
$(x_2 - w)_{max}$	Maximum specified wheel deflection	m
K_p	Proportional PID controller gain in outer control loop	$--$
K_I	Integral PID controller gain in outer control loop	$--$
K_D	Derivative PID controller gain in outer control loop	$--$
k_p	Proportional PID controller gain in inner control loop	$--$
k_I	Integral PID controller gain in inner control loop	$--$
k_D	Derivative PID controller gain in inner control loop	$--$

Differential Evolution

S	A population set of PID gains or DNN parameters	$--$
N	Number of individuals in population set	$--$
$\mathbf{x}_i$	A set controllers gains or network parameters	$--$
$\mathbf{y}_i$	A candidate solution for individual $\mathbf{x}_i$	$--$
$\hat{\mathbf{x}}_i$	A corresponding mutated individual $\mathbf{x}_i$	$--$
$\mathbf{x}_\alpha$	Randomly selected individual from S	$--$
$\mathbf{x}_\gamma$	Randomly selected individual from S	$--$
$\mathbf{x}_\beta$	Randomly selected individual from S	$--$
k	k^{th} parameter of individual of $\mathbf{x}_i$	$--$
R^k	Random number	$--$
C_R	Threshold value	$--$
F	DE parameter	$--$
$f(\mathbf{x}_i)$	Performance index of individual $\mathbf{x}_i$	$--$
$f(\mathbf{y}_i)$	Performance index of candidate solution $\mathbf{x}_i$	$--$

Genetic Algorithm

O	Offspring population set of PID gains or DNN parameters	$--$
N	Number of individuals in population set	$--$
$\mathbf{x}_i$	Set controllers gains or network parameters	$--$
$\mathbf{y}_i$	The i^{th} offspring from O	$--$
j	j^{th} reproduction carried out to create 2 more offspring	$--$
$\mathbf{x}_{aj}$	Randomly chosen individual to compute paternal parent	$--$
$\mathbf{x}_{bj}$	Randomly chosen individual to compute paternal parent	$--$
$\mathbf{P}_{1j}$	Paternal parent used for the j^{th} reproduction	$--$
$\mathbf{x}_{cj}$	Randomly chosen individual to compute maternal parent	$--$
$\mathbf{x}_{dj}$	Randomly chosen individual to compute maternal parent	$--$
$\mathbf{P}_{2j}$	Maternal parent used for the j^{th} reproduction	$--$
$f(\mathbf{x})$	Performance index or fitness value of $\mathbf{x}$	$--$
$\mathbf{y}_{1j}$	First offspring created from the j^{th} reproduction	$--$
$\mathbf{y}_{2j}$	Second offspring created from the j^{th} reproduction	$--$
NN	Number of offspring to be generated in each iteration	

Particle Swarm Optimzation

$\mathbf{x}$	A set of controller gains or network parameters	$--$
$\mathbf{x}_i$	The i^{th} individual in population	$--$
$\mathbf{V}$	Velocity population of population matrix $\mathbf{x}$	$--$
$\mathbf{V}_i$	Velocity vector of x_i	$--$
$\mathbf{P}_{best}$	Personal best matrix	$--$
$\mathbf{P}_{best_i}$	Personal best result of individual x_i	$--$
$\mathbf{G}_{best}$	Global best individual in population	$--$
w_1	Velocity inertial weighting	$--$
w_2	Local search weighting	$--$
w_3	Global search weighting	$--$

Controlled Random Search

n_r	Number of randomly selected individuals to comput centre of gravity	$--$
v_1	Randomly chosen individual to compute trial solution S	$--$
$\mathbf{G}_i$	Centre of gravity	$--$
$\mathbf{y}$	Trial individual S	$--$
$\mathbf{x}_w$	Weakest individual in population$S$	$--$

Pattern Search

A	Incremental spacing vector	$--$
$\mathbf{A}_i$	Increment of the i^{th} dimension	$--$
$\mathbf{w}_i$	Trial individual $\mathbf{x}_i$	$--$

Quarter-Car Intelligent Control

$\mathbf{x}$	Output of each neuron in hidden layer	$--$
$\mathbf{W}$	Hidden layer interconnecting weights	$--$
β	Time constant matrix	$--$
γ	Control input layer weightings	$--$
ζ	Delayed state input weightings	$--$
$\bar{x}_{t-1}$	Delayed states	$--$
$\mathbf{w}$	Weighting matrix in second hidden layer	$--$
n_n	Number of neurons in hidden layer	$--$
$\hat{y}$	Predicted output of the DNN	m
MSE	Mean squared error	$--$
r	Relative degree	
N	Number of samples used for DNN training	
$\mathbf{x}_i$	Output from the i^{th} neuron of the DNN's hidden layer	$--$
λ_0	Intelligent controller gain	$--$
λ_1	Intelligent controller gain	$--$
λ_2	Intelligent controller gain	$--$
υ	Virtual control input	
K_P	Proportional PID controller gain in outer control loop	$--$
K_I	Integral PID controller gain in outer control loop	$--$
K_D	Derivative PID controller gain in outer control loop	$--$
k_p	Proportional PID controller gain in inner control loop	$--$
k_i	Integral PID controller gain in inner control loop	$--$
k_d	Derivative PID controller gain in inner control loop	$--$

Full-Car PID Control

$\ddot{z}_{max}$	Maximum allowable heave acceleration	m/s^2
$\ddot{\theta}_{max}$	Maximum allowable pitch acceleration	rad/s^2
$\ddot{\alpha}_{max}$	Maximum allowable roll acceleration	rad/s^2
$(z_{fr} - z_{tfr)}{}_{max}$	Maximum allowable front right suspension travel	m
$(z_{fl} - z_{tfl)_{max}}$	Maximum allowable front left suspension travel	m
$(z_{rr} - z_{trr)_{max}}$	Maximum allowable rear right suspension travel	m
$(z_{rl} - z_{trl)_{max}}$	Maximum allowable rear left suspension travel	m
$(F_{ktfr} + F_{btfr)_{max}}$	Maximum allowable front right tyre dynamic load	N
$(F_{ktfl} + F_{btfl)_{max}}$	Maximum allowable front left tyre dynamic load	N
$(F_{ktrr} + F_{btrr)_{max}}$	Maximum allowable rear right tyre dynamic load	N
$(F_{ktrl} + F_{btrl)_{max}}$	Maximum allowable rear left tyre dynamic load	N
$F_{a_{max}}$	Maximum allowable actuator force	N

$u_{fr_{max}}$	Maximum allowable control input voltage at front right suspension	V
$u_{fl_{max}}$	Maximum allowable control input voltage at front left suspension	V
$u_{rr_{max}}$	Maximum allowable control input voltage at rear right suspension	V
$u_{rl_{max}}$	Maximum allowable control input voltage at rear left suspension	V
K_P	Proportional PID controller gain in outer control loop	$--$
K_I	Integral PID controller gain in outer control loop	$--$
K_D	Derivative PID controller gain in outer control loop	$--$
k_p	Proportional PID controller gain in inner control loop	$--$
k_i	Integral PID controller gain in inner control loop	$--$
k_d	Derivative PID controller gain in inner control loop	$--$

Full-Car Intelligent Control

$g_{1_{fr}}$	Delayed output weighting matrix for front right suspension	$--$
$g_{2_{fl}}$	Delayed output weighting matrix for front left suspension	$--$
$g_{3_{rr}}$	Delayed output weighting matrix for rear right suspension	$--$
$g_{4_{rl}}$	Delayed output weighting matrix for rear left suspension	$--$
$\gamma_{1_{fr}}$	Control input weighting matrix of for front right suspension	$--$
$\gamma_{2_{fl}}$	Control input weighting matrix of for front left suspension	$--$
$\gamma_{3_{rr}}$	Control input weighting matrix of for rear right suspension	$--$
$\gamma_{4_{rl}}$	Control input weighting matrix of for rear left suspension	$--$
$\hat{y}_j$	DNN predicted output of the j^{th} suspension system	
$\lambda_{0_{r_{ij}}}$	Feedback linearization controller gain of the i, j^{th} suspension	$--$
$\lambda_{1_{r_{ij}}}$	Feedback linearization controller gain of the i, j^{th} suspension	$--$
$\lambda_{2_{r_{ij}}}$	Feedback linearization controller gain of the i, j^{th} suspension	$--$
$\lambda_{3_{r_{ij}}}$	Feedback linearization controller gain of the i, j^{th} suspension	$--$
$\lambda_{4_{r_{ij}}}$	Feedback linearization controller gain of the i, j^{th} suspension	$--$
K_P	Proportional PID controller gain in outer control loop	$--$
K_I	Integral PID controller gain in outer control loop	$--$
K_D	Derivative PID controller gain in outer control loop	$--$
k_p	Proportional PID controller gain in inner control loop	$--$
k_i	Integral PID controller gain in inner control loop	$--$
k_d	Derivative PID controller gain in inner control loop	$--$

1 Introduction

1.1 Background

Vehicle suspension systems are a mechanical arrangement of dampers, springs and actuators that are placed between the wheel and the chassis with the objective of adding value to vehicles by improving ride comfort, suspension travel, vehicle handling, road holding and power consumption [Gillespie (1992)]. Enhanced ride comfort requires that inertial accelerations are kept below the threshold of human discomfort [International Organization for Standardization 2631 (2003)]. Lowering of the suspension travel is paramount so that it does not permanently deform or damage any vehicle components and exceed the physical constraints of the vehicle. Suspension systems reduce the roll and pitch accelerations and subsequently minimise the forces that adversely affect vehicle handling characteristics. They achieve improved road holding by absorbing and dissipating the forces exerted on the wheel, which is an important factor in wheel grip.

However, these tasks are in constant conflict with each other and a compromise is needed to manage these trade-offs. These conflicts are depicted in Figure 1.1 where a stiff suspension with minimal play is required to maintain adequate road holding and vehicle handling properties, whereas a soft and flexible suspension with greater allowance is desired to obtain improved ride comfort [Pedro et al. (2013a)]. Hence, the challenge in designing a vehicle suspension system is resolving these trade-offs for a given vehicle.

1.2 Types of Suspension Systems

Three types of suspension systems are currently employed to manage these aforementioned trade-offs. These include Passive-Vehicle-Suspension-Systems (PVSS),

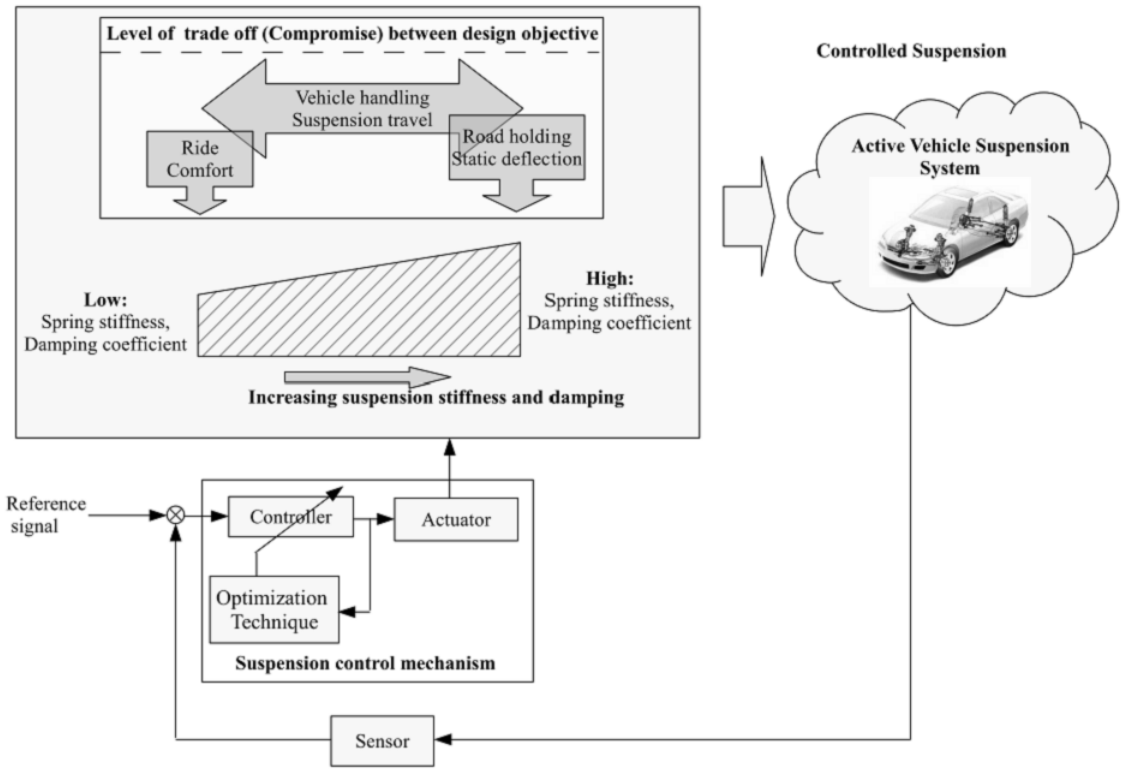

Figure 1.1: Trade-offs associated with suspension systems [Pedro et al. (2013a)]

Semi-Active-Vehicle-Suspension-Systems (SAVSS) and Active-Vehicle-Suspension-Systems (AVSS).

A PVSS comprises of a spring and damper assembly positioned between the chassis and wheel. Springs are designed to absorb and release forces transmitted from the road, whilst the dampers lower the rate at which these forces are transmitted to the chassis. Such a setup improves ride comfort and dampens out the system vibrations in a sinusoidal manner once the disturbance is removed. It has the potential ability to inevitably subdue any force that is transmitted to the vehicle. However, it takes considerably long to dampen out and produce a large number of oscillations once the disturbance is removed. It also tends to push the suspension travel to its limits with large peaks and root-mean-square (RMS) values; and its ride comfort properties usually fall into the "discomfort" range when the vehicle is subjected to severe but realistic disturbances [Gillespie (1992)].

SAVSS attempts to improve system performance by placing a controlled damper into the system. This device adjusts the damping ratio of the system in real time

and this offers the advantage of improving transient performance and settling time. However, it cannot absorb the forces transmitted from the road and hence it does not considerably improve upon ride comfort [Metered et al. (2010), Zapateiro et al. (2009)].

AVSS introduces a controlled actuator between the chassis and the wheel that provides a balancing force which attempts to cancel out any dynamics that were initiated by external disturbances or noise. The magnitude of this actuator force is regulated based on improving selected performance criteria. Figure 1.1 illustrates this concept where a selected performance criteria is observed and fed back to the controller which computes the necessary force required to dampen out the effect of an external disturbance. As a result, it possesses the strength of bringing the system to its desired setpoint significantly quicker after disturbances are removed. Additionally, it cancels out the forces that are transmitted to the vehicle and hence improves ride comfort. Furthermore, it may be manipulated in a specified manner to accomplish various design objectives. Optimization of AVSS may also be performed with the intent of finding the best compromise between the performance trade-offs associated with it for a specific application.

1.3 Challenges Associated with AVSS

In theory, the application of AVSS is promising, but designing an effective AVSS presents several challenges. This is due to the nonlinear nature of AVSS and complexities that arise from actuator dynamics. The major challenges in AVSS design include [Pedro and Dahunsi (2011)]:

1. Parameter uncertainties.
2. Limitations in power supply.
3. Actuator dynamics.
4. Degradation in system components due to chattering of actuators.
5. Rigorous tuning to acquire a suitable trade-off between conflicting performance criteria.

These challenges demand a well-designed linear, nonlinear or intelligent controller. A number of such controllers have been proposed in the literature by various authors.

1.4 Literature Review

The advent of soft computing, microprocessors and sensors has introduced a vast magnitude of both numerical and experimental studies on various AVSS control methodologies that can manage the challenges associated with it. These investigations are centred on specifically selected mathematical models that address certain design specifications and are aimed at finding a better compromise between various AVSS trade-offs. Control techniques employed up to date include linear, nonlinear, intelligent and optimal control policies, each of which possesses positive outcomes and shortfalls. The selection process of appropriate controllers may be synthesized into the following steps:

1. Choice of a mathematical model that can adequately capture the specified dynamics of the plant.
2. Selection of realistic design specifications.
3. Analyses of current AVSS controllers and associated gaps in literature.
4. Proposed controller architecture.

1.4.1 Classification of Mathematical Models

There are effectively three types of mathematical models used in AVSS design. They are quarter-car, half-car and full-car models; which aim to capture the dynamics of a single wheel, two wheels and four wheels respectively as shown in Figures 1.2 to 1.4 respectively. x_1 and x_2 are the vertical displacements of the chassis and the wheel respectively, k_s and b_s are the stiffness and damping of the suspension system respectively, and k_t denotes the stiffness of the tyre. z_c and θ denote the vertical displacement and angular rotation of the chassis respectively, z_{tf} and z_{tr} are the front and rear tyre vertical displacements, F_{ksr}, F_{ksl}, F_{bsr}, F_{bsl}, are the spring and damper force contributions of the respective suspension systems, and F_{ktr}, F_{ktl} are the corresponding spring and damping force load experienced within the tyre. Quarter-car models provide information on the vertical motion of the chassis and wheel and hence they provide information on the heave-related ride comfort, road

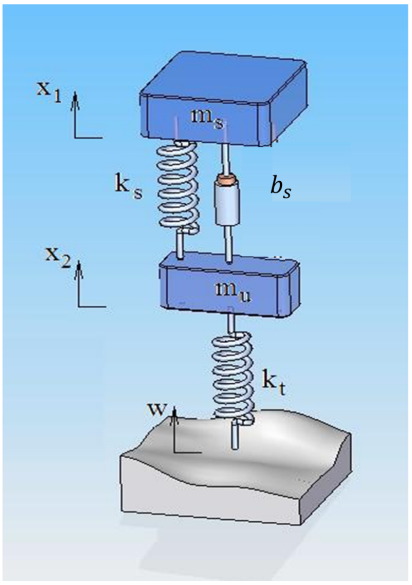

Figure 1.2: Graphical representation of the quarter-car suspension system model

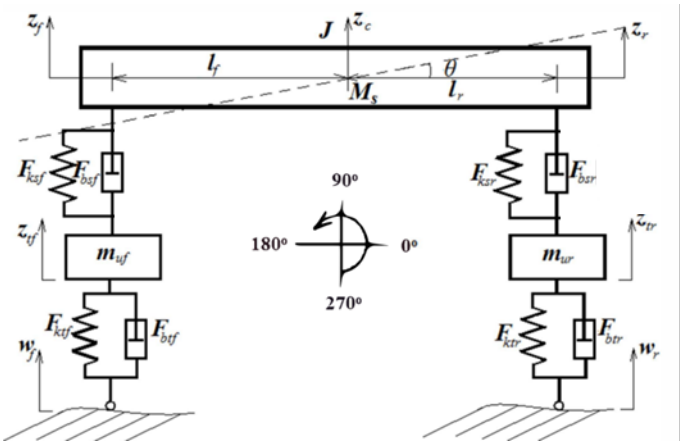

Figure 1.3: Illustration of the half-car configuration [Ekoru and Pedro (2013)]

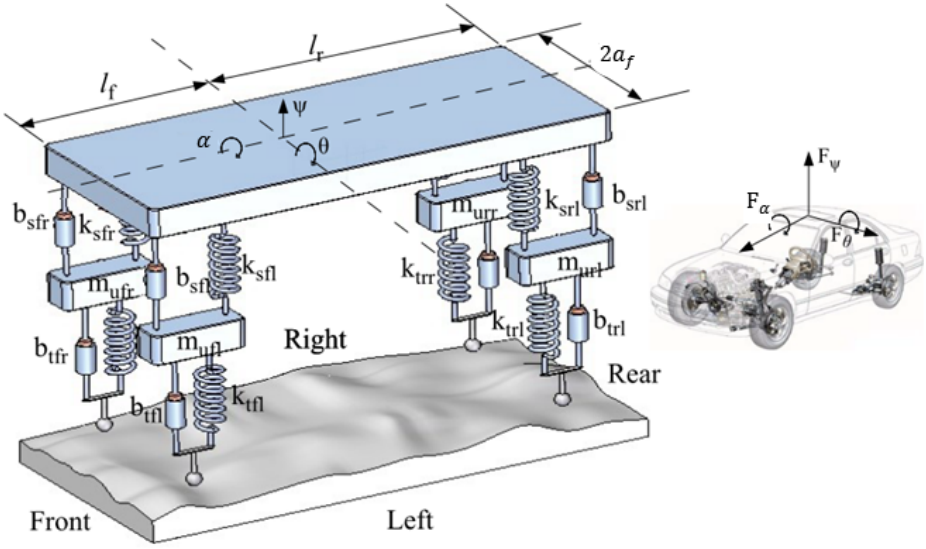

Figure 1.4: Schematic of the full-car model [Pedro et al. (2013a)]

holding and suspension deflection. The simple quarter-car models as opposed to its complex and realistic full-car counterpart has been considerably used in AVSS research, and this makes it a suitable platform to compare various control methods. Thus, a quarter-car study will be conducted in this investigation. Moreover, extensive analyses of quarter-car models are paramount when designing independent suspensions as such systems are effectively a combination of 4 quarter-car systems present at each wheel. Passenger seat dynamics may be also added to these models to enhance the realism of these studies [Spentzas and Kanarachos (2002)].

Quarter-car suspension system models do not capture lateral and longitudinal dynamics of the vehicle. Hence, its handling and sway-based ride comfort cannot be analysed from quarter-car suspension models. Half-car suspension models overcome this problem by extending the quarter-car framework into two coupled wheels. Thus, they are capable of capturing the pitch dynamics of the vehicle. Full-car models extend the quarter-car concept even further by interlacing four wheels such that information pertaining to both the roll and pitch dynamic of the vehicle may be obtained. Therefore, they can successfully acquire relatively more realistic data on the vehicle handling, suspension travel and ride comfort [Sapinski and Rosol (2008), Eski and Yildirim (2009)].

The coupling and large number of output parameters of the half-car and full-car models add further complexity to the mathematical relations and this adds new challenges in formulating a suitable control law and increases the multiplicity of

the optimization algorithm. However, these models are more representative of the actual vehicle suspension system dynamics compared to quarter-car models and control schemes based on the more complex full-car model will be investigated in this research project as well.

With regards to the modelling of the suspension components, spring and damper force contributions as well as the tyre dynamics contain both linear and nonlinear elements. Considerable research has been performed on linear systems as they provide a basic overview on the resulting performance of the vehicle. However, inclusion of nonlinearities is necessary to acquire a better understanding of these systems since springs and dampers are nonlinear by nature, contain hysteresis qualities, and are subject to degradation and deformation. Therefore, a nonlinear model will be utilised in this research [Pedro et al. (2011)].

Another fundamental issue pertaining to AVSS modelling is the inclusion of actuator dynamics. The vast majority of literature pertaining to AVSS tends to neglect actuator dynamics as it introduces nonlinearities, instabilities and complexities that are fairly cumbersome to deal with [Ekoru and Pedro (2013)]. In certain publications the actuator dynamics was partially ignored by replacing it with a time delay [Du and Zhang (2007)]. However, a complete mathematical description is necessary if it is desired to fully capture the realistic dynamics of the AVSS plant. Actuators that are currently employed in AVSS include:

1. Electrohydraulic: An electromechanical device such as a motor regulates the valve motion of the hydraulic cylinder, which in turn alters the flow and consequently affects the pressure and hence the force applied by the actuator onto the suspension system.

2. Electromagnetic: An electromechanical device adjusts the current flowing through the magnetic coils, which subsequently manipulates the magnetic force applied by an electromagnet against the suspension system.

3. Electromechanical: An electromechanical device forces a solid mechanical object to translate and consequently apply a restoring force to the suspension system.

Electrohydraulic suspensions are relatively sensitive in comparison with other actuators as a small change in input voltage produces a considerably large actuator

force, and this is desired in AVSS as it will reduce power consumption and improve precision. Moreover, considerable research has been dedicated to hydraulic actuator dynamics, which provides basis for comparison [Pedro and Dahunsi (2011), Aldair and Wang (2011)]. Hence, an electrohydraulic actuator will be utilised in this project.

1.4.2 Selection of Design Specifications

In order to evaluate the performance of an AVSS, the key performance criteria must be established and their design specifications and tolerances must be defined. The core factors that affect the performance of a vehicle suspension system are quantified as follows [Gillespie (1992)]:

1. Ride comfort: Body-heave acceleration.
2. Suspension travel: Degree of suspension extension and compression.
3. Road holding: Dynamic tyre load and tyre deflection.
4. Vehicle handling: Pitch and roll accelerations.

One of the methods in which the International Organization for Standardization 2631 (2003) quantifies ride comfort is by taking its root-mean-squared (RMS) value for body-heave acceleration for a specific time span as shown in Figure 1.5. The resulting RMS value is qualitatively described in terms of comfort for specific ranges of RMS values listed within Figure 1.5. For satisfactory ride comfort, the International Organization for Standardization 2631 (2003) indicates that the RMS value for body-heave, pitch and roll accelerations fall within the the "Fairly Uncomfortable" or "Not Uncomfortable" ranges described in Figure 1.5. Failure to fall within the "A little uncomfortable" range for the duration of the disturbance may cause serious harm to the human anatomy and may tend limit to the driver's concentration.

The degree of suspension travel should lie within the physical constraints of the suspension, and it should not cause the suspension system to damage and degrade. The tyre deflection should be kept close to zero as larger tyre deflections can cause the tyre to lift off the ground, which consequently reduces road holding. Adequate vehicle handling necessitates minimal pitch and roll accelerations. These accelerations tend to transfer the weight unevenly across the vehicle wheels and this consequently increases under-steer and over-steer, which results in poor handling.

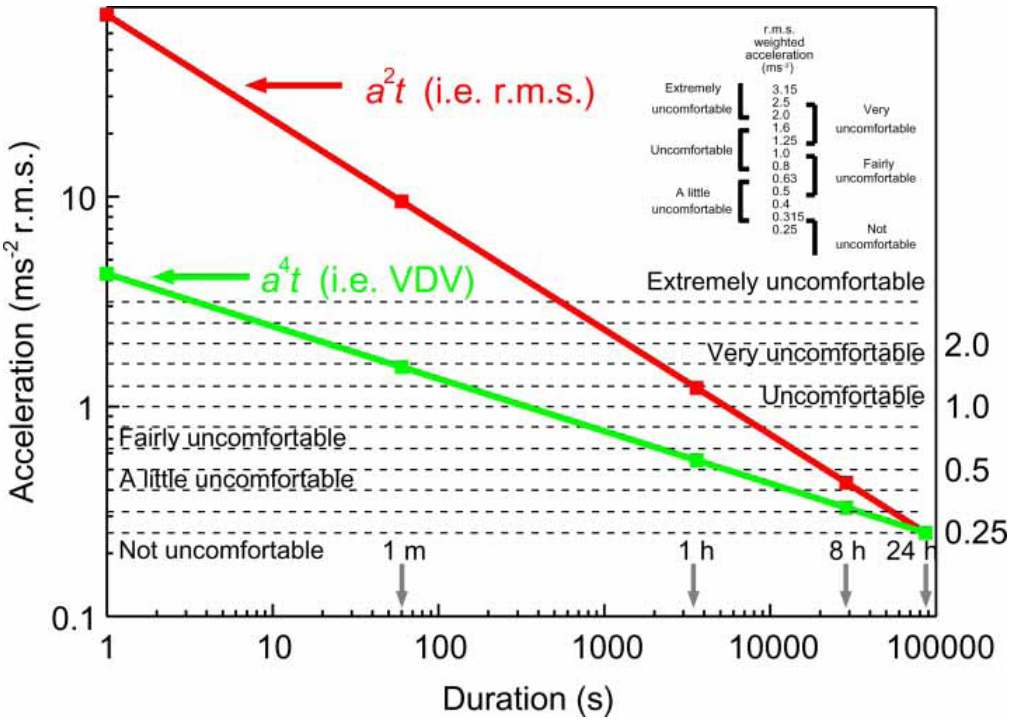

Figure 1.5: Graph summarising ride comfort as per ISO standards (Griffin (2007))

1.4.3 Analysis of Current AVSS Controllers in Literature and Associated Shortcomings

The primary objective of an AVSS is to manipulate the dynamics of the system in real time with the intent of achieving the desired performance. AVSS are closed-loop systems where feedback is relayed from the plant in the form of its controlled variable. Thereafter, the controllers alter the input based on the deviation between the actual value of the controlled variable and its corresponding setpoint. The structure of an AVSS control system is shown in Figure 1.6, where y is the controlled variable of the system and y_d is the desired input signal. The deviation between the setpoint and regulated variable is created from internal system noise, or disturbances induced upon the system. This may be due to the road profile or change in vehicle parameters such as mass, which occurs due to fuel and passengers. The controller may be linear, nonlinear or intelligent and the choice depends on the nature of the system as well as design specifications.

This control system has been setup up as either a Single-Input-Single-Output (SISO) or Multi-Input-Multi-Output (MIMO) configuration, where the input to the system is the control input in the form of a voltage to the actuator or a control force to

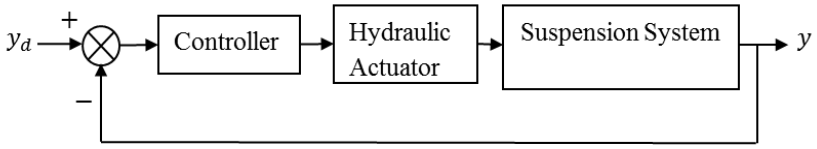

Figure 1.6: Basic AVSS control structure

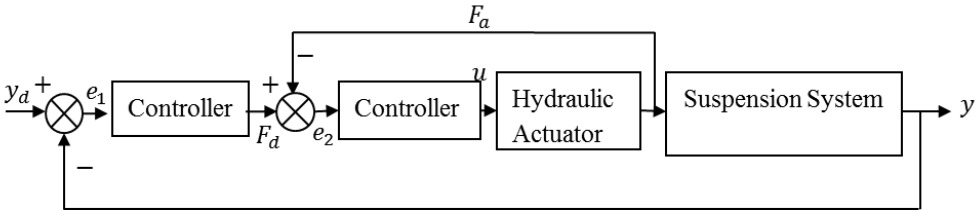

Figure 1.7: Schematic of multi-loop AVSS controller

the system without actuator dynamics. The output of the system may include suspension travel, body acceleration or road holding terms, depending on which output holds the greatest significance and best suits the design problem. In certain cases only suspension travel output was used and controller gains were tuned based on a performance index that included all other major system outputs. [Ekoru and Pedro (2013)]. This is an alternative method that involves all major system outputs while maintaining simplicity. This approach has been largely used for the additional reason that suspension travel is the major factor that is used to model the system.

Other investigations included multiple regulated system outputs to address all conflicting criteria together in real time [Amani et al. (2004), Turaky and Ackay (2011), Tuan et al. (2001)]. However, this adds complexity to the system in both the mathematical model and to intuitive reasoning in understanding the sensitivity of controller gains. Additionally, when dealing with nonlinear coupled systems, the conflicting performance criteria are increasingly rigorous to deal with and monitor. Furthermore, most of such control methods including H_2, H_∞ and linear matrix inequalities are linear control methods, and have proven fairly complex to tune when applied to nonlinear systems [Lin and Huang (2004)].

As previously discussed in section 1.4.1, actuators tend to destabilise the system and an inner loop that regulates the actuator force F_a to ensure that the desired actuator force is adequately tracked (see Figure 1.7) may be added to ensure that the system is not destabilized [Ekoru and Pedro (2013)]. The controller gains are

traditionally altered through a rigorous manual tuning process or by optimal routines which have received considerable attention since the advent of soft computing [Crews et al. (2011)]. These controllers may be further divided into 3 categories: linear, nonlinear and intelligent. Linear controllers formulate a control signal based on the control error and system states, whereas nonlinear controllers generate a control signal based on the mathematical relations, and the intelligent controller derive the control signal based on artificial neural networks, intuitive knowledge and mathematical relationships [Pedro et al. (2013a)].

1.4.3.1 Linear Control

Linear control methods such as Proportional-Integral-Derivative (PID) [Ekoru and Pedro (2013), Wai et al. (2011), Crews et al. (2011), Chiou et al. (2012), and Rajeswari and Lakshmi (2010)]; optimal linear control laws (LQR and LQG) [Pedro and Mgwenya (2004), He and McPhee (2005), Chen et al. (2011), and Kloiber et al. (2010)]; robust linear control methods (H_∞ and H_2) approaches [Fallah et al. (2009), Ryu et al. (2008), Du and Zhang (2007), and Poussot-Vassal et al. (2006)] have been incorporated in AVSS.

PID-based controllers are the most widely used in industry as they offer simple solutions to linear control systems, where system overshoot and rise time may be altered by adjusting the gains. However, their applicability to nonlinear systems is limited as nonlinearities limit system performance robustness against parameter variations. As a result, adaptive linear controllers are often required to overcome these obstacles.

LQG and LQR utilise the Ricatti and Jacobi-Bellman and Guassian formulations to derive an optimal policy that forces the system to reach its goal while incurring the lowest cost in specific performance criteria [Chen et al. (2011)]. Hence, they are suitable for resolving the inherent AVSS trade-offs if applied correctly [Hrovat (1997)]. The success of these optimal control techniques on linear systems has seen the development of reinforced variants of LQG and LQR controllers [Marzbanrad et al. (2004), Lu et al. (2007), Corona et al. (2004)]. However, these aforementioned formulations are derived on the assumption that the system is linear and thus their applicability breaks down once nonlinearities are introduced. H_∞ and H_2 controllers compute the control law based on the state with the largest control error and the root-mean-squared control error of all the states respectively. These controllers did prove to be rather sensitive and attaining a stable system proved rather challenging

[Yamashita et al. (1994)]. Furthermore, when dealing with a coupled multi-degree of freedom system; additional decoupling procedures had to be introduced to design the control system [Hayakawa et al. (1999)]. A hybrid H_∞ and linear matrix inequality strategy was proposed by Chen and Guo. (2005), and Tuan et al. (2001) to augment and improve the performance of conventional H_∞ controllers. This method offered the advantage of addressing all system states individually as well as the root-mean-squared control error of all system states. This level of accountability effectively achieved a better resolve between the various conflicting performance criteria of AVSS. In each of these investigations, the system was approximated as linear and hence the realism and applicability of such control methods is highly limited unless the system is linearized.

Nevertheless, extensive research into the applications of linear control schemes to AVSS has been investigated as they are simple by nature and they tend to provide reasonably acceptable results. In the majority of these cases, the actuator dynamics are often neglected. Such a model is not accurate as AVSS are highly nonlinear by nature and are often destabilised by the inclusion of actuator dynamics [Ekoru and Pedro (2013)].

The simplicity and success of PID controllers in enhancing AVSS performance have made them suitable candidates for optimization techniques which incorporate cost functions to resolve conflicting performance criteria. Hence, extensive research has been conducted to optimise PID-controlled AVSS using evolutionary algorithms such as Genetic-Algorithms (GA), Particle-Swarm-Optimization (PSO) and Differential-Evolution (DE). Most of these algorithms are heuristic procedures, which have been inspired by nature and do not require any function based methods to find minima [Crews et al. (2011)]. Moreover, evolutionary algorithms have been applied to select controller gains to augment the performance of AVSS which were based on LQG and impedance control [Fateh and Zirkohi (2011) and Lu et al. (2007)]. In addition, the success of these methods has been extensively examined and analysed for nonlinear systems and it has been found that these optimization approaches are indeed applicable to Multi-Input-Multi-Output (MIMO) systems. Moreover, global optimization algorithms such as those of evolutionary algorithms have proven useful in computing problem variables and dealing with parameter changes for nonlinear systems [Menon et al. (2008)].

Wai et al. (2011), Crews et al. (2011), Chiou et al. (2012), and Rajeswari and Lakshmi (2010) implemented evolutionary algorithm-based optimization techniques to select PID gains for single loop AVSS. They managed to improve upon the AVSS trade-offs better than conventional tuning methods. However, these authors only considered linear components and did not account for actuator dynamics. Furthermore, the cost functions of these algorithms did not address all the trade-offs associated with AVSS but rather focused only on some compromises. In relation to optimal LQG design, He and McPhee (2005), Chen et al. (2011), and Kloiber et al. (2010) utilised GA to select LQG parameters whilst searching for the optimal policy. This method proved successful with an improvement to the conventional approach, but these investigations also lacked realism as linear elements were only used and actuator dynamics were not considered.

Apart from AVSS, heuristic optimization algorithms have been applied to select controller gains for servo-hydraulic actuators. Sarkar et al. (2013) and Kim and Lee (2006) implemented GA to select PID gains for tracking control of an electrohydraulic system, where the performance index was aimed at minimizing the integral tracking error. Results proved to be superior to the non-optimized PID controllers with a 50% improvement in system performance. Elbayomy et al. (2008) proposed a GA-based PID control to improve system response to a step input. Aly (2011) extended this concept for a tracking problem as well. They both used the integral control error as the performance index and attained favourable results with the GA, which performed better than its non-optimized counterpart. Wu et al. (2012) developed a modified variant of GA to select controller gains of a PID-based electrohydraulic system to manage a step input. The performance index in this case addressed both power consumption, control error and the rate of change of the control error. Both the GA and its modified variant attained reasonable results with the modified GA performing better. It may be concluded from these research studies that global optimization methods performed reasonably well in computing controller gains for both active vehicle suspension systems without actuator dynamics as well nonlinear electrohydraulic systems with varying performance indices. Thus, they do possess the potential to simultaneously improve system performance as well as resolve conflicting trade-offs challenge in nonlinear AVSS with electrohydraulic actuator dynamics.

In light of the preceding discussion, the following conclusions may be drawn: firstly PID have been used extensively in linear AVSS and will thus serve as a good benchmark for comparison. Secondly, AVSS is a multi-objective design process since there are several trade-offs associated with AVSS that need to be resolved. Hence in order to better resolve AVSS trade-offs, the cost function needs to be refined to include all the AVSS compromises: ride comfort, road holding, vehicle handling, suspension travel, and power consumption. Thirdly, no application of global optimization-based PID controller tuning to nonlinear AVSS that includes actuator dynamics could be found. It is therefore concluded that this area has not been investigated thoroughly or not investigated at all. This is therefore a gap in literature that needs to be explored.

Additionally, several other optimization algorithms such as Pattern-Search (PS) and Controlled-Random-Search (CRS) have never been applied to AVSS, but have shown promising results for optimization of various control systems. Kolda et al. (2003) in particular proved that pattern search is an effective routine in solving problem variables for nonlinear system. ElMadany et al. (1990) incorporated PS to find the optimal gain matrix for a semi-active suspension.

Price (1983) first introduced the concept of CRS and applied them to select optimal design parameters for various electrical systems. Convergence characteristics of CRS has been discussed by Ali (1994), who argued that optimization through CRS is an effective approach in dealing with complex nonlinear and coupled systems. Ali et al. (1997) performed CRS-based optimization to control a nonlinear continuously stirred tank reactor (CSTR), whilst Jeżowski et al.(2005) implemented CRS to locate the minimum of a nonlinear multimodal problem. These findings suggest that CRS is an adequate optimization algorithm that can be applied to nonlinear problems such as AVSS. This research will be much complex than previous AVSS linear controllers and other nonlinear control systems as it will include actuator dynamics and hence possess more states and will therefore contain a greater degree of coupling which cannot be handled effectively by linear control laws.

A shortfall of linear controls in general is that they are non-adaptive by nature, and this makes them unreliable and sensitive when dealing with nonlinear systems which contain a vast degree of parameter variations. Sensitivity to parameter variations is a major design challenge in AVSS design as vehicles are subjected to variations

in mass since passengers and fuel alter the weight of the vehicle substantially. Furthermore, tyres lose air pressure, components degrade over time, and different road disturbances are encountered. Hence an adaptive intelligent controller is required to make the AVSS increasingly robust under these conditions.

1.4.3.2 Nonlinear Control

Nonlinear and intelligent controllers are adaptive by nature and this gives them the inherent qualities to deal with nonlinearities and subsequently produce a control system with a satisfactory sensitivity to parameter uncertainties variations. These controllers limit the effects of system nonlinearities and this makes it simpler to resolve the AVSS trade-offs and enhance system response.

AVSS have been designed based on nonlinear control policies such as backstepping, Sliding-Mode-Control (SLMC) and Feedback-Linearization (FBL) [Yagiz and Sakman (2005), Shi et al. (2010), Huang et al. (2000), Lin and Huang (2004), Sam and Hudha (2006), Koshkouei and Burnham (2008), Yahaya et al. (2004), Chamseddine et al. (2006), Yagiz and Hacioglu (2008)]. In contrast to linear controllers, nonlinear control methods generate an input that aims to remove or significantly reduce the effects of nonlinearities in the system. As a result, nonlinear induced issues such as sensitivity to parameter variation and instability are significantly resolved. However, these methods contain added issues such as complexity and instability.

FBL and backstepping control laws are structured on lie algebra and recursion respectively. In order for them to be applied, the system should be input-output linearizable; and secondly zero dynamics are created which may be unstable, which in such cases may be impossible to resolve. When backstepping control is applied to nonlinear systems with a degree greater than 3 and which contain actuator dynamics, there is a large degree of coupling between states and complex interlaced backstepping is required to generate a suitable control law, which in some cases may be impossible to compute [Kaddissi et al. (2009)]. Furthermore, the dynamics of the system needs to be fully understood as the control law is based entirely on the mathematical model of the system. In reality, the system cannot be modelled perfectly due to lack of experimental data and the degradation of components. Nevertheless, these control laws have been used in AVSS design.

Shi et al. (2010) incorporated SLMC to a nonlinear hydro-pneumatic AVSS model which was linearized using FBL. Their results showed significant improvements in both ride comfort and road holding as compared to the PVSS case. There was also an improved level of parameter sensitivity, where system response was adequate for a variety of road disturbances. Minsta et al. (2012) applied FBL to improve tracking control of an electrohydraulic servo system with pressure uncertainty. These results highlight the fact that nonlinear control greatly reduces the effects of parameter uncertainties and variations. Yagiz and Sakman (2005) and Chamseddine et al. (2006) conducted SLMC on a nonlinear full-car system and were able to achieve superior responses in each performance facet as compared to linear control laws. However, in these studies, a large degree of chattering was reported and this was attributed to the sudden change of control surfaces that is often done in SLMC.

Huang et al. (2000) and Lin and Huang (2004) controlled a half-car magnetic AVSS using an adaptive backstepping control scheme. Their model additionally provided a satisfactory bandwidth that was able to reject a large range of road disturbances, which drastically improved the operating range of this suspension system as compared to an AVSS that was controlled using linear control schemes.

Yagiz and Hacioglu (2008) utilised a backstepping controller for a full-car suspension system. The ride comfort of the vehicle improved significantly as compared to passive suspension systems for a variety of input disturbances. This again highlights the fact that nonlinear controllers improves the system's sensitivity to parameter variations. However, the actuator forces were significantly high at low input frequencies. These results show that there is a need for an optimal control policy that can reduce the high power consumption of currently employed controllers.

The major drawback of nonlinear control policies is twofold. Firstly, deriving the control law ensuring stability is challenging and not always possible. This is because non-trivial zero dynamics may arise when the system output is forced to zero and the system may possess positive real roots causing the system to diverge. This adds further complications in selecting controller gains. Secondly, the mathematical model of the system and each component must be fully understood. However, this may not be possible due to the lack of experimental data and intuitive knowledge. Hence, a control law that can easily bypass these limitations is often desired. Intelligent control laws have been suggested and successfully implemented to resolve

these issues.

1.4.3.3 Intelligent Control

Intelligent control laws such as Fuzzy-Logic-Control (FLC) and neural network-based control (NN) may be utilised to solve the problems associated with both linear and nonlinear controllers and have been applied to AVSS [Tang et al. (2009), Eski and Yildirim (2009), Alfi and Fateh (2011), Aldair and Wang (2011), Guclu and Gulez (2008), Pedro and Dahunsi (2011), Pedro et al. (2011) , Zapateiro et al. (2009), Yildirim (2004), Lin et al. (2009), Al-Holou et al. (2002), Rajeswari and Lakshmi (2010), Pekgökgöz et al. (2010), Moon and Kwon (1998), and Chiou et al. (2012)]. Both these policies emulate the human brains ability to control highly nonlinear processes.

FLC uses intuitive reasoning to derive an adaptive control law that regulates nonlinear systems more effectively. However, sufficient intuitive knowledge is required to formulate such laws and these may be limited by lack of experimental data [Behera and Kar (2009)]. However, due to a vast amount of experimental and numerical modelling, sufficient insight into AVSS has been established. Hence intuitive reasoning-based control such as FLC has been applied to AVSS.

In relation to FLC, there has been an improvement in system performance as compared to passive suspension systems and PID-controlled AVSS [Lin et al. (2009)]. It has achieved an improvement in ride comfort and road holding for a range of disturbances compared to linear controllers, and this highlights the ability of FLC to deal with different operating conditions.

FLC has been used in hybrid control schemes to attain improved performance. It has been combined with neural networks to improve its robustness. Lian (2013) and Aldair and Wang (2011) proposed a hybrid neuro-fuzzzy controller. They realised that the control structure performs better than a PID-based control architecture, which makes it more suitable for active suspension systems. Furthermore, considerable knowledge of the mathematical model is not fully required since the neural networks can easily be trained to learn the system dynamics. Al-Holou et al. (2002) and Yagiz et al. (2008) utilised a hybrid SLMC and FLC which generated improved

performance as compared to a conventional SLMC. Moreover the chattering that occurs due to the switching of control surfaces was substantially reduced.

In order to resolve the issues of nonlinear control schemes with regards to adequate modelling, coupling and zero dynamics, a neural network is trained to learn the dynamics of the system and nonlinear control techniques are subsequently employed on theses neural networks to formulate a suitable control law. Neural networks possess two major advantages: firstly, it has the ability to both accurately predict any nonlinear system provided there are enough inputs and neurons; and secondly, its simplicity allows for various nonlinear control laws to be formulated based upon it without considerable complexity and issues associated with conventional nonlinear control. However, the coupling of higher-order systems causes the identification process to become increasingly cumbersome and rigorous [Garces et al. (2003)].

There are two types of neural networks: static and dynamic. Static networks are feedforward neural networks whose neurons are modelled using algebraic equations and those of DNN models contain feedback or recurrent elements and are modelled using differential or difference equations.

With regards to the application of neural network-based control to AVSS, intelligent controllers using multilayer neural networks in system identification and control have improved the vehicle's response as compared to the PVSS. Tang et al. (2009) investigated the performance of a half-car AVSS that was controlled using a multilayer feedforward neural network and GA. There was an improvement in the passenger's vertical displacement response as compared to that of the PVSS.

In terms of training a multilayer neural network through particle swarm optimization for an AVSS, Alfi and Fateh (2011) showed that this method performs better than the conventional neural network training algorithms with quicker convergence speeds, improved accuracy, and had no premature convergence problem.

Guclu and Gulez (2010), and Aldair and Wang (2011) utilised network inversion to control a full-car nonlinear suspension system with actuator dynamics. The neural network controllers for each case displayed superior performance as compared to the PVSS. Eski and Yildirim (2009) also used an adaptive multilayer neural network to

create a robust PID controller for a full-car AVSS model. Their model displayed high identification and tracking capabilities as compared to offline supervised learning algorithms.

Pedro et al. (2011) designed a direct adaptive neural network-based FBL controller for nonlinear quarter-car AVSS using radial basis function neural network (RBFNN). However, the model did not contain any actuator dynamics and ignored zero dynamics that may exist as a result of FBL. The ride comfort and road holding improved as compared to the PVSS and PID-based AVSS. Additionally, the power consumption (or actuation force) was larger for the direct-adaptive neural network case. Pedro and Dahunsi (2011) later utilised a multilayer feedforward neural network to perform direct adaptive control of a servo-hydraulic nonlinear AVSS using FBL. They considered subsequent zero dynamics and their resulting system displayed superior performance as compared to the case where linear controllers were used. The fact that they were able to ensure stability of the zero dynamics for such a system infers that FBL control is possible for both quater-car and full-car AVSS.

Due to the success of FLC and neural network-based control in AVSS, they have been augmented with optimization algorithms to improve system performance. Rajeswari and Lakshmi (2010), Pekgökgöz et al. (2010), Moon and Kwon (1998), and Chiou et al. (2012) used evolutionary algorithms such as PSO and GA to derive the membership functions of a FLC. This method was successful in improving a particular performance criterion such as body-heave acceleration with larger success than a PID controlled system. However, the cost function of these investigations was centred on one objective only such as ride comfort or suspension travel, whereas AVSS is a multi-objective design problem as it contains various trade-offs and compromises. As previously mentioned, this research project will improve upon this weakness by including all the AVSS trade-offs in the objective function of these optimization algorithms. In relation to electrohydraulic systems, Wang et al. (2011) applied GA to determine FLC controller gains for a hydraulic excavator which addressed a complex performance index containing control error, fuel consumption, excavator power output and motor power output. The conflicting trade-offs between these performance criteria were better resolved than what was attained through manual tuning. Such results infer that evolutionary algorithms do indeed have the potential to find a compromise between conflicting performance criteria of a typical vehicle suspension system. Yao et al. (2013) made use of PSO to both learn the system dynamics of the plant and to tune the resulting neuro controller of an electrohydraulic system. They

reported positive results which highlight than heuristic global optimization methods are effective tools for tuning of intelligent controllers.

With regards to DNN models, the advantage of using differential equations in contrast to algebraic equations is that the neuron would then represent a band-pass filter. This will improve its performance since it can now filter out a range of unwanted road disturbances. It also has the advantage of modelling a large range of nonlinear characteristics such as oscillations, chaos and outliers. The problem with static neural networks is that it cannot account for outliers whereas a DNN is able to do so since it filters out the signals that create these outliers. The feedback associated with DNN models allows it to store information in memory. Moreover, it is mathematically simpler to formulate nonlinear control laws such as FBL on a DNN as opposed to conventional static neural networks. Furthermore, stability can be guaranteed much easier as compared with static neural networks [Garces et al. (2003), Nϕrgaard et al. (2000), Gupta et al. (2003)].

Research into the effectiveness of DNN models in AVSS applications is limited. This is because the less complex static neural networks have performed adequately well for a wide range of vehicles. On the other hand, DNN models have been incorporated into various control systems, which will be discussed in the remainder of this subsection. Hence, in order to fill this gap in AVSS design, a DNN will be considered for this investigation.

With regards to the use of neural networks that included recurrent elements for AVSS, Yildirim (2004) designed a recurrent neural controller for a linear quarter-car bus suspension without any actuator dynamics. Zapateiro et al. (2009) performed neural network-based backstepping control on a semi-active suspension that utilised a magnetorheological (MR) damper. Metered et al. (2010) performed neural network inversion control of a MR-based semi-active suspension that was learnt using a recurrent neural network. However, these recurrent neural networks were structured using algebraic equations as opposed to differential equations used in conventional DNNs.

In terms of the applications of DNN models in control system applications, a positive view has been established. Research has been done on a class of nonlinear systems. These include continuously stirred tank reactors (CSTR), flexible robotic

manipulators and evaporator systems. Becerikli et al. (2003) presented a DNN to identify and control a CSTR using a feedback controller. The system displayed adequate performance in the presence of a wide range of disturbances. The start-up and regulation problems of CSTR were resolved better with this configuration as compared to the currently employed control schemes for CSTR tanks.

Al Seyab and Cao (2008) created a DNN to identify a double CSTR plant. They thereafter controlled the system using a robust controller. The identification and system performance were compared to other model predictive control techniques. It was concluded that the DNN decreased the training time and improved the accuracy in the identification process as compared to conventional model predictive control configurations. Li (2011) successfully identified a distillation plant with DNN models and applied it in conjunction with a nonlinear H_∞ controller to augment system performance.

Nanayakkara et al. (2002) utilised a DNN to identify an evaporator. The network was trained using an evolutionary algorithm. This network performance was compared to static networks architectures. The results were then verified using experimental data. It was concluded that the DNN needed less nodes and inputs to accurately predict the plant.

Tian and Collins (2004) introduced a DNN to identify a flexible manipulator system that was controlled using FLC. The neural network was able to identify the plant to a large degree of accuracy and it was also able to track a given trajectory. Their results showed improved performance as compared to conventional controllers. Rodriguez and Yu. (2012) applied an adaptive DNN-based control scheme for a two-link robotic manipulator and achieve improved performance compared to currently employed controllers. Garces et al. (2003) utilised DNN-based FBL controller (DNNFBL) for a variety of control systems. In each case, the network was trained using genetic algorithm and the response of the system displayed superior results as compared to conventional control architectures. Additionally they noticed that this control law can be implemented with linear control such as PID to improve system response. Wang and Chien (2012) developed a generic DNN to be applied with iterative learning control for a class of nonlinear systems.

It is worth mentioning that the complexity of the models used in the DNN-based control methods were fairly simple with a few number of system states. On the other hand, DNN-based control of complex nonlinear coupled systems with a large number of system states such as those of the quarter-car and full-car models have never been attempted before. Thus, it will be worth investigating how these DNN models cope with such systems.

In light of the foregoing discussion, an intelligent controller that can deal with this inherent lack of intuitive and experimental knowledge is required to sufficiently model the AVSS plant. Artificial-Neural Networks (ANN) have been suggested by many authors as they can be trained to learn the dynamics of any nonlinear plant. Furthermore, they can be incorporated with nonlinear control strategies to negate the effects of nonlinearities and they may be further augmented with optimized linear controllers to achieve superior performance [Pedro and Dahunsi (2011), Garces et al. (2003)]. DNN models which apply differential equations in contrast to algebraic equations in particular have not been applied to the AVSS. Thus, in order to add novelty to this project, a DNN modelled on differential equations is proposed. It is also argued that the simple structure of DNN allows it to be easily linearized using FBL with the goal of attaining superior performance [Garces et al. (2003), Gupta et al. (2003)]. Hence, DNNFBL would be an innovative and potentially excellent control methodology for AVSS.

In conclusion, a hybrid control strategy involving PID and DNNFBL could be an effective tool in AVSS design. Furthermore, optimization algorithms may be applied to this control law with a cost function including ride comfort, road holding, vehicle handling, suspension travel, and power consumption to best resolve the inherent compromises of AVSS.

1.4.4 Gaps in Literature

The gaps in the current literature that need to be adressed may be summarized as follows:

1. A vast amount of research concerning FBL and neural networks is limited to quarter-car AVSS and insufficient research has been conducted on full-car models.

2. Nonlinearities and actuator dynamics are often neglected.

3. Optimization-based control laws for systems which included nonlinear AVSS with actuator dynamics have not been considered.

4. Currently employed optimal control techniques do not simultaneously address all the conflicting performance criteria of vehicle suspension systems.

5. Nonlinear electrohydraulic AVSS quarter-car and full-car models have not been identified using DNN techniques.

6. FBL has not been applied with DNN for vehicle suspension systems in particular.

1.5 Proposed Controller Architecture

In this research study, examination of both quarter-car and full-car models will be conducted. The case of the quarter-car is a single-input single-output (SISO) system where the input will be the control voltage supplied to the actuator and suspension travel will be selected as the output or controlled variable. For the full-car model, the control system is a multi-input multi-output (MIMO) system shown in Figure 1.8. The controlled variables $\mathbf{y}$ from the plant will be suspension travel output at each wheel. The setpoints of the system outputs $\mathbf{y_d}$ will be set to zero and will address a regulation problem.

An indirect adaptive intelligent control will be implemented for the AVSS. A Dynamic-Neural-Network (DNN) will be used to identify the dynamics of the plant. The DNN will be trained using evolutionary algorithms. Thereafter, FBL will be performed on the DNN model in order to obtain a feedback law that will remove all nonlinearities in the system. The deviation between the outputs and their setpoints will be passed through a multi variable PID controller. The controllers will be tuned manually or through optimization methods which operate by minimising a performance index J with the objective of achieving a compromise between road holding, ride comfort, vehicle handling and power consumption. In the case of PID-based optimization, the DNN and FBL controller are bypassed and optimization is conducted on the PID controllers only.

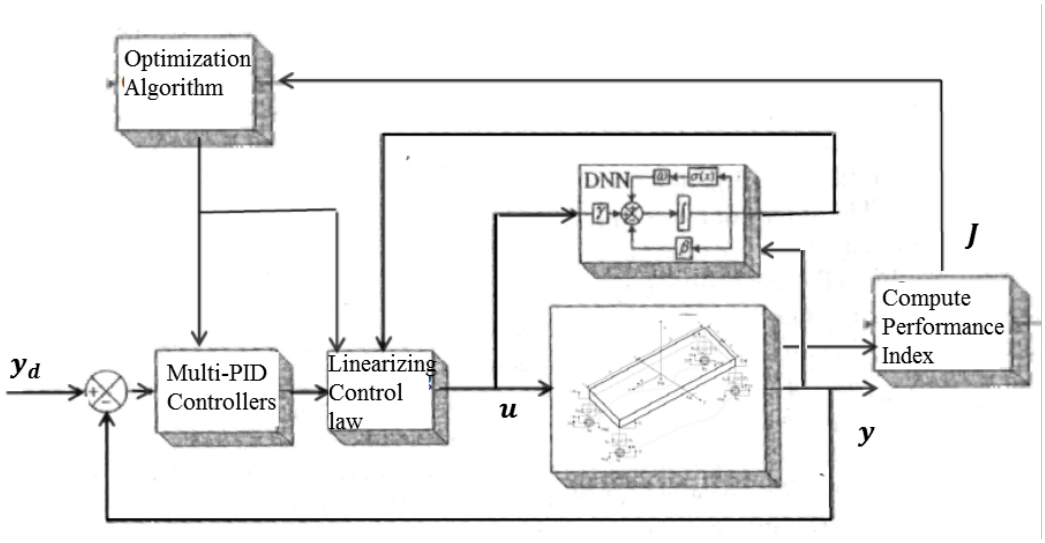

Figure 1.8: Proposed network architecture

1.6 Research Objectives

In accordance with the gaps in current AVSS design, the following objectives are proposed to resolve these issues:

1. Implement an optimal PID controller for the AVSS to improve upon the most widely used PID-based AVSS with the intention of resolving its trade-offs.
2. Successfully identify the nonlinear system using DNN techniques in order to predict the response of the system without the need of any mathematical modelling.
3. Develop an intelligent controller that performs FBL on the identified system with the purpose of removing system nonlinearities and system instability.
4. Augment the neural network-based FBL controller with a PID controller with the intent of achieving improved performance.
5. Optimise the hybrid PID and DNNFBL controller in order to better resolve AVSS trade-offs.
6. Test the designed intelligent controller for sensitivity to parameter variations and uncertainties.

1.7 Design Assumptions

The constraints imposed due to the schedule of the project as well as the lack of experimental data dictate that several assumptions be made to form a compromise with these margins. Such assumptions include:

1. The wheel and chassis are rigid structures.
2. The chassis and wheel assembly has a uniform mass distribution.
3. Ideal components are used and the connections between joints are ideal.
4. Vibrations that are induced by the engine and other components apart from the suspension system are ignored.
5. The nonlinear dynamics of the tyre are neglected.

1.8 Research Questions

Based upon the objectives of this project, the following research questions will be thoroughly investigated:

1. Can global optimization-based controller tuning for PID and DNNFBL controllers improve vehicle suspension performance criteria.
2. What is the most effective global optimization method to be used for controller tuning.
3. Are DNN models capable of learning the nonlinear quarter-car and full-car suspension dynamics.
4. How does the optimized PID-based and hybrid intelligent DNN controllers perform relative to one another.

1.9 Research Strategy and Methodology

This project can be broken down into several tasks which include literature review, system modelling, controller design, simulation and the dissertation writing. The following tasks will be carried out:

1. The mathematical modelling will be performed for a quarter-car and full-car system. The model will include nonlinear elements and consider electrohydraulic actuator dynamics.
2. The performance specifications, disturbance inputs and the model parameters will be selected based on real life scenarios.
3. A linear PID controller will be tuned using global optimization algorithms with the aim of improving the trade-offs that is associated with the AVSS.
4. An indirect adaptive optimal intelligent controller will then be designed to improve upon the linear controller. The plant will be identified using a DNN approach.
5. FBL will then be employed to linearize the dynamics of the system.
6. Linear control techniques such as PID control will be incorporated to control the system.
7. The resulting controller will be tuned using an evolutionary algorithm.
8. Numerical simulation will be carried out in Matlab/Simulink.
9. The performance of the intelligent controller will be compared to the optimized PID controller.
10. A dissertation will be drawn up.

Figure 1.9 shows the methodology to be followed in this investigation.

1.10 Contributions to Knowledge

The envisaged contributions to knowledge from this research are as follows:

1. Optimization of PID control scheme for a electrohydraulic nonlinear AVSS with the aim of attaining optimal trade-offs amongst the conflicting performance criteria.
2. Learning of the dynamics of the full-car electrohydraulic AVSS using DNN.
3. Training of the DNN using global optimization algorithms.
4. Application of an indirect adaptive DNN approach based on FBL controller.

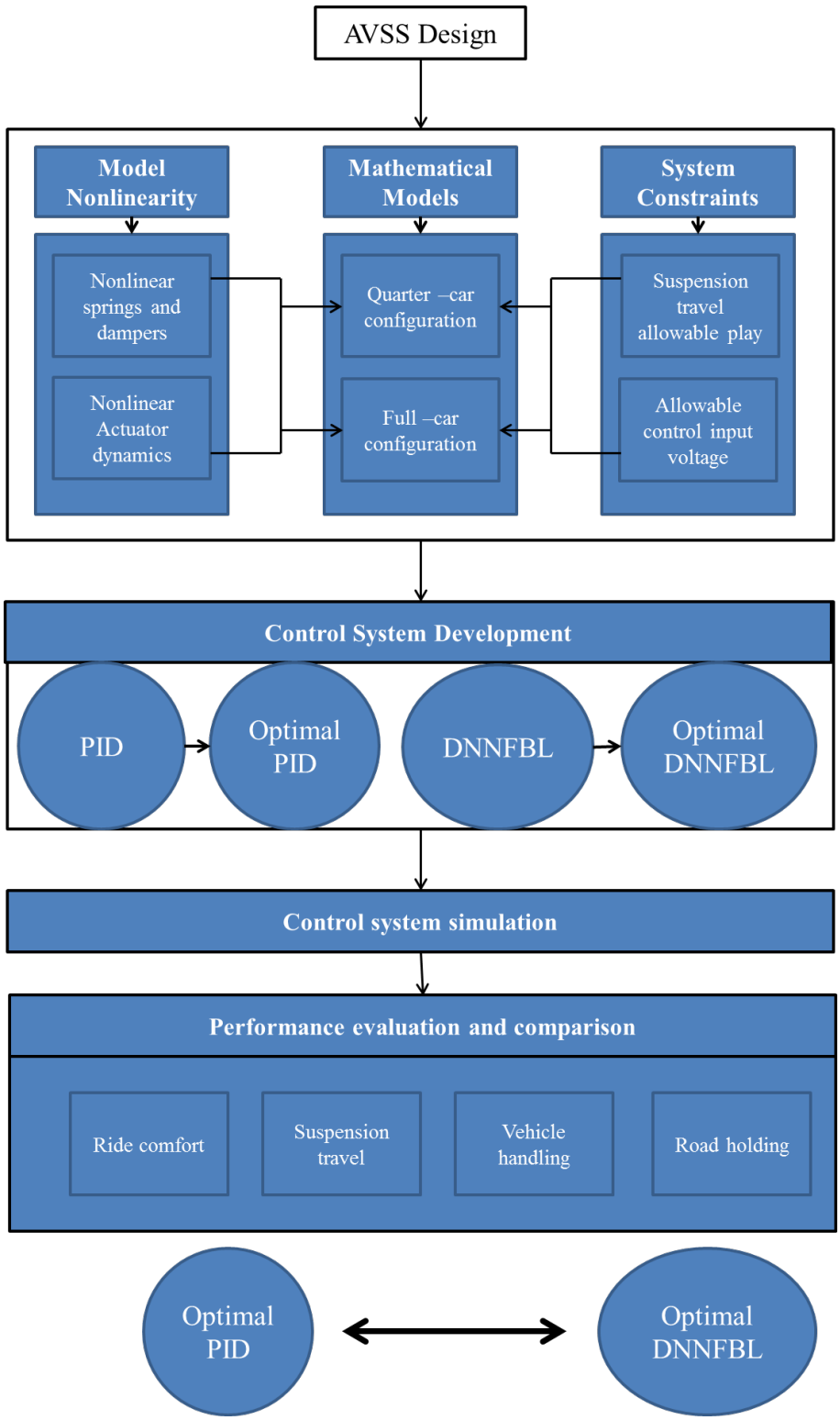

Figure 1.9: Road map to be followed in this research investigation

5. Augmentation of the proposed intelligent controller with PID control to enhance performance

6. Tuning controller gains with various global optimization techniques.

1.11 Layout of Dissertation

This research study begins with a detailed mathematical description of the quarter-car and full-car suspension models as well as input disturbances. Thereafter, the benchmark PID controller is presented and subsequently global optimization techniques are applied to improve the AVSS performance. Detailed development and analyses of an intelligent controller for the quarter-car and full-car systems are then presented and compared to the PID benchmark. The outcomes of this study are then presented with a short list of recommendations for future work.

2 System Description and Mathematical Modelling

2.1 Description of the Quarter-Car Model

A schematic of the quarter-car model used in this investigation is presented in Figure 2.1. The mass of the wheel assembly is m_u and that of the chassis is m_s. These two components are coupled through the suspension elements (spring k_s and damper b_s) which in essence aim to add value to the vehicle by assisting to improve ride comfort, road holding and vehicle handling. In the case of AVSS, an actuator is placed in parallel with the suspension elements and supplies an actuator force F_a which supports the passive suspension components in fulfilling their tasks. The flexural nature of the wheel as well as its interaction with the road is captured by coupling the wheel to the road by means of a spring with stiffness k_t.

With regards to the co-ordinate system, several state variables are appointed with the intent of capturing the heave kinematics of the arrangement. Hence, a reference frame is created at the wheel, chassis and road surface with x_w, x_c and w denoting the vertical movement of the wheel, vertical movement of the chassis and the road profile respectively. The associated velocity and accelerations of these bodies are represented as $\dot{x}$ and $\ddot{x}$ respectively. The governing equations of the system are derived by applying Newton's laws to both the wheel and chassis. The free-body-diagrams illustrating the forces acting on these bodies are shown in Figures 2.2 and 2.3 respectively, where F_{ks} and F_{bs} are the respective spring and damping forces exerted by the suspension, F_w is the force produced by the disturbance and F_a is the force supplied by the hydraulic actuator. Application of Newton's second law to both these components yields the following equations:

$$m_s\ddot{x}_c = F_{ks} + F_{bs} - F_a \tag{2.1}$$

$$m_u\ddot{x}_w = -F_{ks} - F_{bs} + F_a + F_w \tag{2.2}$$

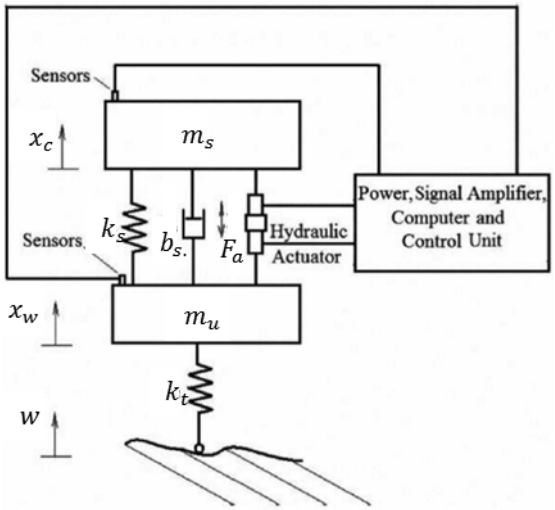

Figure 2.1: Graphical representation of the quarter-car configuration [Pedro et al. (2011)]

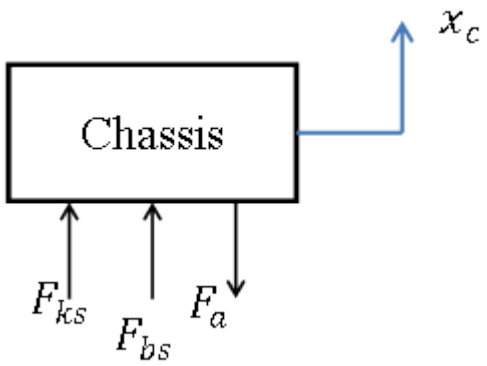

Figure 2.2: Free-body-diagram describing the forces acting on the chassis

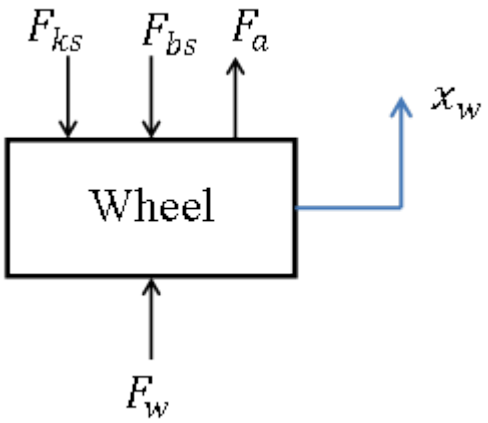

Figure 2.3: Free-body-diagram describing the forces acting on the chassis

Through close intuitive deduction of the free body diagrams, several conclusions regarding the mechanics of the system may be drawn. Firstly, it is evident that a road disturbance such as bump would drive the tyre into compression and consequently force the wheel to deflect vertically upward. Thereafter, the wheel would force against the suspension systems and force its elements into compression as well and hence move the chassis upward. In order to counteract these dynamics and bring the system to equilibrium, the actuator produces a force that opposes the motion produced by the suspension rattle. According to this reasoning, it is apparent that the wheel and suspension elements compress such that $w > x_w$ and $x_w > x_c$.

Both the spring and damping forces are functions of the suspension travel $(x_w - x_c)$ and suspension travel velocity $(\dot{x}_w - \dot{x}_c)$ respectively. In order to account for nonlinearities, the suspension components are set to have linear, symmetric and nonlinear elements which are fundamentally a function of the suspension travel and its velocity and are described as follows [Pedro and Dahunsi (2011)]:

$$F_s = k_s^l(x_w - x_c) + k_s^{nl}(x_w - x_c)^3 \tag{2.3}$$

$$F_b = b_s^l(\dot{x}_w - \dot{x}_c) + b_s^{nl}\sqrt{|(\dot{x}_w - \dot{x}_c|}sgn(\dot{x}_w - \dot{x}_c) - b_s^{sym}|(\dot{x}_w - \dot{x}_c| \tag{2.4}$$

where k_s^l and b_s^l are the linear spring stiffness and linear damping constant of the suspension system, k_s^{nl} and b_s^{nl} are the corresponding nonlinear spring stiffness and damping constant of the suspension system, and b_s^{sym} is the associating symmetric damping constant. The elastic behaviour of the tyre is assumed linear and the force produced due to its interaction with the road is as follows:

$$F_w = k_t(w - x_w) \tag{2.5}$$

where k_t is the spring stiffness of the tyre and $(w - x_w)$ is the deflection of the tyre. Whilst monitoring the behaviour of the passive or uncontrolled system, the control force F_a is set to zero and the governing equations are reduced to:

$$m_s\ddot{x}_c = F_{ks} + F_{bs} \tag{2.6}$$

$$m_u\ddot{x}_w = -F_{ks} - F_{bs} + F_w \tag{2.7}$$

In the case of control, the actuator force F_a is manipulated through an electrohydraulic actuator which aims to return the system to rest after the vehicle is disturbed by the profile of the road or any disturbance for that matter. A schematic of the actuator explaining the flow of hydraulic fluid and pressure changes in the system is shown in Figure 2.4. The actuator essentially consists of two subcomponents which are a voltage-regulated-electro-mechanic device and a three land four-way spool-valve hydraulic system. The system operates as follows: firstly, a controlled voltage

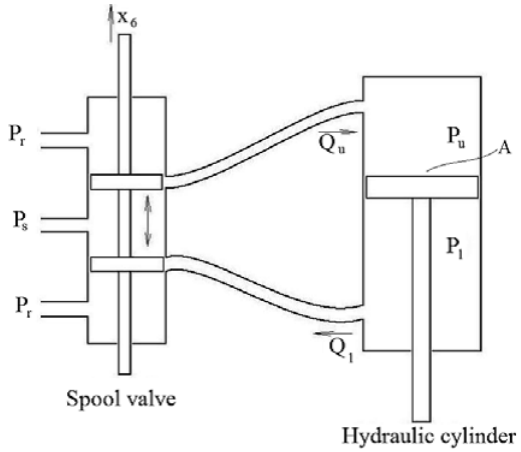

Figure 2.4: Depiction of the fluid flows and pressures within the hydraulic actuator [Pedro et al. (2011)]

produce by a specific control law drives an electro-mechanical device which regulates the spool valve. This consequent motion of the spool valve induces flow inside the hydraulic cylinder and this subsequently develops a pressure difference across the piston of the hydraulic cylinder. This pressure difference gives rise to the actuator force F_a which attempts to bring the system to a specific setpoint. The dynamics of the actuator are described through Newtonian fluid mechanics and these laws demand that continuity be maintained. Therefore, the variation of the applied hydraulic force is derived as follows [Jelali and Kroll (2003), Merritt (1967)]. Firstly, steady flow produces the following continuity equation:

$$\dot{m}_f = \rho \upsilon A = constant \tag{2.8}$$

where $\dot{m}_f$ is the mass flow rate through a specified control volume, ρ is the density of the working fluid, υ is the velocity of the liquid, and A is the cross-sectional area of the control volume. Application of the conservation of mass equation to a control tube of elemental length ds may be written in differential co-ordinate free form as follows:

$$(d\rho)/dt + div(\rho\upsilon) = 0 \tag{2.9}$$

where div is a shorthand for the vector field operator "divergence". For example,

$$div.\mathbf{F} = \nabla.\mathbf{F} = \left(\frac{\partial}{\partial x} + \frac{\partial}{\partial z} + \frac{\partial}{\partial y}\right).F = \frac{\partial U}{\partial x} + \frac{\partial V}{\partial y} + \frac{\partial W}{\partial z} \tag{2.10}$$

where F is a vector field give by: $\mathbf{F} = Ui + Vj + Wk$, and i, j and k are unit vectors in the Cartesian coordinate directions x, y and z respectively.

To account for all mass flowing through a control volume V, the rate at which mass is stored has to be equivalent to the difference of incoming and outgoing mass. This

reasoning yields the following:

$$\sum \dot{m}_{fin} - \sum \dot{m}_{fout} = \frac{\partial \rho V}{\partial t} = \rho \dot{V} + V \dot{\rho} \tag{2.11}$$

Since the volume of the hydraulic cylinder remains fixed, the rate of change of the volume i.e. $\dot{V}$ is set to zero. Additionally, the density of the hydraulic fluid varies with pressure and bulk modulus at constant temperature according to:

$$\rho = \rho_i + \frac{V}{\beta} \dot{P} \tag{2.12}$$

with initial density ρ_i, bulk modulus β, pressure P and the rate of change of pressure $\dot{P}$. Dividing Eq. (2.11) by Eq. (2.12) produces:

$$\dot{P} = \frac{\beta}{V}(Q_{in} - Q_{out}) \tag{2.13}$$

where Q_{in} is the volumetric flow rate of the fluid entering the control volume and Q_{out} is that of the fluid leaving the control volume. Application of the above relation to the hydraulic cylinder produces the following:

$$\dot{P} = \frac{\beta}{V}(Q_l - Q_{leakage} - Q_{piston}) \tag{2.14}$$

with hydraulic flow Q_l, losses $Q_{leakage}$, and flow induced as the result of the motion of the piston Q_{piston}. The hydraulic flow is effectively the flow through the spool valve which may be modelled using Euler's equation and may be further approximated as flow through an orifice. This results in the following relation:

$$Q_l = sgn[P_s - sgn(x_v)P_L] C_d \Omega x_v \sqrt{|P_s - sgn(x_v)P_L|} \tag{2.15}$$

where Q_l is the flow out of the spool valve, x_v is the spool-valve displacement, $P_s - sgn(x_v)P_L$ is the pressure differences that induces the flow, where P_s is the supply pressure and P_L is the pressure load within the hydraulic cylinder; $sgn(x_v)$ accounts for direction in which the valve displaces, C_d is the co-efficient of discharge out of the orifice approximated spool valve, and Ω is the spool-valve gradient. The leakage flow is modelled using Euler's equation and is described as [Jelali and Kroll (2003), Merritt (1967)]:

$$Q_{leakage} = C_{tp} P_L \tag{2.16}$$

with coefficient of discharge C_{tp}. The flow induced by the motion of the piston is given as:

$$Q_{piston} = A_{hyd}(\dot{x}_w - \dot{x}_c) \tag{2.17}$$

The preceding equations pertaining to hydraulic actuator dynamics may be structured to a simpler form that is suitable for feedback linearization using the following relations:

$$\dot{P}_L = \gamma \Phi x_v - \beta P_L + \alpha A(\dot{x}_w - \dot{x}_c) \tag{2.18}$$

where

$\Phi = \phi_1 \times \phi_2$, with $\phi_1 = sgn(P_s - sgn(x_v)P_L)$ and $\phi_2 = \sqrt{(P_s - sgn(x_v)P_L)}$,

$\alpha = \frac{4\beta}{V}$, $\beta = \alpha C_t p$, $\gamma = C_d \Omega \sqrt{\frac{1}{\rho}}$

In order to reduce complexity, it is assumed that the electro-mechanical device that controls the motion of the spool valve is a first-order element with a time constant τ and is defined as:

$$\dot{x}_v = \frac{1}{\tau}(K_v u - x_v) \tag{2.19}$$

where K_v is the valve gain and u is the control input voltage. Values of the parameters used in the quarter-car model are given in Table 2.1. The system may

Table 2.1: System parameters for the quarter-car model

Parameter	**Numerical Value**
Chassis or Sprung mass m_s	$290kg$
Wheel or Unsprung mass m_u	$40kg$
Suspension spring linear stiffness k_s^l	$2.35\times10^4 N/m$
Suspension spring nonlinear stiffness k_s^{nl}	$2.35\times10^6 N/m^3$
Tyre stiffness k_t	$190\times10^5 N/m$
Suspension linear damping coefficient b_s^l	$700Ns/m$
Suspension nonlinear damping coefficient b_s^{nl}	$400Ns^{0.5}/m^{0.5}$
Suspension symmetric damping coefficient b_s^{sym}	$400Ns/m$
Actuator Parameters (α, β, γ)	4.515×10^{13}, 1 , 1.545×10^9
Piston Area A	$3.35\times10^{-4}m^2$
Supply Pressure P_s	$10342500Pa$
Time constant τ	$\frac{1}{30}s$
Servo valve gains k_v	$0.001m/V$

be further rearranged into a form that is suitable for formulating control laws by defining the following state variables: $\dot{x_1} = x_3$, $\ddot{x}_1 = \dot{x}_3$, $\dot{x}_w = x_4$, $\ddot{x}_w = \dot{x}_4$, $x_5 = P_L$, and $x_6 = x_v$. The system may then be represented in state-space form as follows [Pedro and Dahunsi (2011)]:

$$\mathbf{x=f(x)+g(x)u\ +w(x)} \tag{2.20}$$

$$y = h(\mathbf{x}) = x_1 - x_2 \tag{2.21}$$

where the state vector is given by $\mathbf{x} = \begin{bmatrix} x_1 & x_2 & x_3 & x_4 & x_5 & x_6 \end{bmatrix}^T$, The system matrices $\mathbf{f}$ and $\mathbf{g}$ are denoted by:

$$\mathbf{f(x)} = \begin{bmatrix} f_1 & f_2 & f_3 & f_4 & f_5 & f_6 \end{bmatrix}^T \tag{2.22}$$

$$\mathbf{g(x)} = \begin{bmatrix} 0 & 0 & 0 & 0 & 0 & \frac{k_v}{\tau} \end{bmatrix}^T \tag{2.23}$$

The disturbance matrix **w** on the other hand is represented by:

$$\mathbf{w(x)} = \begin{bmatrix} 0 & 0 & 0 & \frac{w(t)}{m_u}k_t & 0 & 0 \end{bmatrix}^T \tag{2.24}$$

The elements of these matrices are as follows [Pedro and Dahunsi (2011)]:

$$f_1(x) = x_3 \tag{2.25}$$

$$f_2(x) = x_4 \tag{2.26}$$

$$\begin{aligned} f_3(x) &= \frac{1}{m_s}[k_s^l(x_2 - x_1) + k_s^{nl}(x_2 - x_1)^3 + b_s^l(x_4 - x_3) - \\ &\quad b_s^{sym}|x_4 - x_3| + b_s^{nl}\sqrt{|x_4 - x_3|}sgn(x_4 - x_3) - Ax_5] \end{aligned} \tag{2.27}$$

$$\begin{aligned} f_4(\mathbf{x}) &= \frac{1}{m_u}[-k_s^l(x_2 - x_1) - k_s^{nl}(x_2 - x_1)^3 - b_s^l(x_4 - x_3) + \\ &\quad b_s^{sym}|x_4 - x_3| - b_s^{nl}\sqrt{|x_4 - x_3|}sgn(x_4 - x_3) + Ax_5] \end{aligned} \tag{2.28}$$

$$f_5(x) = \gamma\Phi x_6 - \beta x_5 + A(x_3 - x_4) \tag{2.29}$$

$$f_6(x) = \frac{1}{\tau}(-x_6) \tag{2.30}$$

2.2 Development of the Full-Car Model

A representation of the full-car model is presented in Figure 2.5. The chassis is supported by four wheels, which are connected to it through four individual suspension systems. These suspension systems are aimed at enhancing ride comfort, while maintaining adequate road holding and vehicle handling capabilities. In contrast to the quarter-car model, it provides information relating to both the lateral and longitudinal dynamics of the vehicle. As a result, data concerning pitch and roll and consequently squat, under-steer and over-steer may be obtained. Hence, full-car models provide extensive details pertaining to the vehicle handling characteristics [Noura et al. (2009)].

In relation to the model architecture, full-car systems are approximated as a rectangular chassis of mass M_s that is supported at its respective corners by a suspension system which in turn is linked to one of the vehicle's wheels of mass m_{uij}, with i and j representing the position of the wheel. As in the case of the quarter-car model, each suspension system comprises of a spring component, a damper element and

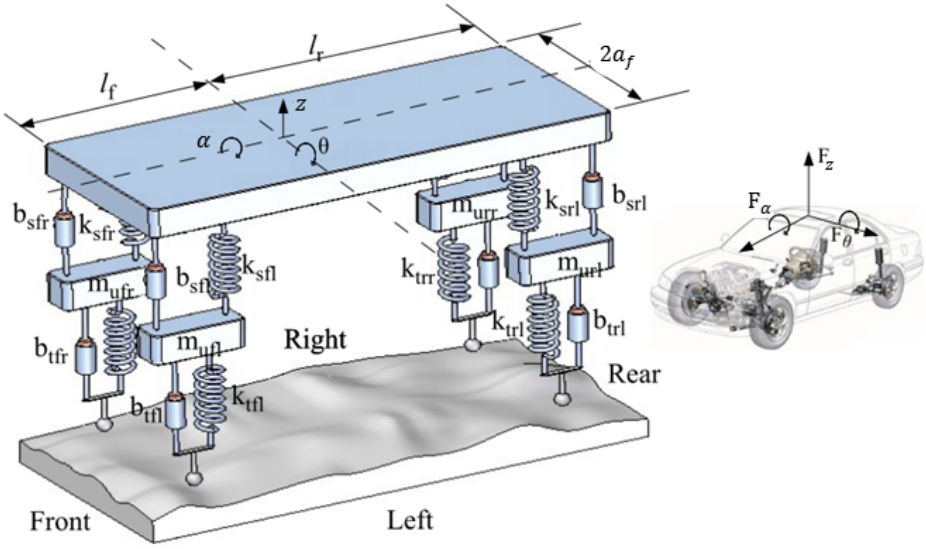

Figure 2.5: Schematic describing the full-car model

a hydraulic actuator. Furthermore, the flexural nature of the tyre is captured by coupling the wheel to the road surface through a damper and spring. In order to make the model more realistic in terms of weight distribution, the model geometry is set accordingly with most of the vehicle weight concentrated at the front. This is because analytical reviews of vehicles in general dictate that the centre of gravity be closer to the front of the vehicle to account for the weight of the engine. Furthermore, the tyre damping ratios at the front and rear of the vehicle are adjusted to account for the variation in tyre pressure between the front and rear of the vehicle [Ekoru and Pedro (2013)].

For adequate analysis of a full-car model, several reference frames are established to capture the ride comfort, road holding and vehicle handling characteristics. Similar to the quarter-car model, these include the road profiles at each wheel w_{fl}, w_{rl}, w_{fr} and w_{rr}, where the first subscripts f and r denote the front and the rear longitudanal positions of the vehicle respectively, and the second subscripts l and r refer to the left and right lateral positions of the wheel respectively. Moreover, the displacements at each corner of the chassis are denoted as: z_{lf}, z_{lr}, z_{rf} and z_{rr}. The vertical displacement at the centre of gravity (COG) is denoted as z, and the pitch and roll angles of the vehicle are given by θ and α respectively. The longitudinal and lateral moment of inertias are represented as I_θ and I_α respectively. The corresponding velocities and accelerations at each of these positions are represented as $\dot{z}$ and $\ddot{z}$. Additionally, the vertical displacement of each wheel is defined as: z_{tfl},z_{trl},z_{tfr} and z_{trr}, where the first subscript t denotes the vertical displacement of the tyre being considered, the following subscript takes either f or r which denotes the front or rear

longitudanal position of that wheel. The third subscript takes either l or r which denotes the left or right lateral position of the wheel.

In relation to the forces acting on the system, F_{ij} denotes the force generated within the suspension system at the (i, j) longitudanal and lateral positon of the vehicle as a result of disturbances. This force includes the damping force contribution F_{bij}, spring force F_{kij} and the compensating actuator force F_{aij}. Similarly, F_{ktij} and F_{btij} are the damping and stiffness forces experience within the various wheels respectively. The governing equations of the model are derived through Newton's laws. The free-body-diagram of the chassis presented in Figure 2.6 shows the forces and moments acting upon them.

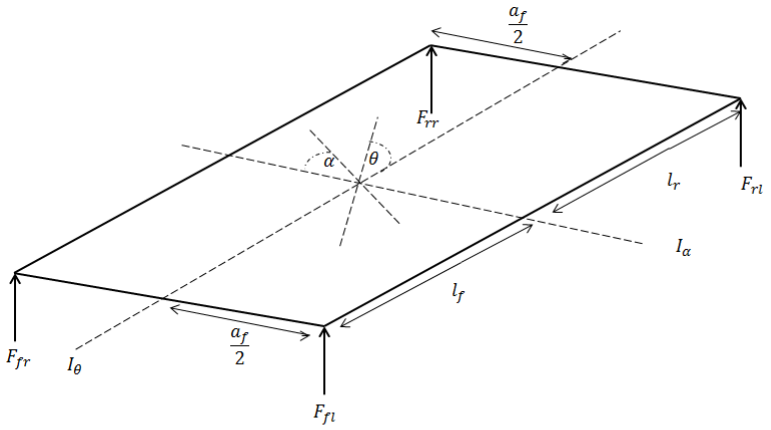

Figure 2.6: Free-body-diagram depicting the forces acting on the full-car chassis

The forces generated within each of the suspension systems at the front right, front left, rear right and rear left corners of the chassis are given as:

$$F_{fr} = F_{kfr} + F_{bfr} - F_{afr} \tag{2.31}$$

$$F_{fl} = F_{kfl} + F_{bfl} - F_{afl} \tag{2.32}$$

$$F_{rr} = F_{krr} + F_{brr} - F_{arr} \tag{2.33}$$

$$F_{rl} = F_{krl} + F_{brl} - F_{arl} \tag{2.34}$$

These aforementioned forces induce vertical forces and moments on the chassis. Application of Newton's second law to the chassis gives following governing equations. Body-heave acceleration at the chassis centre of gravity:

$$M_s\ddot{z} = F_{fr} + F_{fl} + F_{rr} + F_{rl} \tag{2.35}$$

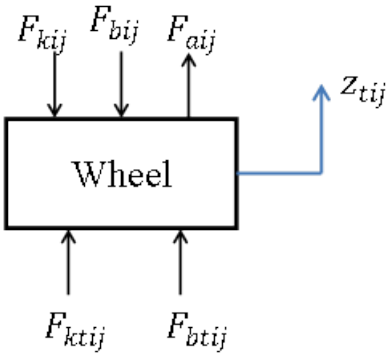

Figure 2.7: Free-body-diagram showing the forces acting on each wheel

Pitching motion of the chassis about the centre of gravity:

$$I_\theta \ddot{\theta} = -F_{fr} l_f - F_{fl} l_f + F_{rr} l_r + F_{rl} l_r \tag{2.36}$$

Rolling motion of the chassis about the centre of gravity:

$$I_\alpha \ddot{\alpha} = \frac{a_f}{2}[F_{fr} - F_{fl} + F_{rr} - F_{rl}] \tag{2.37}$$

The vertical displacements at each corner are computed as follows:

$$z_{fr} = z - l_f sin\theta + \frac{a_f}{2} sin\alpha \tag{2.38}$$

$$z_{fl} = z - l_f sin\theta - \frac{a_f}{2} sin\alpha \tag{2.39}$$

$$z_{rr} = z + l_r sin\theta + \frac{a_f}{2} sin\alpha \tag{2.40}$$

$$z_{rl} = z + l_r sin\theta - \frac{a_f}{2} sin\alpha \tag{2.41}$$

A free-body diagram depicting the dynamics at each wheel is presented in Figure 2.7 and the application of Newton's second law to this system produces the following equation:

$$m_{uij} \ddot{z}_{tij} = -F_{kij} - F_{bij} + F_{aij} + F_{ktij} + F_{btij} \tag{2.42}$$

Furthermore, to account for nonlinearities, the springs and dampers within the system are set to have linear and nonlinear components which are described as follows[Ekoru and Pedro (2013)]:

$$F_{kij} = k^l_{sij}(z_{tij} - z_{ij}) + k^{nl}_{sij}(z_{tij} - z_{ij})^3 \tag{2.43}$$

$$F_{bij} = b^l_{sij}(\dot{z}_{tij} - \dot{z}_{ij}) + b^{nl}_{sij}\sqrt{|\dot{z}_{tij} - \dot{z}_{ij}|}sgn(\dot{z}_{tij} - \dot{z}_{ij}) - b^{sym}_{sij}|\dot{z}_{tij} - \dot{z}_{ij}| \tag{2.44}$$

$$F_{ktij} = k_{tij}(w_{ij} - z_{tij}) \tag{2.45}$$

$$F_{ktij} = b_{tij}(\dot{w}_{ij} - \dot{z}_{tij}) \tag{2.46}$$

where k^l_{sij} and $k^n_{sij}l$ denotes the linear and nonlinear spring force contributions of the suspension system at location (i,j) on the chassis with $i\epsilon(front, rear)$ and $j\epsilon(left, right)$. b^l_{sij},b^{nl}_{sij} and b^{sym}_{sij} are the linear, nonlinear and symmetric damping contributions of the suspension system located at (i,j). Similarly k_{tij} and b_{tij} are the spring and damping contributions of the wheels.

The hydraulic actuator dynamics that give rise to the control force $F_{a_{ij}}$ at each wheel is the same as in the case of the quarter-car model. The forces produced by the hydraulic actuators are as follows:

$$\dot{F}_{a_{ij}} = A_{ij}\dot{P}_{Lij} = A_{ij}\left[\gamma_{ij}\Phi_{ij}x_{vij} - \beta_{ij}P_{Lij} + \Theta_{ij}A_{ij}(\dot{z}_{ij} - \dot{z}_{tij}\right] \tag{2.47}$$

where $\Theta = \frac{4\Gamma}{V_t}$, $\beta = \Theta C_t p$, $\gamma = C_d S\frac{1}{\rho}$ where(i,j) relates to the actuator components in the $(i,j)^{th}$ suspension system with $i\epsilon(front, rear)$ and $j\epsilon(left, right)$, A_{ij} are the surface areas of each hydraulic cylinder, P_{Lij} are the pressure drops across the hydraulic cylinders,$\gamma_{ij}\Phi_{ij}x_{vij}$ are the pressure changes produced as a result of spool-valve displacements x_{vij}, $\beta_{ij}P_{Lij}$ are the pressure losses that occur due to leakages, and $\Theta_{ij}A_{ij}(\dot{z}_{ij}-\dot{z}_{tij})$ are the induced pressures created by the motion of the suspension systems. The spool valves are controlled by electro-mechanical devices that are regulated by input control voltages. First-order differential equations are used to model the dynamics of these devices, which are given by:

$$\dot{x}_{vij} = \frac{1}{\tau_{ij}}\left(K_{vij}u_{ij} - x_{vij}\right) \tag{2.48}$$

where K_{vij} are the valve gains and u_{ij} are the control input voltage of the $(i,j)^{th}$ actuator.

A list of system parameter values is presented in Table 2.2. This model may be reduced into state-space form, which is necessary for incorporating feedback linearization control. This form is as follows:

$$\dot{\mathbf{x}} = \mathbf{f}(\mathbf{x}) + \mathbf{g_{fr}}(\mathbf{x})u_{fr} + \mathbf{g_{fl}}(\mathbf{x})u_{fl} + \mathbf{g_{rr}}(\mathbf{x})u_{rr} + \mathbf{g_{rl}}(\mathbf{x})u_{rl} + \mathbf{w}(\mathbf{x}) \tag{2.49}$$

where the state vector is given by $\mathbf{x} = \begin{bmatrix} x_1 & x_2 & \dots & \dots & \dots & x_{22} \end{bmatrix}^T$, and is defined as follows:

$$\begin{aligned}\mathbf{x} = [&z_{tfr} \quad \dot{z}_{tfr} \quad P_{Lfr} \quad x_{vfr} \quad z_{tfl} \quad \dot{z}_{tfl} \quad P_{Lfl} \quad x_{vfl} \quad z_{trr} \quad \dot{z}_{trr} \quad P_{Lrr} \quad \dots \\ &\dots \quad x_{vr} \quad z_{trl} \quad \dot{z}_{trl} \quad P_{Lrl} \quad x_{vrl} \quad z \quad \dot{z} \quad \theta \quad \dot{\theta} \quad \alpha \quad \dot{\alpha}]^T\end{aligned} \tag{2.50}$$

The system matrices $\mathbf{f}$ and $\mathbf{g}$, and the road disturbance matrix $\mathbf{w}$ are of the form:

$$\mathbf{f}(\mathbf{x}) = \begin{bmatrix} f_1(\mathbf{x}) & f_2(\mathbf{x}) & \dots & \dots & \dots & f_{22}(\mathbf{x}) \end{bmatrix}^T \tag{2.51}$$

Table 2.2: Values of the system parameters for the full-car AVSS

Parameter	**Numerical Value**
Chassis or Sprung mass M_s	$1060kg$
Wheel or Unsprung mass m_{ufr}, m_{ufl}, m_{ubr}, m_{ubl}	40, 40, 35, $35kg$
Pitch Moment of inertia I_θ	$2200kg.m^2$
Roll Moment of inertia I_θ	$460kg.m^2$
Length from vehicle front to centre of gravity l_f	$1m$
Length from vehicle rear to centre of gravity l_r	$1.5m$
Lateral length of vehicle a_f	$1.5m$
Suspension spring linear stiffness at each wheel k^l_{sij}	$2.3\times10^2N/m$
Suspension spring nonlinear stiffness at all wheels k^{nl}_{sij}	$2.35\times10^4N/m^3$
Tyre stiffness at each wheel k_{tij}	$190\times10^5N/m$
Tyre damping at each wheel b_{tfr}, b_{tfl}, b_{trr}, b_{trl})	80,80,70,70Ns/m
Suspension linear damping coefficient b^l_s	$700Ns/m$
Suspension nonlinear damping coefficient at all wheels b^{nl}_{sij}	$400Ns^{0.5}/m^{0.5}$
Suspension symmetric damping coefficient at all wheels b^{sym}_{sij}	$400Ns/m$
Actuator Parameters (Θ_{ij} ,β_{ij} ,γ_{ij})	4.515×10^{13}
	1, 1.545×10^9
Piston Area A_{ij}	$3.35\times10^{-4}m^2$
Supply Pressure P_s	$10342500Pa$
Time constant τ	$\frac{1}{30}s$
Servo valve gains k_{vij}	$0.001m/V$

$$\mathbf{g_{fr}}(\mathbf{x}) = \begin{bmatrix} 0 & \dots & g_4(\mathbf{x}) & \dots & \dots & \dots & 0 \end{bmatrix}^T \tag{2.52}$$

$$\mathbf{g_{fl}}(\mathbf{x}) = \begin{bmatrix} 0 & \dots & \dots & g_8(\mathbf{x}) & \dots & \dots & 0 \end{bmatrix}^T \tag{2.53}$$

$$\mathbf{g_{rr}}(\mathbf{x}) = \begin{bmatrix} 0 & \dots & \dots & \dots & g_{12}(\mathbf{x}) & \dots & 0 \end{bmatrix}^T \tag{2.54}$$

$$\mathbf{g_{rl}}(\mathbf{x}) = \begin{bmatrix} 0 & \dots & \dots & \dots & \dots & g_{16}(\mathbf{x}) & 0 \end{bmatrix}^T \tag{2.55}$$

$$\mathbf{w}(\mathbf{x}) = \begin{bmatrix} 0 & w_2(\mathbf{x}) & \dots & w_6(\mathbf{x}) & \dots & w_{10}(\mathbf{x}) & \dots & w_{14}(\mathbf{x}) & \dots \end{bmatrix}^T \tag{2.56}$$

The system matrix $\mathbf{f}$ can be broken down into several subsets, namely the dynamics at each of the four wheels and the dynamics at the centre of gravity of the chassis, each of which are of the following forms [Noura et al. (2009)]:

Front Right Wheel Dynamics

$$f_1(\mathbf{x}) = x_2 \tag{2.57}$$

$$
\begin{aligned}
f_2(\mathbf{x}) &= \frac{1}{m_{ufr}}[k^l_{sfr}(x_1 - [x_{17} - l_f sinx_{19} + \\
&\quad \frac{a_f}{2}sinx_{21}]) + k^{nl}_{sfr}(x_1 - [x_{17} - l_f sinx_{19} + \\
&\quad \frac{a_f}{2}sinx_{21}])^3 + b^l_{sfr}(x_2 - [x_{18} - l_f x_{20}cosx_{19} + \frac{a_f}{2}x_{22}cosx_{21}]) - \\
&\quad b^{nl}_{sfr}\sqrt{x_2 - [x_{18} - l_f x_{20}cosx_{19} + \frac{a_f}{2}x_{22}cosx_{21}]} \times \\
&\quad sgn(x_2 - [x_{18} - l_f x_{20}cosx_{19} + \frac{a_f}{2}x_{22}cosx_{21}]) \\
&\quad b^{sym}_{sfr}|x_2 - [x_{18} - l_f x_{20}cosx_{19} + \frac{a_f}{2}x_{22}cosx_{21}]| \\
&= -A_{fr}x_3 - k_{tfr}x_1 - b_{tfr}x_2] \qquad (2.58)
\end{aligned}
$$

$$
f_3(\mathbf{x}) = \gamma_{fr}\Phi_{fr}x_4 - \beta_{fr}x_3 + \Theta_{fr}A_{fr}(x_2 - [x_{18} - l_f x_{20}cosx_{19} + \frac{a_f}{2}x_{22}cosx_{21}]) \qquad (2.59)
$$

$$
f_4(\mathbf{x}) = \frac{1}{\tau_{fr}}(-x_4) \qquad (2.60)
$$

Front Left Wheel Dynamics

$$
f_5(\mathbf{x}) = x_6 \qquad (2.61)
$$

$$
\begin{aligned}
f_6(\mathbf{x}) &= \frac{1}{m_{ufl}}[k^l_{sfl}(x_5 - [x_{17} - l_f sinx_{19} - \frac{a_f}{2}sinx_{21}]) + \\
&\quad k^{nl}_{sfl}(x_5 - [x_{17} - l_f sinx_{19} - \\
&\quad \frac{a_f}{2}sinx_{21}])^3 + b^l_{sfl}(x_6 - [x_{18} - l_f x_{20}cosx_{19} - \frac{a_f}{2}x_{22}cosx_{21}]) - \\
&\quad b^{nl}_{sfl}\sqrt{x_6 - [x_{18} - l_f x_{20}cosx_{19} - \frac{a_f}{2}x_{22}cosx_{21}]} \times \\
&\quad sgn(x_6 - [x_{18} - l_f x_{20}cosx_{19} - \frac{a_f}{2}x_{22}cosx_{21}]) \\
&\quad b^{sym}_{sfl}|x_6 - [x_{18} - l_f x_{20}cosx_{19} - \frac{a_f}{2}x_{22}cosx_{21}]| \\
&\quad -A_{fl}x_7 - k_{tfl}x_5 - b_{tfl}x_6] \qquad (2.62)
\end{aligned}
$$

$$
f_7(\mathbf{x}) = \gamma_{fl}\Phi_{fl}x_8 - \beta_{fl}x_7 + \Theta_{fl}A_{fl}(x_6 - [x_{18} - l_f x_{20}cosx_{19} - \frac{a_f}{2}x_{22}cosx_{21}]) \qquad (2.63)
$$

$$
f_8(\mathbf{x}) = \frac{1}{\tau_{fl}}(-x_8) \qquad (2.64)
$$

Rear Right Wheel Dynamics

$$
f_9(\mathbf{x}) = x_{10} \qquad (2.65)
$$

$$
\begin{aligned}
f_{10}(\mathbf{x}) &= \frac{1}{m_{urr}}[k^l_{srr}(x_9 - [x_{17} + l_r sinx_{19} + \frac{a_f}{2} sinx_{21}]) + \\
&\quad k^{nl}_{srr}(x_9 - [x_{17} + l_r sinx_{19} + \\
&\quad \frac{a_f}{2} sinx_{21}])^3 + b^l_{srr}(x_{10} - [x_{18} + l_r x_{20} cosx_{19} + \frac{a_f}{2} x_{22} cosx_{21}]) - \\
&\quad b^{nl}_{srr}\sqrt{x_{10} - [x_{18} + l_r x_{20} cosx_{19} + \frac{a_f}{2} x_{22} cosx_{21}]} \times \\
&\quad sgn(x_{10} - [x_{18} + l_r x_{20} cosx_{19} + \frac{a_f}{2} x_{22} cosx_{21}]) \\
&\quad b^{sym}_{srr}|x_{10} - [x_{18} + l_r x_{20} cosx_{19} + \frac{a_f}{2} x_{22} cosx_{21}]| \\
&\quad -A_{rr} x_{11} - k_{trr} x_9 - b_{trr} x_{10}]
\end{aligned} \tag{2.66}
$$

$$
f_{11}(\mathbf{x}) = \gamma_{rr}\Phi_{rr}x_{12} - \beta_{rr}x_{11} + \Theta_{rr}A_{rr}(x_{10} - [x_{18} + l_r x_{20} cosx_{19} + \frac{a_f}{2} x_{22} cosx_{21}]) \tag{2.67}
$$

$$
f_{12}(\mathbf{x}) = \frac{1}{\tau_{rr}}(-x_{12}) \tag{2.68}
$$

Rear Left Wheel Dynamics

$$
f_13(\mathbf{x}) = x_{14} \tag{2.69}
$$

$$
\begin{aligned}
f_{14}(\mathbf{x}) &= \frac{1}{m_{url}}[k^l_{srl}(x_13 - [x_{17} + l_f sinx_{19} - \frac{a_f}{2} sinx_{21}]) + \\
&\quad k^{nl}_{srl}(x_13 - [x_{17} + l_r sinx_{19} - \\
&\quad \frac{a_f}{2} sinx_{21}])^3 + b^l_{srl}(x_{14} - [x_{18} + l_r x_{20} cosx_{19} - \frac{a_f}{2} x_{22} cosx_{21}]) - \\
&\quad b^{nl}_{srl}\sqrt{x_{14} - [x_{18} + l_r x_{20} cosx_{19} - \frac{a_f}{2} x_{22} cosx_{21}]} \times \\
&\quad sgn(x_{14} - [x_{18} + l_r x_{20} cosx_{19} - \frac{a_f}{2} x_{22} cosx_{21}]) \\
&\quad b^{sym}_{srl}|x_{14} - [x_{18} + l_r x_{20} cosx_{19} - \frac{a_f}{2} x_{22} cosx_{21}]| \\
&\quad -A_{rl} x_{15} - k_{trl} x_{13} - b_{trl} x_{14}]
\end{aligned} \tag{2.70}
$$

$$
f_{15}(\mathbf{x}) = \gamma_{rl}\Phi_{rl}x_{16} - \beta_{rl}x_{15} + \Theta_{rl}A_{rr}(x_{14} - [x_{18} + l_r x_{20} cosx_{19} - \frac{a_f}{2} x_{22} cosx_{21}]) \tag{2.71}
$$

$$
f_{16}(\mathbf{x}) = \frac{1}{\tau_{rl}}(-x_{16}) \tag{2.72}
$$

Centre of gravity Dynamics Heave motion

$$
f_{17}(\mathbf{x}) = x_{18} \tag{2.73}
$$

$$
\begin{aligned}
f_{18}(\mathbf{x}) \;=\; & \frac{-1}{M_s}[k^l_{sfr}(x_1 - [x_{17} - l_f sinx_{19} + \frac{a_f}{2} sinx_{21}]) + \\
& k^{nl}_{sfr}(x_1 - [x_{17} - l_f sinx_{19} + \frac{a_f}{2} sinx_{21}])^3 + \\
& b^l_{sfr}(x_2 - [x_{18} - l_f x_{20} cosx_{19} + \frac{a_f}{2} x_{22} cosx_{21}]) - \\
& b^{nl}_{sfr}\sqrt{x_2 - [x_{18} - l_f x_{20} cosx_{19} + \frac{a_f}{2} x_{22} cosx_{21}]} \times \\
& sgn(x_2 - [x_{18} - l_f x_{20} cosx_{19} + \frac{a_f}{2} x_{22} cosx_{21}]) \\
& b^{sym}_{sfr}|x_2 - [x_{18} - l_f x_{20} cosx_{19} + \frac{a_f}{2} x_{22} cosx_{21}]| - A_{fr} x_3 + \\
& k^l_{sfl}(x_5 - [x_{17} - l_f sinx_{19} - \frac{a_f}{2} sinx_{21}]) + \\
& + k^{nl}_{sfl}(x_5 - [x_{17} - l_f sinx_{19} - \frac{a_f}{2} sinx_{21}])^3 + \\
& b^l_{sfl}(x_6 - [x_{18} - l_f x_{20} cosx_{19} - \frac{a_f}{2} x_{22} cosx_{21}]) - \\
& b^{nl}_{sfl}\sqrt{x_6 - [x_{18} - l_f x_{20} cosx_{19} - \frac{a_f}{2} x_{22} cosx_{21}]} \times \\
& sgn(x_6 - [x_{18} - l_f x_{20} cosx_{19} - \frac{a_f}{2} x_{22} cosx_{21}]) \\
& b^{sym}_{sfl}|x_6 - [x_{18} - l_f x_{20} cosx_{19} - \frac{a_f}{2} x_{22} cosx_{21}]| - A_{fl} x_7 + \\
& k^l_{srr}(x_9 - [x_{17} + l_r sinx_{19} + \frac{a_f}{2} sinx_{21}]) + + \\
& k^{nl}_{srr}(x_9 - [x_{17} + l_r sinx_{19} + \frac{a_f}{2} sinx_{21}])^3 + \\
& b^l_{srr}(x_{10} - [x_{18} + l_r x_{20} cosx_{19} + \frac{a_f}{2} x_{22} cosx_{21}]) - \\
& b^{nl}_{srr}\sqrt{x_{10} - [x_{18} + l_r x_{20} cosx_{19} + \frac{a_f}{2} x_{22} cosx_{21}]} \times \\
& sgn(x_{10} - [x_{18} + l_r x_{20} cosx_{19} + \frac{a_f}{2} x_{22} cosx_{21}]) \\
& b^{sym}_{srr}|x_{10} - [x_{18} + l_r x_{20} cosx_{19} + \frac{a_f}{2} x_{22} cosx_{21}]| - A_{rr} x_{11} + \\
& k^l_{srl}(x_13 - [x_{17} + l_f sinx_{19} - \frac{a_f}{2} sinx_{21}]) + + \\
& k^{nl}_{srl}(x_13 - [x_{17} + l_r sinx_{19} - \frac{a_f}{2} sinx_{21}])^3 + \\
& b^l_{srl}(x_{14} - [x_{18} + l_r x_{20} cosx_{19} - \frac{a_f}{2} x_{22} cosx_{21}]) - \\
& b^{nl}_{srl}\sqrt{x_{14} - [x_{18} + l_r x_{20} cosx_{19} - \frac{a_f}{2} x_{22} cosx_{21}]} \times \\
& sgn(x_{14} - [x_{18} + l_r x_{20} cosx_{19} - \frac{a_f}{2} x_{22} cosx_{21}]) \\
& b^{sym}_{srl}|x_{14} - [x_{18} + l_r x_{20} cosx_{19} - \frac{a_f}{2} x_{22} cosx_{21}]| - A_{rl} x_{15}] \qquad (2.74)
\end{aligned}
$$

Pitch motion

$$
f_{19}(\mathbf{x}) = x_{20} \qquad (2.75)
$$

$$
\begin{aligned}
f_{20}(\mathbf{x}) \;=\; & \frac{-1}{I_\theta}[-l_f[(k^l_{sfr}(x_1 - [x_{17} - l_f sinx_{19} + \frac{a_f}{2} sinx_{21}]) + \\
& k^{nl}_{sfr}(x_1 - [x_{17} - l_f sinx_{19} + \frac{a_f}{2} sinx_{21}])^3 + \\
& b^l_{sfr}(x_2 - [x_{18} - l_f x_{20} cosx_{19} + \frac{a_f}{2} x_{22} cosx_{21}]) - \\
& b^{nl}_{sfr}\sqrt{x_2 - [x_{18} - l_f x_{20} cosx_{19} + \frac{a_f}{2} x_{22} cosx_{21}]} \times \\
& sgn(x_2 - [x_{18} - l_f x_{20} cosx_{19} + \frac{a_f}{2} x_{22} cosx_{21}]) \\
& b^{sym}_{sfr}|x_2 - [x_{18} - l_f x_{20} cosx_{19} + \frac{a_f}{2} x_{22} cosx_{21}]| - A_{fr} x_3] - \\
& l_f[k^l_{sfl}(x_5 - [x_{17} - l_f sinx_{19} - \frac{a_f}{2} sinx_{21}]) + \\
& k^{nl}_{sfl}(x_5 - [x_{17} - l_f sinx_{19} - \frac{a_f}{2} sinx_{21}])^3 + \\
& b^l_{sfl}(x_6 - [x_{18} - l_f x_{20} cosx_{19} - \frac{a_f}{2} x_{22} cosx_{21}]) - \\
& b^{nl}_{sfl}\sqrt{x_6 - [x_{18} - l_f x_{20} cosx_{19} - \frac{a_f}{2} x_{22} cosx_{21}]} \times \\
& sgn(x_6 - [x_{18} - l_f x_{20} cosx_{19} - \frac{a_f}{2} x_{22} cosx_{21}]) \\
& b^{sym}_{sfl}|x_6 - [x_{18} - l_f x_{20} cosx_{19} - \frac{a_f}{2} x_{22} cosx_{21}]| - A_{fl} x_7] + \\
& l_r[k^l_{srr}(x_9 - [x_{17} + l_r sinx_{19} + \frac{a_f}{2} sinx_{21}]) + \\
& k^{nl}_{srr}(x_9 - [x_{17} + l_r sinx_{19} + \frac{a_f}{2} sinx_{21}])^3 + \\
& b^l_{srr}(x_{10} - [x_{18} + l_r x_{20} cosx_{19} + \frac{a_f}{2} x_{22} cosx_{21}]) - \\
& b^{nl}_{srr}\sqrt{x_{10} - [x_{18} + l_r x_{20} cosx_{19} + \frac{a_f}{2} x_{22} cosx_{21}]} \times \\
& sgn(x_{10} - [x_{18} + l_r x_{20} cosx_{19} + \frac{a_f}{2} x_{22} cosx_{21}]) \\
& b^{sym}_{srr}|x_{10} - [x_{18} + l_r x_{20} cosx_{19} + \frac{a_f}{2} x_{22} cosx_{21}]| - A_{rr} x_{11}] + \\
& l_r[k^l_{srl}(x_13 - [x_{17} + l_f sinx_{19} - \frac{a_f}{2} sinx_{21}]) + \\
& k^{nl}_{srl}(x_13 - [x_{17} + l_r sinx_{19} - \frac{a_f}{2} sinx_{21}])^3 + \\
& b^l_{srl}(x_{14} - [x_{18} + l_r x_{20} cosx_{19} - \frac{a_f}{2} x_{22} cosx_{21}]) - \\
& b^{nl}_{srl}\sqrt{x_{14} - [x_{18} + l_r x_{20} cosx_{19} - \frac{a_f}{2} x_{22} cosx_{21}]} \times \\
& sgn(x_{14} - [x_{18} + l_r x_{20} cosx_{19} - \frac{a_f}{2} x_{22} cosx_{21}]) \\
& b^{sym}_{srl}|x_{14} - [x_{18} + l_r x_{20} cosx_{19} - \frac{a_f}{2} x_{22} cosx_{21}]| - A_{rl} x_{15}] \qquad (2.76)
\end{aligned}
$$

Roll motion

$$
f_{21}(\mathbf{x}) = x_{22} \qquad (2.77)
$$

$$
\begin{aligned}
f_{22}(\mathbf{x}) \;=\; & \frac{a_f}{2}\frac{-1}{I_\alpha}[+[(k^l_{sfr}(x_1 - [x_{17} - l_f sinx_{19} + \frac{a_f}{2}sinx_{21}]) + \\
& k^{nl}_{sfr}(x_1 - [x_{17} - l_f sinx_{19} + \frac{a_f}{2}sinx_{21}])^3 + \\
& b^l_{sfr}(x_2 - [x_{18} - l_f x_{20}cosx_{19} + \frac{a_f}{2}x_{22}cosx_{21}]) - \\
& b^{nl}_{sfr}\sqrt{x_2 - [x_{18} - l_f x_{20}cosx_{19} + \frac{a_f}{2}x_{22}cosx_{21}]} \times \\
& sgn(x_2 - [x_{18} - l_f x_{20}cosx_{19} + \frac{a_f}{2}x_{22}cosx_{21}]) \\
& b^{sym}_{sfr}|x_2 - [x_{18} - l_f x_{20}cosx_{19} + \frac{a_f}{2}x_{22}cosx_{21}]| - A_{fr}x_3] - \\
& [k^l_{sfl}(x_5 - [x_{17} - l_f sinx_{19} - \frac{a_f}{2}sinx_{21}]) + \\
& k^{nl}_{sfl}(x_5 - [x_{17} - l_f sinx_{19} - \frac{a_f}{2}sinx_{21}])^3 + \\
& b^l_{sfl}(x_6 - [x_{18} - l_f x_{20}cosx_{19} - \frac{a_f}{2}x_{22}cosx_{21}]) - \\
& b^{nl}_{sfl}\sqrt{x_6 - [x_{18} - l_f x_{20}cosx_{19} - \frac{a_f}{2}x_{22}cosx_{21}]} \times \\
& sgn(x_6 - [x_{18} - l_f x_{20}cosx_{19} - \frac{a_f}{2}x_{22}cosx_{21}]) \\
& b^{sym}_{sfl}|x_6 - [x_{18} - l_f x_{20}cosx_{19} - \frac{a_f}{2}x_{22}cosx_{21}]| - A_{fl}x_7] + \\
& [k^l_{srr}(x_9 - [x_{17} + l_r sinx_{19} + \frac{a_f}{2}sinx_{21}]) + \\
& k^{nl}_{srr}(x_9 - [x_{17} + l_r sinx_{19} + \frac{a_f}{2}sinx_{21}])^3 + \\
& b^l_{srr}(x_{10} - [x_{18} + l_r x_{20}cosx_{19} + \frac{a_f}{2}x_{22}cosx_{21}]) - \\
& b^{nl}_{srr}\sqrt{x_{10} - [x_{18} + l_r x_{20}cosx_{19} + \frac{a_f}{2}x_{22}cosx_{21}]} \times \\
& sgn(x_{10} - [x_{18} + l_r x_{20}cosx_{19} + \frac{a_f}{2}x_{22}cosx_{21}]) \\
& b^{sym}_{srr}|x_{10} - [x_{18} + l_r x_{20}cosx_{19} + \frac{a_f}{2}x_{22}cosx_{21}]| - A_{rr}x_{11}] - \\
& [k^l_{srl}(x_13 - [x_{17} + l_f sinx_{19} - \frac{a_f}{2}sinx_{21}]) + \\
& k^{nl}_{srl}(x_13 - [x_{17} + l_r sinx_{19} - \frac{a_f}{2}sinx_{21}])^3 + \\
& b^l_{srl}(x_{14} - [x_{18} + l_r x_{20}cosx_{19} - \frac{a_f}{2}x_{22}cosx_{21}]) - \\
& b^{nl}_{srl}\sqrt{x_{14} - [x_{18} + l_r x_{20}cosx_{19} - \frac{a_f}{2}x_{22}cosx_{21}]} \times \\
& sgn(x_{14} - [x_{18} + l_r x_{20}cosx_{19} - \frac{a_f}{2}x_{22}cosx_{21}]) \\
& b^{sym}_{srl}|x_{14} - [x_{18} + l_r x_{20}cosx_{19} - \frac{a_f}{2}x_{22}cosx_{21}]| - A_{rl}x_{15}] \qquad (2.78)
\end{aligned}
$$

The constituents of the input matrices $\mathbf{g_1}(\mathbf{x})$, $\mathbf{g_2}(\mathbf{x})$, $\mathbf{g_3}(\mathbf{x})$ and $\mathbf{g_4}(\mathbf{x})$ are of the form:

$$g_4(\mathbf{x}) = \frac{K_{vfr}}{\tau_{fr}} \qquad (2.79)$$

$$g_8(\mathbf{x}) = \frac{K_{vfl}}{\tau_{fl}} \tag{2.80}$$

$$g_{12}(\mathbf{x}) = \frac{K_{vrr}}{\tau_{rr}} \tag{2.81}$$

$$g_{16}(\mathbf{x}) = \frac{K_{vrl}}{\tau_{rl}} \tag{2.82}$$

The terms of disturbance matrix $\mathbf{w}(\mathbf{x})$ is as follows:

$$w_2(\mathbf{x}) = \frac{1}{m_{ufr}}(k_{tfr}w_{fr} + b_{tfr}\dot{w}_{fr}) \tag{2.83}$$

$$w_6(\mathbf{x})) = \frac{1}{m_{ufl}}(k_{tfl}w_{fl} + b_{tfr}\dot{w}_{fl}) \tag{2.84}$$

$$w_{10}(\mathbf{x}) = \frac{1}{m_{urr}}(k_{trr}w_{rr} + b_{trr}\dot{w}_{rr}) \tag{2.85}$$

$$w_{14}(\mathbf{x}) = \frac{1}{m_{url}}(k_{trl}w_{fr} + b_{trl}\dot{w}_{rl}) \tag{2.86}$$

2.3 Model of Realistic Road Disturbances

The performance of the proposed systems in terms of ride comfort, road holding, vehicle handling, suspension travel, and power consumption will be analysed as the vehicle passes over a deterministic road bump. For the case of the quarter-car model, the vehicle is set to travel at a steady speed of $40km/h$ and pass over an $11cm$ high and $5m$ long road bump.

The road bump is a sinusoidal profile as this profile adequately fits the nature of road bumps [Pedro and Dahunsi (2011), Pedro et al. (2011), and Ekoru and Pedro (2013)]. With regards to modelling it, a typical sin wave is described as follows:

$$W = a\sin(2\pi f) \tag{2.87}$$

The frequency f of this wave is the inverse of the time t taken to cross the bump (i.e. $\frac{1}{t}$). Since the vehicle is moving at constant speed, it can be described through the half-wavelength λ of the bump and the vehicle speed V as follows:

$$t = \frac{\lambda}{V} \tag{2.88}$$

The height of the bump is essentially the amplitude of this sinusoidal wave a. To create a specific bump that appears at certain point in time, some mathematical manipulation is required. This resulting profile is modelled according to Eq. (2.89). The specifications of the road bump are aimed at capturing the worst case scenario

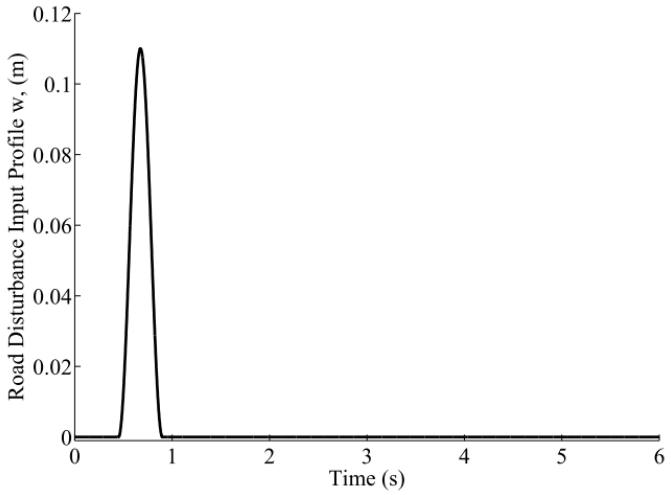

Figure 2.8: Road disturbance input for the quarter-car suspension system study

and if the system performs adequately for this case, it should perform adequately for various other road bump disturbances as well. [Pedro et al. (2011)]

$$w(t) = \begin{cases} a\frac{1-\cos\frac{2\pi Vt}{\lambda}}{2} & \text{if } 0.45 <= t <= 0.9. \\ 0 & \text{otherwise.} \end{cases} \tag{2.89}$$

with bump amplitude a, vehicle speed V, and bump wavelength λ. A schematic of the road profile is presented in Figure 2.8. This specific road profile is chosen as bumps are one of the major sources of ride discomfort and they also have the tendency to minimise vehicle handling and they increase the degree of suspension rattle, and hence they address the broad spectrum of trade-offs associated with suspension systems.

The road profile for the full-car model is more complex as it is required to produce both roll and pitch dynamics which are the key issues associated with vehicle handling. To generate roll, a bump amplitude 6cm is used for the right hand side of the vehicle as compared to the left hand side of the vehicle where the bump height is 4cm. As the rear tyres pass over the bump sometime after the front tyres do, pitch is naturally induced. The respective road profiles are described as follows:

$$w_{fr}(t) = \begin{cases} a_1\frac{(1-\cos\frac{2\pi Vt}{\lambda})}{2} & \text{if } 0.45 <= t <= 0.9. \\ 0 & \text{otherwise.} \end{cases} \tag{2.90}$$

$$w_{fl}(t) = \begin{cases} a_2\frac{(1-\cos\frac{2\pi Vt}{\lambda})}{2} & \text{if } 0.45 <= t <= 0.9. \\ 0 & \text{otherwise.} \end{cases} \tag{2.91}$$

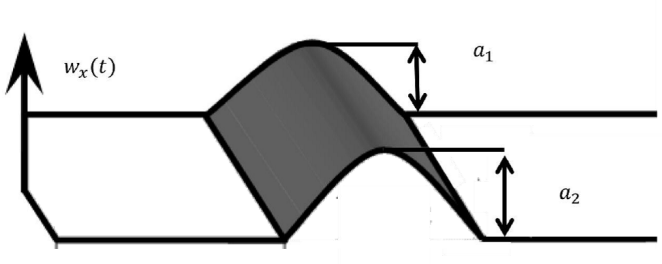

Figure 2.9: Road disturbance input for the full-car suspension system study

Table 2.3: Parameter values for the deterministic road bumps

Parameter	**Numerical Value**
Bump height a_1	$6cm$
Bump height a_2	$4cm$
Vehicle forward velocity V	$40km/hr$
Bump wavelength λ	$5m$

$$w_{rr}(t) = \begin{cases} a_1 \frac{(1-\cos\frac{2\pi Vt}{\lambda})}{2} & \text{if } 0.45 + \frac{\lambda}{V} <= t <= 0.9 + \frac{\lambda}{V}. \\ 0 & \text{otherwise.} \end{cases} \tag{2.92}$$

$$w_{rl}(t) = \begin{cases} a_2 \frac{(1-\cos\frac{2\pi Vt}{\lambda})}{2} & \text{if } 0.45 + \frac{\lambda}{V} <= t <= 0.9 + \frac{\lambda}{V}. \\ 0 & \text{otherwise.} \end{cases} \tag{2.93}$$

This disturbance is graphically explained in Figure 2.9. The parameter values for the above road profiles are listed in Table 2.3.

3 PID Benchmark Controller Design and Optimization

3.1 Quarter-Car PID-Based Control

3.1.1 Introduction

PID control is of prime importance in this study as it is widely applied in industry and hence serves as a suitable benchmark of comparison for the proposed optimal and intelligent controllers. Furthermore, the simple structure of a PID controller makes its implementation easy and consequently provides reasonable intuitive understanding into AVSS control. Moreover, optimal control of PID controllers and hybrid PID-Intelligent controllers are of prime importance in this research study and in order to develop these proposed controllers, sufficient knowledge pertaining to basic PID control is required. As opposed to the dominant trend in PID-based design, actuator dynamics will be included in this research. This will subsequently increase the number of system states and add complexity to the model. Furthermore, the nature of hydraulic actuators is such that a small change in displacement produces a large variation in force. This sensitivity causes the system to become increasingly unstable under various conditions. A multi-loop PID controller is incorporated to track the control force such that the system does not become unstable.

3.1.2 Controller Design of Quarter-Car AVSS

The control system for the nonlinear electrohydraulic AVSS comprises of two control loops of which the outer loop regulates the controlled variable and the inner loop maintains actuator stability. Force feedback is incorporated into the inner loop as it has been proven successful in previous applications. Suspension travel, $x_w - x_c$

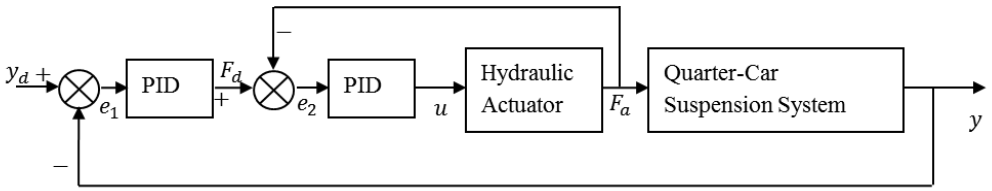

Figure 3.1: Schematic describing the PID-based AVSS for quarter-car model

has been selected as the controlled variable y of the outer control loop since it is the primary parameter that captures the dynamics of the suspension system as it is the chief constituent of the spring and damping forces. A schematic of the control system is presented in Figure 3.1. The setpoint y_d reference command input, which is set to zero to address a regulation problem, e_1 and e_2 are error signals that will be minimised in the outer and inner control loops respectively, F_a is the actuator force that will be regulated in the inner control loop with F_d being its respective setpoint, y is the suspension travel that will be manipulated through the outer control loop, and u is the control input voltage that is passed into the hydraulic actuator of the AVSS, and is regulated by the proposed controller. PID controllers operate according to the following equations:

$$e_1(t) = y_d - y(t) = y_d(t) - x_w(t) + x_c(t) \tag{3.1}$$

$$F_d(t) = K_P e_1(t) + K_D \frac{de_1(t)}{dt} + K_I \int_0^T e_1(t)dt \tag{3.2}$$

$$e_2(t) = F_a(t) - F_d(t) \tag{3.3}$$

$$u(t) = k_p e_2(t) + k_d \frac{de_2(t)}{dt} + k_i \int_0^T e_2(t)dt \tag{3.4}$$

where K_P and k_p are the proportional gains of the outer and inner loops respectively, K_I and k_i are the corresponding integral gains of the controllers, and K_D and k_d are the derivative gains of the respective control loops.

The proportional P constituent of the PID controller produces a command signal that is proportional to the control error and a consequent increase in its associated gains tends to bring the system to rest quicker. However, the amount that the proportional gain may be increased is limited by the power supply. Moreover, the characteristic delay that is present in all control system creates instability if the chosen gains are significantly high. Additionally, increasing higher proportional gains tend to increase the steady state error of the system. On the other hand, the

integral gain I generates a control signal that depends primarily on the error history of the system. This component of the PID controller possesses the added advantage of a guaranteed zero steady-state error, but it deteriorates the system performance by introducing a large degree of oscillations. [O'Dwyer (2006)]

In contrast to the P and I components of the PID controller, the derivative D gains produce a control signal that is based on the rate of change of the error signal, and hence it has the ability to predict the future response of the system and produce a control signal that deals with the error before it actually occurs. An optimistic outlook of derivative gains argues that they improve rise time and reduce settling time, whereas another pessimistic viewpoint debates that it tends to add oscillatory behaviour to the system. [O'Dwyer (2006)]

In accordance with these findings, it is clear that PID tuning requires both intuitive reasoning and experience to acquire improved system performance without incurring instability and weak transient qualities.

3.1.3 Design Specifications of Quarter-Car AVSS

The design specifications chosen for the quarter-car system are as follows [Dahunsi and Pedro (2010)]:

1. The suspension travel must be limited to 0.1m as this is the maximum suspension travel for a typical sedan vehicle.
2. The control input voltage is constrained to 10volts which is primarily based on the restrictions of the power supply.
3. The actuation force must be less than the static weight of the vehicle so the vehicle wheels do not leave the ground, which would otherwise render the mathematical model inadequate, $F_a \leq m_s g$
4. The maximum body-heave acceleration: $\ddot{x}_c \leq 4.5 m/s^2$ and the associated Root-Mean-Squared (RMS) acceleration should be less than $1 m/s^2$ so ride comfort lies in "Little discomfort" region of the International Organization for Standardization 2631 (2003).

In order to cope with the suspension trade-offs, the performance index used to select controller gains given in Eq. (3.2) and (3.4) and is principally based on minimising each of the suspension performance criterion is as follows: [Ekoru and Pedro (2013)].

$$J = \frac{1}{T}\int_0^T \left[\left(\frac{y}{y_{max}}\right)^2 + \left(\frac{F_a}{F_{a_{max}}}\right)^2 + \left(\frac{\ddot{x}_c}{\ddot{x}_{c_{max}}}\right)^2 + \left(\frac{u}{u_{max}}\right)^2 + \left(\frac{(x_w - w)}{(x_w - w)_{max}}\right)^2\right] dt \tag{3.5}$$

where y and y_{max} are the suspension travel and maximum allowable suspension travel respectively and this subcomponent is added to the performance index to minimise suspension rattle. F_a and $F_{a_{max}}$ are the actuator force and maximum allowable actuator force respectively which are placed to address work done. $\ddot{x}_c$ and $\ddot{x}_{cmax}$ are the body-heave acceleration and maximum allowable body-heave acceleration respectively and these terms draws attention to ride comfort. u and u_{max} are the control voltage and limiting control voltage respectively and they represent power consumption. Finally, $(x_2 - w)$ and $(x_2 - w)_{max}$ are the tyre deflection and maximum allowable tyre deflection respectively and they are augmented to J to enhance road holding.

This performance index J is specifically setup to also account for design specifications. To keep the suspension travel y, heave acceleration $\ddot{x}_c$, voltage u, force F and tyre dynamic load $x_w - w$ below its limits, the associating weighting factor of each term in Eq.(3.5) is chosen to be the inverse of its limits [i.e. $\frac{1}{y_{max}}$, $\frac{1}{\ddot{x}_{c_{max}}}$, $\frac{1}{u_{max}}$, $\frac{1}{F_{max}}$, $\frac{1}{(x_w - w)_{max}}$]. If the systems maintains these limits imposed by the specifications, the terms $\frac{y}{y_{max}}$, $\frac{u}{u_{max}}$, $\frac{F}{F_{max}}$, $\frac{(x_w - w)}{(x_w - w)_{max}}$, and $\frac{\ddot{x}_c}{\ddot{x}_{c_{max}}}$ in Eq.(3.5) will be a fraction with a value less than 1. Since each of thes terms are squared, the magnitude of these values will be even smaller. This essentially keeps the performance index comparatively small if specifications are met. However, if the limits are exceeded, each term will produce a value greater than 1 and when squared produces an even greater value which makes the value of the performance index significantly larger. Since the optimization methods aim to minimise the performance index, responses that do not meet specifications produce significantly larger performance index values and are thus automatically discarded by the algorithm

The controller gains are chosen by firstly using Ziegler-Nichols rules in order to acquire a sufficient starting point, after which rigorous fine tuning is conducted with the aim of improving the performance index J and resolving the trade-offs between conflicting suspension performance criteria.

The resulting gains obtained through manual tuning are given in Table 3.1. Sev-

Table 3.1: PID gains obtained using manual tuning for the quarter-car AVSS

Control Loop	**Outer PID Loop Gains**			**Inner PID Loop Gains**		
Gain	K_P	K_I	K_D	k_p	k_i	k_d
Manual Tuning	17000	50	1400	0.002	0.004	0

eral comments may be made concerning the gains that were computed in Table 3.1. Firstly, the high K_P gains in the outer loop is anticipated and PID controllers in general possess the shortfall of generating large proportional gains that will raise the control input and may lead to actuator saturation [O'Dwyer (2006)]. Secondly, the integral gains in both control loops are necessary to achieve zero steady-state error for both regulating the control variable y and ensuring that the actuator follows its desired trajectory with minimal chattering [Pedro et al. (2011)]. The derivative gain of the inner control loop k_d was set to zero as this gains proved to be rather sensitive where small variations created large changes in the system response.

It is also worth commenting that small variations in the gains of the inner control loop have a major impact on the response of the system. Furthermore, these gains have the tendency to affect chattering and system stability as divergence was observed when the magnitude of these values fall out of a certain range. This is in accordance with the literature, which argue that the inner loop maintains stability.

3.1.4 Comparative Study between Passive and PID-Based AVSS Response

Plots showing the response of both the PVSS and AVSS as the quarter-car vehicle passes over a deterministic road bump described by Eq. (2.89) are shown in Figures 3.4 to 3.6, respectively. These plots describe the behaviour of the system in each of its performance benchmarks and quantitative data extracted from these plots are listed in Table 3.2.

From the results obtained, it is clear that the PID-based AVSS was able to significantly improve the performance of the suspension system in each of its performance aspects in both peak and RMS values. Furthermore, it displayed improved transient behaviour, where the system oscillated to a lesser extent before it settled to steady-state. However, the system failed to meet the design specification relating to ride

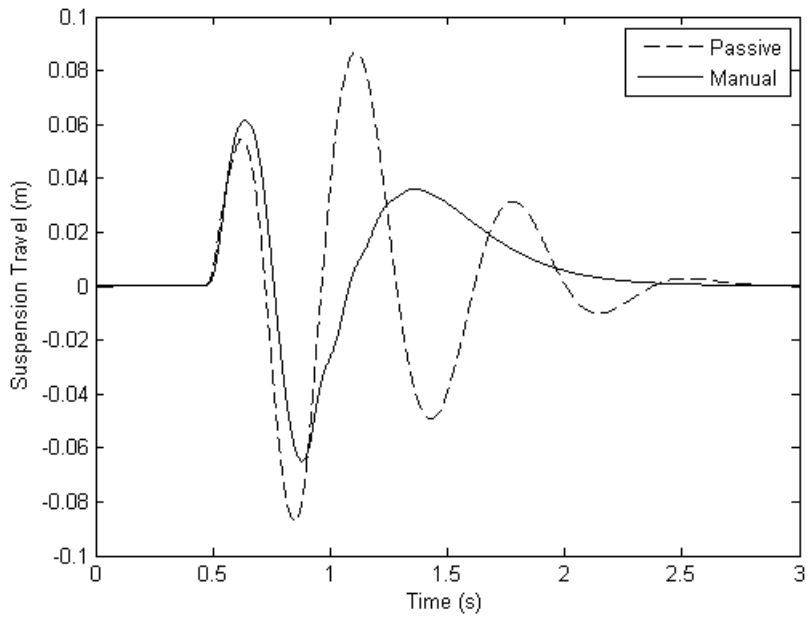

Figure 3.2: Suspension travel response for both PVSS and manually-tuned PID-controlled AVSS

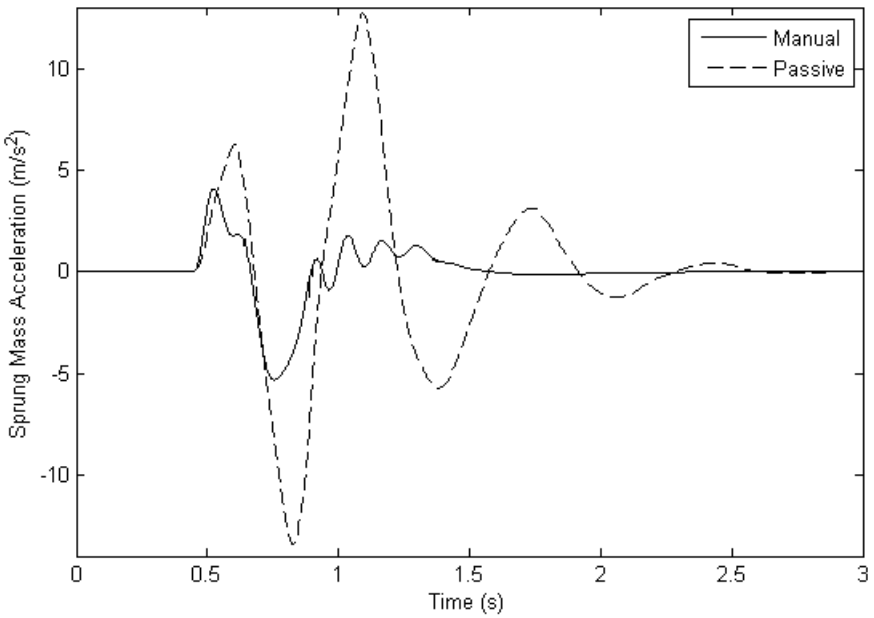

Figure 3.3: Sprung mass acceleration response for both PVSS and manually-tuned PID-controlled AVSS

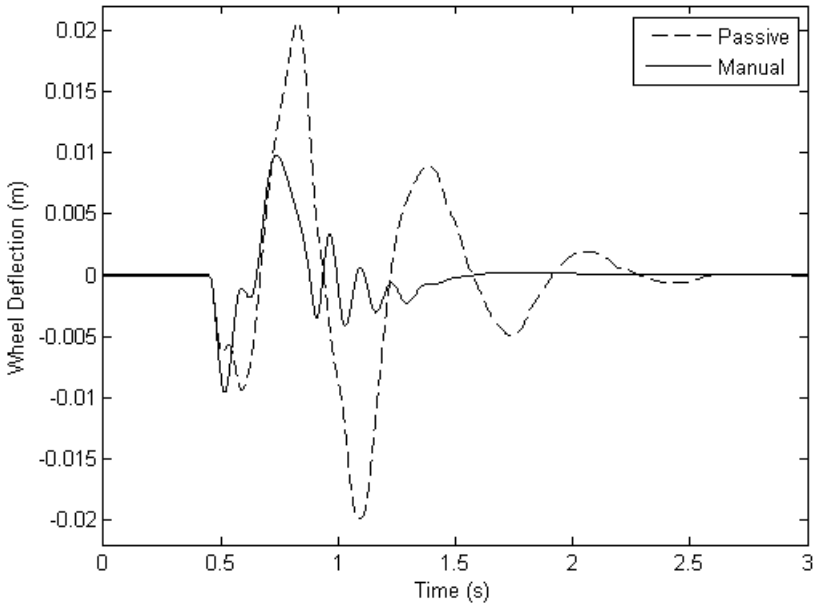

Figure 3.4: Road holding characteristics of PVSS and manually-tuned PID-controlled AVSS

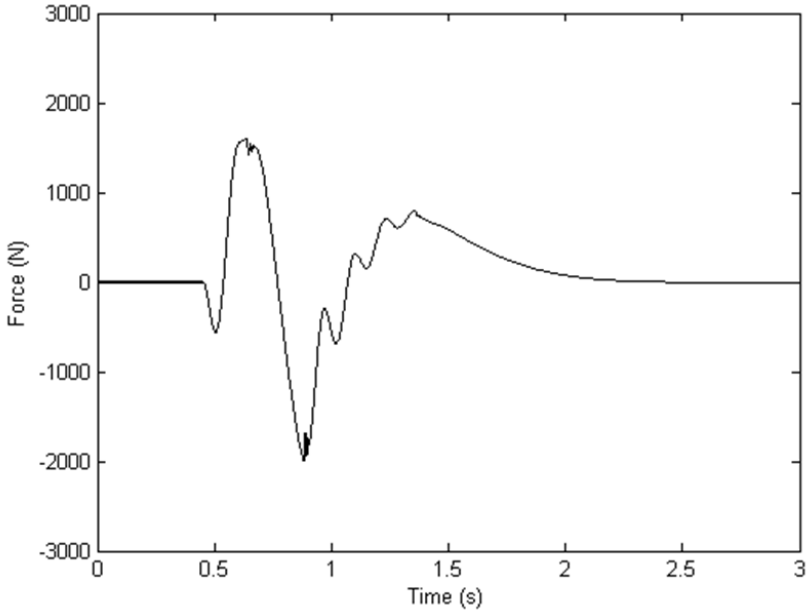

Figure 3.5: Actuator force supplied for manually-tuned PID-controlled AVSS

Table 3.2: Performance characteristics of PVSS and manually-tuned PID-controlled AVSS

Cases	**Passive**	**Manual**	**Passive**	**Manual**
Performance Criteria	Suspension Travel m		Ride Comfort m/s^2	
RMS	0.025	0.023	4.1	1.62
Peak	0.087	0.064	13.3	5.3
Performance Criteria	Road Holding m		Control Voltage V	
RMS	0.0064	0.0024	N/A	0.784
Peak	0.0206	0.0098	N/A	2.9
Performance Criteria	Actuation Force N		Settling Time s	
RMS	N/A	300	N/A	N/A
Peak	N/A	2100	2.8	2.5
Performance Criteria	Performance Index			
Passive	12			
Manual	5.2			

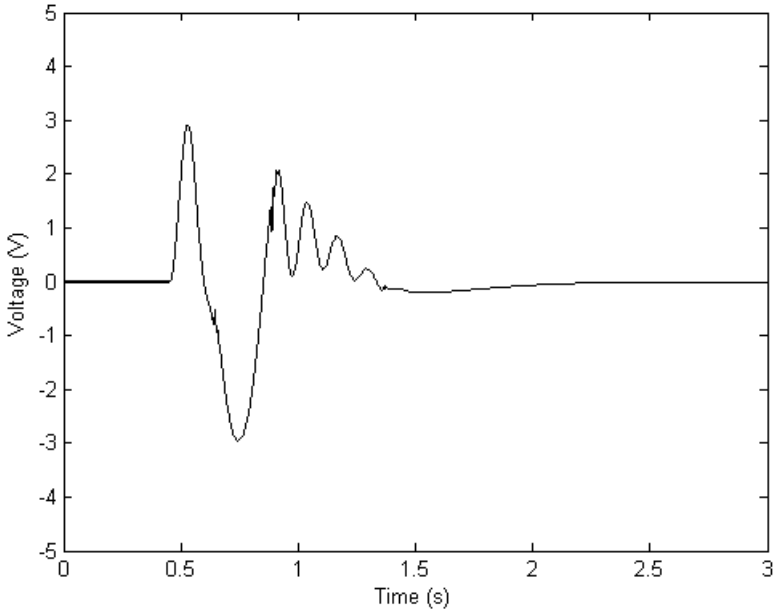

Figure 3.6: Control input voltage supplied for manually-tuned PID-controlled AVSS

comfort and peak body acceleration. In addition, its settling time did not improve considerably from that of the PVSS and it dampened out relatively slowly after the disturbance was removed. These drawbacks may be overcome by implementing a constrained optimization policy or by applying intelligent control.

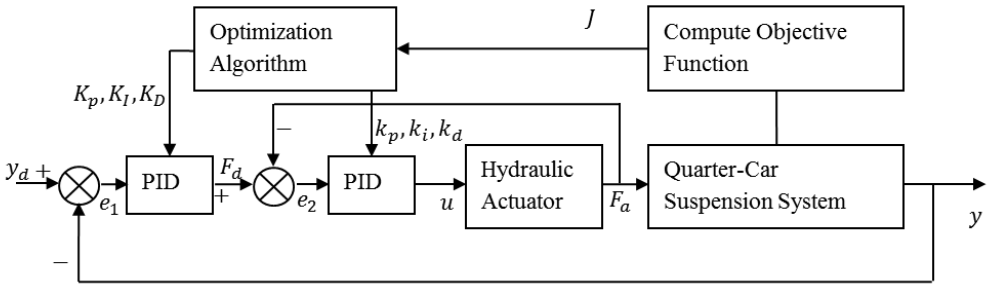

Figure 3.7: Closed-loop diagram for optimal PID controller design

3.1.5 Application of Global Optimization Methods to Controller Tuning of Quarter-Car AVSS

To improve upon the deficiencies and complexities associated with manual PID tuning, global optimization methods used for controller tuning have been suggested for this task with the aim to best manage the performance index. Evolutionary and global optimization algorithms such as Differential-Evolution (DE), Genetic-Algorithm (GA), Particle-Swarm-Optimization (PSO), Controlled-Random-Search (CRS) and Pattern-Search (PS) are proposed to determine controller gains which best minimise the performance index and simultaneously remove the drawbacks and rigorous tuning routine associated with manual PID tuning. Moreover, these methods are heuristic and random search methods and do not require any function-based methods to locate minima. However, it is worth noting that these algorithms possess several shortcomings. Firstly, the absolute minimum cannot be guaranteed, but rather a solution that is close to the minimum. Secondly, the choice of the bounds and optimization parameters must be such that the solution does not get caught in a local minimum and premature convergence problems not occur. Nevertheless, the optimization algorithms have been used in a variety of nonlinear constrained optimization problems and display potential to solve the nonlinear AVSS trade-offs.

The control structure for this algorithm is shown in Figure 3.7. It is essentially the same as the non-optimal PID-controlled manually-tuned case, except that the performance index or objective function J presented in Eq.(3.5) is computed within the loop and fed to the optimization routine which subsequently computes the PID gains for both the inner and outer control loops. Hence the total number of problem variables used for a quarter-car AVSS is six namely $K_P, K_I, K_D, k_p, k_i, k_d$. The optimization is performed offline using DE, GA, PSO, CRS and PS algorithms respectively. With regards to the general notation used in these algorithms, a given set of problem variables or each set of controller gains or a set of neural network

parameters (as in the case of system identification described in intelligent control applications) are represented by a vector of size m, where m is the total number of controller gains or network parameters that are being computed using the respective algorithms. These vectors are given the notation x_n where n corresponds to the n^{th} individual or set of controller gains (vector) in the population. The fitness of each individual is denoted as $f(x_n)$. Hence for the quarter-car AVSS, the number of problem variables is six and each individual x is a 6×1 vector.

3.1.5.1 DE Global Optimization Method

Evolutionary algorithms which include DE, GA, and PSO are random search optimization methods where the optimal solution is produced through the evolution of a random population set $S = \{\mathbf{x_0}, \mathbf{x_1}, \mathbf{x_2}, ., \mathbf{x_N}\}$ with each individual denoted as $\mathbf{x}_i$. These individuals are vectors with each of its elements pertaining to a specific controller gain for the case of controller tuning or a network parameter in the case of system identification. Each of the proposed algorithms only differ in the manner in which the population changes through each generation as well as the conditions that must be satisfied in order for the respective individuals to change. The search space may be predefined to operate within a feasible region in order to improve computation time and convergence characteristics. Such a search space is chosen through intuitive reasoning and experience gained through manual tuning as in the case of PID controller tuning. [Kaelo and Ali (2007), Wu et al. (2012), Nagaraj and Vijayakumar (2011)]

In each generation step of DE, an associated trial individual $\mathbf{y}_i$ is generated for each targeted individual $\mathbf{x}_i$ in S. This trial individual $\mathbf{y}_i$ is a function of $\mathbf{x}_i$ and a mutated individual $\hat{\mathbf{x}}_i$. $\hat{\mathbf{x}}_i$ is a mutation that is generated from three distinct randomly chosen individuals $\mathbf{x}_\alpha$, $\mathbf{x}_\beta$, and $\mathbf{x}_\gamma$ from the population set S with $\mathbf{x}_\alpha$ being the fittest of the three. Each problem variable k (namely each PID gain or neural network weighting parameter for the case of system identifications) of the mutated individual $\hat{\mathbf{x}}_i$ is determined using the following relation:

$$\hat{x}_{i_k} = x_{\alpha_k} + F(x_{\beta_k} - x_{\gamma_k}) \tag{3.6}$$

where, α, β, and γ are representative of the three distinctive randomly selected individuals from the population S, k signifies the k^{th} parameter, gain, or network weighting of these individuals, i is the i^{th} individual that is currently being mutated,

and F is the primary DE scaling parameter.

Crossover is thereafter performed between the targeted individual $\mathbf{x}_i$ and its mutated counterpart $\hat{\mathbf{x}}_i$ to produce a corresponding new trial point $\mathbf{y}_i$. In crossover, each parameter k within $\mathbf{y}_i$ either equals the associating k^{th} parameter in $\mathbf{x}_i$ or $\hat{\mathbf{x}}_i$. This decision is made by producing a random number R^k and if R^k exceeds a predefined threshold number C_R the k^{th} parameter of $\mathbf{y}_i$ becomes the k^{th} parameter of $\mathbf{x}_i$. Conversely, if this condition is not met the k^{th} parameter of $\mathbf{y}_i$ is given the same value as the k^{th} parameter of $\hat{\mathbf{x}}_i$. These relationships are explained mathematically as follows:

$$y_{i_k} = \begin{cases} \hat{x}_{i_k} & \text{if } R^k \leq C_R. \\ x_{i_k} & \text{otherwise.} \end{cases} \tag{3.7}$$

The trial vector $\mathbf{y}_i$ of the targeted individual $\mathbf{x}_i$ from S is only accepted and replaces its predecessor or previous values $\mathbf{x}_i(t-1)$ if and only if it possesses a superior fitness to that of $\mathbf{x}_i(t-1)$ which may be summarised as:

$$\mathbf{x}_i = \begin{cases} \mathbf{y}_i & \text{if } f(\mathbf{y}_i) < f(\mathbf{x}_i). \\ \mathbf{x}_i & \text{otherwise.} \end{cases} \tag{3.8}$$

where $f(\mathbf{y}_i)$ is the fitness value of the trial vector, and $f(\mathbf{x}_i)$ is the fitness of the targeted individual. After the whole population S has evolved the process is repeated until the stopping criterion is met. Thereafter, the optimal solution is chosen to be the individual in S with the best fitness value. In the case of this investigation, the algorithm was set to stop after a predefined number of iterations. This routine may be shortened in the ensuing steps [Kaelo and Ali (2007)]:

Step 1 Create a random population, $S = \{\mathbf{x_0}, \mathbf{x_1}, .., \mathbf{x_N}\}$ and let $\mathbf{x}_0$ be the initial condition which in the case of controller tuning matches the set of controller gains attained through manual tuning.

Step 2 If stopping criterion has been met, select the fittest individual in S as the optimal solution; otherwise continue to the next step.

Step 3 In each iteration, evolve the i^{th} individual $\mathbf{x}_i$ in population S as follows: Randomly choose three mutually independent individuals from S and denote them as $\mathbf{x}_\alpha$, $\mathbf{x}_\beta$ and $\mathbf{x}_\gamma$.

- Create a mutated individual $\hat{\mathbf{x}}_i$ according to Eq. (3.6).
- Compute the trial candidate $\mathbf{y}_i$ by applying crossover with the individual $\mathbf{x}_i$ and the mutated individual $\hat{\mathbf{x}}_i$ according to Eq. (3.7):

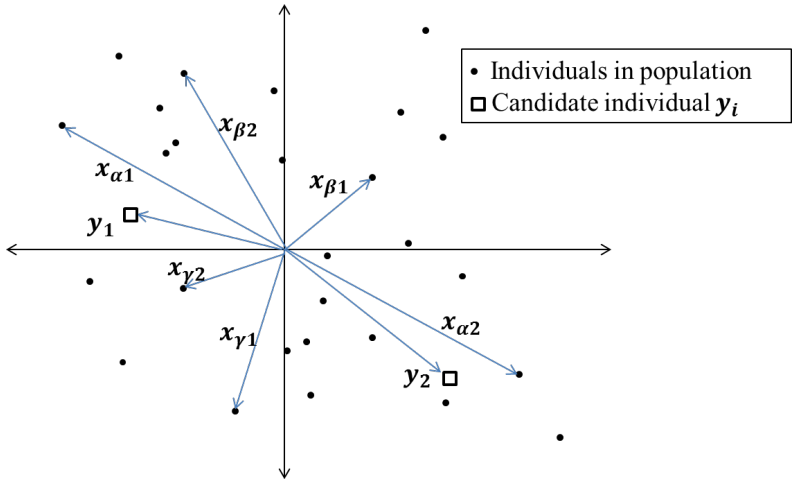

Figure 3.8: Schematic illustrating the search capabilities of DE-based optimization

- Replace the i^{th} individual $\mathbf{x}_i$ in S with the candidate solution $\mathbf{y}_i$ if and only if $\mathbf{y}_i$ contains a better fitness value than its predecessor.
- Repeat the process for each individual within S and return to step 2.

In relation to the structure of the DE, it is worth commenting on its potential to solve the problem from a computational point of view. Firstly, this algorithm has the ability to search the solution space more efficiently than most optimization algorithms. This is because the mutated individual $\hat{\mathbf{x}}_i$ for each individual $\mathbf{x}_i$ is determined based on only 3 randomly selected mutually independent individuals $\mathbf{x}_\alpha$, $\mathbf{x}_\beta$ and $\mathbf{x}_\gamma$ from the solution space S. Such a setup creates excellent flexibility that permits candidate individuals to form anywhere in the solution space. Hence, many portions of the solutions space are expected to be explored with this configuration. This concept is further explained in an analogous 2-dimensional plot shown in Figure 3.8.

The simulation was performed using the first two memenbers in S. Each individual in the population is represented as a dot. The subscripts 1 and 2 in Figure 3.8 correspond to the first and second individuals in the populations respectively. From Figure 3.8, it is evident that the trial points $\mathbf{y}_i$ which is represented as squares, can fall anywhere in the search space depending on the random selection of its respective parental individuals $\mathbf{x}_\alpha$, $\mathbf{x}_\beta$ and $\mathbf{x}_\gamma$ from which they were determined as per Eq. (3.6). Therefore, it is evident that DE possesses excellent exploration abilities. The second quality of the DE that makes it stand out compared to other optimization algorithms is the fact that the $\mathbf{x}_i$ individual is replaced only if its respective candidate solution $\mathbf{y}_i$ has a better fitness value. This condition basically

only allows progression or evolution of the individual if its fitness improves. Such a rule guarantees that the algorithm will converge to a solution. However, this condition does tend to slow down convergence speed.

3.1.5.2 GA Global Optimization Method

After the random population S has been generated as in the case of DE, a new set of NN offspring $Of(\mathbf{y_0}, \mathbf{y_1}, \mathbf{y_2}, ., \mathbf{y_{NN}})$ are produced through the reproduction of parent individuals from S. Each pair of parents reproduces two offspring. The choice of parents is based on tournament selection where the individuals with a better fitness value are more likely to reproduce. Tournament selection operates by randomly choosing two random individuals $\mathbf{x}_{aj}$ and $\mathbf{x}_{bj}$ from S and the individual with the superior fitness is chosen as the paternal parent $\mathbf{P}_{1j}$ of two future offspring that will be created from the j^{th} reproduction. Thereafter, two additional individuals $\mathbf{x}_{cj}$ and $\mathbf{x}_dj$ are randomly selected from S and the corresponding fitter individual is chosen as the maternal parent $\mathbf{P}_{2j}$. Tournament selection may be summarised through the following relations:

$$\mathbf{P}_{1j} = \begin{cases} \mathbf{x}_{aj} & \text{if } f(\mathbf{x}_{aj}) \leq f(\mathbf{x}_{bj}) \\ \mathbf{x}_{bj} & \text{otherwise} \end{cases} \tag{3.9}$$

$$\mathbf{P}_{2j} = \begin{cases} \mathbf{x}_{cj} & \text{if } f(\mathbf{x}_{cj}) < f(\mathbf{x}_{dj}) \\ \mathbf{x}_{dj} & \text{otherwise} \end{cases} \tag{3.10}$$

Two new offspring are generated from the j^{th} maternal and paternal parents [$\mathbf{P}_{1j}$ and $\mathbf{P}_{2j}$] according to the following equations:

$$\mathbf{y}_{1j} = \mathbf{P}_{1j} rand(1, N) + \mathbf{P}_{2j}(1 - rand(1, N)) \tag{3.11}$$

$$\mathbf{y}_{2j} = \mathbf{P}_{1j}(1 - rand(1, N)) + \mathbf{P}_{2j} rand(1, N) \tag{3.12}$$

where $rand(1, N)$ is an N-dimensional vector of random numbers, N is the number of parameters or problem variables being determined through the optimization routine, and $\mathbf{y}_{1j}$ and $\mathbf{y}_{2j}$ are the two new offspring that are produced as a result of reproduction.

The process of tournament selection and subsequent reproduction is repeated until all offspring in Of are computed. The set of NN offspring thereafter replace the NN worst individuals in S. The aforementioned process is repeated for each generation until the stopping criterion is met. Thereafter, the optimal solution is chosen to be

the individual in S with the best fitness value. This routine may be summarised as follows [Crews et al. (2011)]:

Step 1 Generate a random set of individuals, $S = \{\mathbf{x_0}, \mathbf{x_1}, .., \mathbf{x_N}\}$, in addition to the initial condition $\mathbf{x}_0$which in controller tuning corresponds to the set of controller gains obtained through manual tuning.

Step 2 If stopping criterion has been met, select the fittest individual in S as the optimal solution; otherwise continue to the next step.

Step 3 Check if the specified number of offspring NN has been produced. If so proceed to step 8, otherwise continue to step 4.

Step 4 Randomly select two individuals $\mathbf{x}_{aj}$ and $\mathbf{x}_{bj}$ from the population S and thereafter choose the individual with the superior fitness value as the paternal parent $\mathbf{P}_{1j}$ as described in Eq. (3.9).

Step 5 Randomly select two individuals $\mathbf{x}_{cj}$ and $\mathbf{x}_{dj}$ from the population S and thereafter choose the individual with the superior fitness value as the maternal parent $\mathbf{P}_{2j}$ as described in Eq. (3.10).

Step 6 Produce two new offspring by applying crossover between the paternal $\mathbf{P}_{1j}$ and maternal $\mathbf{P}_{2j}$ parents as outlined in Eqs. 3.11 and Eq. (3.12) and continue to step 7.

Step 7 If the offspring set O is completed, continue to the next step, otherwise return to step 3.

Step 8 Replace the NN individuals with the weakest fitness values in S with the newly produced NN offspring and return to step 2.

With regards to the strengths and weakness of this algorithm, there are several characteristics that assure convergence but there are also some aspects that limit the efficiency of the algorithm. Firstly, parental selection which is depicted in Figure 3.9 is an effective method in finding good offspring for the next generation. This is primarily due to the fact that offspring (represented as triangles) are produced from the superior individuals in the solution space. This mandate secures successively fitter generations. In Figure 3.9, each individual in the population is represented as a dot. Randomly selected individuals $\mathbf{x}_{aj}$ and $\mathbf{x}_{bj}$ undergo tournament selection to obtain the paternal parent $\mathbf{P}_{1j}$, whereas randomly chosen individuals $\mathbf{x}_{cj}$ and $\mathbf{x}_{dj}$ also go through tournament selection where the fitter individual is chosen as the maternal parent $\mathbf{P}_{2j}$. From the process of reproduction, an offspring $\mathbf{y}_{1j}$ (represented

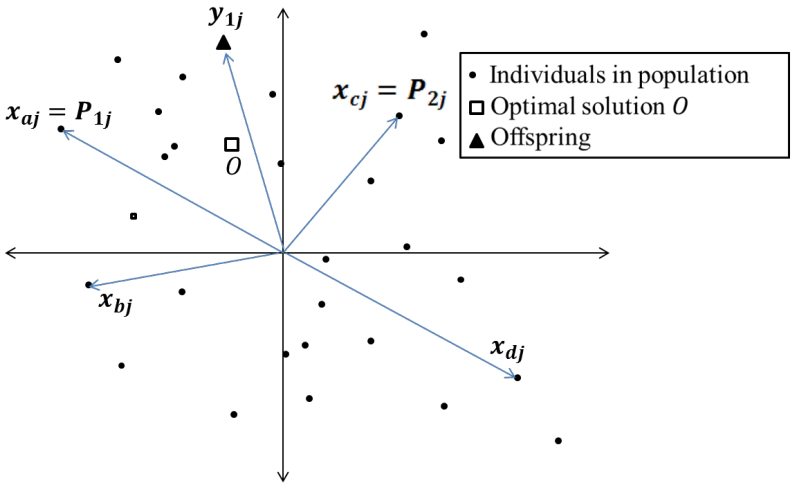

Figure 3.9: Vector plot showing the process of reproduction

as a triangle) is created which resides in the vicinity of the fitter individuals within the population and hence close to the optimal solution O, which is represented as a square.

However, due to the nature of nonlinear problems and the multi-dimensional vector space used in this investigation, superior offspring may not always be generated. Sometimes the offspring may be weaker than all the discarded individuals from the previous generation. Furthermore, since GA replaces the NN individuals with the weakest fitness values regardless of the fitness of the offspring, the overall grade of the new generation may be weaker. Such a scenario will lead to the same parents reproducing repetitively due to the probabilistic nature of parental selection. This would lead to similar weak offspring being produced during each generation and this would subsequently create premature convergence

3.1.5.3 PSO Global Optimization Method

In the case of PSO, the search space is reflected as an n-dimensional world (n-represents the number of parameters being optimized) where swarms of animals or particles of a random population set $S = \{\mathbf{x_0}, \mathbf{x_1}, \mathbf{x_2}, ., \mathbf{x_N}\}$ flock to search for food or in this case the optimal solution. After the initial population or swarm in this case has been defined as in the case of DE and GA, the fittest individual or particle is registered and every particle in the swarm is programmed to travel to a new position

described as:

$$\mathbf{x}(t+1) = \mathbf{x}(t) + \mathbf{V}(t+1) \tag{3.13}$$

where $\mathbf{x}$ is the population position matrix with each row containing the set of problem variables or parameters pertaining to each particle. $\mathbf{V}$ is the matrix of particle velocity and holds the velocities at which each particle travels in each direction in the n dimensional world. In essence this refers to the amount at which the particles increment by in each direction. t signifies information relating to the previous iteration and $t+1$ denotes the information concerning the next iteration.

The velocity at which each particle travels in each direction depends on the particle's previous velocity in that specified direction, the corresponding position of the fittest particle in that direction, and on the corresponding position of the particle's personal best position. To record the personal best results of each particle, the matrix $\mathbf{P}_{best}$ which contains the personal best parameter values for each particle is created and updated for all iterations.

In each iteration, every particle converges to some extent towards both the fittest individual in the population $\mathbf{G}_{best}$, and in the direction of its personal best solution $\mathbf{P}_{best}$. The convergence towards the global best particle is known as the global search and that towards its corresponding personal best particle is known as local search. The rate of convergence in these neighbourhoods are primarily factors of how much weighting is placed on local and global search. The PSO weighting parameters may be adjusted to attain optimal convergence. The velocity matrix is constructed on local and global search vectors and their associated weighting and is described as follows:

$$\begin{aligned} \mathbf{V}(t+1) &= w_1\mathbf{V}(t) + w_2 rand1(1,N) \times (\mathbf{P}_{best} - \mathbf{x}(t)) + \\ &\quad w_3 rand2(1,N) \times (\mathbf{G}_{best} - \mathbf{x}(t)) \end{aligned} \tag{3.14}$$

where, $\mathbf{G}_{best}$ is the position of global best solution, $\mathbf{P}_{best}$ is a matrix containing positions of the personal best solution for each particle in the swarm, $(\mathbf{P}_{best} - \mathbf{x}(t))$ represents the local search and $(\mathbf{G}_{best} - \mathbf{x}(t))$ denotes the global search contributions. w_1 is the weighting factor of the previous velocity and determines how much the particle's previous velocity affects the particle's new velocity; w_2 is the social weighting and regulates how much the local search affects the particle's new velocity; w_3 is the global weighting and controls how much the global search affects the particle's new velocity; and $rand1(1,N)$ and $rand2(1,N)$ are vectors of random numbers with a size of that of the swarm and these vectors ensures the local and global searches for

each particle occurs at different rates.

By changing the position of each particle according to the aforementioned equations, each particle has the potential to improve upon its personal best location and has the ability to become the global best particle. Hence after each iteration, the fitness value of each particle is analysed and if it improves from its personal best solution, its personal best location is replaced with its current location. This is further explained as follows:

$$\mathbf{P}_{best_i} = \begin{cases} \mathbf{x}_i(t+1) & \text{if } f(\mathbf{x}_i(t+1)) < f(P_{best_i}) \\ \mathbf{P}_{best_i} & \text{otherwise} \end{cases} \tag{3.15}$$

where $\mathbf{P}_{best_i}$ is the personal best location of the i^{th} particle in the swarm, and $\mathbf{x}_i(t+1)$ is the corresponding position of the i^{th} particle that has been computed in the most recent iteration.

Moreover, the global best particle may be defined as the fittest particle from personal best matrix. The process is repeated in each iteration and terminates once the stopping criterion has been met and the optimal solution is chosen as the global best particle at the end of that iteration. The tasks involved in this algorithm are further clarified in the following steps:

Step 1 Produce a random swarm of particles $S = \{\mathbf{x_0}, \mathbf{x_1}, .., \mathbf{x_N}\}$, as in the case of DE and GA.

Step 2 Define the global best particle as the fittest particle in the swarm and let the personal best particles be the same as the initial population

Step 3 If stopping criterion is met, advance to step 7, or else carry on to step 3.

Step 4 Calculate the new set of positions $\mathbf{x}(t+1)$ for the various particles using Eqs. 3.13- 3.14.

Step 5 For each particle perform the following actions: If the fitness of the newly computed particle is better than its personal best location, then replace the personal best particle's location with those of the newly computed particle as described by Eq. (3.15)

Step 6 Register the best particle in the personal best matrix as the global best particle.

Step 7 Use the global best particle as the optimal solution.

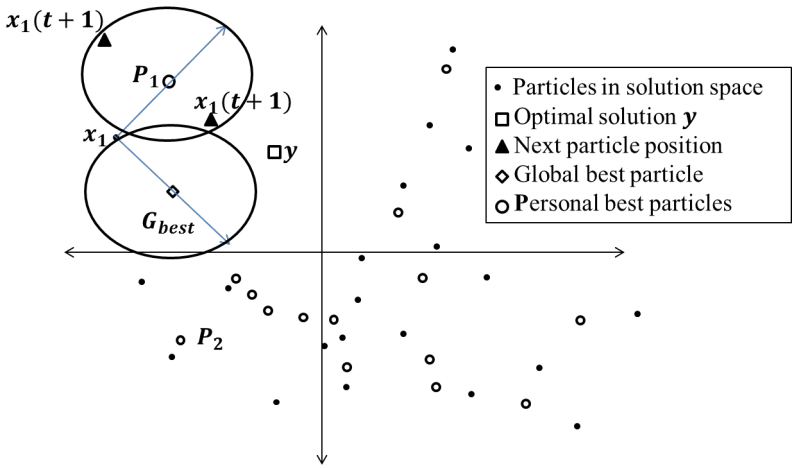

Figure 3.10: Vector plot demonstrating the process of Particle Swarm Optimization

In relation to expected performance of the PSO routine, several comments may be made by drawing an analogy of a 2-dimensional with 2 variables shown in Figure 3.10. In this figure, each particle $\mathbf{x}_i$ is represented as a dot, the correpsonding personal best particle position $\mathbf{P}_{best_i}$ is represented as a circle, the global minimum is a square, that of the global best particle computed thus far $\mathbf{G}_{best}$ is a diamond, and the position of the particle in the next iteration $\mathbf{x}_i(t+1)$ is a triangle. The first performance aspect worth noting is that each particle in the solution space explores potentially successive regions where an optimal solution may be. Areas around the global best particle and personal best position of each particle are potentially plausible areas to search as they are known to contain superior fitness values than other regions in the search space. Hence, searching these regions creates a successful and efficient searching routine which assures convergence to a solution.

However, each particle will continue to change or move in the solution space even if they are continuously producing a weak solution. Such particles would add no value to the algorithm and only reduce the speed of the algorithm. The region explored particle $\mathbf{x}_1$ is around the vicinity of the particle's $\mathbf{x}_1$ personal best solution $\mathbf{P}_1$ is the area enclosed by the upper circle in Figure 3.10, whereas the section inspected around the global best solution $\mathbf{G}_{best}$ is the neighbourhood enclosed by the lower circle. The resulting particle's new position $\mathbf{x}_1(t+1)$ will lie within one of the two circles and as shown in the Figure 3.10, it may be closer to the optimal solution or drift further away from it. [Chiou et al. (2012), Nagaraj and Vijayakumar (2011)]

3.1.5.4 CRS Global Optimization Method

Firstly, an initial population $S = \{\mathbf{x_0}, \mathbf{x_1}, ..\mathbf{x_N}\}$ is the number of problem variables being computed) is generated as in the case of DE, GA and PSO; but in contrast to the preceding algorithms, the size of this population N is set to be exactly ten times larger than the number of variables present in the problem (i.e. $N = 10n$). Each iteration consists of several steps, the first of which involves randomly selecting $n+1$ distinct individuals $\{\mathbf{v_1}, \mathbf{v_2}, ..\mathbf{v_{n+1}}\}$ from the population set. Next, the median or centre of gravity $\mathbf{G}$ of the first n_r selected individuals $\{\mathbf{v_1}, \mathbf{v_2}, ..\mathbf{v_n}\}$ is computed with $\mathbf{G}$ denoting the median of the i^{th} problem variable. Thereafter, a candidate individual $\mathbf{y}$ is calculated based on $\mathbf{G}$ and the individual $\mathbf{v}_{n+1}$ that was earlier chosen from the population set and not incorporated in calculating $\mathbf{G}$. The governing equation for the candidate individual is as follows:

$$\mathbf{y} = 2\mathbf{G} - \mathbf{v}_{n+1} \tag{3.16}$$

This candidate solution $\mathbf{y}$ is accepted and replaces the weakest individual in the population if and only if its fitness is superior to that of the weakest individual $\mathbf{x}_w$ in the population. This reasoning can be modelled mathematically as follows:

$$\mathbf{x}_w = min\mathbf{S} \tag{3.17}$$

$$\mathbf{x}_w = \begin{cases} \mathbf{y} & \text{if } f(\mathbf{y}) \leq f(\mathbf{x}_w) \\ \mathbf{x}_w & \text{otherwise} \end{cases} \tag{3.18}$$

After the above steps are completed, the procedure is continued until the stopping criterion is met. The procedure for CRS global optimization algorithm is summarized in the following steps:

Step 1 Generate a randomly distributed population set that uniformly spans the search space.

Step 2 Check if the stopping criterion is met and if not continue to the next step, otherwise proceed to step 7.

Step 3 Randomly select $n_r + 1$ distinct individuals from the population set S.

Step 4 Compute the median for each problem variable from the first n_r individuals that were chosen in the previous step.

Step 5 Formulate a candidate individual $\mathbf{y}$ according to Eq. (3.16).

Step 6 Replace the weakest individual in the population $\mathbf{x}_w$ with the candidate individual $\mathbf{y}$ if the $\mathbf{y}$ incurs a lowest cost than $\mathbf{x}_w$, and thereafter return to step 2.

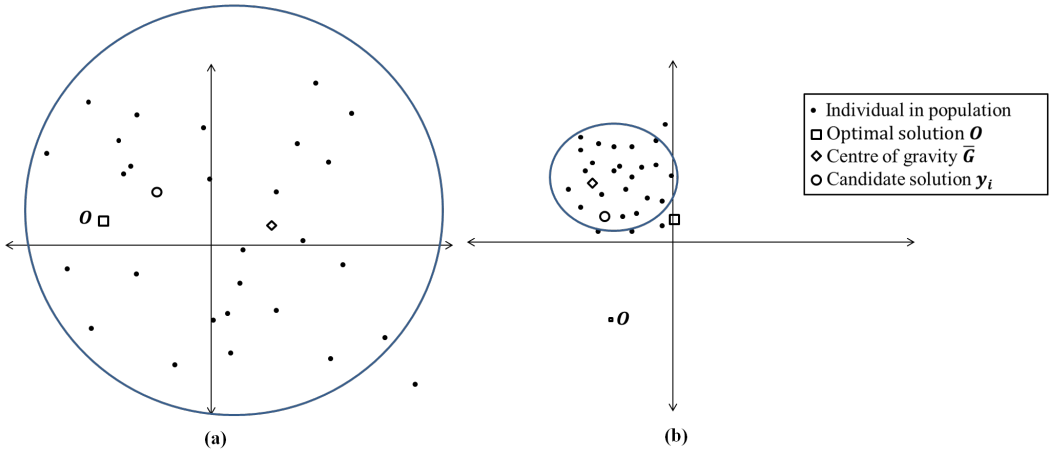

Figure 3.11: Impact of the centre of gravity on the Controlled Random Search algorithm

Step 7 Select the individual with the best fitness value as the optimal solution.

Several points may be made regarding the strengths and defects of this algorithm. Firstly, the candidate solution $\mathbf{y}$ is only accepted if it produces a satisfactory fitness value that is better than the worst individual in the population. Like the DE, this condition will guarantee progression towards better solutions, but will however tend to slow down the convergence speed of the algorithm. Eq. (3.16) suggests that the centre of gravity $\mathbf{G}$ plays a major role in computing the candidate solution $\mathbf{y}$. This relationship may have an adverse effect and create early convergence. Such a situation plays out if the particles begin to clutter around one another and this would consequently cause $\mathbf{G}$ to be bounded to a certain region no matter what individuals from the population are used to compute $\mathbf{G}$. Consequently, early convergence will occur and the algorithm will be stuck in a local minima. This scenario is further explained in Figure 3.11, where each individual in the population is represented as a dot.

The circles in Figure 3.11 are the regions where the centre of gravity $\mathbf{G}$ may lie within for a specific scenario. The centre of gravity of $n+1$ randomly selected particles $\mathbf{G}$ can reside anywhere over a greater range as the population is distributed across a greater area as illustrated in Figure 3.11a. In this case there is more flexibility in the search exploration of the CRS, which gives it a better probability of finding the optimal solution O. However, if the population is cluttered in a certain region as shown in Figure 3.11b, the centre of gravity $\mathbf{G}$ will be restricted to a certain range of values which are relatively far from the optimal solution O. This will ultimately limit the flexibility of the algorithm and consequently the algorithm will

never approach the optimal solution. [Price (1983), Ali (1994), Ali et al. (1997), Jeżowski et al.(2005)]

3.1.5.5 PS Global Optimization Method

In contrast to the aforementioned optimal policies, pattern search (PS) is not population-based and no initial population set is created but rather a trial solution continuously travels within the search space with the aim of attaining a better fitness value. This algorithm operates by first discretizing the search space into an n-dimensional mesh with n indicating the number of problem variables as in the case of PSO. In other words, each problem variable is associated with each coordinate axis. The incremental spacing along each dimension within this mesh is scaled according to the order of magnitude of the problem variable that each dimension signifies. The incremental spacing of the i^{th} problem variable is denoted as A_i with $\mathbf{A}$ being a one-dimensional vector containing the incremental spacing of each problem variable. An initial condition $\mathbf{x}_0$ is entered and is now defined as the trial solution $\mathbf{y}$. In each iteration, the trial solution migrates along one of its axis by one step and thus is at new position $\mathbf{w}$, which is calculated as:

$$\mathbf{w} = \mathbf{y} + A_i e_i \tag{3.19}$$

where e_i is the i^{th} unit vector. If the solution does not improve through this relocation i.e. $f(\mathbf{w}) \geq f(\mathbf{y})$, the trial solution returns to its original location $\mathbf{y}$ and proceeds along the next unexplored dimension. As soon as the solution improves $f(\mathbf{w}) \geq f(\mathbf{y})$, its new position w becomes the best solution $\mathbf{y}$. Thereafter, the incremental spacing of each of the dimensions increases by a scaling factor ϵ and the iteration is complete [Kolda et al. (2003)]. However, if the solution did not improve after each dimension had been explored, the step size of each dimension is scaled down by ϵ and the next iteration proceeds. The mathematical equivalence of these decisions is represented as follows:

$$\mathbf{y} = \begin{cases} \mathbf{w} & \text{if } f(\mathbf{w}) \leq (\mathbf{y}) \\ \mathbf{y} & \text{otherwise} \end{cases} \tag{3.20}$$

The scaling factor is defined as:

$$\epsilon = \begin{cases} \epsilon \times 2 & \text{if } f(\mathbf{w}) \leq (\mathbf{y}) \\ \epsilon \times 0.5 & \text{otherwise} \end{cases} \tag{3.21}$$

$$\mathbf{A}(t+1) = \mathbf{A}(t) \times \epsilon \tag{3.22}$$

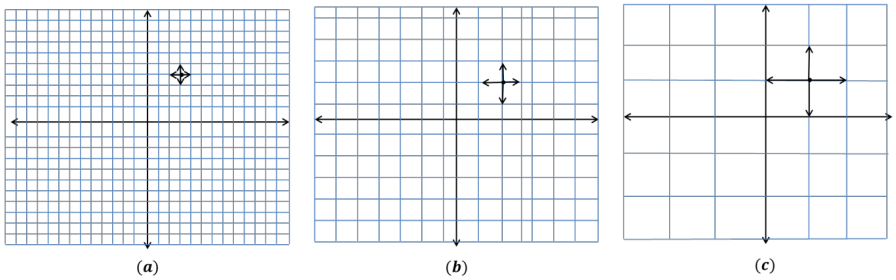

Figure 3.12: Demonstration of the Pattern Search local optimization technique

where $(t+1)$ denotes the next iteration and t signifies the current iteration. The algorithm continues until the incremental step size of the scale factor ϵ falls below its threshold values. PS optimization routines may be summarized as follows:

Step 1 Discretise the search space into an n-dimensional mesh and specify the initial incremental spacing along each its dimensions.

Step 2 If the scaling factor ϵ drops below its threshold value, stop the algorithm, and use $\mathbf{y}$ as the optimal solution; otherwise continue to the next step.

Step 3 Check if all dimensions have been explored, if not continue to the next step; otherwise proceed to step 7.

Step 4 Migrate the best solution $\mathbf{y}$ along one of its unexplored dimensions to a new position $\mathbf{w}$ which is computed using Eqs. 3.19.

Step 5 If the new position $\mathbf{w}$ has a superior fitness than its original location $f(\mathbf{w}) \leq (\mathbf{y})$, let the new position $\mathbf{w}$ replace the best position $\mathbf{y}$ (refer to Eq. (3.20); and increase the scaling factor ϵ according to Eq. (3.21)

Step 6 Return to step 3 if $f(\mathbf{w}) \leq (\mathbf{y})$, otherwise continue to the next step.

Step 7 If the solution has not improved after each dimension has been explored, decrease the incremental spacing according to Eq. (3.21) and return to step 2 and reinitiate the exploration process.

Figure 3.12 presents a graphical representation of the algorithm for the case of a 2-variable system. The trajectory of the solution $\mathbf{y}$ is made of discrete steps as shown in Figure 3.12b and if the solution improves the steps sizes are decreased as shown in 3.12a and the opposite occurs if the solution does not (see Figure 3.12c). This simple set of condition will cause the algorithm to converge to the optimal solution. Furthermore, the solution only moves if the fitness improves. This will tend to slow the convergence speed but will guarantee efficient exploration. However, the sheer

number of variables to be computed in AVSS design as well as the nonlinear nature of AVSS and the dynamic neural networks may not be easily captured by these simple conditions. As a result, early convergence may occur where the solution gets trapped in a local minimum. [Kolda et al. (2003), ElMadany et al. (1990)]

3.1.5.6 Optimization Set Up and Initialization

The performance index presented in Eq. (3.5) aims to minimize four vehicle trade-off qualities and hence this task is an iterative design process. Furthermore, the presence of nonlinearities, the nonlinear and comparatively severe deterministic road disturbance explained in Eq. (2.89), as well as actuator dynamics add further complexities to the investigation. In order to prevent inherent difficulties associated with these issues, the bounds of the search space is defined with the aim of attaining minimal computational expense, improve speed and prevent early convergence of the various routines. Before global optimization was performed, the search space or range of values where each gain is set to lie is determined through the process of manual tuning. This is to ensure that areas that are known to produce a result that contradicts the design specifications is not searched. Furthermore this search space is refined to regions where the global minimum is intuitively anticipated to lie. Moreover, as the objective of these optimization routines is to improve the results obtained through manual tuning, the initial condition used in each algorithm will correspond to the set of PID gains attained through manual tuning.

A complete list of the parameters of each algorithm is listed in Table 3.3.

Table 3.3: Global optimization parameter settings for the suggested routines

Routine	**DE**	**GA**	**PSO**	**CRS**	**PS**
Population Size	100	300	100	60	1
Stopping Criteria Criteria	100 Generations	100 Generations	100 Iterations	100 Iterations	Scaling factor $\epsilon \leq 1 \times 10^{-8}$
Optimization Parameters	F=2	K=100	w_1=0.5 $w_2 = 2$ w_3=2	n=6	A_1=8000 A_2=200 A_3=200 A_4=0.005, A_5=0.005 A_6=0.00001

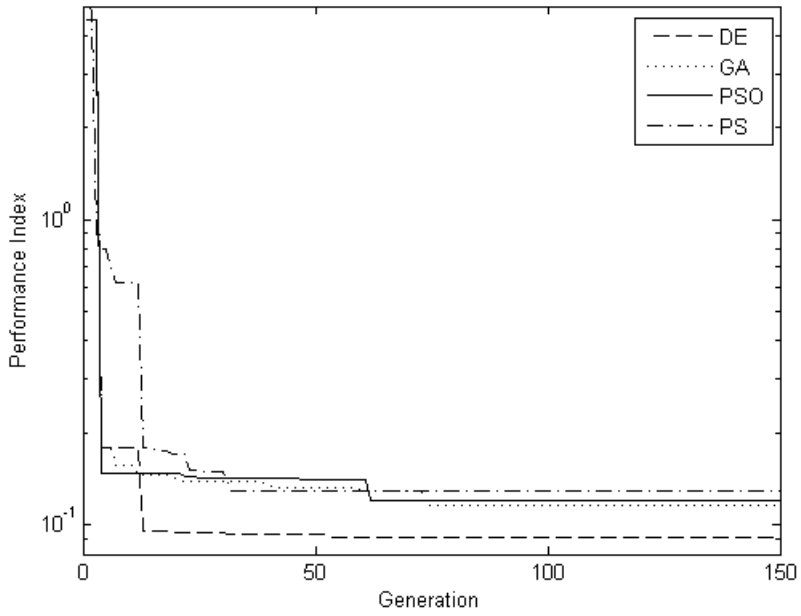

Figure 3.13: Performance index convergence history of the DE, GA and PSO algorithms

3.1.6 Examination of System Response Attained through the use of Global Optimization Methods

The convergence history of the DE, GA, PS and PSO algorithms are superimposed in Figure 3.13 and that of the CRS optimization routine is presented in Figure 3.14.

Several issues are worth discussing regarding the convergence histories of the optimization algorithms. Each of the optimization algorithms produced a significant lowering of the performance index from that of the manually-tuned case. From all the optimization routines, the DE tuning method obtained the best performance index value followed by the GA, PSO, PS and CRS respectively. The effective performance achieved by DE was expected due to two reasons: DE possesses efficient exploration capabilities; and it contains a hard constraint where trial individuals are only accepted if they produce a better performance index value. GA and PSO performed slightly weaker than the DE. This is because they do not apply hard conditions in accepting trial individuals or particles, but rather the particles in the PSO continue to move regardless of the variation in fitness values; and the weakest individuals in the population set of the GA are replaced by offspring irrespective of their fitness values.

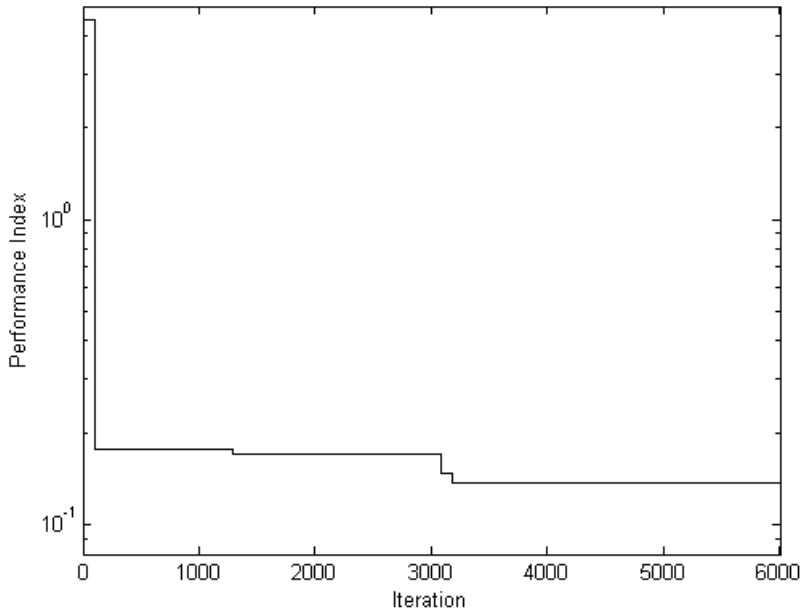

Figure 3.14: Convergence history of performance index when applying CRS-based controller tuning

Nevertheless, GA, CRS, PS and PSO did perform well as compared to the manually-tuned PID controller with a substantially superior performance index. From a GA standpoint, this is anticipated as tournament selection and its reproduction sub-routines ensure that the fittest individuals in the population are most likely to reproduce. This inherently creates offspring which are either slightly weaker or fitter than their parent individuals. Furthermore, the fittest individuals in the population are retained in successive generation until they are surpassed by a great number of offspring. These characteristics certify that the GA will converge to an adequate solution as was observed in this investigation.

With regards to the PSO performance, both explorations in the vicinity around each particles best position P_{best_i} in search space S and around the neighbourhood of the fittest particle G_{best} improves the flexibility and efficiency in searching the solution space S. This in turn yields effective convergence and guarantees an acceptable optimal solution. The gains computed through each case are presented in Table 3.4. Some of the gains reported were negative and others were of a low order of magnitude. The k_d gains of the inner loop are smaller than 1×10^{-9} may effectively be replaced by zero and such reported values also indicate the high sensitivity of these gains. The negative gains reported were nothing more than a consequence of the optimization. The K_P gains in the outer-loop are substantial and these high loop

gains are not unusual for PID-based control. It must be ensured that these high loop gains do not cause the power supply to saturate. The outer loop integral gains K_I computed through the optimization algorithms are important as they ensure that the steady-state error of the controlled variable is effectively zero, and those of the inner loop k_i are necessary to ensure that the desired actuator force is adequately tracked.

Table 3.4: PID gains computed using the various global optimization schemes

Control Loop	**Outer Loop**			**Inner Loop**		
Gain	K_P	K_I	K_D	k_p	k_i	k_d
DE	23681	10	1597	0.00193	0.00389	3.348×10^{-9}
GA	23518	15	2507	0.00134	0.00282	4.612×10^{-9}
PSO	23005	-3	1681	0.00195	0.00527	3.319×10^{-9}
CRS	23188	198	3174	0.00118	0.00241	3.319×10^{-9}
PS	2400	-200	1700	0.00209	0.00374	3.122×10^{-9}

The convergence to a better performance index indicates that global optimization methods improve the overall system performance. However, these plots do not explicitly show whether the conflicting trade-offs of AVSS have been resolved. Hence, as in the case of the PID-based AVSS; the response of the various AVSS trade-offs namely suspension travel, sprung mass acceleration, road holding and power consumption are presented Figures 3.20 to 3.24, respectively for further examination. Quantitative information relating to these various plots as well as those used in previous investigations is presented in Table 3.5 and are graphically summarized in bar graphs presented in Figures 3.15 to 3.19. The analysis of the these controllers in relation to other controllers is an important aspect of this investigation as it highlights the performance of the proposed controller architecture to those of linear, optimal and intelligent controllers.

In relation to these groups of controllers, Amani et al. (2004) applied an optimal policy through QFT control, and Kumar and Vijayarangan (2007) incorporated PID control but for a system that did not contain actuator dynamics, whilst Lin et al. (2009) utilised an intelligent controller which is a hybrid of sliding mode and fuzzy logic control.

However, in contrast to this investigation Kumar and Vijayarangan (2007) and Lin et al. (2009) measured the performance of a vehicle travelling at a horizontal speed

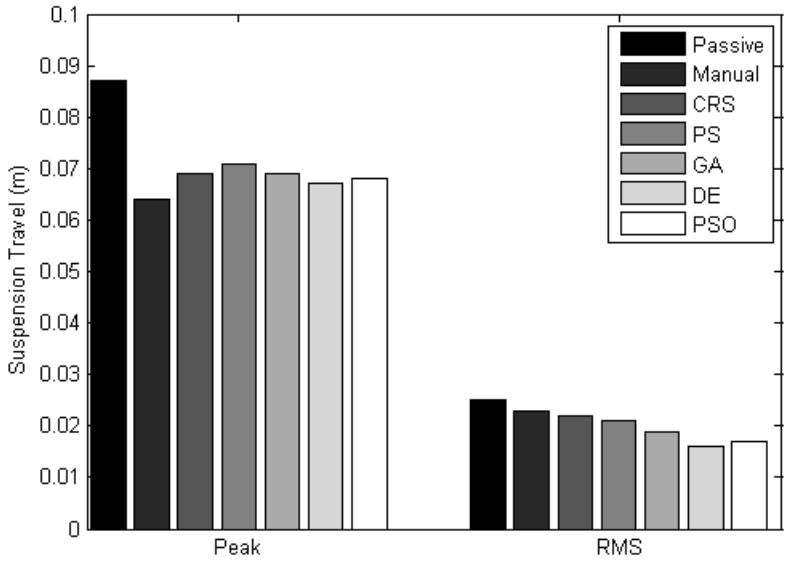

Figure 3.15: Bar graphs depicting the variation in suspension travel for each control law

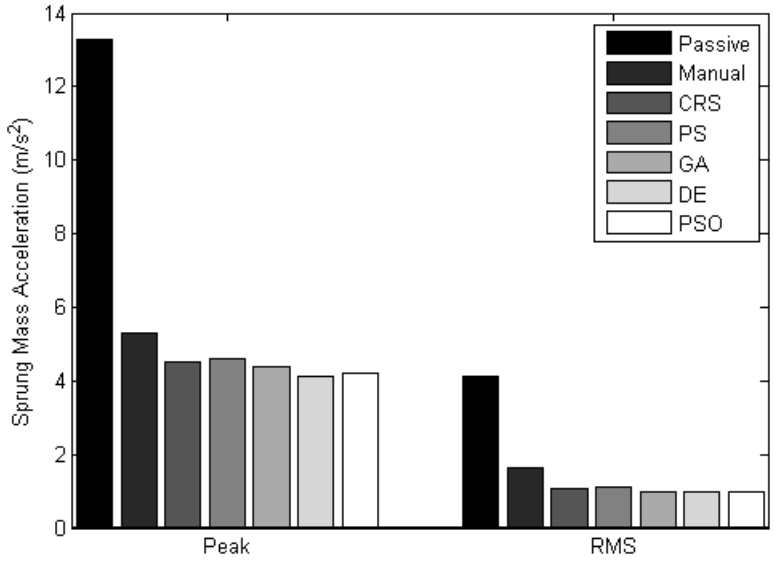

Figure 3.16: Bar graphs illustrating the difference in heave acceleration for the proposed controllers

of $40km/h$ as it passed over a less severe bump with height of 4cm. Moreover, Amani et al. (2004) based their investigation on a vehicle with a horizontal speed of 20km/h and a 5cm bump amplitude. As in this investigation, Amani et al. (2004) incorporated actuator dynamics which makes his model a better benchmark for comparison.

Table 3.5: Summary of selected suspension performance incorporating the various optimization routines

Technique	**Suspension Travel**(m)		**Sprung Mass Acceleration**(m/s^2)	
	RMS	**Peak**	**RMS**	**Peak**
PVSS	0.025	0.087	4.1	13.35
CRS	0.022	0.069	0.99	4.2
PS	0.021	0.071	0.93	4.1
GA	0.019	0.069	0.98	4.4
DE	0.018	0.071	0.99	4.1
PSO	0.017	0.068	0.96	4.2
Ling	N/A	N/A	N/A	2.5
Kumar	N/A	0.0048	N/A	3.1
Amani	N/A	0.0045	N/A	6
Technique	**Control Input Voltage**(V)		**Force** (N)	
	RMS	**Peak**	**RMS**	**Peak**
CRS	0.99	4.2	749	2746
PS	0.93	4	631	2369
GA	0.98	4.4	593	2289
DE	0.99	4.1	631	2369
PSO	0.96	4.2	659	2509
Technique	**Settling Time**(s)		**Wheel Deflection**(m)	
	Peak		**RMS**	**Peak**
PVSS	2.8		0.0064	0.0206
CRS	1.9		0.0025	0.0104
PS	2.4		0.002	0.0090
GA	1.9		0.0021	0.0089
DE	1.8		0.0023	0.0090
PSO	1.8		0.0022	0.0093
Ling	1.8		N/A	0.0060
Kumar	3.01		N/A	0.0080
Amani	3.5		N/A	N/A
Performance Index J				
CRS	PS	GA	DE	PSO
0.148	0.145	0.13	0.092	0.134

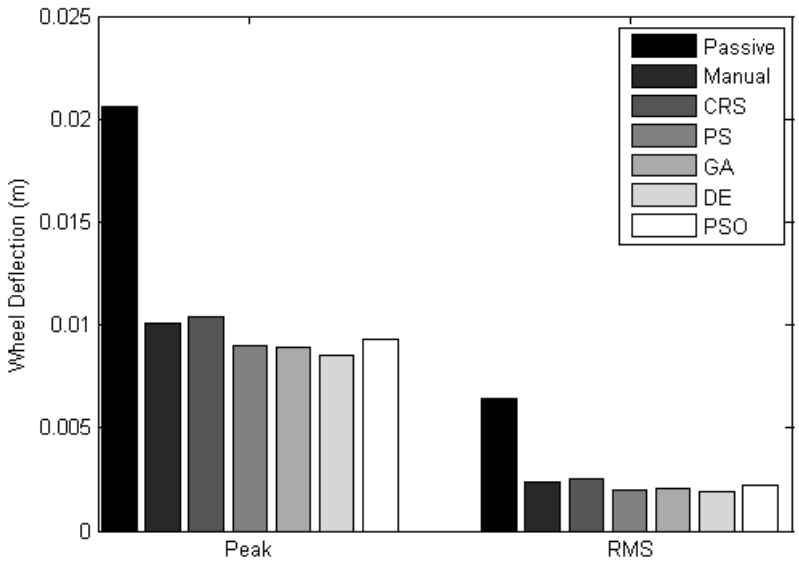

Figure 3.17: Bar graphs summarizing the road holding data for each control case

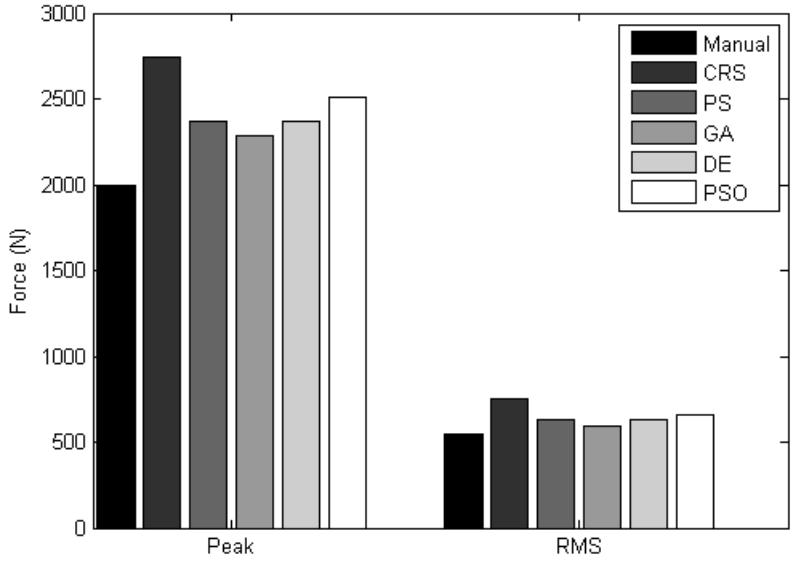

Figure 3.18: Bar graphs summarizing the results obtained for global optimization for the case of actuator force

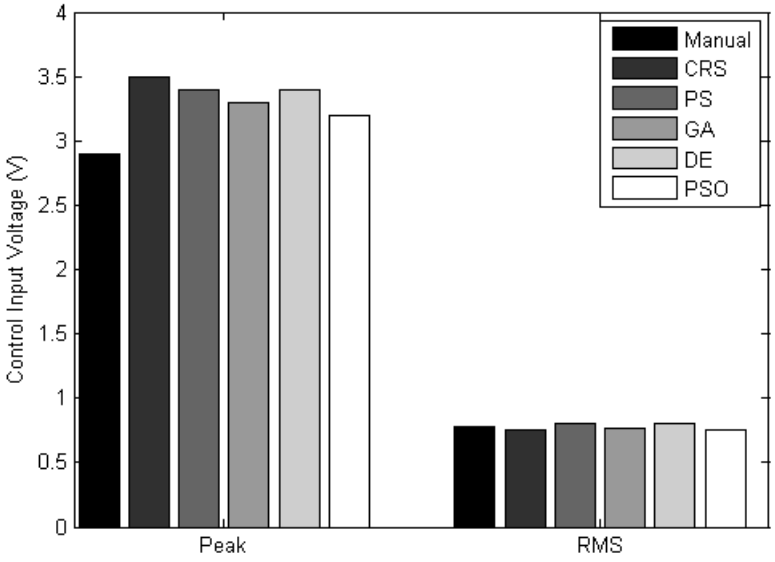

Figure 3.19: Quantitative information pertaining to the control input voltage response

Suspension travel plots clearly indicate that each of the optimal policies apart from the CRS completely remove the effects of the disturbance within 1.8 seconds, which is additionally better than that obtained in previous investigations which had less severe disturbances (namely Amani et al. (2004), Lin et al. (2009), and Kumar and Vijayarangan (2007)). Secondly, each of these PID-based routines displayed a valuable transient characteristic, where oscillations immediately dampened out as soon as the disturbance was passed, whereas the manually-tuned case exhibited an additional peak before it settled. This subsequently reduced the RMS value of the suspension travel. The only drawback is that, the peak suspension travel for the optimal cases was greater than that of the manually-tuned case, but they never exceeded their stipulated limit.

The ride comfort and road holding responses of optimal policies shown in Figures 3.21 and 3.22 clearly point out that they were far superior to the manually-tuned case and PVSS with reduced RMS and peak values, but their peak values were still greater than those obtained in previous studies. However, these studies included less severe road profiles, which suggest the response obtained here is still a significant improvement to previous investigations. Furthermore, the optimal-based PID routines displayed a large degree of chattering where the PSO was the worst followed by the CRS, PS, GA and DE respectively. This may be as a result of the high derivative gain K_D computed for the outer loop using these optimal routines, since

derivative gains create rapid rise time which may incur larger oscillations for more sensitive outputs (such as the wheel deflection) in the system.

Body-heave acceleration plots (see Figure 3.21) which characterise the ride comfort experienced by the passengers show that the force experienced by the passenger was most severe as the vehicle passed peak of the bump. The manually-tuned PID and PVSS cases could not manage this facet particularly well whereas every optimal policy brought down this peak to $4.5m/s^2$ and was thus able to meet the desired ride comfort specifications with DE and PS performing the best in this respect. Furthermore, the optimal policies greatly reduced the RMS acceleration and brought it to the "Fairly uncomfortable" range of the International Organization for Standardization 2631 (2003). In relation to the ride comfort response of previous studies, Kumar and Vijayarangan (2007) and Lin et al. (2009) investigations had lower acceleration peaks but these investigations did not include actuator dynamics and used less severe road disturbances which must be taken into account.

These positive performances may be attributed to the objective function which placed considerably large weightings on suspension travel, ride comfort and road holding. The large peaks obtained for suspension travel are expected as it is required to help drive the ride comfort lower such as to meet the ride comfort specifications.

With regards to power consumption, actuator force and control input voltage incurred a greater cost for global optimization based-controller tuning as compared to that of the manually-tuned case. This infers that the advantageous aspects of optimal AVSS design are attained at the cost of power consumption. This is expected for one of two reasons, firstly, the ratio of control voltage to its respective weighting factor was much smaller than the other suspension performance criteria and hence did not contribute significantly to the performance index. Secondly, in order to meet the desired acceleration specifications, a larger actuator force is needed to cancel out the effects of the road disturbance and hence a larger actuator force was needed to improve ride comfort. Furthermore, it is worth mentioning that even though the optimization algorithms computed high outer loop gains (see Table 3.4), they did not cause the control input to saturate.

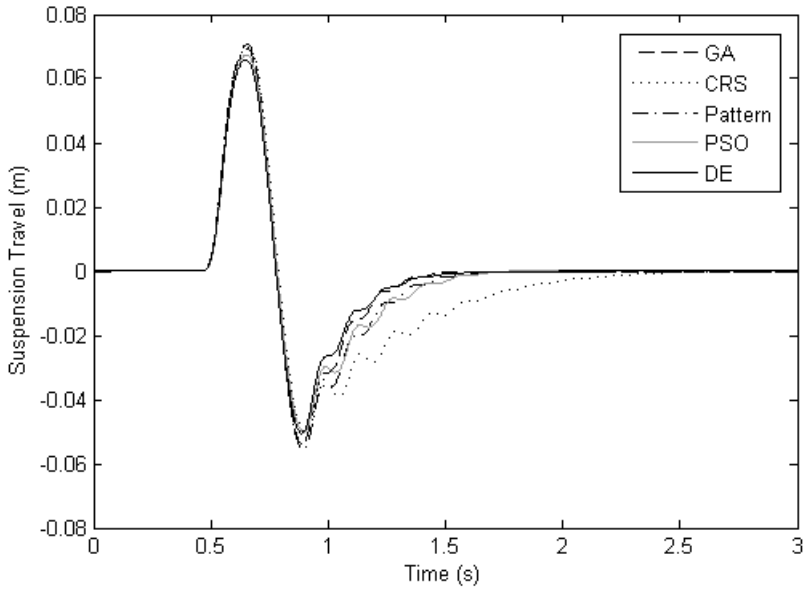

Figure 3.20: Suspension travel response for optimized PID-based AVSS

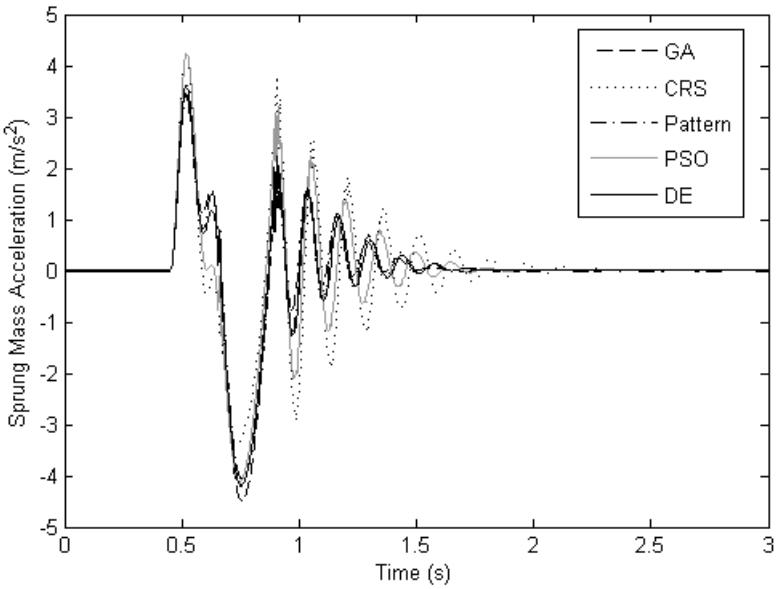

Figure 3.21: Sprung mass acceleration response for optimized PID-based AVSS

With regards to the best optimal policy, DE incurred the least cost with the best ride comfort, road holding, suspension travel and least degree of chattering. Hence, DE will only be used for the case of the full-car optimal PID design.

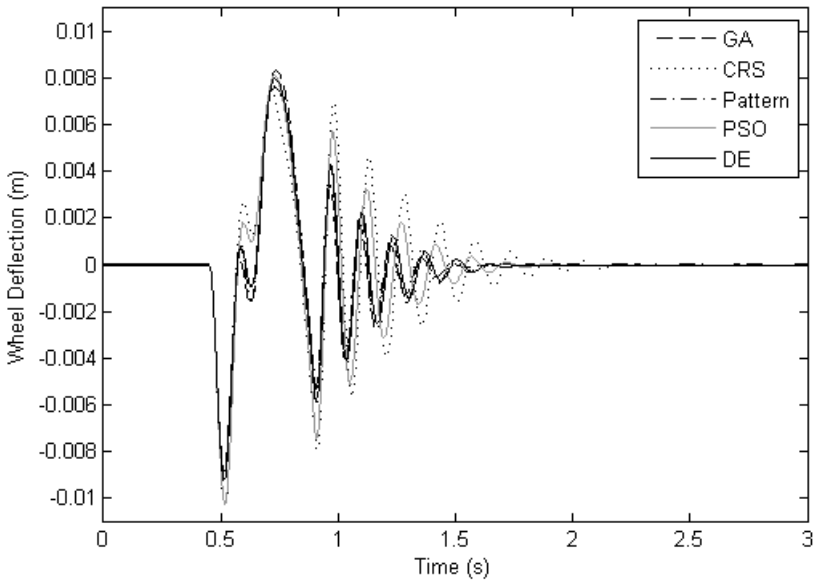

Figure 3.22: Road holding characteristics for optimized PID-based AVSS

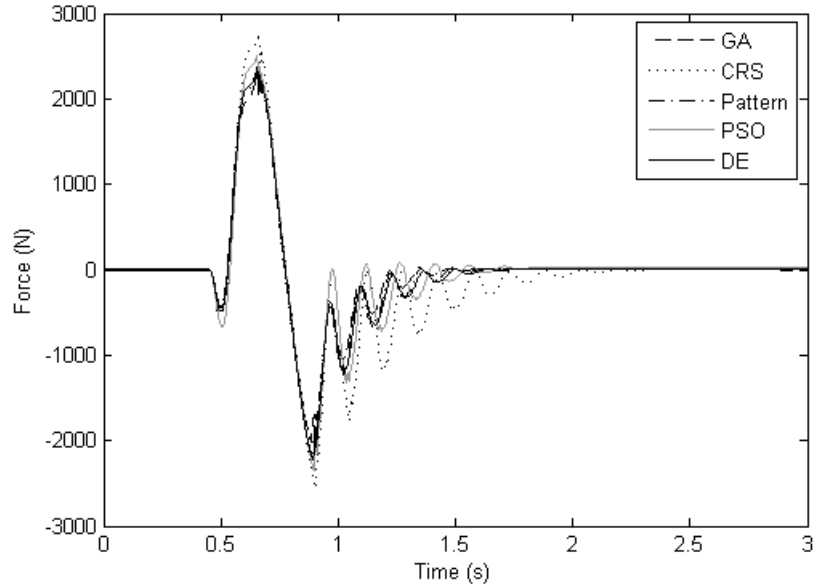

Figure 3.23: Actuator force supplied for the optimized PID-based AVSS

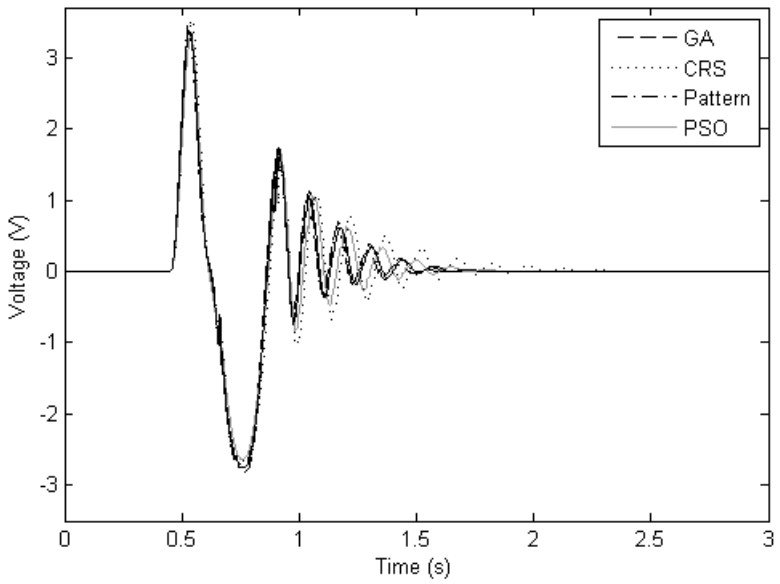

Figure 3.24: Control input voltage supplied for optimized PID-based AVSS

3.1.7 Sensitivity to Parameter Variations and Frequency-Domain Analysis for PID-Based AVSS

Figures 3.4 and 3.20 clearly indicate that the control system is stable in the Bounded-Input-Bounded-Output (BIBO) sense as the system clearly settled with a steady-state error in the order of magnitude of $0.0001m$. Investigation into the effects of parameter changes is also studied for the cases of changes in mass, tyre stiffness and speed to further examine the stability of the system. These specific parameters are altered as these changes will occur in reality, as passengers and fuel will alter over time, tyres will lose pressure and the vehicle will be travelling at different speeds. As the DE performed best, stability sensitivity will be carried out for the DE-optimized PID-controlled AVSS. Parameter variation plots relating to suspension travel are presented in Figures 3.25 and 3.26.

With regards to the variation in vehicle speed, the steady-state error increased for both a 20% increase and decrease in vehicle speed. An increase in vehicle speed produced weaker transient behaviour with an additional peak. The order of magnitude of the steady-state error for this parameter uncertainty is comparatively high but is acceptable considering the large degree of nonlinearities as well as the adverse effects of actuator dynamics. Variation in vehicle mass up to 20% did produce a steady-state error but it was 7% of the peak value and this is within an acceptable tolerance. The same may be concluded for the case of a 20% variation in tyre stiffness as the

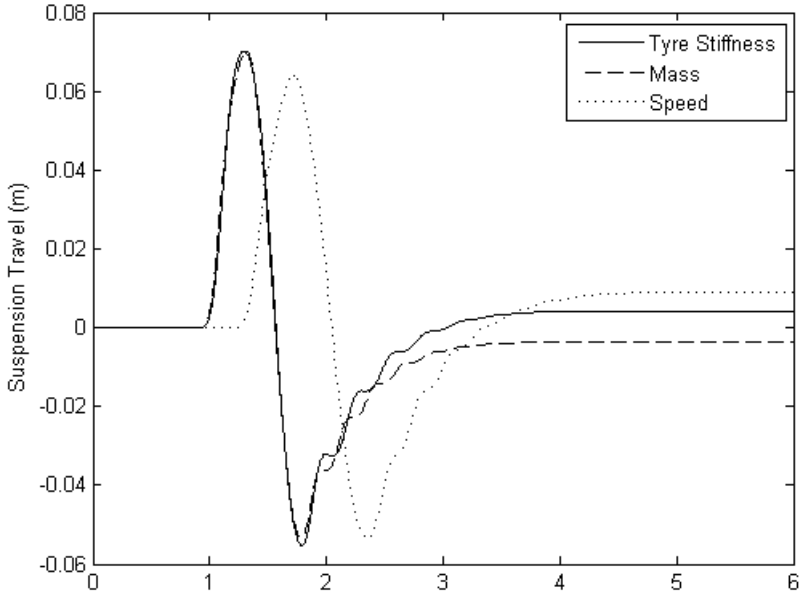

Figure 3.25: System response for a -20% variation in some selected system parameters

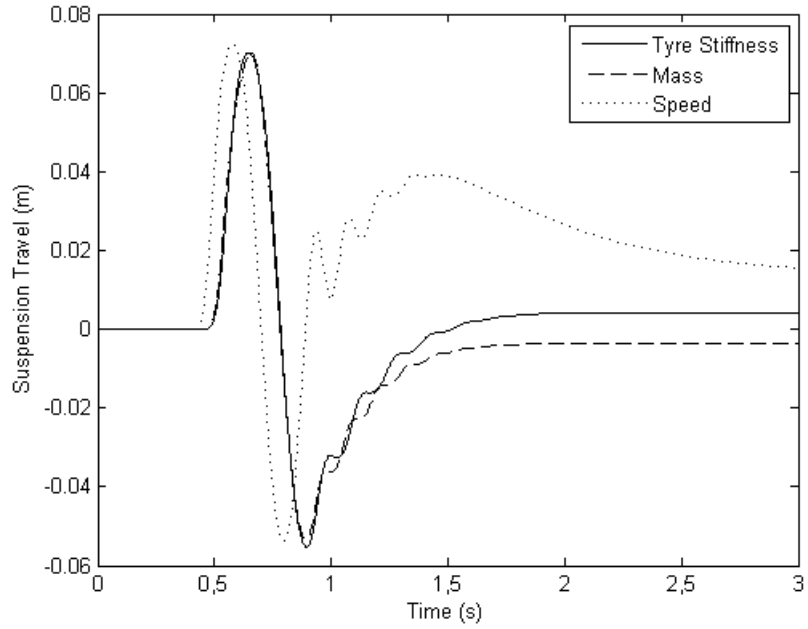

Figure 3.26: System response for a +20% variation in some selected system parameters

largest steady-state error was only 12% of the peak value. Moreover, the system remained BIBO stable for all the considered cases and this implies that the system is stable and has an acceptable degree of sensitivity to parameter variations. Implementation of gain scheduling for variation in vehicle speed may resolve this weakness.

European Commission (2002) demands satisfactory ride comfort for human exposure to Whole-Body-Vibration (WBV) frequencies ranging between 0.5Hz to 80Hz. Hence, it is paramount that vehicle ride comfort be studied for these frequencies. The European Commission (2002) and International Organization for Standardization 2631 (2003) argued that the high/low frequencies of vibrations in the range of 1Hz to 8Hz typically cause the most discomfort to the human body. The International Organization for Standardization 2631 (2003) and Griffin (2007) quantify ride comfort in terms of the RMS value of body-heave acceleration and have provided the range of RMS values that are satisfactory for human comfort. On the other hand, European Commission (2002) provided specifications for WBV. The frequency-domain plots for ride comfort and road holding for the various cases are presented in Figures 3.27 and 3.28 respectively. These plots were generated using the Power-Spectral-Density (PSD) estimates which were performed in the signal processing toolbox of the Matlab/Simulink environment. The PSD was estimated using the Fourier analysis. This essentially captures the response in the complex plain where thereafter the behaviour may be studied in terms of frequencies. The transformation is as follows:

$$\mathbf{X} = \sum_{n=0}^{NNFT-1} \mathbf{x}_n \mathrm{e}^{-2i\pi k \frac{n}{NNFT}} \quad k = 0, ..., NNFT - 1 \tag{3.23}$$

The resulting transformation in the complex plain ($\mathbf{x}_n$) is computed through the welch algorithm with a configuration listed in Table 3.6. Stability or convergence is ensured as long as the exponent in the above terms stays negative, which is the case for the current study.

Table 3.6: PSD configuration settings for frequency-domain study

Parameter	**Setting**
Computation	Algorithm Welch
Windowing Function	Hanning
Number of points included in fourier transform (NNFT)	1024
Length of Window (NWind)	256
Sampling Frequency	80Hz

The worst ride comfort experienced by the vehicle was at the lower frequencies which ranged from $0.1Hz$ to $0.8Hz$. The frequency weighted RMS acceleration of the PVSS case exceeded the maximum Exposure-Limit (ELV) stipulated by the European Commission (2002) for this range, whereas the AVSS cases stayed comfortably

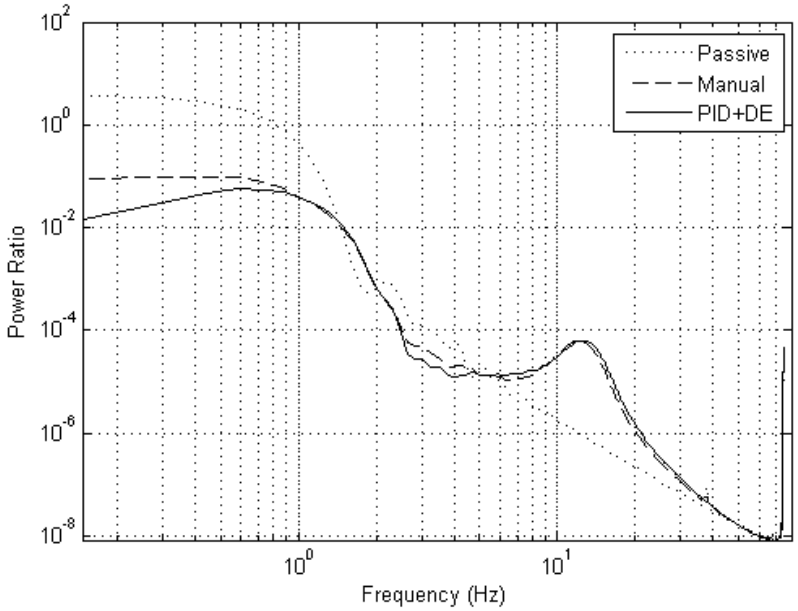

Figure 3.27: Frequency response for body-heave acceleration of the passive system and the proposed control schemes

below them. In this respect, the AVSS cases were able to achieve a considerable improvement from the PVSS case, with the optimal AVSS case being the better of the two. Additionally, the AVSS cases produced RMS values that fell in the "less discomfort range" of the International Organization for Standardization 2631 (2003) At the onset of $2Hz$, the signals were successfully attenuated for all cases with marginal differences between them. Beyond $8Hz$ the passive system performed the best. In this range AVSS cases displayed a resonance peak and a minor peak at $15Hz$ and $80Hz$ respectively.

With regards to road holding, the frequency response for the range between $0.01Hz$ to $80Hz$ resembled that of a high pass filter. From $20Hz$ onward signals for each case were attenuated, whereas the highest peaks occurred in the range $0.01Hz$ to $1Hz$. The AVSS cases did outperform the PVSS case in this range with a minimal difference between the two of them. Furthermore, as both road holding and ride comfort frequency plots indicated an improvement from the passive system, it infers that the proposed AVSS schemes have found a better compromise between these conflicting performance criteria as compared to that of the passive system.

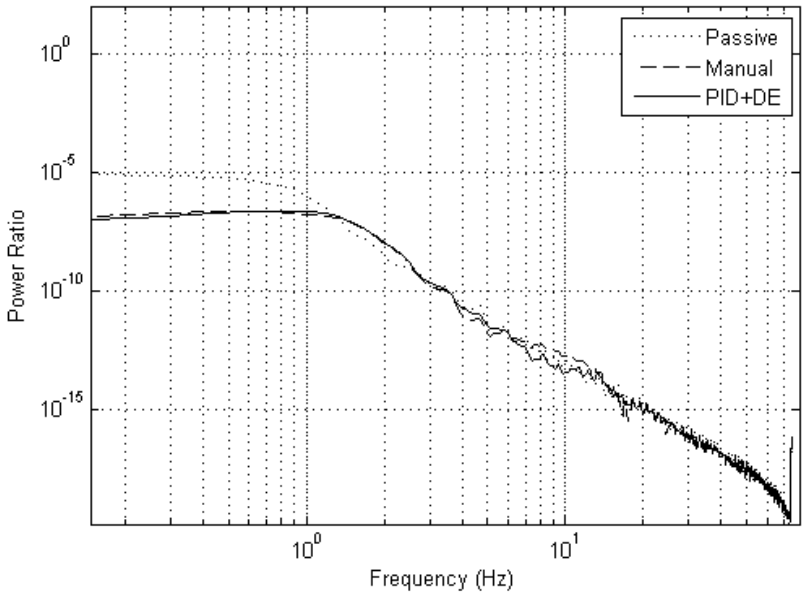

Figure 3.28: Road holding frequency response for passive, PID-controlled and DE-controlled cases

3.1.8 Summary

Optimal design of PID control is an effective tool in meeting hard design specifications such as those placed on ride comfort. They tend to improve suspension travel, and road holding as well as transient behaviour. However, this is attained at the cost of power consumptions as a greater force and control input is needed to improve ride comfort, road holding and suspension travel. Furthermore, they tend to produce large derivative gains whose inherent ability to increase rise time tends to add chattering to the more sensitive outputs of the system. DE is the best optimal routine and also exhibits a satisfactory robustness to parameter changes. In terms of frequency response, each case was able to attenuate signals from $5Hz$ to $80Hz$. In the lower frequencies ($0.01Hz$ to $5Hz$) the exposure levels were the worst. However, the AVSS cases did produce a significant improvement in this domain with RMS ride comfort values falling within the "Less Discomfort" range of the International Organization for Standardization 2631 (2003).

3.2 PID-Controlled Full-Car System

3.2.1 Introduction

Numerical studies of full-car AVSS design are better than those of quarter-car AVSS as they provide insight into the lateral and longitudinal dynamics of the vehicle. Such information is necessary to qualitatively describe the vehicle handling characteristics. Full-car models also contain coupling between the wheels, where a disturbance at one wheel affects the dynamics of all the vehicle's states. Consequently, this model has more system states and more Degrees-of-Freedom (DOF) and these features tend to make the model more complex. However, studies using this model must be conducted as it is the most realistic model that captures all the major dynamics of the vehicle namely pitch, roll and heave.

3.2.2 Controller Design

As in the case of the quarter-car PID-based AVSS design discussed in section 3.1, the suspension travel dynamics at each wheel is regulated by an individual electro-hydraulic actuator. A schematic of the control law is illustrated in Figure 3.29. The suspension travel at each wheel is chosen as the controlled variable for the same reasons previously discussed. As before, a two-loop PID controller is used where the outer loop ensures that the system returns to its desired set point and the inner loop maintains actuator stability.

y_{ij_d} corresponds to the equilibrium set point of the i, j^{th} wheel, which is set to zero to address regulation problem; the subscripts ij are representative of the front right fr, front left fl, rear right rr and rear left rl wheels respectively; $e_{1_{ij}}$ is the outer loop control error of the i, j^{th} suspension whereas $e_{2_{ij}}$ denotes that of the respective inner loops; $F_{a_{ij}}$ is the actuator force applied at the i, j^{th} actuator present at the i, j^{th} suspension with $F_{d_{ij}}$ signifying its respective desired force which is being tracked using the inner PID controllers. y_{fr}, y_{fl}, y_{rr}, and y_{rl} are the suspension travel that are manipulated through the outer control loops, and u_{fr}, u_{fl}, u_{rr}, and u_{rl} are the control signals that are passed into the respective actuators of the AVSS. As in the case of the quarter-car model, the PID controllers operate according to the following equations:

$$e_{1_{ij}} = y_{ij} - y_{d_{ij}} = z_{ij} - z_{tij} - y_{d_{ij}} \tag{3.24}$$

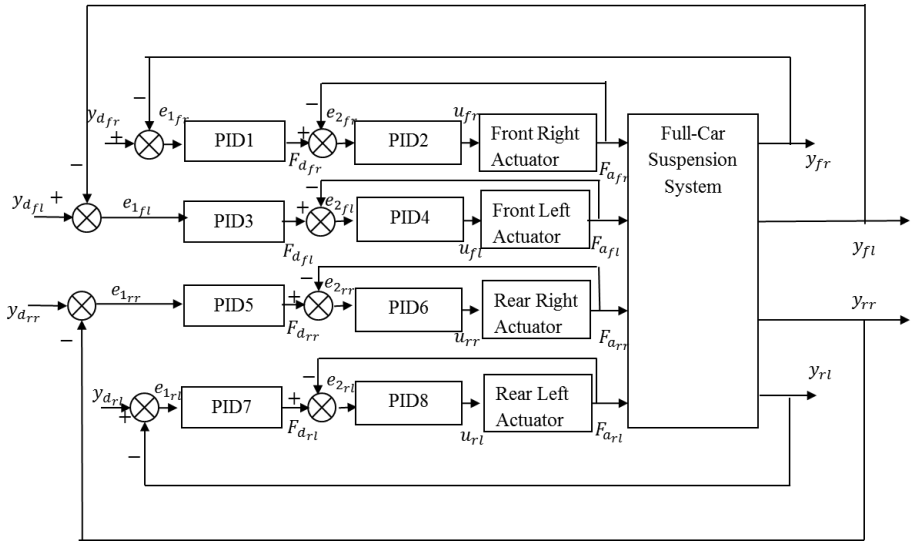

Figure 3.29: Schematic of the PID control architecture for full-car AVSS

$$F_{d_{ij}} = K_{P_{ij}} e_{1_{ij}} + K_{D_{ij}} \frac{de_{1_{ij}}}{dt} + K_{I_{ij}} \int_0^T e_{1_{ij}} dt \tag{3.25}$$

$$e_{2_{ij}} = F_{d_{ij}} - F_{a_{ij}} \tag{3.26}$$

$$u_{ij} = k_{p_{ij}} e_{2_{ij}} + k_{d_{ij}} \frac{de_{2_{ij}}}{dt} + k_{i_{ij}} \int_0^T e_{2_{ij}} dt \tag{3.27}$$

where y_{ij} is the suspension travel experienced at the i^{th} forward longitudinal position and j^{th} lateral position of vehicle, where i may take either f(front) or r(rear), and j is either r(right) or l(left); $k_{p_{ij}}$ and $K_{P_{ij}}$ are the proportional gains of the controllers regulating the i, j^{th} suspension and they correspond to the inner and outer control loops gains respectively; similary $k_{i_{ij}}$ and $K_{I_{ij}}$ are the corresponding integral gains of the controllers; $k_{d_{ij}}$ and $K_{D_{ij}}$ are the derivative gains of the respective control loops; and T is the simulation time. The dynamics of each suspension is controlled by six controller gains and as there are four suspensions, the total number of controller gains stands at 24.

Manual tuning of the PID controllers is performed to select controller gains and to provide insight into the effects that each gain has on the system performance. With such knowledge, the bounds of the optimal routines may be chosen intuitively with the aim of speeding up the process of the selecting gains through optimal policies.

3.2.3 Performance Criteria and Design Specifications

The design specifications chosen for the full-car system are as follows [Dahunsi et al. (2011)]:

1. The suspension travels y_{ij} is constrained to a maximum of $\pm 0.1m$.
2. The control input voltage is limited to $\pm$10volts due to the limitations of the power supply.
3. The total actuation force must be less than the vehicle weight to ensure that the vehicle does not leave the ground. $F_{a_{ij}} \leq M_s g$
4. Body-heave acceleration: $\ddot{z} \leq 4.5 m/s^2$ and the corresponding (RMS) acceleration should be as low as possible, typically in the range of $0-1 m/s^2$ for the ride comfort to lie in the "less discomfort" region of the International Organization for Standardization 2631 (2003).
5. The controller gains are chosen on the basis of minimising the performance index presented in Eqs. (3.28) to (3.33). This performance index addresses vehicle handling, road holding, ride comfort, power consumption and suspension travel. [Ekoru et al. (2011)].

$$J = J_1 + J_2 + J_3 + J_4 + J_5 \tag{3.28}$$

$$J_1 = \frac{1}{T}\int_0^T \left[\left(\frac{\ddot{z}}{\ddot{z}_{max}} \right)^2 + \left(\frac{\ddot{\theta}}{\ddot{\theta}_{max}} \right)^2 + \left(\frac{\ddot{\alpha}}{\ddot{\alpha}_{max}} \right)^2 \right] dt \tag{3.29}$$

$$J_2 = \frac{1}{T}\int_0^T \left[\frac{(F_{ktij} + F_{btij})}{(F_{ktij} + F_{btij})_{max}} \right]^2 dt \tag{3.30}$$

$$J_3 = \frac{1}{T}\int_0^T \left[\frac{y_{ij}}{y_{ij_{max}}} \right]^2 dt \tag{3.31}$$

$$J_4 = \frac{1}{T}\int_0^T \left[\frac{F_{a_{ij}}}{F_{a_{ij_{max}}}} \right]^2 dt \tag{3.32}$$

$$J_5 = \frac{1}{T}\int_0^T \left[\frac{u_{ij}}{u_{ij_{max}}} \right]^2 dt \tag{3.33}$$

where: the performance index J is the cumulative sum of J_1, J_2, J_3, and J_4. J_1 addresses both vehicle ride comfort and vehicle handling which are characterised by

body-heave acceleration and, rotational accelerations respectively. J_2 aims to minimise the road holding properties which are captured through the wheel dynamic load, J_3, J_4 and J_5 pertain to the suspension travel, actuation force, and control input voltage at each wheel respectively. The maximum permitted heave acceleration, pitch acceleration, roll acceleration, tyre dynamic load, suspension rattle, actuation force and control input voltage are denoted by $\ddot{z}_{max}$, $\ddot{\theta}_{max}$, $\ddot{\alpha}_{max}$, $(F_{ktij} + F_{btij})_{max}$, $y_{ij_{max}}$, $F_{a_{ij_{max}}}$ and $u_{ij_{max}}$ respectively. The controller gains are determined manually or through optimization techniques. Manual tuning is largely based on intuitive reasoning and the optimization algorithms will include DE, and a Modified PSO and CRS schemes.

3.2.4 Global Optimization Tuning Methods Applied for Gain Selection

Optimal PID controller tuning for the case of the quarter-car model was the most successful through the use of DE. Therefore, DE is a suitable candidate for computing gains for the case of full-car AVSS, which possesses a more complex performance index with a greater number of controller variables, namely the twenty four PID controller gains. On the other hand, the PSO routine produced favourable results that were almost as good as the DE. Hence, it deserves the opportunity to be tested in the intricate full-car AVSS model as well. Moreover, the PSO is open to modification and may be augmented with certain rules or conditions such that it attains better convergence. CRS is another algorithm which may be altered to achieve better performance. Although it behaved the worst for the case of the quarter-car AVSS, it still managed to meet hard design specifications and generated a decent solution. However, it is anticipated that the proposed CRS modifications will produce some improvement and it is a novel approach whose performance will be interesting from a computational point of view. Furthermore, since the full-car model is more complex and requires more variables to calculate, it serves a better platform to analyse the CRS modifications as opposed to the quarter-car model.

In accordance with the preceding argument, four optimal policies will be used to select the controller gains for the full-car AVSS. These include DE, PSO, modified PSO (MPSO), CRS and modified CRS (MCRS). In this section the resulting system performance of the AVSS will be studied as well and the performance of the optimal routines in terms relative to one another.

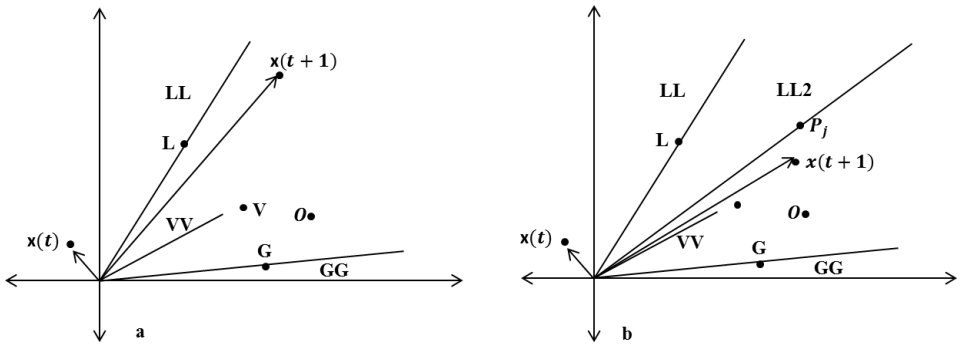

Figure 3.30: Schematic illustrating the effect of the proposed modified PSO

The DE, PSO and CRS routines are exactly the same as the ones described in the quarter-car case discussed in section 3.1.5. The only variations is that the number of problem variables to be calculated are now twenty four, and secondly the objective function or performance index is now in accordance with the full-car model and hence has the form presented in Eqs. (3.28) to (3.33). The rest of this subsection is devoted to explaining the MCRS and MPSO algorithms.

3.2.4.1 Modified Particle Swarm Optimization (MPSO)

To explain the modification and its resulting impact in comparison to the PSO, the analogy of a swarm of particles in 2D search space with two variables is drawn and presented in Figure 3.30. Further study of both the PSO governing equations presented in Eqs. (3.13) to (3.14), and the analogous PSO two-dimensional vector plot, several inferences can be made regarding convergence on the basis of the search in the neighbourhood of each particle (i.e. $\mathbf{P}_{best} - \mathbf{x}(t)$).

In Figure 3.30, **O** denotes the position of the optimal solution, $\mathbf{x}_i(t)$ signifies the position of the i^{th} particle in the search space **L** denotes the personal best position that the i^{th} particle had previously passed through, **G** is the global best position attained thus far, $\mathbf{x}_i(t+1)$ is the next position of the particle which is computed using the PSO equations as presented in Eq. (3.13) to (3.14).

According to the PSO equations and vector plots, each particle is programmed to search for the optimal solution in the vicinity of its personal best solution, in the region around the particle in the solution space which has the best solution, whilst subjected to the momentum of its velocity from the previous iteration. In the vector

plot, the vector of local search, global search and velocity are represented as **L**, **G** and **V**; and the resultant position vector is denoted as $\mathbf{x}_i(t+1)$. Moreover, the particles sizes of these vectors are dictated by the inertial weightings (w_1, w_2) and random numbers used in Eq. (3.14). Subsequently, the local and global search vectors **L**, **G** and **V** will randomly fall within the ranges **LL**, **GG** and **VV** respectively.

In relation to convergence properties, it is evident from the vector plots in Figure 3.30a that the resultant vector and hence the resulting particle position may be considerably swayed by the local search vector **L** based on the ratio $\frac{rand1}{rand2}$. Moreover, if the personal best position of the particle happens to be poor, the resulting position of the particle may fall even further away from the optimal solution **O**. Such a scenario is highly possible as early iterations have shown poor convergence [Alfi and Fateh (2011)].

In accordance with this reasoning, it would be appropriate to alter Eq. (3.14) by replacing the personal best position of the particle of interest with the personal best position of any particle in the solution space which has a superior personal best result than that of the particle of interest(which is denoted as $\mathbf{P}_j$). This is achieved by arranging the personal best matrix $\mathbf{P}_{best}$ according to fitness value. This new matrix is dentoed as **P**, with $\mathbf{P}_1$ being the weakest one. $\mathbf{P}_j \epsilon (\mathbf{P}_a, ..., \mathbf{P}_z)$ taken at random, where $f(\mathbf{P}_a), ..., f(\mathbf{P}_z) \geq f(\mathbf{P}_{best_i})$. In light of these alterations, Eq. (3.14) now becomes:

$$\begin{aligned} \mathbf{V}_i(t+1) &= w_1\mathbf{V_i}(t) + w_2 rand1(1,N) \times (\mathbf{P}_j - \mathbf{x}_i(t)) + \\ & \quad w_3 rand2(1,N) \times (\mathbf{G}_{best} - \mathbf{x}_i(t)) \end{aligned} \tag{3.34}$$

where $\mathbf{V}_i$, and $\mathbf{x}_i$ are the velocity and position of the i^{th} particle in the solution space; $\mathbf{P}_j$ is the personal best position of any particles in the solution space whose personal best position is fitter than the i^{th} particle. Such a modification would tend to bend the resultant vector closer towards the optimal solution **O** and hence improve convergence. This alteration is also depicted in the vector plot in Figure 3.30b. The algorithm is summarized in the following steps:

Step 1 Produce a random swarm of particles $S = \{\mathbf{x}_0, \mathbf{x}_1, .., \mathbf{x}_n\}$, as before.

Step 2 Define the global best particle as the fittest particle in the swarm and let the personal best particles be the same as the initial population

Step 3 If stopping criterion is met, advance to step 7, or else proceed to step 3.

Step 4 Calculate the new set of positions $\mathbf{x}(t+1)$ for the various particles using Eqs. 3.13 and 3.34.

Step 5 For each particle perform the following actions:

- If the fitness of the newly computed particle is better than its personal best location, then replace the personal best particle's location with those of the newly computed particle.

Step 6 Register the best particle in the personal best matrix as the global best particle.

Step 7 Use the global best particle as the optimal solution.

3.2.4.2 Modified Controlled Random Search (MCRS)

In the fundamental CRS equations presented in Eqs. (3.16) to (3.18) the centre of gravity $\mathbf{G}$ has a major impact on the candidate solution $\mathbf{y}$. As $\mathbf{G}$ is primarily dependent on the n_r selected individuals $(\mathbf{v_1}, \mathbf{v_2}, ..\mathbf{v_n})$, its value may become fixed and hence the routine will lack flexibility if the individuals in the solution space become relatively cluttered as shown in Figure 3.11. Consequently, this will lead to early convergence and limit the success rate (number of times the weakest individual $\mathbf{x}_w$ is replaced) of the algorithm.

To overcome this shortfall, the 3 random individuals will be selected from the solution space S, as opposed to the $n+1$ individuals that were previously chosen. Secondly these individuals will be in ascending order according to their fitness values with the $\mathbf{x}_1$ being the fittest individual followed by $\mathbf{x}_2$ and $\mathbf{x}_3$ respectively. $\mathbf{G}$ will correspond to the mean of $\mathbf{x}_1$ and $\mathbf{x}_2$, and the candidate solution $\mathbf{y}$ will be computed as follows:

$$\mathbf{y} = 2\mathbf{G} - \mathbf{x}_3 \tag{3.35}$$

By doing so, the flexibility of the $\mathbf{G}$ and hence the flexibility in the candidate solution will improve. Furthermore, the weakest of the randomly selected individual $\mathbf{x}_3$ shows greater potential in improving as argued in the vector plot shown in Figure 3.31, where the candidate solution $\mathbf{y}$ is driven closer to the fitter solutions of $\mathbf{x}_1$ and $\mathbf{x}_2$ and may randomly fall closer to the optimal solution $\mathbf{O}$. Hence, the success rate of the algorithm will improve. This MCRS algorithm may be summarized in the following steps:

Step 1 Generate a randomly distributed population set S that uniformly spans the search space.

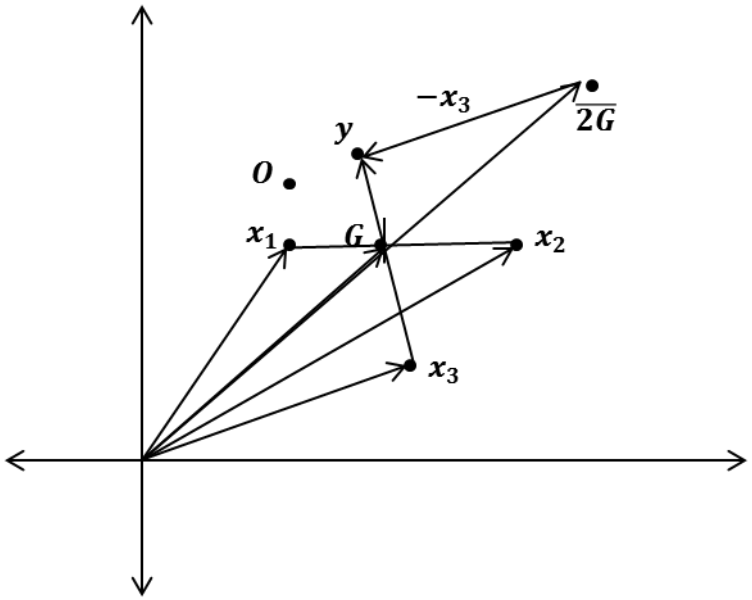

Figure 3.31: Illustration of the contributing effect of the modified CRS routine

Step 2 Check if the stopping criterion is met and if not continue to the next step, otherwise proceed to step 7.

Step 3 Randomly select 3 distinct individuals from the population set S.

Step 4 Order these individuals in ascending order according to their fitness values with $\mathbf{x}_1$ being the fittest individual followed by $\mathbf{x}_2$ and $\mathbf{x}_3$ respectively.

Step 5 Set the centre of gravity $\mathbf{G}$ to be the mean of the two fittest individuals $\mathbf{x}_1$ and $\mathbf{x}_2$.

Step 6 Determine the trial individual using Eq. (3.35).

Step 7 Replace the weakest individual in the population $\mathbf{x}_w$ with the candidate individual $\mathbf{y}$; if the candidate solution $\mathbf{y}$ incurs a lower cost than $\mathbf{x}_w$, then return to step 2.

Step 8 Select the individual with the best fitness value as the optimal solution.

The parameter settings for each of the optimization routines are listed in Table 3.7.

Table 3.7: Optimization parameter settings for full-car PID-based AVSS optimal polices

Routine	**DE**	**PSO**	**MPSO**	**CRS**	**MCRS**
Population Size	100	100	100	24×10	24×10
Stopping Criteria (Iterations)	150	150	150	6000	6000
Optimization Parameters	F=2	K=100 w_2=2 w_3=2	w_1=0.5 w_2=2 w_3=2	n=24	n=3

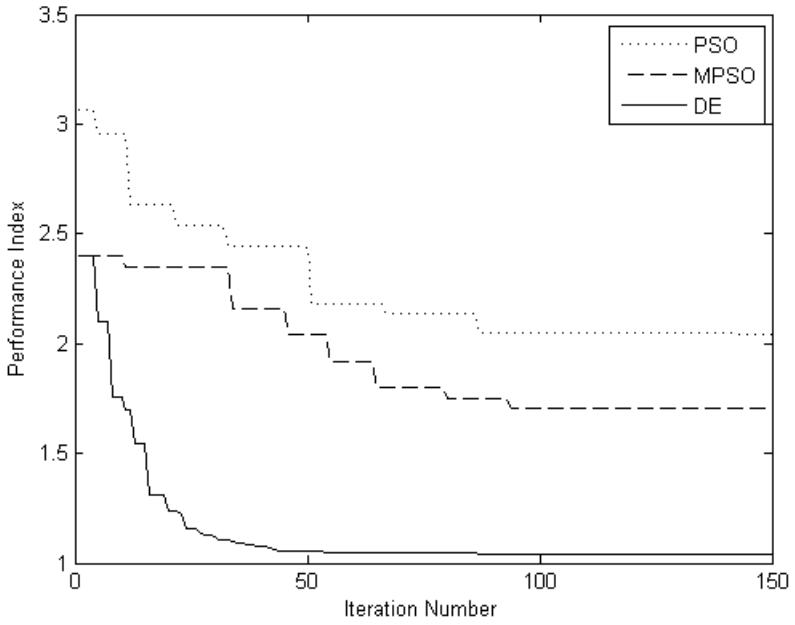

Figure 3.32: Evolution of performance index using the suggested evolutionary algorithms

3.2.4.3 Analysis of the Convergence of the Various Routines

The convergence histories of the fitness value using the proposed optimal routines are plotted in Figures 3.32 and 3.33. The modified CRS and PSO algorithms outperformed their predecessors with improved fitness value and quicker convergence. Hence, it may be concluded that the suggested modifications made improve the respective policies with the CRS becoming more flexible and the PSO showing better convergence of weaker particles. Performance of the CRS routines may also be evaluated in terms of success rate. It measures the ratio of how often the weakest

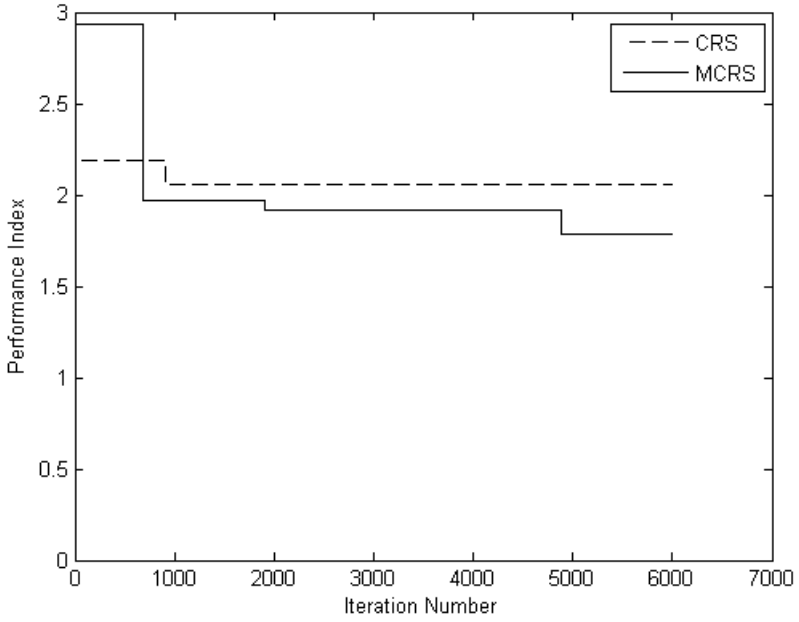

Figure 3.33: Comparative plot depicting the variation in performance index between the CRS and MCRS routines

individual in the population $\mathbf{x}_w$ is replaced and is hence given as:

$$\text{success rate} = \frac{\text{number of times } \mathbf{x}_w \text{ replaced}}{\text{number of iterations}} \tag{3.36}$$

The resulting success rate of the CRS was 0.075 and that of the MCRS was 0.15, and this infers that MCRS produces more improved solutions than its counterpart.

It is evident from Figures 3.32 and 3.33 that the suggested modifications in the CRS and PSO routines yielded superior results. This infers that the hypotheses debated in relation to these modifications are indeed correct. Hence, it may be established that by altering the local search characteristics of each particle in the PSO method improves the effectiveness and efficiency of the algorithm. Furthermore, it may also be concluded that increasing the flexibility of the CRS using the proposed method outlined in section 3.1.5.4 adds value to the algorithm with a better success rate, and prevents early convergence and produces a better resulting fitness value. Moreover, the DE produces the best results followed by the MPSO and MCRS respectively. The controller gains computed by these superior algorithms in addition to the manually-tuned controller are listed in Table 3.8. A number of gains obtained through the various routines have negative values. From a computational standpoint, this is acceptable as it is solely a consequence of the optimization algorithms. However, when applying in an actual system, this will require a compatible microprocessor

that can deal with it or with the aid of specific digital circuits. Moreover the outer loop proportional gains K_P proved to smaller than the high loop gains attained for the quarter-car case. The inner loop derivative controller gains k_d is of a small order of magnitude and may be ignored for practical purposes.

Table 3.8: Gains computed through the various optimization algorithms for full-car PID controller

	Front Right Suspension System					
	Outer PID Loop Gains			Inner PID Loop Gains		
Technique	K_P	K_I	K_D	k_p	k_i	k_d
Manual	1100	360	140	0.002	0.001	0
DE	1692	267	166	0.0038	0.0010	3×10^{-9}
MCRS	17251	-145	-92	0.0029	0.0700	5×10^{-9}
MPSO	7270	320	-769	0.0061	-0.00063	$3. \times 10^{-9}$
	Front Left Suspension System					
	Outer PID Loop Gains			Inner PID Loop Gains		
Technique	K_P	K_I	K_D	k_p	k_i	k_d
Manual	1050	170	220	0.002	0.001	0
DE	1692	267	166	0.0038	0.0010	3×10^{-9}
MCRS	16003	184	158	0.0028	0.0665	4×10^{-9}
MPSO	5025	-1250	-1350	0.0080	0.0024	3×10^{-9}
	Rear Right Suspension System					
	Outer PID Loop Gains			Inner PID Loop Gains		
Technique	K_P	K_I	K_D	k_p	k_i	k_d
Manual	1200	340	150	0.002	0.001	0
DE	1692	267	166	0.0038	0.0010	3×10^{-9}
MCRS	6723	-87	19	0.0020	0.0182	3×10^{-9}
MPSO	8566	-1274	-5	0.0033	0.0046	4×10^{-9}
	Rear left Suspension System					
	Outer PID Loop Gains			Inner PID Loop Gains		
Technique	K_P	K_I	K_D	k_p	k_i	k_d
Manual	1000	200	200	0.002	0.001	0
DE	1692	267	166	0.0038	0.0010	3×10^{-9}
MCRS	4579	302	178	0.0030	0.0233	2×10^{-9}
MPSO	-788	-372	950	0.0055	-0.0002	6×10^{-9}

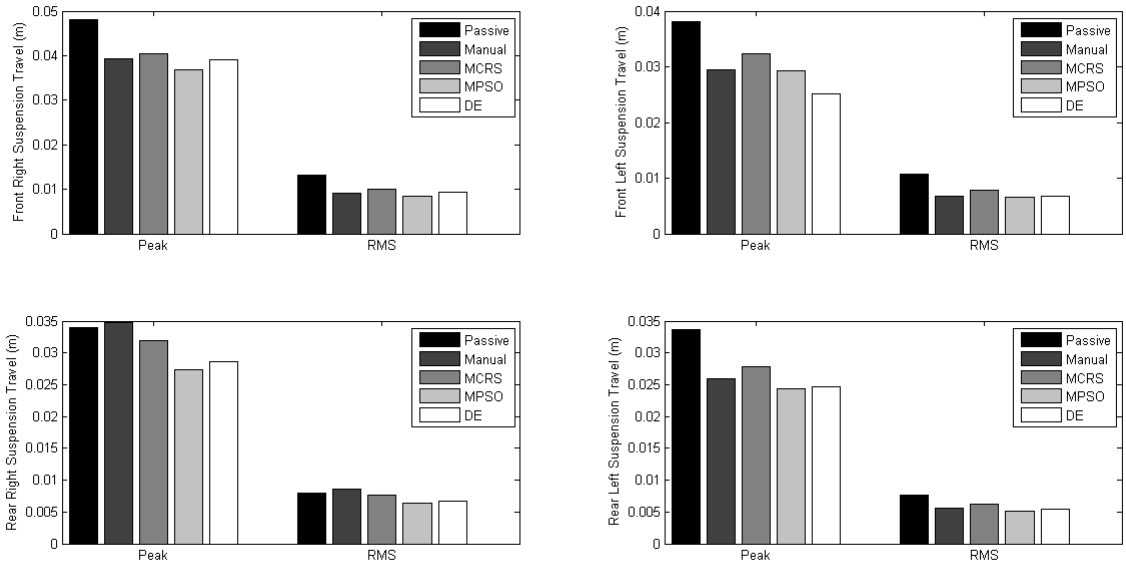

Figure 3.34: Bar graphs depicting the variation in suspension travel for each control law

3.2.5 Simulation Results and Discussion

The evolution of the performance index through the use of the proposed tuning routines presented in Figures 3.32 and 3.33 clearly illustrates that the DE routine gave the best performance index followed by the MPSO and MCRS respectively. However, these plots cannot provide information on how well the suspension trade-offs have been resolved. Hence plots for each suspension performance criterion will be plotted for the non-optimized, DE, MCRS and MPSO cases respectively.

Simulations were performed in the Matlab/Simulink environment and the simulation time was set to 5 seconds. Suspension travel performance; road holding which is captured through the tyre dynamic load; and power consumption which is characterised by the control input voltage are plotted in Figures 3.38 to 3.40 respectively. These plots focus on the rear left suspension corner only as the worst behaviour in these facets were observed at this location. Vehicle handling, which is primarily a function of roll and pitch accelerations is presented in Figures 3.41 and 3.42 respectively. Ride comfort, which is centred on body-heave acceleration is shown in Figure 3.43 and the cumulative hydraulic force applied to the vehicle body is plotted in Figure 3.44. The peak and root-mean-square (RMS) values pertaining to these criteria are summarised and compared in Table 3.9 and 3.10 as well as the bar graphs in Figures 3.34 to 3.37.

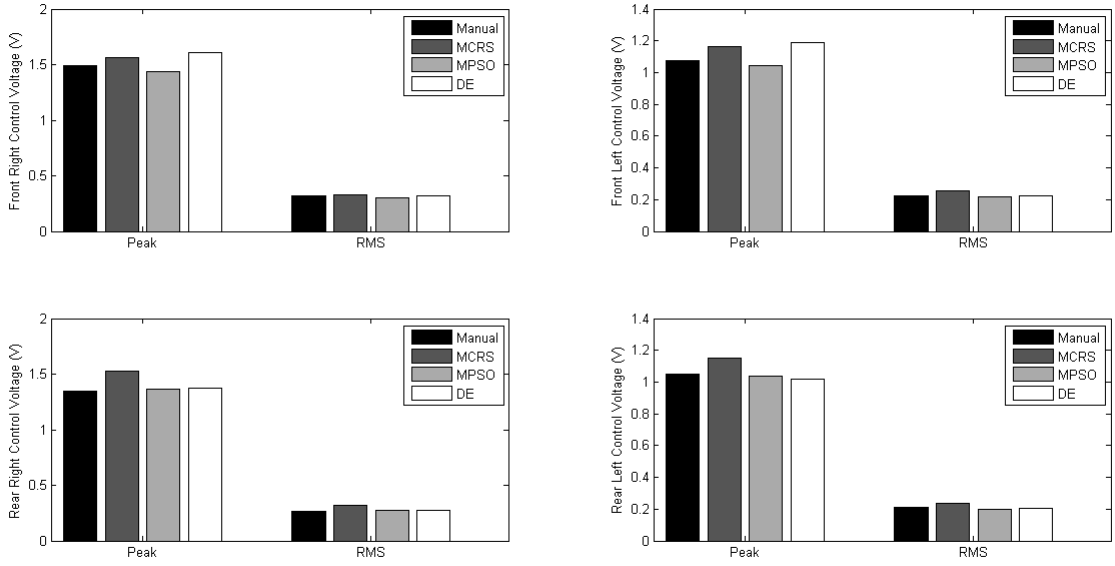

Figure 3.35: Bar graphs illustrating the difference in control input voltage for the proposed controllers

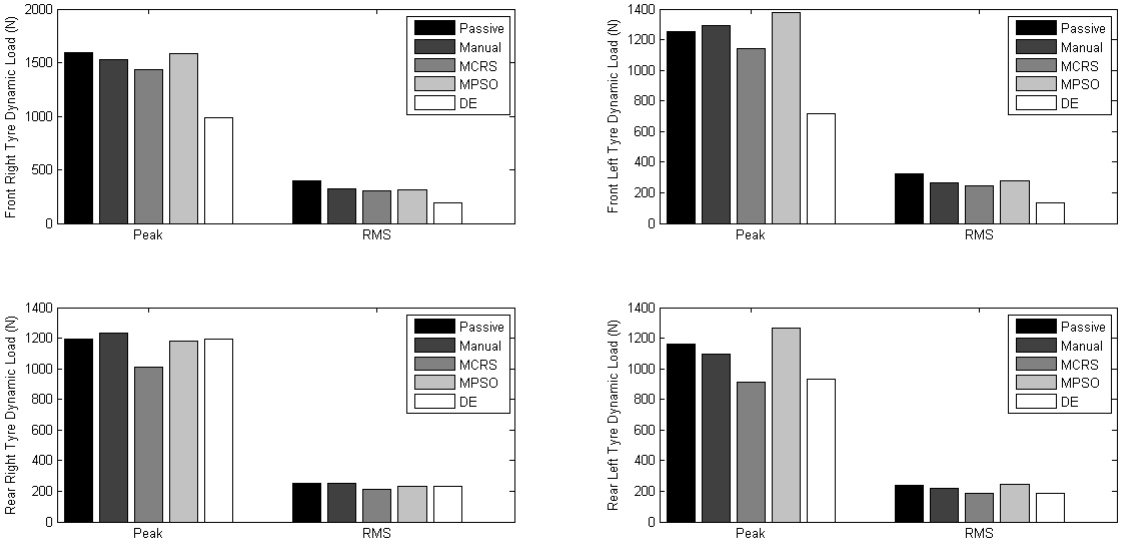

Figure 3.36: Bar graphs summarizing the road holding aspect for each control case

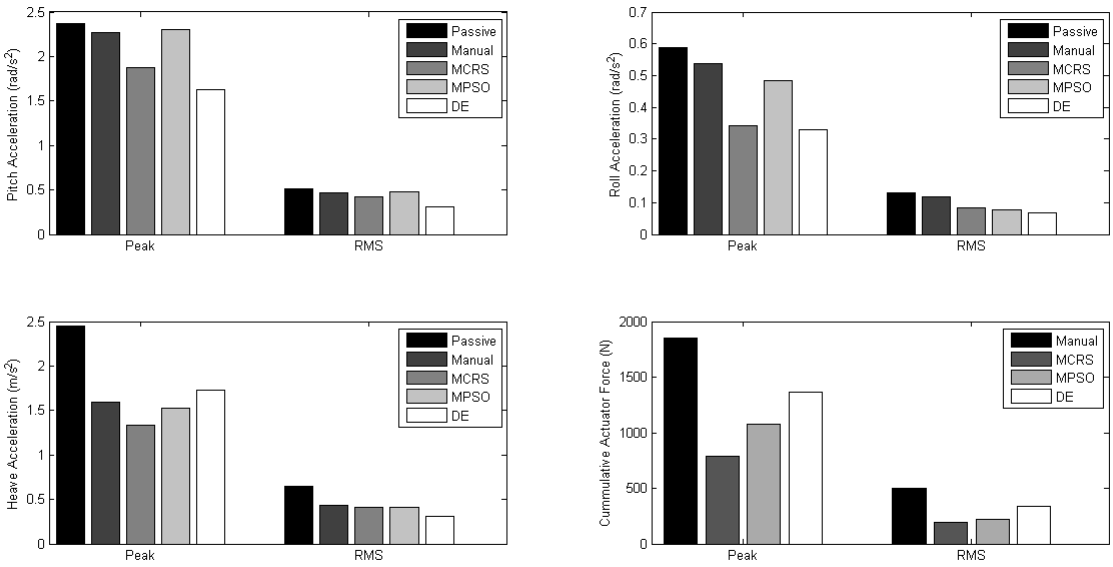

Figure 3.37: Quantitative information pertaining to vehicle handling, ride comfort and actuator force supplied

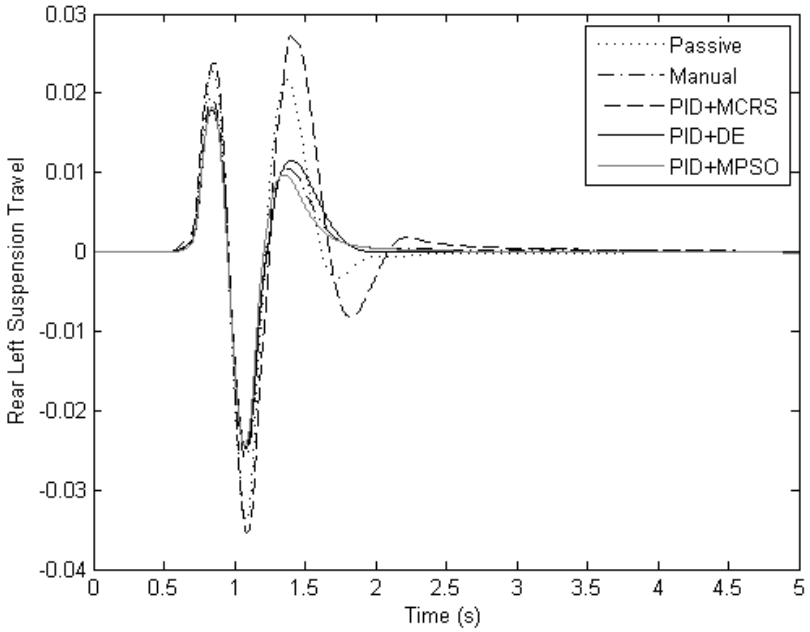

Figure 3.38: Illustration of the variation in suspension travel response using the proposed tuning methods

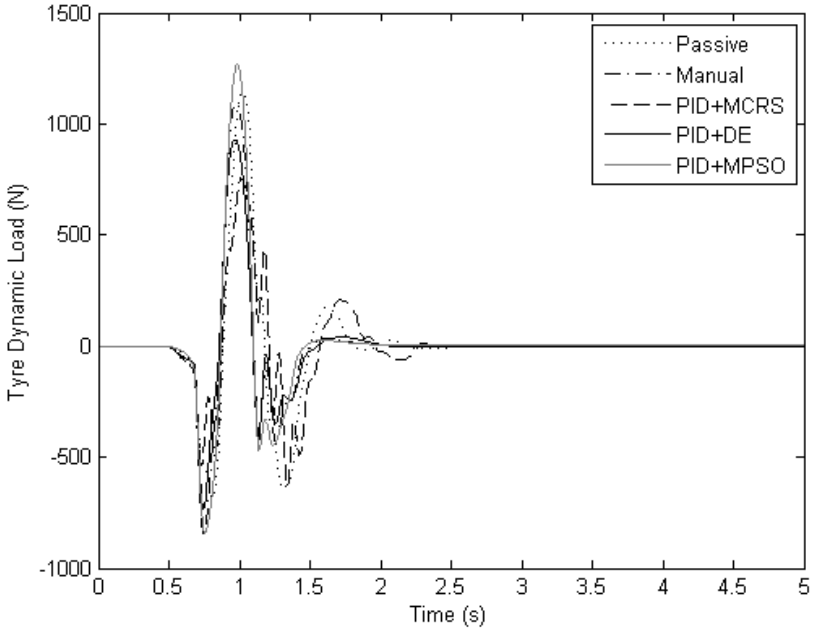

Figure 3.39: Variation in the tyre dynamic load experienced at the rear left suspension system for the various tuning policies

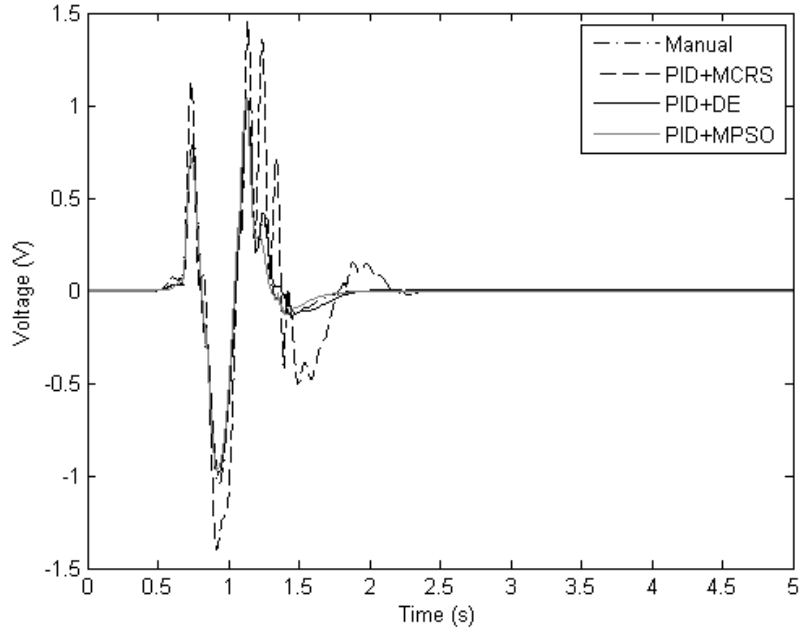

Figure 3.40: Difference in control input voltage produced using the suggested tuning approaches

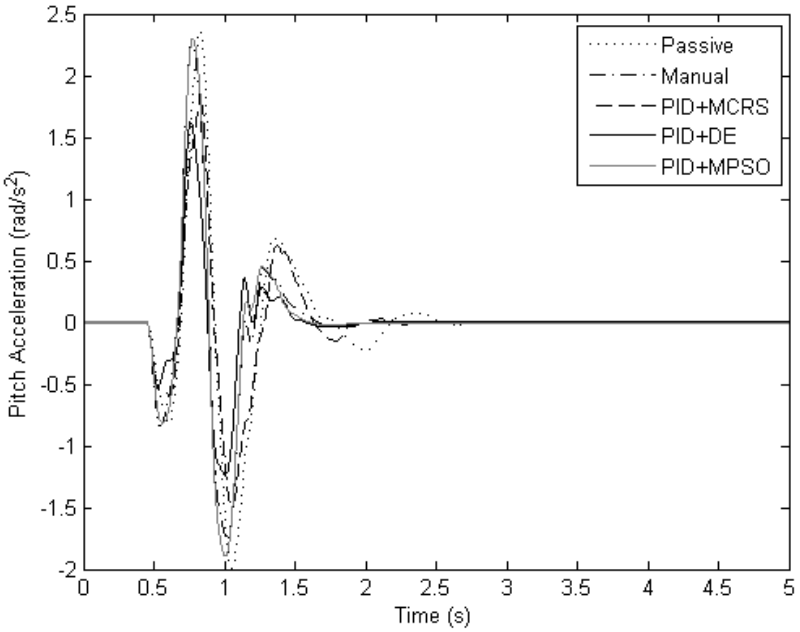

Figure 3.41: Vehicle body pitch acceleration for each of the tuning routines

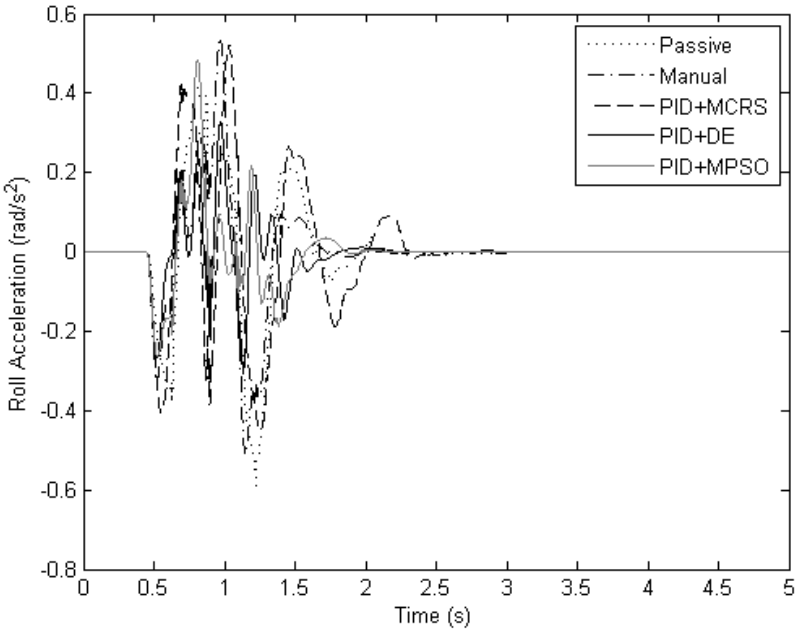

Figure 3.42: Vehicle body roll acceleration for the various tuning policies

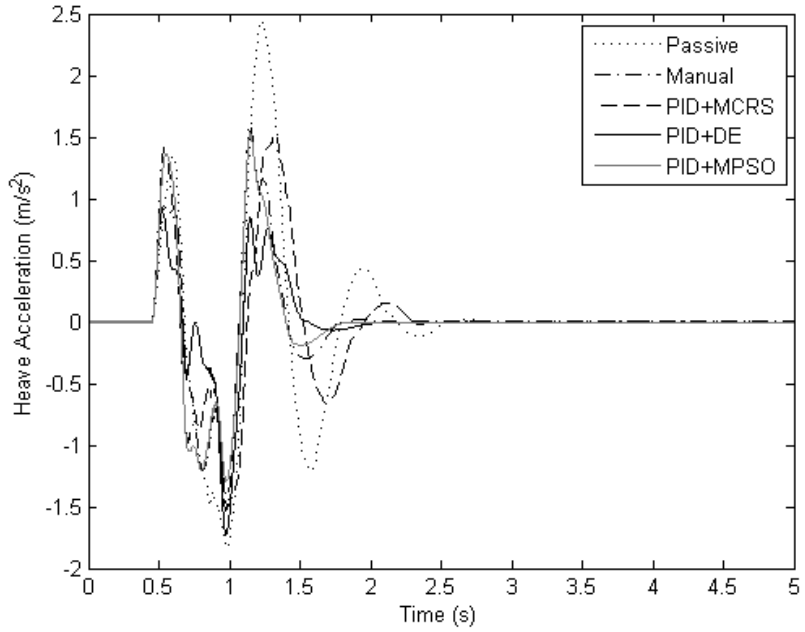

Figure 3.43: Ride comfort experienced for each of the proposed tuning methods

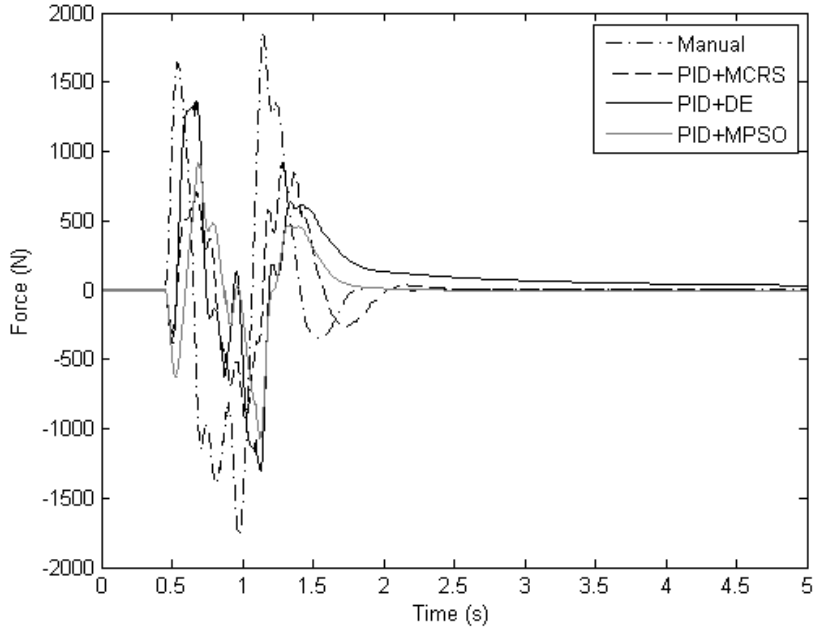

Figure 3.44: Effective hydraulic force applied to the vehicle chassis for the various tuning algorithms

Table 3.9: Summary of selected suspension performance incorporating the various optimization routines

Technique	**Front Right Suspension Travel**(m)		**Front Left Suspension Travel**(m)	
	RMS	**Peak**	**RMS**	**Peak**
Passive	0.038	0.0107	0.048	0.0131
Manual	0.039	0.0091	0.029	0.0066
MCRS	0.040	0.0099	0.032	0.0077
MPSO	0.036	0.0085	0.029	0.0065
DE	0.039	0.0094	0.025	0.0067
Technique	**Rear Right Suspension Travel**(m)		**Rear Left Suspension Travel**(m)	
	RMS	**Peak**	**RMS**	**Peak**
Passive	0.033	0.0079	0.033	0.0076
Manual	0.034	0.0086	0.025	0.0055
MCRS	0.032	0.0076	0.027	0.0062
MPSO	0.027	0.0064	0.024	0.0051
DE	0.028	0.0067	0.024	0.0054
Technique	**Front Right Tyre Dynamic Load**(N)		**Front Left Tyre Dynamic Load**(N)	
	RMS	**Peak**	**RMS**	**Peak**
Passive	1594	395	1254	321
Manual	1531	321	1295	263
MCRS	1432	299	1139	245
MPSO	1587	310	1375	275
DE	984	189	713	132
Technique	**Rear Right Tyre Dynamic Load**(N)		**Rear Left Tyre Dynamic Load**(N)	
Passive	1194	248	81158	240
Manual	1234	248	1096	218
MCRS	1010	214	913	184
MPSO	1183	233	1267	245
DE	1196	229	930	185

The suspension travel response obtained when implementing each of the optimal routines displayed reduced peak and RMS values in comparison with PVSS and manually-tuned PID cases respectively. Moreover, they exhibited better transient

Table 3.10: Summary of selected suspension performance incorporating the various optimization routines

Technique	**Front Right Control Input Voltage**(V)		**Front Left Control Input Voltage**(V)	
	RMS	**Peak**	**RMS**	**Peak**
Manual	1.49	0.316	1.07	0.225
MCRS	1.56	0.333	1.16	0.255
MPSO	1.43	0.300	1.04	0.220
DE	1.61	0.318	1.18	0.225
Technique	**Rear Right Control Input Voltage**(V)		**Rear Left Control Input Voltage**(V)	
	RMS	**Peak**	**RMS**	**Peak**
Manual	1.34	0.265	1.04	0.212
MCRS	1.52	0.315	1.15	0.234
MPSO	1.36	0.277	1.03	0.201
DE	1.37	0.278	1.01	0.204
Technique	**Pitch Acceleration** (rad/s^2)		**Roll Acceleration** (rad/s^2)	
	RMS	**Peak**	**RMS**	**Peak**
Passive	2.36	0.516	0.588	0.130
Manual	2.26	0.463	0.538	0.116
MCRS	1.88	0.421	0.340	0.083
MPSO	2.30	0.479	0.484	0.076
DE	1.62	0.314	0.328	0.066
Technique	**Heave Acceleration** (m/s^2)		**Effective Hydraulic Force**(N)	
	RMS	**Peak**	**RMS**	**Peak**
Passive	2.44	0.648	N/A	N/A
Manual	1.59	0.429	849	498
MCRS	1.33	0.413	786	189
MPSO	1.52	0.410	1072	222
DE	1.72	0.306	1363	342
Performance Index J				
Passive	Manual	MCRS	MPSO	DE
5	3.2	1.8	1.75	1.1

behaviour by damping out with no further peaks immediately after the road disturbance was removed. These results were anticipated as the performance index did

indeed address suspension travel with a fair and considerable weighting factor. However, there were shortfalls as well using these policies as their respective damping rates were considerably low and appear to lag the passive case once the disturbance was removed. Consequently, they each had slightly higher settling time than that of the PVSS case.

The road holding capabilities acquired for the DE and MCRS cases were similar and superior to those of the PVSS and manually-tuned cases with lower peaks, better RMS values, quicker settling times, and improved transient response that had fewer peaks and reduced oscillations where the system dampened out immediately once the disturbance was taken away. This favourable response is attributed to its inclusion in the performance index where road holding was given a substantial weighting. This greatly affected the performance index J and this was exploited in such a way as to ensure that the subsequent lowering of the performance index J would produce an improvement in road holding. On the other hand, the MPSO case did manage to improve the RMS value, transient behaviour and settling time; but still produced the largest peak values. Such an occurrence is expected to be suppressed as the performance index aims to minimize the RMS value of road holding. However even with the inter-relationship between RMS and peak values, it is not guaranteed that reducing the RMS value will always reduce the peak values and hence such a shortfall is possible. It is suggested that like settling time of suspension travel, peak values in each performance criteria be added to the performance index such that its value improves.

Regarding vehicle handling and ride comfort, the optimal policies produced lower peak and RMS values with quicker settling times than those of the manually-tuned and PVSS cases. However, each policy contained a greater degree of chattering which would tend to deteriorate system components. In terms of ride comfort and handling performance, the MPSO case was the worst from the optimal methods followed by the MCRS and DE cases respectively. Its weak performance is due to the fact that this routine produced a lower performance index value as compared to the DE case. It is worth noting that although the MCRS had a similar performance index; it did perform adequately in vehicle handling, but lacked quality in suspension travel. In conclusion, both algorithms produced a weaker performance index than DE; but they did exhibit desired responses in certain performance aspects whilst performing weaker in other aspects. This implies that these algorithms were not as good as the DE in resolving the trade-offs between the various performance criteria.

Furthermore, DE produced the best performance index which was approximately 40% better than its counterparts.

The comparative plot pertaining to control input voltage and cumulative hydraulic force showed that all the optimal tuning policies produced lower peak and RMS values than the manually-tuned case whilst at the same time they were able to enhance the RMS values and response of ride comfort, road holding and vehicle handling criteria. From a computational standpoint, this is projected as control input voltage and supplied hydraulic forces are substantial factors of the performance index. However, from an engineering point of view, such data is rather contradictory to both typical quarter-car models and linear control techniques as a larger force or voltage is demanded to improve the various performance benchmarks. These results infer that the coupling and nonlinearities of the full-car nonlinear system is a major factor that supplements the outcomes of the system and it is thus imperative that they are thoroughly investigated.

3.2.6 Sensitivity to Parameter Variations and Frequency-Domain Analysis

Simulation results presented in the previous section indicate a marginally low steady-state error with an order of magnitude ranging within 0.001% of the peak values. This signifies that each of the proposed tuning methods produced a resulting control system that is bounded-input-bounded-output (BIBO) stable. It has been reported that PID-based systems such as the ones proposed in this study have a weak sensitivity to parameter variations. Thus, it is imperative that this problem be investigated in order to ensure that the parameter sensitivity lies within a satisfactory region to anticipated parameter variations. In this stability study, parameters such as mass, inertia, tyre damping, tyre stiffness and vehicle speed are altered as this will occur in reality due to the changes in mass and inertia as a result of passenger movements and fuel variations, fluctuations in tyre pressure, and variability in vehicle speed. With regards to the preceding argument; plots showing a -20% and +20% variations in mass, roll inertia, pitch inertia, tyre stiffness, tyre damping and vehicle speeds for the DE case are presented in Figures 3.45 and 3.46 respectively. Figures 3.45 and 3.46 clearly show that the control system remains BIBO stable within an acceptable steady-state error for all anticipated parameter variations. For all cases apart from an increase in vehicle speed, the suspension travel response showed low peaks,

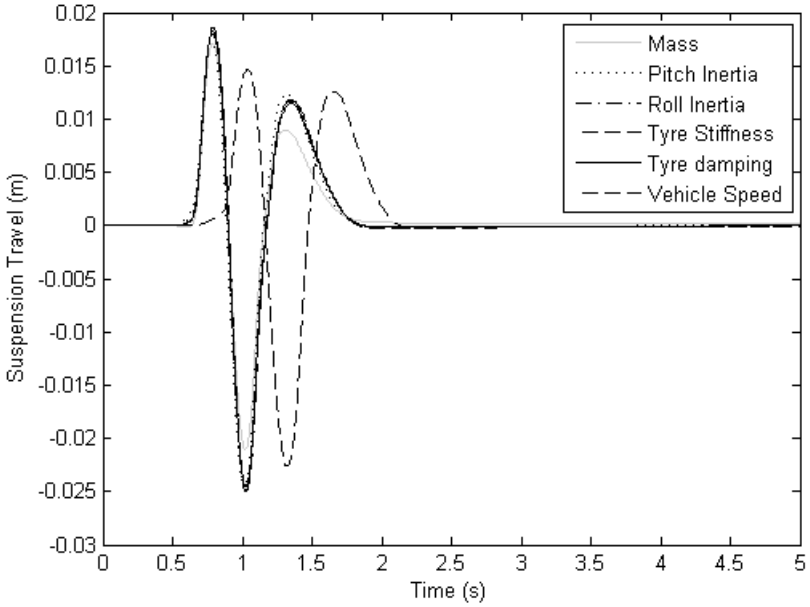

Figure 3.45: Suspension travel response of the DE+PID case for a -20% variation in selected parameters

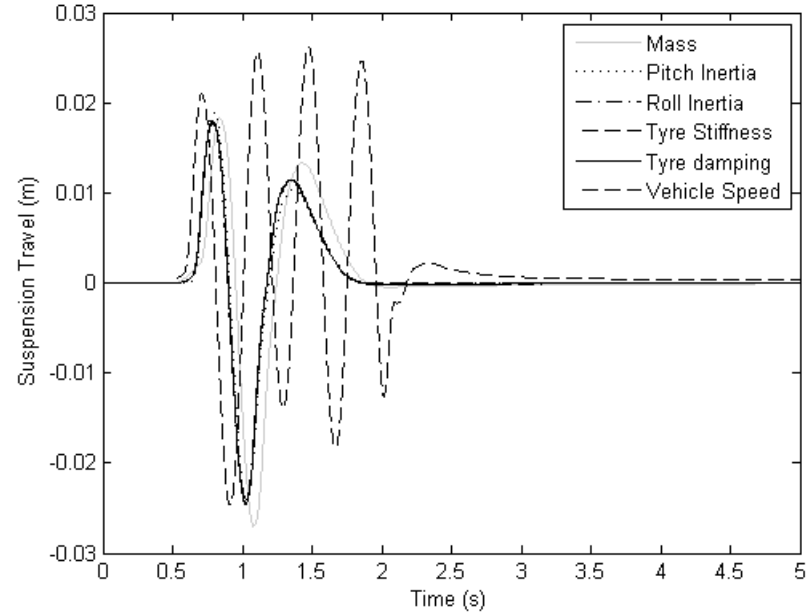

Figure 3.46: Suspension travel response of the DE+PID case for a +20% variation in selected parameters

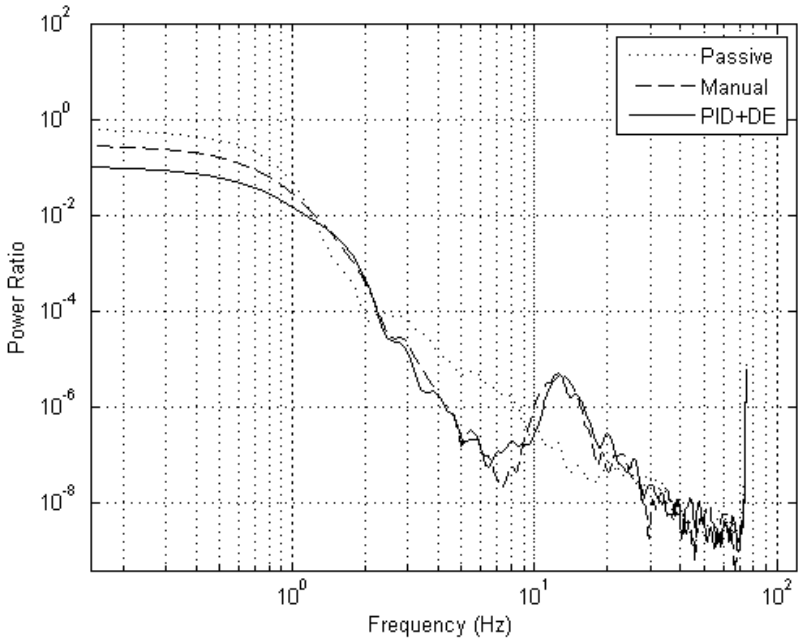

Figure 3.47: Frequency response comparative plot for the body-heave acceleration

good transient behaviour and quick settling times. However, the case of a 20% increase in vehicle speed deteriorates transient behaviour producing multiple peaks before settling. A gain scheduling approach for variations in vehicle speed may be implemented to overcome this issue. On a whole, it may be concluded that the optimal DE-based PID controller has an acceptable sensitivity to parameter variations.

The International Organization for Standardization 2631 (2003) argue that human exposure to frequencies ranging from $0.5Hz$ to $80Hz$ significantly affects human comfort. Thus it is imperative that relevant AVSS performance criteria be analysed in this range. Bode plots pertaining to ride comfort, vehicle handling and road holding for the passive, PID and PID+DE cases are illustrated in Figures 3.47 to 3.50. These plots were generated using the power spectral density (PSD) estimates of the Matlab/Simulink signal processing toolbox. The relevant parameter settings are summarized in Table 3.11.

In terms of ride comfort which is characterised by body-heave acceleration, the passive system effectively behaved as a high-pass filter, whose high frequency signals were successfully attenuated. It possessed the worst attenuation at the onset where it had a magnitude of approximately 1 in the range of 0.01-1Hz. On the contrary, the AVSS methods produced a significant improvement in this range as they were

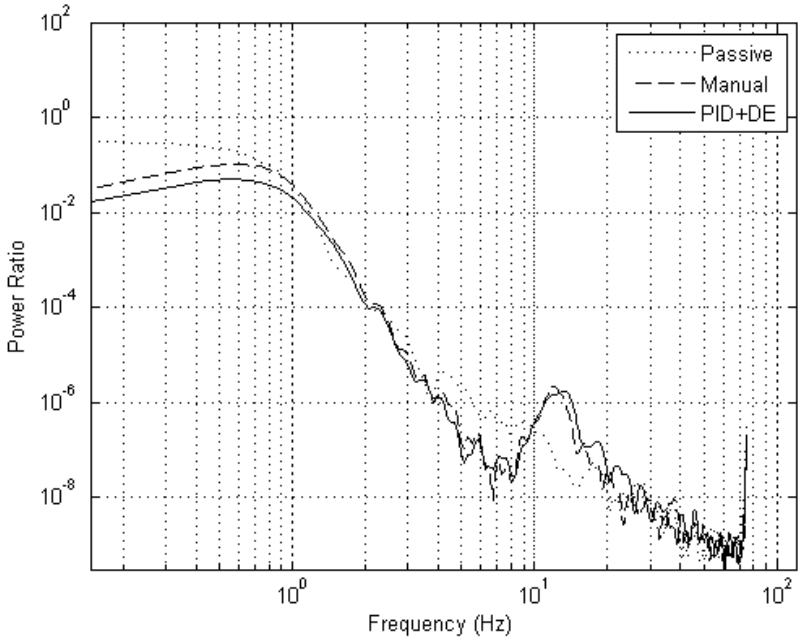

Figure 3.48: Comparative plot of frequency response pertaining to body pitch acceleration

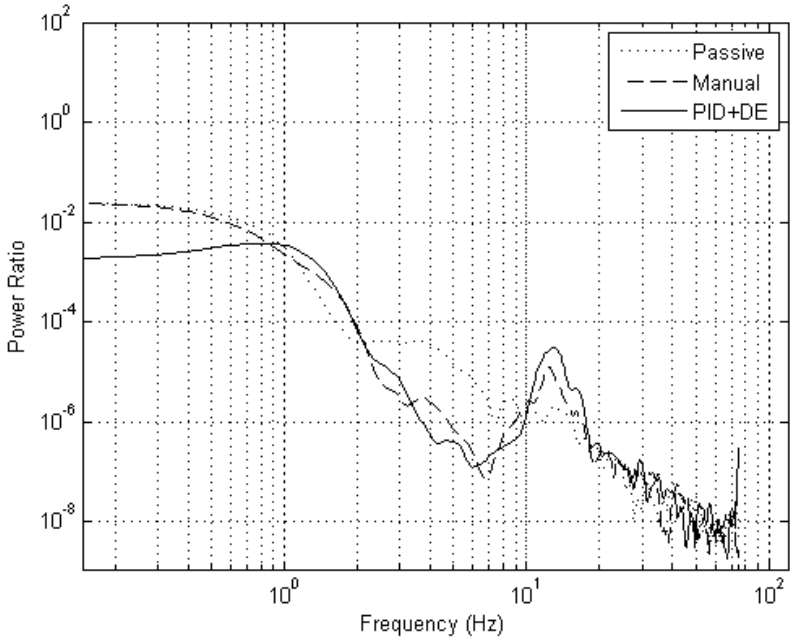

Figure 3.49: Roll acceleration frequency response comparative plot for relevant cases

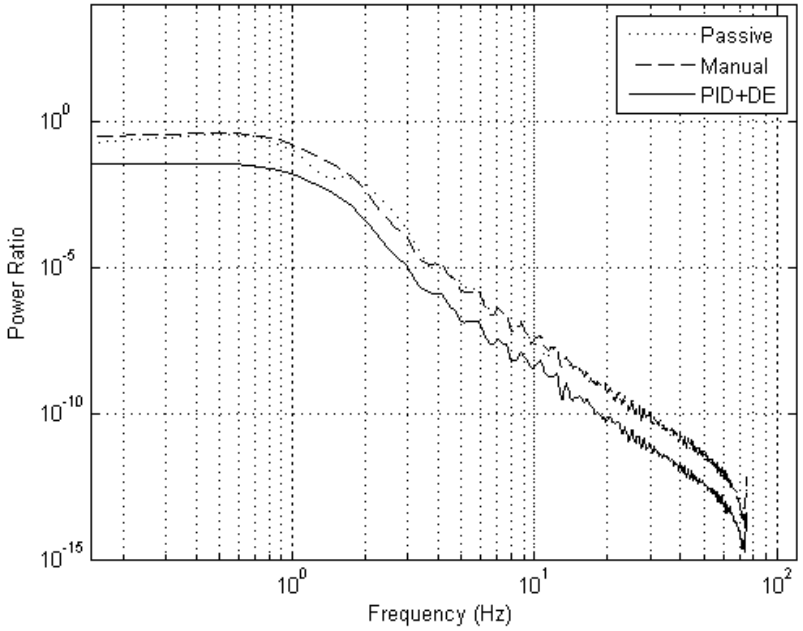

Figure 3.50: Frequency response for road holding

Table 3.11: Configuration settings used to obtain frequency response

Parameter	**Setting**
Computation	Algorithm Welch
Windowing Function	Hanning
Number of points included in fourier transform (NNFT)	1024
Length of Window (NWind)	256
Sampling Frequency	80Hz

able to successfully attenuate signals therein, with the optimal controller performing best. Thereafter, the PVSS case possessed superior attenuation properties up until $2Hz$. Afterwards, the AVSS cases performed similarly and produced better attenuation results up to $10Hz$, where a resonant peak developed.

In relation to pitch acceleration, the PVSS performed the worst at the onset which is by the standard regarded by the European Commission (2002) as the most sensitive frequencies experienced by humans. The AVSS cases showed an improvement in comparison with PVSS in this regard, with the optimal case performing the best. In this range the power ratio did increase with increasing frequency but was still able to perform better than the PVSS case. At the onset of 1Hz the power ratios of each case dropped off sharply inferring successful signal attenuation. The AVSS cases did however experience a resonance peak later at around $12Hz$, but the power

ratios were comparatively low at these high frequencies, which implies successful attenuation.

With regards to roll acceleration, there was only a marginal variation between the PID-controlled and PVSS cases at the sensitive low frequencies. The DE-optimized case performed significantly better than its predecessors in this range but it produced an increasingly higher power ratio with increasing frequency. Thereafter, at around $1Hz$ it began to perform worse than the other cases. From $11Hz$ onwards the power ratio dropped off substantially indicating that the signals were henceforth attenuated considerably. A resonant peak did however develop for the AVSS cases at $10.5Hz$, but the power ratio was low enough which saw the continued attenuation of input signals.

Road holding frequency plots resemble that of a high-pass filter where the sensitive low-frequencies produced the largest peaks and the less sensitive high frequency signals were successfully attenuated. The PID-controlled and PVSS cases produced similar results for the whole range of frequencies where the optimal DE case performed significantly better. The continued superior performance of the optimal PID controller in relation to its counterparts for all suspension criteria in the sensitive low frequency ranges suggests two things. Firstly, it was more successful than both its predecessor in resolving the conflicting trade-offs in ride comfort, road holding and vehicle handling as outlined in Figure 1.1. Secondly, it was successful in managing the sensitive low-frequency signals for all suspension criteria. These results imply that controller tuning through global optimization methods does play a significant role in both resolving AVSS trade-offs and improving parameter variations sensitivity.

3.2.7 Summary

The proposed modified CRS routine performed better than its predecessor with improved flexibility and convergence. Similarly, the MPSO accomplished a superior performance index and hence overcame its shortfall pertaining to early convergence. The DE produced the best performance from both a computational and engineering standpoint as it gave a more enhanced performance index than the other tuning routines and resolved the compromises in all performance aspects to a superior extent. On the other hand, the MCRS and MPSO did not show significant improvements in every performance criteria. Vehicle handling, road holding and ride comfort were

better attenuated in the sensitive low-frequency range as compared to the passive and non-optimal PID schemes.

4 Dynamic Neural Network-Based Feedback Linearization Control of a Nonlinear Quarter-Car Electrohydraulic Vehicle Suspension System

4.1 Introduction

As discussed in the literature review (Section 1.4), the primary shortcoming of PID control is that it is a linear control strategy whose non-adaptive nature limits its robustness when dealing with nonlinear systems. Such a setback makes it unsuitable to deal with a vast range of disturbance inputs, parameter variations, and chattering when controlling nonlinear systems. Moreover, system performance is limited and hence in relation to AVSS, its inherent ability to resolve the conflicting performance criteria is limited as its linear control structure is inadequate for nonlinear AVSS. Such characteristic behaviour had been observed when comparing it to intelligent control schemes. Hence, an adaptive control law such as nonlinear control or intelligent control is proposed by many researchers for AVSS control [Pedro and Dahunsi (2011)].

Feedback linearization (FBL) is a nonlinear control technique whose objective is to develop a linearizing feedback law which removes the detrimental effects of system nonlinearities and hence achieve better control when augmented with linear control laws such as PID. The drawbacks of FBL controllers are that they require the model to be fully understood, which in reality may be impossible due to modelling uncertainties, parameter variations, and the lack of experimental data. To overcome this hurdle, an intelligent controller that implements neural network models in conjunction with FBL is formulated. In order to add novelty to AVSS design, ensure

stability without considerable complexity and as well as to simplify the mathematical procedure, dynamic neural networks (DNN) are utilised to assist in predicting the next control action. This method of control will be named dynamic neural network-based feedback linearization (DNNFBL) control.

This above mentioned control method may be conducted using two approaches, one of which is to follow a direct adaptive control method in which the DNN is trained to predict and FBL law. The second is an indirect adaptive methodology where the system response is predicted using a DNN and subsequently FBL is performed on the trained DNN to produce a linearizing feedback law. In this investigation an indirect adaptive policy is carried out for one of several reasons. Firstly, there is no need for any mathematical model when deriving this control law and secondly FBL is less complex when applied to DNN models as opposed to the nonlinear electrohydraulic suspension system used in this research.

4.2 Stability Analysis

Before the control law is developed, it is imperative to test whether feedback linearization is applicable to such a system and secondly to ensure stability of the system is guaranteed and the steady-state error is limited to an acceptable value. Stability is analysed by applying the input-output feedback linearization method (FBL) on the actual system. [Shi et al. (2010), Pedro and Dahunsi (2011), Isidori (1989), Jelali and Kroll (2003)]

A block diagram of a control system which incorporates FBL is shown in Figure 4.1. In this methodology, the actual plant input u is formulated through FBL such that there exists a linear mapping between the virtual input υ and the system output y. Additionally, the virtual control υ may be the product of any linear control law which may be formulated on the basis of the control error e.

The state-space representation of the quarter-car AVSS model presented in Eqs. (2.20) to (2.30) and the resulting control law that creates a linear mapping between the new virtual input υ and output y is as follows:

$$u = P(\mathbf{x}) + Q(\mathbf{x})\upsilon \tag{4.1}$$

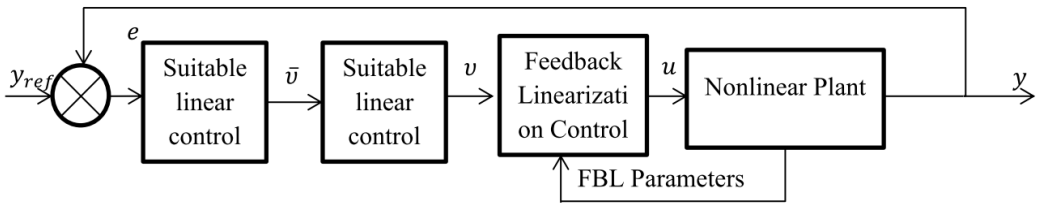

Figure 4.1: General structure of FBL control scheme

This is known as the feedback form with $P(\mathbf{x})$ and $Q(\mathbf{x})$ being functions of the system states $\mathbf{x}$. However, for Eq. (4.1) to hold true, the following conditions must be met [Shi et al. (2010)]:

1. State vector $\mathbf{x}\epsilon\mathbb{R}^n$.
2. Input vector $u\epsilon\mathbb{R}^1$.
3. Output $y\epsilon\mathbb{R}^m$.
4. System output y: $\mathbb{R}^n \rightarrow \mathbb{R}^n$) are smooth functions on the state-space $\mathbb{R}^n$.

For the quarter-car state-space system, the above conditions hold true and hence the suggested control technique may be employed. FBL controller design may be summarised in the following steps:

Step 1 Continuously take the time derivative of the output y until a corresponding derivative y^r is explicitly a function of the system input u such that:

$$y^r = a(\mathbf{x}) + b(\mathbf{x})u \tag{4.2}$$

where $a(\mathbf{x})$ and $b(\mathbf{x})$ are nonlinear functions that have been produced as a consequence of the above computation.

Step 2 In order for the r^{th} derivative of the output y and all subsequent derivatives to be linearly related to the virtual control input υ, u must take the ensuing form:

$$u = \frac{\upsilon - a(\mathbf{x})}{b(\mathbf{x})} \tag{4.3}$$

In accordance with step 1 of FBL, the first derivative of the output is computed as:

$$\begin{aligned} y^{(1)} &= \frac{\partial y}{\partial t} = \frac{\partial y}{\partial \mathbf{x}}\frac{\partial \mathbf{x}}{\partial t} = \frac{\partial y(\mathbf{x})}{\partial x}\dot{\mathbf{x}} \\ &= \frac{\partial y}{\partial \mathbf{x}}\left[f(\mathbf{x}) + g(\mathbf{x})u\right] \\ &= \mathfrak{L}_f y(\mathbf{x}) + \mathfrak{L}_g y(\mathbf{x})u = \mathfrak{L}_f y(\mathbf{x}) = x_2 - x_1 \end{aligned} \tag{4.4}$$

where $\frac{\partial y}{\partial \mathbf{x}} f(\mathbf{x})$ is defined as $\mathfrak{L}_{\mathfrak{f}} y(\mathbf{x})$, which is referred as the Lie derivative of $y(\mathbf{x})$ along f. In this case, $\mathfrak{L}_{\mathfrak{g}} y(\mathbf{x})$ was calculated to be zero, which subsequently infers that the first derivative of the output $y^{(1)}$ is not explicitly dependent on the control input u, i.e.

$$y^{(1)} = \mathfrak{L}_{\mathfrak{f}} y(\mathbf{x}) \tag{4.5}$$

Computation of the latter derivative yields:

$$\begin{aligned} y^{(2)} &= \frac{\partial^2 y}{\partial^2 t} = \frac{\partial \frac{\partial y}{\partial t}}{\partial \mathbf{x}} \frac{\partial \mathbf{x}}{\partial t} = \frac{\partial \frac{\partial y}{\partial t}}{\partial \mathbf{x}} \dot{\mathbf{x}} \\ &= \frac{\partial \mathfrak{L}_f y(\mathbf{x})}{\partial \mathbf{x}} \left[f(\mathbf{x}) + g(\mathbf{x}) u \right] \\ &= \mathfrak{L}_f^2 y(\mathbf{x}) + \mathfrak{L}_g y(\mathbf{x}) \mathfrak{L}_f y(\mathbf{x}) u = \mathfrak{L}_f y(\mathbf{x}) = x_4 - x_3 \end{aligned} \tag{4.6}$$

As in the case of the preceding derivative, $y^{(2)}$ is not explicitly a function of u and thus $\mathfrak{L}_g \mathfrak{L}_f y(\mathbf{x}) = 0$. The next derivative $y^{(3)}$ produces:

$$\begin{aligned} y^{(3)} &= \frac{\partial^3 y}{\partial^3 t} = \frac{\partial \frac{\partial^2 y}{\partial^2 t}}{\partial \mathbf{x}} \frac{\partial \mathbf{x}}{\partial t} = \frac{\partial \frac{\partial^2 y}{\partial^2 t}}{\partial \mathbf{x}} \dot{\mathbf{x}} \\ &= \frac{\partial \mathfrak{L}_f^2 y(\mathbf{x})}{\partial \mathbf{x}} \left[f(\mathbf{x}) + g(\mathbf{x}) u \right] \\ &= \mathfrak{L}_f^3 y(\mathbf{x}) + \mathfrak{L}_g \mathfrak{L}_f^2 y(\mathbf{x}) u = \mathfrak{L}_f y(\mathbf{x}) = \dot{x}_4 - \dot{x}_3 \end{aligned} \tag{4.7}$$

$y^{(3)}$ is also independent of u as $\mathfrak{L}_g \mathfrak{L}_f^2 y(\mathbf{x}) u = 0$. The subsequent derivative of the output generates:

$$\begin{aligned} y^{(4)} &= \frac{\partial^4 y}{\partial^4 t} = \frac{\partial \frac{\partial^3 y}{\partial^3 t}}{\partial \mathbf{x}} \frac{\partial \mathbf{x}}{\partial t} = \frac{\partial \frac{\partial^3 y}{\partial^3 t}}{\partial \mathbf{x}} \dot{\mathbf{x}} \\ &= \frac{\partial \mathfrak{L}_f^3 y(\mathbf{x})}{\partial \mathbf{x}} \left[f(\mathbf{x}) + g(\mathbf{x}) u \right] \\ &= \mathfrak{L}_f^4 y(\mathbf{x}) + \mathfrak{L}_g \mathfrak{L}_f^3 y(\mathbf{x}) u \end{aligned} \tag{4.8}$$

However, the above relation is explicitly dependent on the control input u with $\mathfrak{L}_g \mathfrak{L}_f^3 y(\mathbf{x}) u \neq 0$. Hence, the system possesses a relative degree r of 4. Furthermore, since the relative degree is less than the number of system states $n_s = 6$, the system is therefore input-output linearizable. Thus, the control law described by Eq. (4.3) may be applied to create a linear mapping between the new virtual input υ and output y. Moreover, the coordinate system may be transformed into a new differential homeomorphic coordinate system which is described by Eq. (4.9). This co-ordinate system essentially separates the observable and non-trivial or influential dynamics that remain in the system once the output is forced to zero. The relative degree indicates the number of observable dynamics that lie within this control system. Furthermore, the difference between the system states and the relative degree corresponds to the number of unobservable dynamics present in the system.

$$z = \Psi(\mathbf{x}) = \begin{bmatrix} \boldsymbol{\xi} & \boldsymbol{\eta} \end{bmatrix}^T \tag{4.9}$$

where $\boldsymbol{\xi}$ is the observable dynamics of the system which corresponds to 4 states as the relative degree is 4 with $\boldsymbol{\xi} = [\ z_1 \quad z_2 \quad z_3 \quad z_4\ ]^T$, and $\boldsymbol{\eta}$ is the unobservable or zero dynamics of the system which contains 2 states since the difference between the number of states and relative degree is 2, and hence: $\boldsymbol{\eta} = [\ \psi_1(\mathbf{x}) \quad \psi_2(\mathbf{x})\ ]^T$. In accordance with Eq. (4.9), observable system states are thus defined as: $z_1 = y, z_2 = y^{(1)}, z_3 = y^{(2)}, z_4 = y^{(3)}$, and the zero dynamics are represented as: $z_5 = \psi_1(\mathbf{x}), z_6 = \psi_2(\mathbf{x})$. The new differential homeomorphic coordinate system may also be expressed in state-space with:

$$\dot{\boldsymbol{\eta}} = \mathbf{f}_0(\boldsymbol{\xi}, \boldsymbol{\eta}) \tag{4.10}$$

$$\dot{\boldsymbol{\xi}} = \mathbf{A}_c\boldsymbol{\xi} + \mathbf{B}_c\upsilon + \bar{\mathbf{p}}(w) \tag{4.11}$$

$$\dot{\boldsymbol{\xi}} = \mathbf{A}_c\boldsymbol{\xi} + \mathbf{B}_c\left[\frac{u(t) - a(\mathbf{x})}{b(\mathbf{x})}\right] + \bar{\mathbf{p}}(w) \tag{4.12}$$

$$y = \mathbf{C}_c\boldsymbol{\xi} \tag{4.13}$$

where the system matrices are defined as follows:

$$\mathbf{A}_c = \begin{bmatrix} 0 & 1 & 0 & 0 \\ 0 & 0 & 1 & 0 \\ 0 & 0 & 0 & 1 \\ \lambda_0 & \lambda_1 & \lambda_2 & \lambda_3 \end{bmatrix} \mathbf{B}_c = \begin{bmatrix} 0 \\ 0 \\ 0 \\ 1 \end{bmatrix} \mathbf{C}_c = \begin{bmatrix} 1 & 0 & 0 & 0 \end{bmatrix}^T \bar{\mathbf{p}}(w) = \begin{bmatrix} 0 & 0 & 0 & 1 \end{bmatrix}^T \tag{4.14}$$

However, in order for the diffeomorphism to successfully produce differential homeomorphic coordinate system, the following condition must be ensured [Pedro and Dahunsi (2011)]: Ψ must be invertible such that:

$$\mathfrak{L}_f\psi_i = \frac{d\psi_i}{dx}g(\mathbf{x}), \quad r+1 \leq i \geq n_s \tag{4.15}$$

With regards to guaranteed stability, both the observable $\boldsymbol{\xi}$ and unobservable $\boldsymbol{\eta}$ system dynamics must be stable. To reiterate, the unobservable system dynamics $\boldsymbol{\eta}$ are defined as non-trivial internal dynamics that remain once the output and observable system dynamics are forced to zero such that $\boldsymbol{\xi} = 0$ and hence $\dot{\boldsymbol{\eta}}_0(\boldsymbol{\eta}, 0)$. Such dynamics may be also termed as the zero dynamics, and they tend to have a significant impact on the stability of the system. Asymptotic stability of the system is confirmed if the origin of the transformed system ($\boldsymbol{\eta} = 0, \boldsymbol{\xi} = 0$) is an equilibrium point. Such stability reduces the dynamics of the r^{th} derivative of the output described by Eq. (4.8) to:

$$\lambda_4 y^{(4)} = \upsilon \tag{4.16}$$

The above relation implies that the control law u is of the form

$$u = \frac{1}{\lambda_4\mathfrak{L}_g\mathfrak{L}_f^3 y\mathbf{x}}\left[\upsilon - \lambda_4\mathfrak{L}_f^4 y\mathbf{x}\right] \tag{4.17}$$

Application of this control law to the system's feedback form described in Eq. (4.3) produces a linear mapping between the output y and the virtual input υ or $V(s)$ and this creates a linear input-output affiliation according to Eq. (4.18) with a transfer function given by:

$$G(s) = \frac{Y(s)}{V(s)} = \frac{1}{\lambda_4 s^4} \tag{4.18}$$

Designing the virtual input v according to a linear control law such as pole placement yields:

$$\upsilon = -\lambda_3 y^{(3)} - \lambda_2 y^{(2)} - \lambda_1 y^{(1)} - \lambda_0 y + \bar{\upsilon} \tag{4.19}$$

where $\bar{\upsilon}$ is the new external input, which may be based on any linear control law. In this investigation, it is set to be a function of the reference signal y_{ref} and the output signal y and hence the control signal e. Hence, the new transfer function mapping the new external input $\bar{\upsilon}$ to the system output y is given as:

$$G(s) = \frac{Y(s)}{\bar{V}(s)} = \frac{1}{\lambda_4 s^4 + \lambda_3 s^3 + \lambda_2 s^2 + \lambda_1 s^1 + \lambda_0} \tag{4.20}$$

The resulting closed-loop polynomial is of the form:

$$p(s) = \lambda_4 s^4 + \lambda_3 s^3 + \lambda_2 s^2 + \lambda_1 s^1 + \lambda_0 \tag{4.21}$$

To ensure the stability of this system, the coefficients of the closed-loop characteristic polynomial described by Eq. (4.21) is selected such that the roots of this polynomial are strictly in the left-half of the complex plane. In accordance with the aforementioned equations, the control input u may be further simplified into the following:

$$u = \frac{1}{\lambda_4 \mathfrak{L}_g \mathfrak{L}_f^3 y\mathbf{x}} \left[\bar{\upsilon} - \lambda_4 \mathfrak{L}_f^4 y\mathbf{x} - \sum_{i=1}^{4} \lambda_{i-1} \mathfrak{L}_f^{i-1} y\mathbf{x} \right] \tag{4.22}$$

As previously discussed, the external input $\bar{\upsilon}$ must be a function of the control error e and hence a PID output feedback controller is selected to produce the external input $\bar{\upsilon}$. This PID operates in the outer-most control loop and the external input $\bar{\upsilon}$ may be written as:

$$\bar{\upsilon} = K_p e + K_i \int_0^T e.dt + K_d \frac{de}{dt} \tag{4.23}$$

where Kp, K_i and K_d are the proportional, integral and derivative gains of the PID controller respectively.

4.3 Proposed Control Structure

The suggested indirect adaptive design of DNNFBL controller is illustrated in Figure 4.2 and essentially comprises of two stages, namely system identification and controller implementation. During system identification, the DNN learns the dynamics

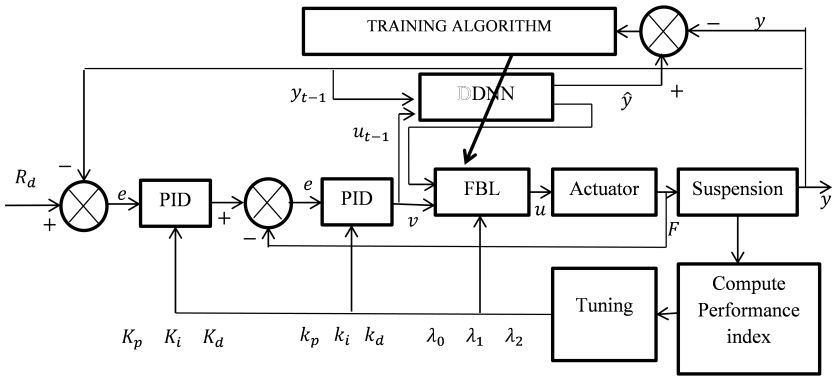

Figure 4.2: Controller architecture of the DNNFBL-based AVSS

of the plant with the sole intent of predicting the response of the plant for a given set of input data. In controller implementation, FBL is carried out on the DNN model with the objective of producing an adaptive control signal that linearizes the plant and hence eliminates the detrimental issues that occur as a result of nonlinearities. Furthermore, the DNNFBL controller may be augmented with a linear controller (such as the multi-loop PID controllers that were earlier employed) with the intent of supplementing system performance. Additionally, the gains of each of the controllers may be tuned manually or through an optimization algorithm. The rest of this subsection is devoted to providing a detailed analysis into system identification and controller design.

4.4 System Identification

A DNN is a neural network that includes recurrent or feedback elements. This neural network is modelled using differential equations in contrast to the algebraic equations that are used to describe static neural networks. The structure of a DNN is further explained in Figure 4.3. The dynamics of the neurons are mathematically described as a first-order differential equation with a time constant $\boldsymbol{\beta}$. Additionally, each neuron receives feedback from neurons in its respective hidden layer $\bar{\mathbf{x}}_{t-1}$ of the neural network, as well as from the input layer of the neural network u_t. Both the network and neuron to neuron inputs are essentially added to the right hand side of the differential equation that describes the dynamics of the neuron. However, the output of each neuron is passed through an activation function $\sigma(\mathbf{x})$ before it is fedback to each neuron in the corresponding hidden layer. Additionally, each neuron has two external inputs, namely control input u and one delayed system state $\bar{x}_{t-1}$, each of which possesses its own associating weighting value. Hence, a neuron in the

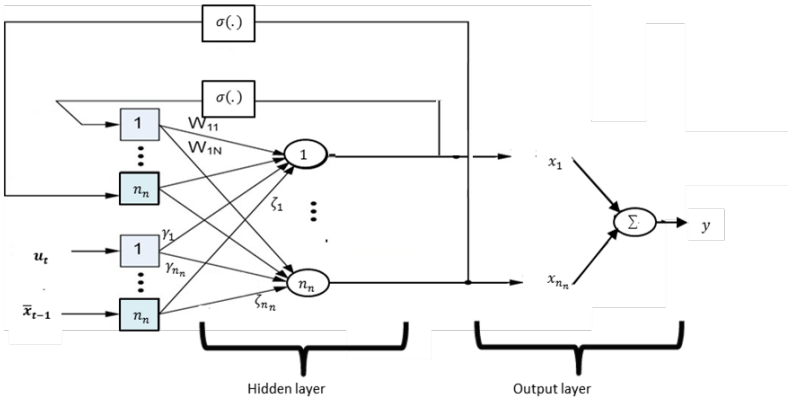

Figure 4.3: Schematic describing the operation of a DNN

first hidden layer of the neural network is described by the following mathematical relationship:

$$\dot{\mathbf{x}} = -\boldsymbol{\beta}\mathbf{x} + \mathbf{W}\sigma(\mathbf{x}) + \boldsymbol{\gamma}\mathbf{u}_t + \boldsymbol{\zeta}\bar{x}_{t-1} \tag{4.24}$$

where $\mathbf{x}$ is a vector denoting the outputs of each neuron, $\boldsymbol{\beta}$ is the matrix containing the time constants of each neuron in the hidden layer, $\sigma(\mathbf{x})$ is the vector containing the neuron outputs after it had passed through the activation function, $\mathbf{W}$ is the inter-connecting neuron weights, u_t is a vector that holds the various control input signals that are being passed into the real system, $\boldsymbol{\gamma}$ is a matrix which holds the weighting contributions that each control input has on each neuron, $\bar{x}_{t-1}$ is a vector that holds the actual system output or delayed output at the previous time step, and $\boldsymbol{\zeta}$ is the contribution of these aforementioned outputs on each neuron.

The output layer of the DNN comprises of a single neuron and is fundamentally an algebraic equation, which is essentially the weighted sum of the neuron outputs from the preceding hidden layer $\mathbf{x}$. Thus, the neuron in this layer is described as follows:

$$\hat{y} = h_n(\mathbf{x}) = \sum_{i=1}^{n_n} w_i x_i \tag{4.25}$$

where x_i is a vector comprising of the output of the i^{th} neuron from the hidden layer, w_i is the associating weighting contribution of the i^{th} neuron in the hidden layer, n_n is the number of neurons in the hidden layer.

In order, to further simplify the model and subsequent computation, the output of the neural network y will depend solely on the output from the first neuron in the

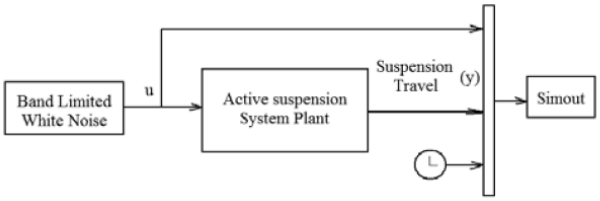

Figure 4.4: Method explaining the process of system identification [Dahunsi and Pedro (2010)]

preceding hidden layer. Consequently, the output layer will be simplified to:

$$\hat{y} = h_1 = w_1 x_1 \tag{4.26}$$

Furthermore, the selection of network parameters such as the number of hidden layer, size of the hidden layer n_n and the activation function $\sigma(.)$ will be based on two items, namely network stability and through the method of pruning outlined by Nϕrgaard et al. (2000). In pruning, the primary network parameters such as the hidden layer size are increased until the predicted system output $\hat{y}$ stops changing topology with further increase in the hidden layer size. Garces et al. (2003) argues that $\sigma(.)$ should be bounded to within ± 1 so that the free response of the DNN converges to zero and thus stabilises once the networks inputs are removed. Hence, the hyperbolic tangent function is chosen as activation function $\sigma(.)$ so that this condition is met. The next condition may only be fulfilled after the selection of appropriate input-output data.

An important step in system identification is to select a range of input-output data that covers the range of signals that will be anticipated in reality. In indirect adaptive control the DNN must predict the output of the suspension system for a given set of control input voltage. As in the case of PID-based control, suspension travel is chosen as the output as it is the fundamental property used to model the suspension system. White-Band-Limited noise (WBL) is used to create a set of input data, specifically because WBL can successfully create a random set of input signals which span the space of the expected input signals. Figure 4.4 illustrates the process of system identification. Selection of an appropriate data set is a rather rigorous process that requires several conditions to be met. Firstly, the dynamics of the subsystem with the smallest time constant must be captured and this demands that the seed strength of the WBL be significantly high. Secondly, the input data must span the space of all possible input voltages, which is known to be in the range of $\pm 10V$. Similarly, the set of suspension travel output must span the region in which it is expected to operate, which corresponds to $\pm 0.1m$. From Figures 3.27 and 3.28, it

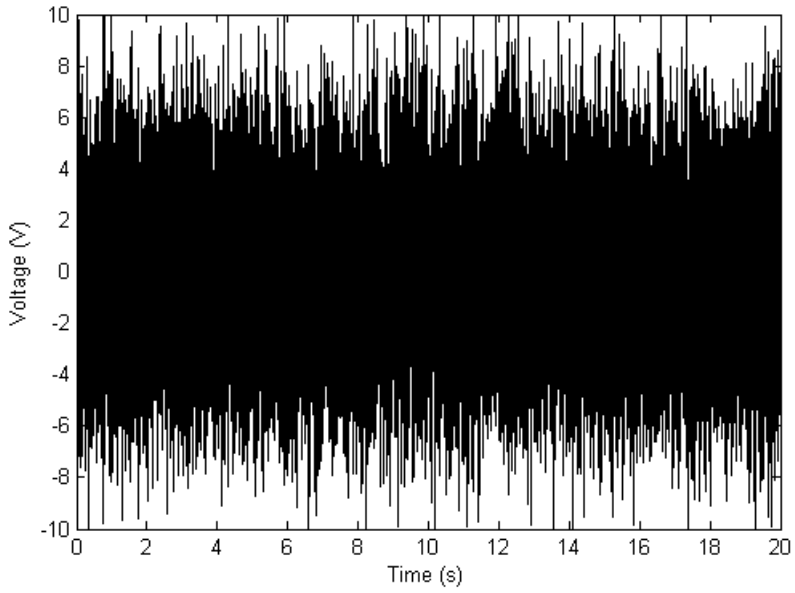

Figure 4.5: Quarter-car AVSS control input voltage supplied for system identification

is evident that both the PVSS and AVSS are sensitive in the frequency range of $0.5Hz$ to $80Hz$, and it is thus paramount that the system identification input covers these frequencies [Dahunsi and Pedro (2010)]. In order, to satisfy the preceding conditions, the WBL may be set as follows:

i. Control input u operates within $\pm 10V$.

ii. WBL has the following properties:

- Seed strength of 22641.
- 0.001s sampling time.

iii. Hyperbolic Tangent is used for the activation function $\sigma(\mathbf{x})$ as this ensures the DNN stability [Garces et al. (2003)].

Plots showing the input and corresponding output data sets are presented in Figures 4.5 and 4.6 respectively. With regards to pruning and the choice of hidden layer size n_n the response of the DNN is analysed for a range of n_n starting from one. The network size increased until satisfactory results are attained for a credible range of randomly selected network parameters. Figure 4.7 shows the general trend of the suspension travel output for the various hidden layer sizes. From the preceding figure, it is evident that a hidden layer size n_n of 8 is capable of capturing the sensitive dynamics of the system as it can pick up the sudden rate of change of suspension travel more adequately than the 4-neuron and 6-neuron configurations. Hence, it is

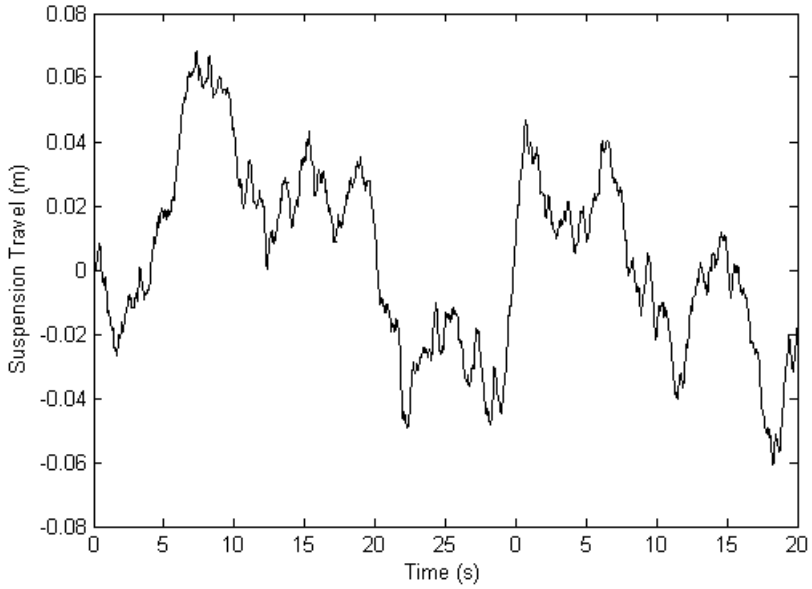

Figure 4.6: Quarter-car model suspension travel output for the training phase of system identification

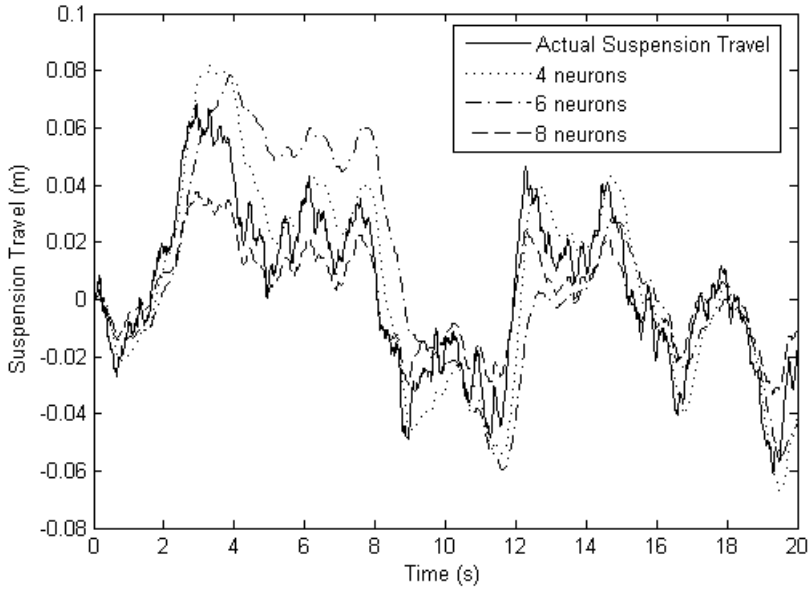

Figure 4.7: Quarter-car suspension travel output for different hidden layer sizes

Table 4.1: Configuration of applied dynamic neural networks for the quarter-car system

Property	**Numerical Value**
Number of hidden layers	2
Number of neurons in first hidden layer	8
Number of delayed system inputs	1
Number of delayed system outputs	1

suitable for system identification. The structure of the DNN is summarised in Table 4.1. DNN training is performed with the aid of various optimization algorithms including CRS, DE, GA, PS and PSO described in section 3.2.4. In this learning process, the DNN parameters namely $\boldsymbol{\beta}$, $\mathbf{W}$, $\boldsymbol{\gamma}$, and $\boldsymbol{\zeta}$ are the problem variables that are determined by the same approach in which the PID-based AVSS controller gains were selected using the proposed optimal routines. $\boldsymbol{\beta}$ is a 1×8 vector with β_n denoting the time constant of the n^{th} neuron from the 8 present in the first hidden layer. The same applies to $\boldsymbol{\gamma}$ and $\boldsymbol{\zeta}$ as well. W is the weighting matrix that connects each of the neurons of the hidden layer to each other and it is a sqaure 8×8 matrix with W_{jh} denoting the feedback weighting of the h^{th} neuron into the j^{th} neuron.

The problem variables computed by the optimal routines are now the network parameters as opposed to the controller gains that were computed in the optimal PID-based AVSS. Furthermore, the performance index or objective function of these optimal policies will now be changed to suit system identification instead of suspension performance. The objective function will measure the extent of deviation or error between the network output $\hat{y}$ and the real suspension output y. Pedro et al. (2011) chose the mean squared error (MSE) of this deviation as the objective function and the same approach will be followed in this investigation as well. Hence, the objective function will be:

$$J = MSE = \frac{1}{2N} \sum_{i=0}^{N} (y - \hat{y})^2 \tag{4.27}$$

where N is the total number of samples used in the input-output data. The set-up of these optimal policies is altered to better meet the need of system identification as opposed to controller tuning. The new set-up is reported in Table 4.2. The progression of the objective function through the various training techniques involving CRS, DE, GA, PS and PSO are plotted in Figure 4.8 and that of the CRS-based training method is shown in Figure 4.9. These results are relevant as it will determine which algorithms are successful for system identification. Furthermore, they will also provide insight into the performance of these algorithms from a computational point of

Table 4.2: Optimization parameters used in each optimal policy for system identification of the quarter-car system

Routine	**DE**	**GA**	**PSO**	**CRS**	**PS**
Population Size	100	300	100	60	1
Stopping Criteria Criteria	50 Generations	50 Generations	50 Iterations	6000 Iterations	Scaling factor factor $\epsilon \leq 1 \times 10^{-8}$
Optimization Parameters	F=2	K=100	w_1=0.5 $w_2 = 2$ w_3=2	n=89	

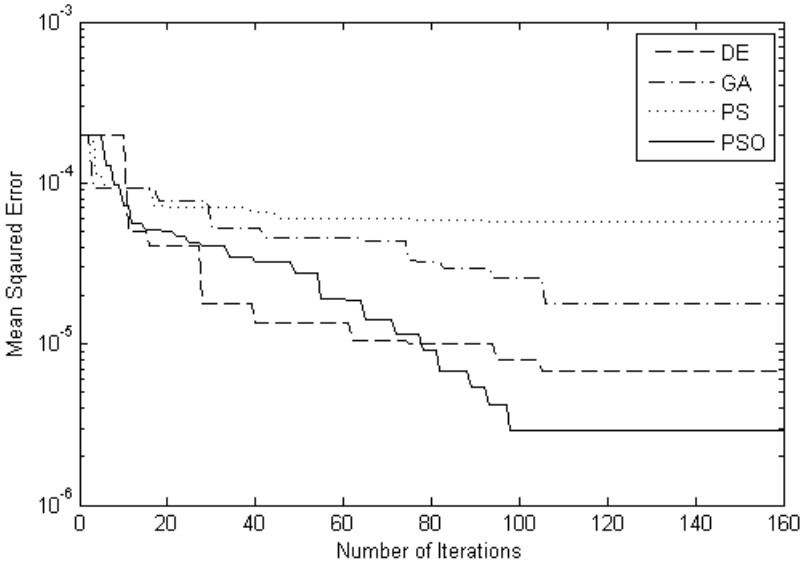

Figure 4.8: Convergence history of the various training algorithms used in system identification of the quarter-car AVSS

view such as information pertaining to convergence speed and accuracy.

Figures 4.8 and 4.9 infer that evolutionary algorithms such as DE, GA, PSO are adequate polices to use for DNN with improved accuracy and convergence speeds whilst CRS and PS are clearly deficient in this regard with considerably lower accuracy and longer convergence speeds . However, it is worth mentioning that CRS and PS did perform adequately well for PID controller design where fewer variables were optimized, and this implies that the CRS, and PS optimization algorithms in general are not effective in computing a large amount of problem variables as in the case of DNN training. Additionally, the PSO performed the best from the evolutionary

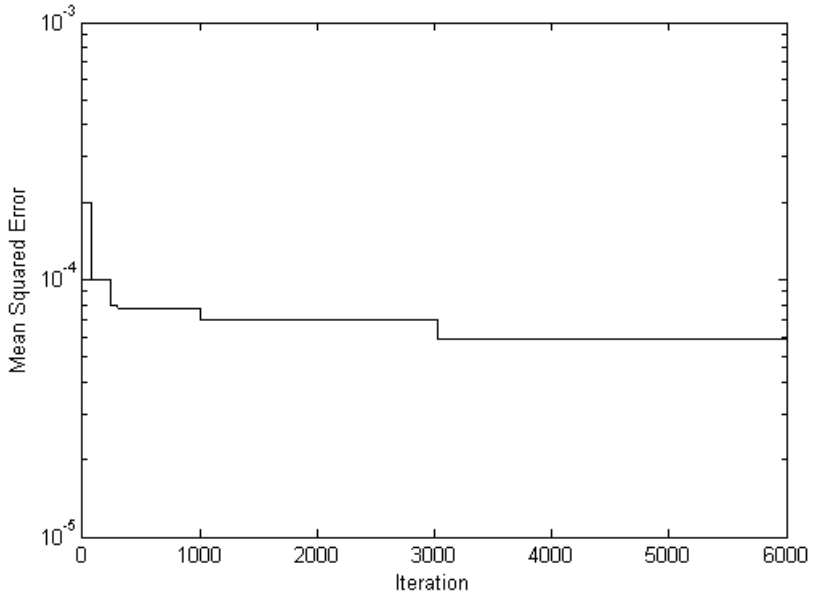

Figure 4.9: Convergence history of the MSE value when incorporating CRS-based system identification

algorithms with the best MSE value followed by the DE and GA respectively. The performance of the GA is still significantly weaker with a noticeably larger MSE as compared to the DE and PSO. The identification and validation results of the DE, GA and PSO routines plotted are in Figures 4.10 and 4.11 respectively. It is worth mentioning that the PSO's results show greater structure and display superior accuracy in picking up the rate of change of the system output as opposed to the DE data. It is also worth noting that the system identification results for the same quarter-car electrohydraulic system learnt with static neural networks that were trained using various currently employed function-based algorithms [Dahunsi et al. (2011)]. The results of these identification methods produced MSE values ranging within an order of magnitude of 1×10^{-6}, which is equivalent to the MSE values obtained in this research study. Thus, the proposed DNN model and its training scheme is as good as those static neural networks. Before controller design can begin, the stability of the DNN model must be ensured. Isidori (1989) and Garces et al. (2003) argue that network stability is ensured if the following conditions hold:

Step i. The activation function $\sigma(\mathbf{x})$ is continuously differentiable.

Step ii. $\sigma(\mathbf{x})$ is bounded to $0 \leq \sigma(\mathbf{x}) \leq 1$

Step iii. Given $u_t \epsilon \mathbb{R}_+$, there is a symmetric and positive solution P to the Eq. (4.28)

$$\beta^{\mathbf{T}}\mathbf{P} - \mathbf{P}\beta = -\mu\mathbf{I} \tag{4.28}$$

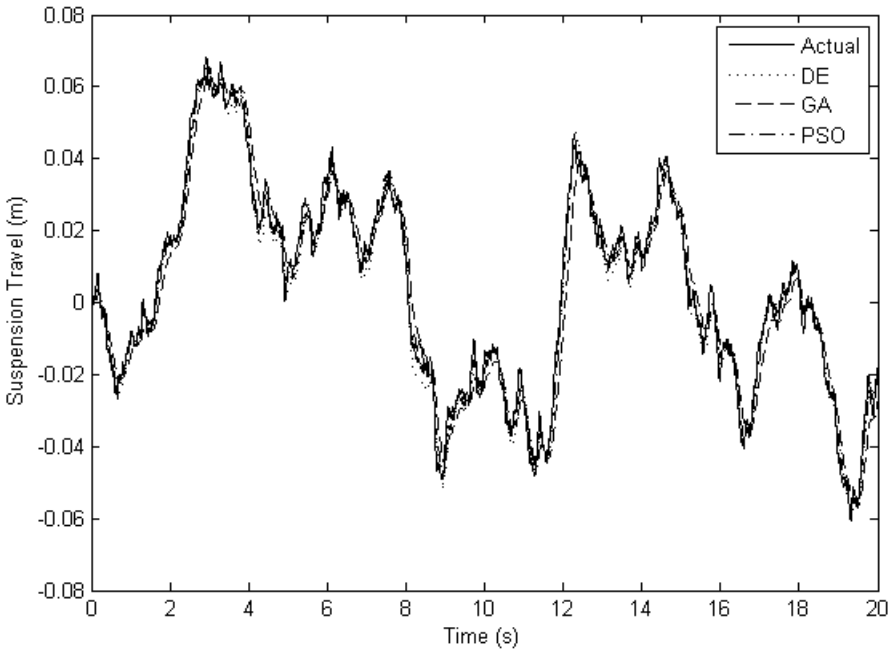

Figure 4.10: DNN identification results for quarter-car intelligent controller using proposed global optimization methods

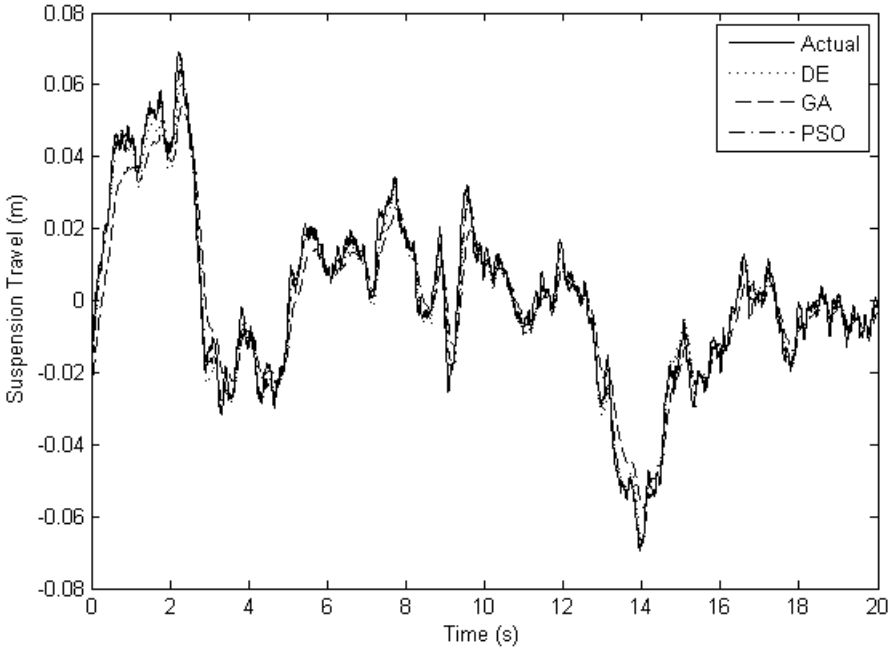

Figure 4.11: DNN validation results for quarter-car intelligent controller using proposed global optimization methods

where $\mathbf{I}$ is an identity matrix and μ is a scaling factor, which Garces et al. (2003) suggested should have a value of 1.

Step iv. The inequality of Eq. (4-28) must be satisfied:

$$||\mathbf{W}||^2 \leq \frac{\mu - 2||P||}{||P||} \tag{4.29}$$

where $||.||$ signifies the Euclidean norm of the specified matrix.

As the activation function $\sigma(\mathbf{x})$ is the hyperbolic tangent function, conditions i. and ii. are fulfilled. With both the networks computed through DE and PSO algorithms, both Eq. (4.28) and the inequality of Eq. (4.29) are satisfied. Hence, it may be concluded that the DNN models attained through training are indeed stable.

4.5 Control Law Formulation

The control law is formulated using the same approach used in the stability analysis of the system (Section 4.2). The only modification is that an indirect adaptive control, the method will be applied to the DNN model rather than the actual system as was done in the stability analysis. Firstly, the DNN is rearranged into the compatible affine form that is required to derive the feedback law as follows:

$$\dot{\mathbf{x}} = \mathbf{f}(\mathbf{x}) + \mathbf{g}(\mathbf{x})u_t + \boldsymbol{\zeta}\bar{\mathbf{x}}_{t-1} \tag{4.30}$$

where $\mathbf{f}(\mathbf{x}) = \mathbf{W}(\mathbf{x}) - \beta\mathbf{x}$, and $\mathbf{g}(\mathbf{x}) = \boldsymbol{\gamma}$. The following steps involve computing the consecutive derivatives of the DNN model outputs until a corresponding derivative is explicitly a function of the control input u_t. The first derivative of the network output is computed as follows:

$$\begin{aligned}
\hat{y}^{(1)} &= \frac{\partial \hat{y}}{\partial t} = \frac{\partial \hat{y}}{\partial \mathbf{x}}\frac{\partial \mathbf{x}}{\partial t} = \frac{\partial h_1(\mathbf{x})}{\partial x}\dot{\mathbf{x}} \\
&= \frac{\partial h_1}{\partial \mathbf{x}}\left[\mathbf{f}(\mathbf{x}) + \mathbf{g}(\mathbf{x})u\right] = \mathfrak{L}_f h_1(\mathbf{x}) + \mathfrak{L}_g h_1(\mathbf{x})u \\
&= \left[\begin{array}{ccccc} \frac{\partial h_1}{\partial x_1} & \frac{\partial h_1}{\partial x_2} & \ldots & \ldots & \frac{\partial h_1}{\partial x_8} \end{array}\right]\left[\mathbf{f}(\mathbf{x}) + \mathbf{g}(\mathbf{x})u\right]^T \\
&= w_1\left[-\beta_1 x_1 + \sum_{i=1}^{8} W_{1i}\sigma(x_i)\right] = \mathfrak{L}_f h_1(\mathbf{x})
\end{aligned} \tag{4.31}$$

$\mathbf{g}(\mathbf{x})$ is nothing more than the consequent of DNN training, and its resulting matrix has its first element $g_1(\mathbf{x}) = 0$. Furthermore, $\frac{\partial h_1}{\partial x_1}.....\frac{\partial h_1}{\partial x_8}$ are zero as h_1 is a function of x_1 only as per Eq. (4.26). Such values give rise to the Eq. (4.31), where clearly the

first derivative of the DNN model output $\dot{\hat{y}}$ is not a function of the control input u_t. Subsequent computation of the second derivative of the network output produces:

$$\begin{aligned}
\hat{y}^{(2)} &= \frac{\partial^2 \hat{y}}{\partial t} = \frac{\partial \frac{\partial \hat{y}}{\partial t}}{\partial \mathbf{x}} \frac{\partial \mathbf{x}}{\partial t} \\
&= \frac{\partial \mathfrak{L}_f h_1(\mathbf{x})}{\partial x} \left[\mathbf{f}(\mathbf{x}) + \mathbf{g}(\mathbf{x})u\right] \\
&= w_1[-\beta_1 x_1 + W_{11}(1 - \sigma(\mathbf{x_1})^2) + W_{12}(1 - \sigma(\mathbf{x_2})^2)..... \\
&= +W_{18}(1 - \sigma(\mathbf{x_8})^2)] \left[\mathbf{f}(\mathbf{x}) + \mathbf{g}(\mathbf{x})u\right] \\
&= d(\mathbf{x}) + e(\mathbf{x})u_t \\
&= \mathfrak{L}_f^2 h_1(\mathbf{x}) + \mathfrak{L}_g \mathfrak{L}_f h_1(\mathbf{x}) u_t
\end{aligned} \tag{4.32}$$

where $d(\mathbf{x})$ or $\mathfrak{L}_f^2 h_1(\mathbf{x})$ is the free response of the system and $e(x)u_t$ or $\mathfrak{L}_g \mathfrak{L}_f h_1(\mathbf{x})u_t$ is the free response of the system. In the above derivative of the output, the DNN of both the PSO and DE training yielded a matrix where $g_1(\mathbf{x})$,$g_2(\mathbf{x})$....$g_3(\mathbf{x})$ were considerably large constants. Hence the computation of the second derivative of the network output $\hat{y}^2$ produced a solution which was explicitly dependent on the control input u_t. Hence, the relative degree of the system is two, which infers that the DNN is input-output linearizable as its relative degree is less than the number of states of the DNN (which corresponds to 8 as there are eight neurons in the hidden layer).

The next step in controller formulation demands that the DNN dynamics now be transformed into a co-ordinate system which separates the observable and zero dynamics. As in the case of input-state feedback linearization outlined in section 4.2, the DNN may be described in terms of its observed and unobserved zero dynamics using the diffeomorphism as follows:

$$\dot{\boldsymbol{\eta}} = \mathbf{f}_0(\boldsymbol{\xi}, \boldsymbol{\eta}) \tag{4.33}$$

$$\dot{\boldsymbol{\xi}} = \mathbf{A}_c \boldsymbol{\xi} + \mathbf{B}_c \upsilon + \bar{\mathbf{p}}(w) \tag{4.34}$$

$$\dot{\boldsymbol{\xi}} = \mathbf{A}_c \boldsymbol{\xi} + \mathbf{B}_c \left[\frac{u(t) - a(\mathbf{x})}{b(\mathbf{x})}\right] + \bar{\mathbf{p}}(w) \tag{4.35}$$

$$\hat{y} = \mathbf{C}_c \boldsymbol{\xi} \tag{4.36}$$

As the relative degree of the DNN is 2, the transformation yields a slightly different set of system matrices which are:

$$\mathbf{A}_c = \begin{bmatrix} 0 & 1 \\ \lambda_0 & \lambda_1 \end{bmatrix} \mathbf{B}_c = \begin{bmatrix} 0 \\ 1 \end{bmatrix} \mathbf{C}_c = \begin{bmatrix} 1 & 0 \end{bmatrix}^T \bar{\mathbf{p}}(w) = \begin{bmatrix} 0 & 1 \end{bmatrix}^T \tag{4.37}$$

The control law aims to create a linear mapping between the virtual input υ and the system network output $\hat{y}$ as explained in Figure 4.3 such that:

$$\lambda_2 \hat{y}^2 = \upsilon \tag{4.38}$$

Ψ must be invertible such that:

$$\mathfrak{L}_f \psi_i = \frac{d\psi_i}{dx} g(\mathbf{x}), \quad r+1 \leq i \leq n_s \tag{4.39}$$

With regards to guaranteed stability, both the observable $\boldsymbol{\xi}$ and unobservable $\boldsymbol{\eta}$ system dynamics must be stable. To reiterate, the unobservable system dynamics $\boldsymbol{\eta}$ are defined as non-trivial internal dynamics that remain once the output and observable system dynamics are forced to zero such that $\boldsymbol{\xi} = 0$ and hence $\dot{\boldsymbol{\eta}}_0(\boldsymbol{\eta}, 0)$. Such dynamics may also be termed the zero dynamics, and they tend to have a significant impact on the stability of the system. Asymptotic stability of the system is confirmed if the origin of the transformed system ($\boldsymbol{\eta} = 0, \boldsymbol{\xi} = 0$) is an equilibrium point. Such stability reduces the dynamics of the r^{th} derivative of the output described by Eq. (4.8) to:

$$\lambda_2 \hat{y}^{(2)} = \upsilon \tag{4.40}$$

Hence the FBL control law required to linearize the DNN and to acquire the linear mapping preferred in Eq. (4.40) is of the form:

$$u = \frac{1}{\lambda_4 \mathfrak{L}_g \mathfrak{L}_f \hat{y}(\mathbf{x})} \left[\upsilon - \lambda_4 \mathfrak{L}_f^2 \hat{y} \mathbf{x} \right] \tag{4.41}$$

As discussed previously, the virtual input υ may be designed using pole placement such that:

$$\upsilon = -\lambda_1 \hat{y}^{(1)} - \lambda_0 \hat{y} + \bar{v} \tag{4.42}$$

Consequently, the actual control law will take the following form:

$$u = \frac{1}{\lambda_1 \mathfrak{L}_g \mathfrak{L}_f^1 \hat{y}(\mathbf{x})} \left[\bar{v} - \lambda_2 \mathfrak{L}_f^2 \hat{y}(\mathbf{x}) - \sum_{i=0}^{1} \lambda_{i-1} \mathfrak{L}_f^{i-1} \hat{y} \mathbf{x} \right] \tag{4.43}$$

As per Figure 4.2, multi-loop PID control can be applied with the proposed feedback linearizing control. As previously explained in section 4.2, the new virtual control input $\bar{v}$ is determined through a multi-loop PID control system described in Figure 4.2 for one of two reasons. Firstly, PID is the most widely used controller in industry and a hybrid formulation with it will be received in a more favourable light as opposed to other linear or nonlinear controllers. Secondly, it is to maintain consistency and to create an effective basis of comparison with the optimal multi-loop PID controllers that were previously used in this research project.

With regards to controller gains, there are now 9 gains to be controlled; namely the 6 PID gains of the multi-loop PID controller, and the 3 FBL controller gains $(\lambda_0, \lambda_1, \lambda_2)$. The performance index used to select this gains is the same as that of quarter-car PID-based AVSS design presented in Eq. (3.5). The process of fine tuning the intelligent controller was rather cumbersome and rigorous as very small

variations in λ_0, λ_1, and λ_2, cause a considerable variation in system response. The best gains that could be obtained through manual tuning are listed in Table 4.4.

4.6 Controller Tuning Approaches

The nine controller gains of the DNNFBL may also be tuned using optimal policies such as those implemented in the PID-based AVSS. In order to maintain consistency the controller gains are computed through PSO and DE as they were the only algorithms that produced satisfactory identification results. The initial values chosen correspond to those acquired through manual tuning. The bounds for each variable or controller gain are chosen based on the intuitive knowledge gained through rigorous manual tuning. The configurations of these policies is further summarised in Table 4.3. Figure 4.12 shows the convergence of the performance index J through the use of both the DE and PSO algorithms.

The results obtained on the migration history of the particles in the PSO and the

Table 4.3: Optimization parameters used in the selected optimization algorithms for controller tuning of the quarter-car DNNFBL controller

Routine	**DE**	**PSO**
Population Size	100	100
Stopping Criteria	100 Generations	100 Iterations
Optimization	F=2	$w_1 = 0.5$
Parameters	$CR = 0.5$	S $w_1 = 0.5$
		$w_1 = 0.5$

evolution of individuals in the DE in the controller tuning case clearly indicate that the PSO converges faster with a superior fitness value. The slower convergence of the DE is expected as DE only permits the replacement of an individual if the fitness of its respective trial individual is better. This condition slows the convergence of DE, but it is expected to produce a much better result than the other algorithms.

Similar to the DE, the PSO stores information on the best position of each particle or individual. However, unlike the DE each particle is free to move (each individual is free to change to its new trial point) without needing to satisfy the conditions of replacement implemented in the DE. This consequently produces quicker convergence than that of the DE. However, the replacement condition of the DE is

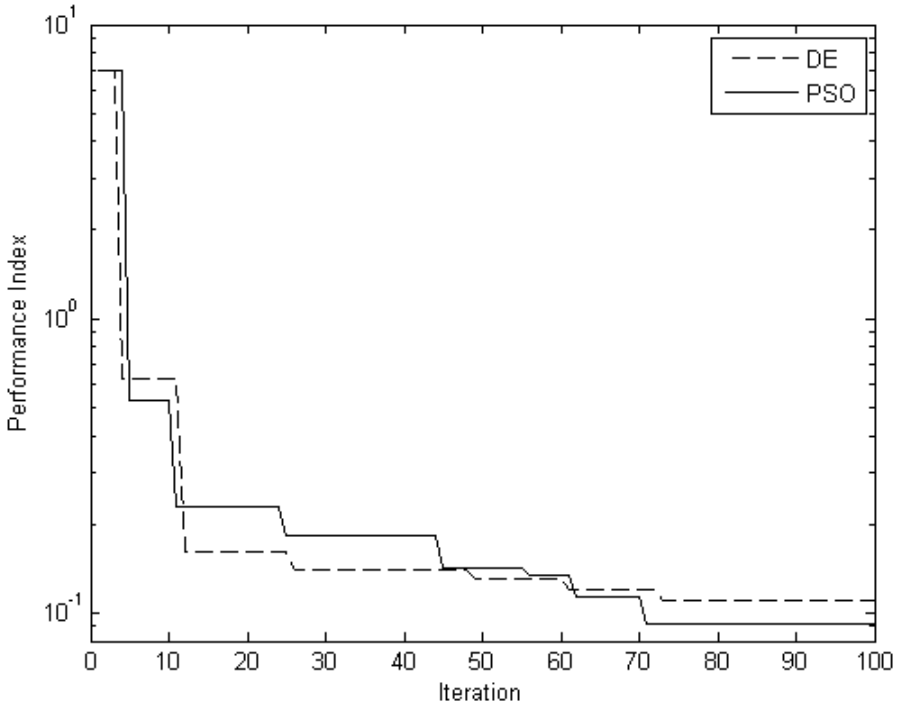

Figure 4.12: Convergence history of evolutionary algorithms used for intelligent controller tuning of the quarter-car AVSS

specifically set to prevent premature convergence towards a local minimum and is thus expected to converge to a better solution.

In contrast to the aforementioned theory, the PSO produced a better result. This may be due to one of three reasons. Firstly, the variation in the network weights values of the DNN between the DE and PSO could have had an effect on the variation in results. This is because the control law is an indirect adaptive law and is thus dependent on the weighting matrices of the DNN. Furthermore, since the PSO produced better results in the identification phase, it is expected to track the system output better and hence produce better results than that of the DE. Secondly, the success of the PSO over the DE may be attributed to the nature of this problem. Thirdly, due to the fact that the evolutionary algorithms are heuristic search methods; the PSO may have produced a better result on randomness alone. The optimal controller gains obtained for each of the algorithms are listed in Table 4.4.

Table 4.4: Controller gains acquired for the proposed DNNFBL controllers

Control Loop	**Outer Loop**			**Inner Loop**			**FBL Gains**		
Gain	K_p	K_i	K_d	k_p	k_i	k_d	λ_0	λ_1	λ_2
Manual	15000	0	0	0.001	0.002	0	0	0	0.1
DE	21500	35	3	0.001	0.0006	5×10^{-7}	0.001	0.013	0.02
PSO	23500	220	45	0.001	0.0009	3×10^{-8}	0.002	0.008	0.015

4.7 Simulation Results and Comparative Examination of Tuning Approaches

The proposed global optimization methods did indeed improve overall system performance, but there is no evidence that the conflicting performance criteria of AVSS have been resolved. Hence, each performance facet of AVSS must be investigated. Figures 4.13 to 4.17 shows the response of the DNNFBL and optimally-tuned DNNFBL systems in all aspects of suspension performance, namely suspension travel, ride comfort, road holding, power consumption and actuation force. This is done to compare the performance of the manually-tuned DNNFBL, DE-based DNNFBL and the PSO-based DNNFBL. Furthermore, the data is compared to those of the best PID-based AVSS with the aim of evaluating the performance of an intelligent controller relative to a linear PID controller. The results are further summarised in Table 4.5 as well as the bar graphs in Figures 4.18 to 4.22.

The suspension performance response (see Figures 4.13 to 4.22) was weak for the manually-tuned case which behaved only better than the uncontrolled system presented in section 3.1.4. This may be due to the intuitive approach used in manual tuning and its associated difficulty as small variations in DNNFBL gains generated a large variation in system outputs. As this tuning was rigorous, a satisfactory compromise could not be attained through manual tuning. On the other hand, global optimization-based tuning attained superior results which closely match the PID+DE case (Section 3.1.6).

These results are coherent with optimal PID control, as the use of optimal policies produced better results than the manually-tuned with a superior performance index, smoother ride comfort and better road holding and improved suspension travel. These results were obtained due to the placement of high weighting values on each

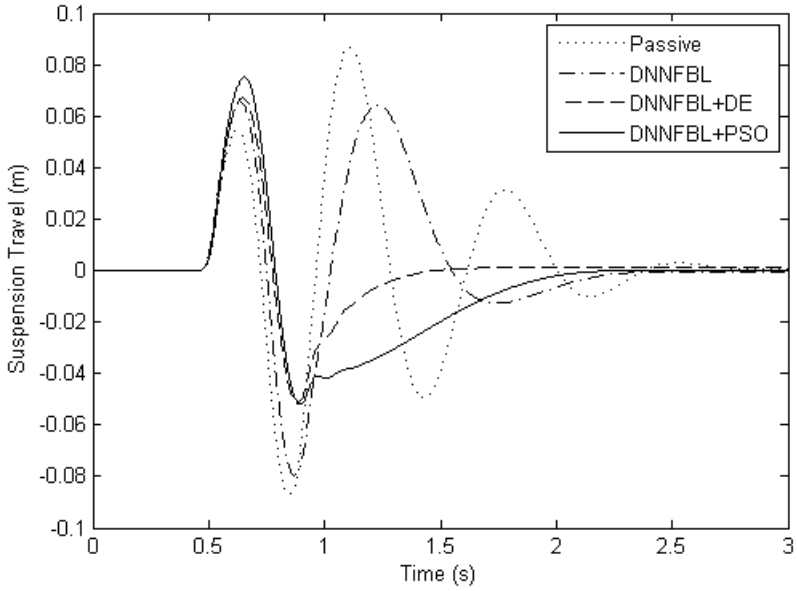

Figure 4.13: Comparison of suspension travel response for the proposed intelligent controllers

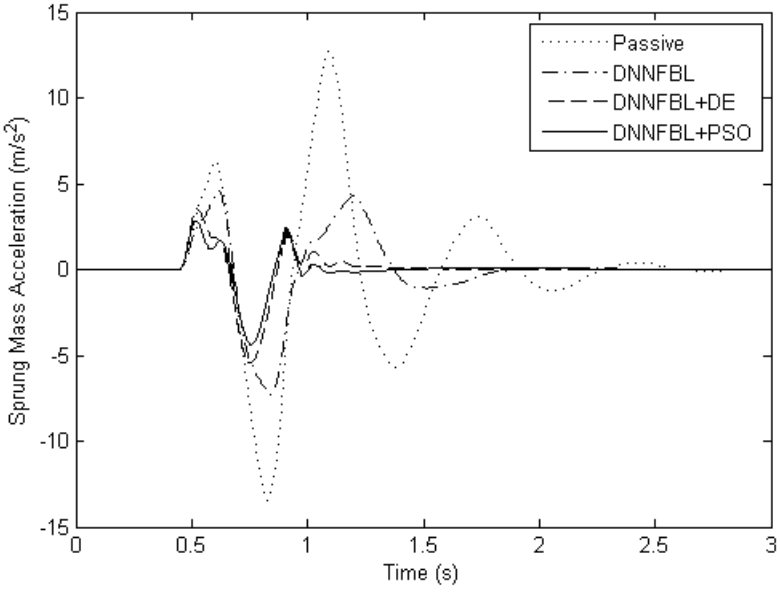

Figure 4.14: Comparison between the various controllers on the basis of ride comfort

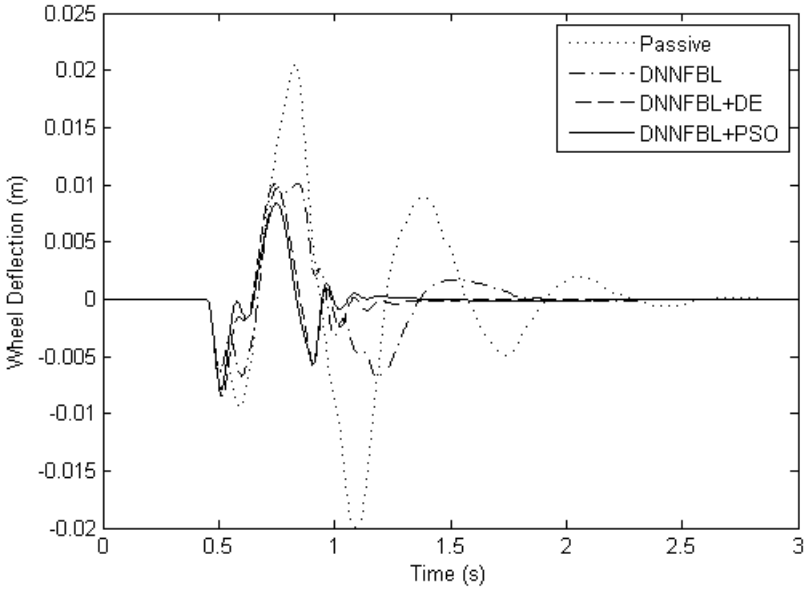

Figure 4.15: Wheel deflection characteristics obtained through the various control methodologies

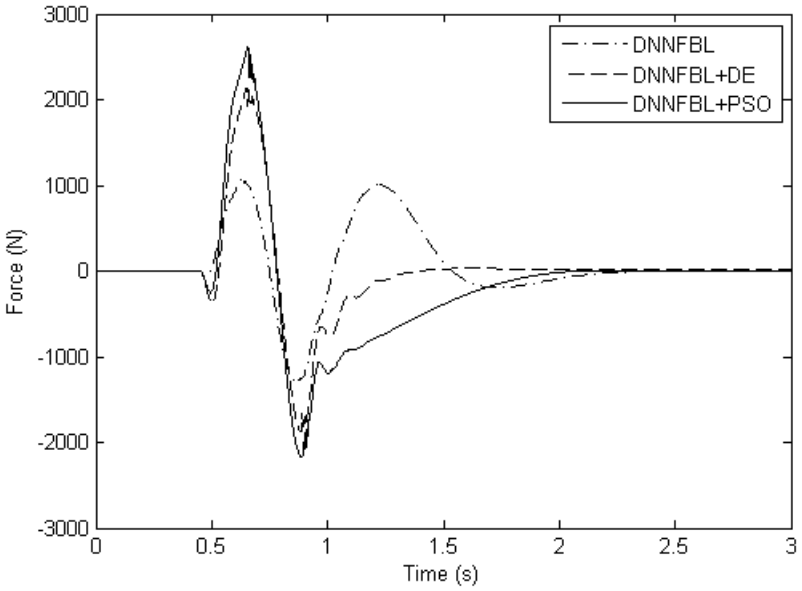

Figure 4.16: Comparison of actuation force applied between the chassis and the wheel for each case

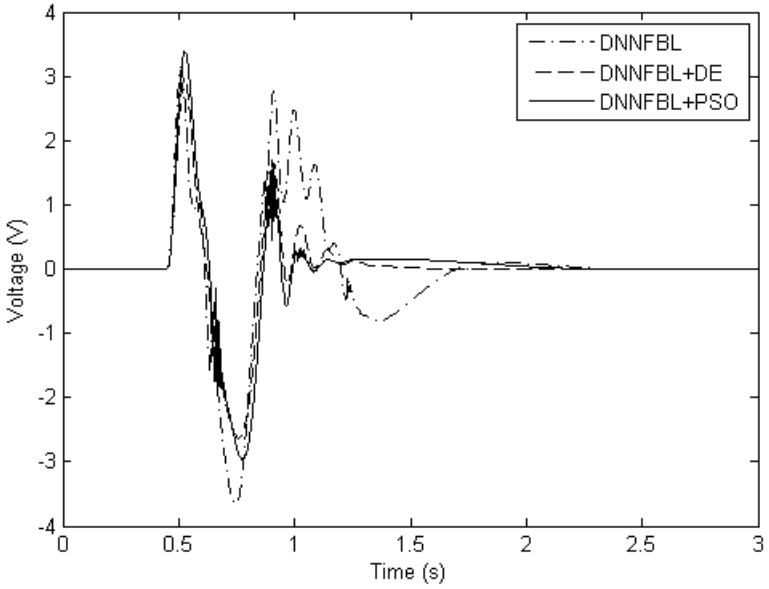

Figure 4.17: Variation of control input for each control methodology

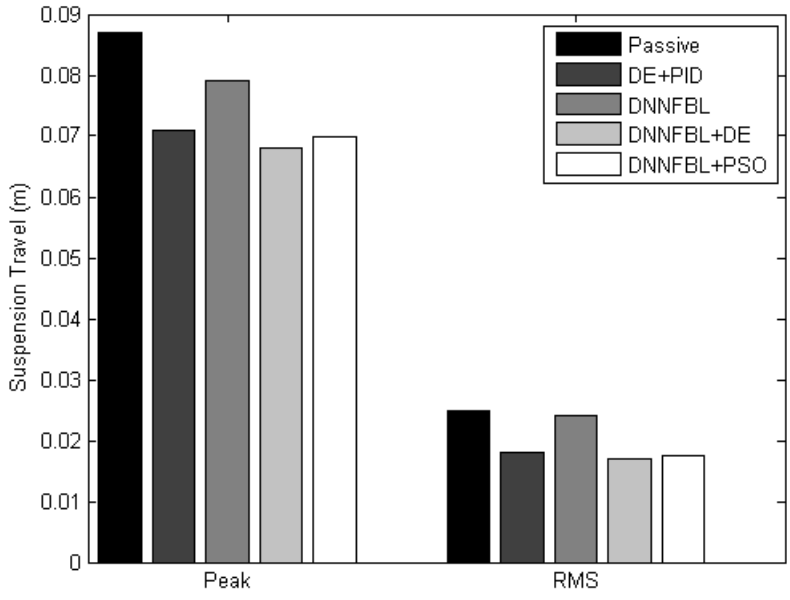

Figure 4.18: Bar graphs depicting the variation in suspension travel for each control law

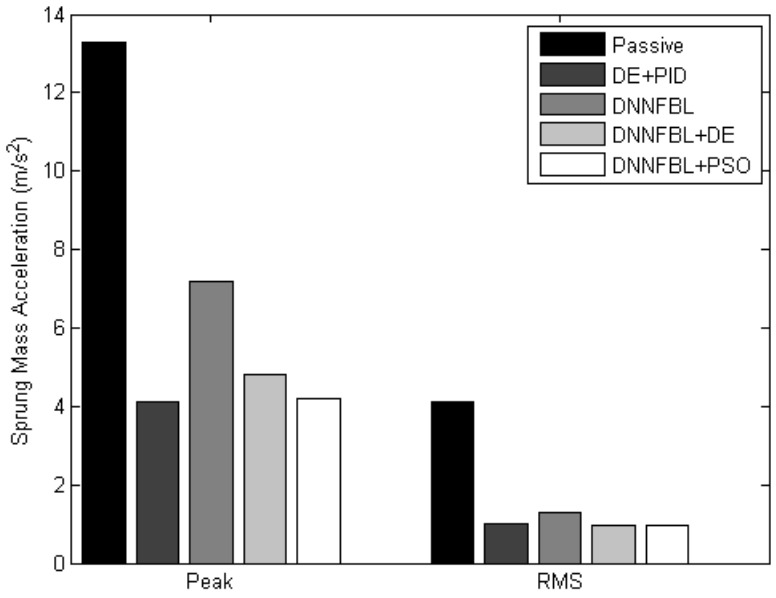

Figure 4.19: Bar graphs illustrating the difference in body-heave acceleration for the proposed controllers

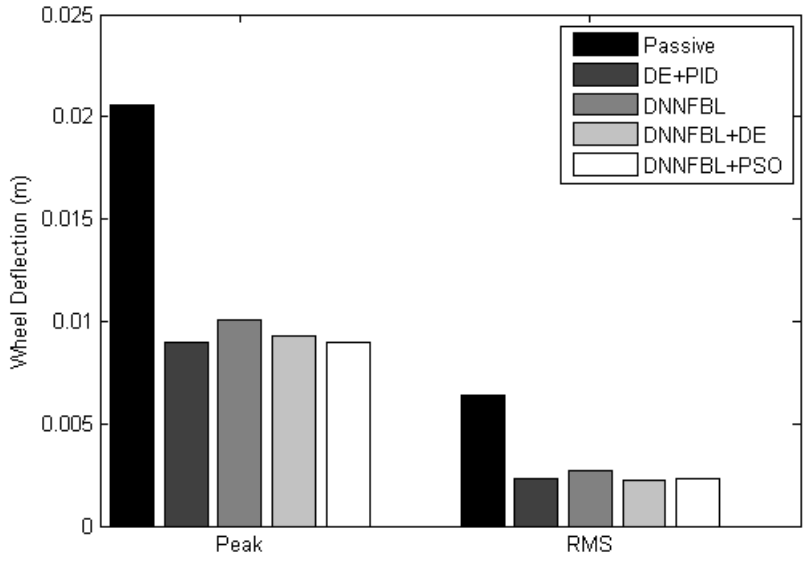

Figure 4.20: Bar graphs summarizing the road holding data for each control case

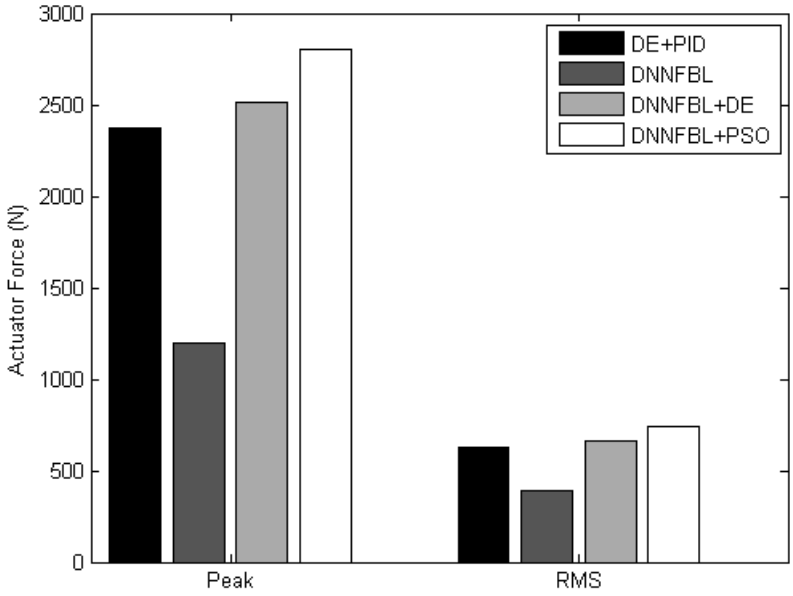

Figure 4.21: Actuator force bar graphs summarizing the results obtained for the various control schemes

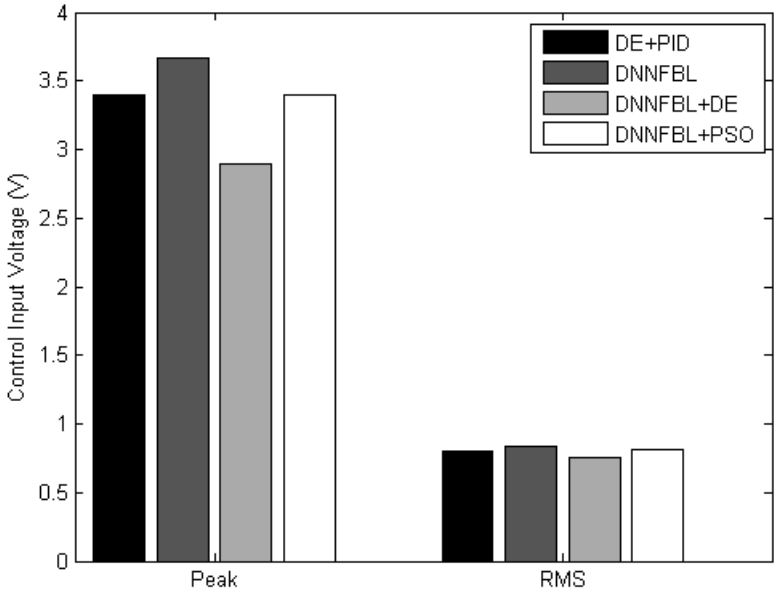

Figure 4.22: Quantitative information pertaining to the control input voltage response

Table 4.5: Summary of selected suspension performance incorporating the various optimization routines

Technique	**Suspension Travel**(m)		**Control Input Voltage**(V)	
	RMS	**Peak**	**RMS**	**Peak**
PID+DE	0.018	0.071	0.8	3.4
DNNFBL	0.024	0.079	0.84	3.67
DNNFBL+DE	0.017	0.068	0.757	2.9
DNNFBL+PSO	0.0175	0.070	0.813	3.4
Technique	**Sprung Mass Acceleration**(m/s^2)		**Force** (N)	
	RMS	**Peak**	**RMS**	**Peak**
PID+DE	0.98	4.1	631	2369
DNNFBL	1.3	7.2	386	1200
DNNFBL+DE	0.96	4.2	659	2509
DNNFBL+PSO	0.98	4.8	744	2800
Technique	**Settling Time**(s)		**Wheel Deflection**(m)	
	RMS	**Peak**	**RMS**	**Peak**
PID+DE	N/A	4.1	0.0023	0.0090
DNNFBL	N/A	2.5	0.0027	0.0101
DNNFBL+DE	N/A	2.1	0.0022	0.0093
DNNFBL+PSO	N/A	2.1	0.0023	0.0090
Performance Index J				
Passive	PID+DE	DNNFBL	DNNFBL+DE	DNNFBL+PSO
12	0.092	7	0.11	0.92

of these performance criteria in the performance index. However, as in the case of the PID-based AVSS, these advantageous results were obtained at the cost of power consumption, actuation force and peak suspension travel. This may be accredited to the very same reasons that were discussed in the PID-based AVSS design.

In relation to the performance of DNNFBL+DE controller relative to that of the PSO-based DNNFBL controller, the PSO-based case indicated a better performance index (see Figure 4.12). However, the use of PSO controller tuning only produced significantly better results in ride comfort and road holding, whereas the DE case performed marginally superior in suspension travel, actuator force and input voltage

and settling time. This further infers that the conflicting performance criteria were resolved differently through these algorithms, but it may be concluded that the PSO performed better as it reported an overall lower performance index. The lower performance index of the DE implies that the DE was either caught in a local minimum or did not fully converge due to a limited number of iterations. The variation in performance between DE and PSO may be ascribed to the same reasons that were discussed at the end of the previous subsection (section 4.4) which include: the nature of the problem, the consequent effect of the weaker DNN that was trained by DE, and the randomness characteristics on the input signal that favours the PSO-based case.

With regards to the literature and previous studies that were reported in Table 3.10, this DE and PSO-based DNNFBL outperformed previous studies of which induced weaker disturbances than the one included in this research study. They possessed better transient behaviour with quicker settling times, less chattering and fewer peaks. The ride comfort fell into a more comfortable zone as per International Organization for Standardization 2631 (2003) as compared to Amani et al. (2004). For the other counterparts from literature, the ride comfort and suspension travel of the proposed controller were worse than in the literature, but this may be attributed to the weak nature of the disturbances used in those investigations.

4.8 System Robustness to Parameter Variations and Frequency-Domain Analysis

In order to analyse the system robustness to parameter variations, certain system parameters of the system will be altered in a realistic manner. This is done in exactly the same way as that of the PID-based AVSS (see section 3.2.6), where vehicle mass, tyre stiffness and vehicle speed are altered by 20%. These results are plotted in Figures 4.23 and 4.24.

From the parameter sensitivity plots, it is evident that the steady-state error increases as the parameter is varied more extensively. Variation in system mass had the most detrimental impact on the steady-state error followed by the variation in speed and tyre load respectively. However, the system remained BIBO stable to acceptable limits and hence the performance of the controller may be deemed successful.

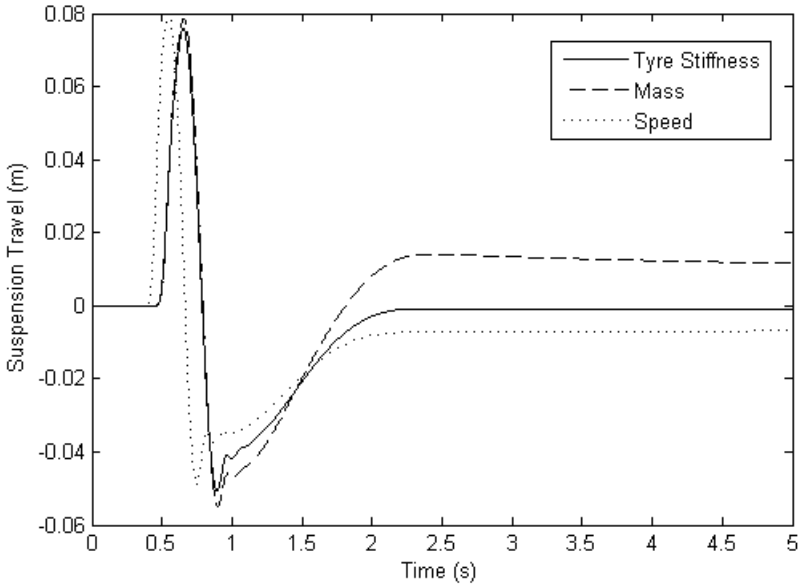

Figure 4.23: Suspension travel response for a +20% variation in selected parameters

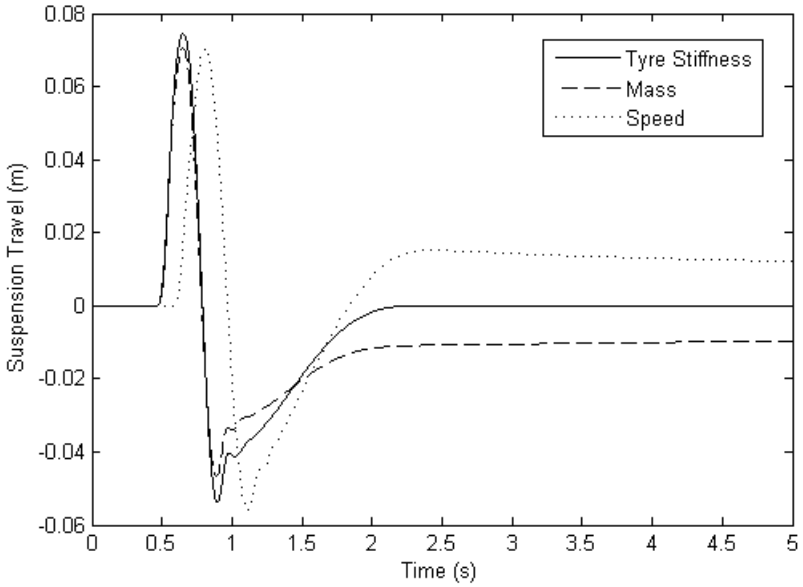

Figure 4.24: Suspension travel response to -20% variation in selected parameters

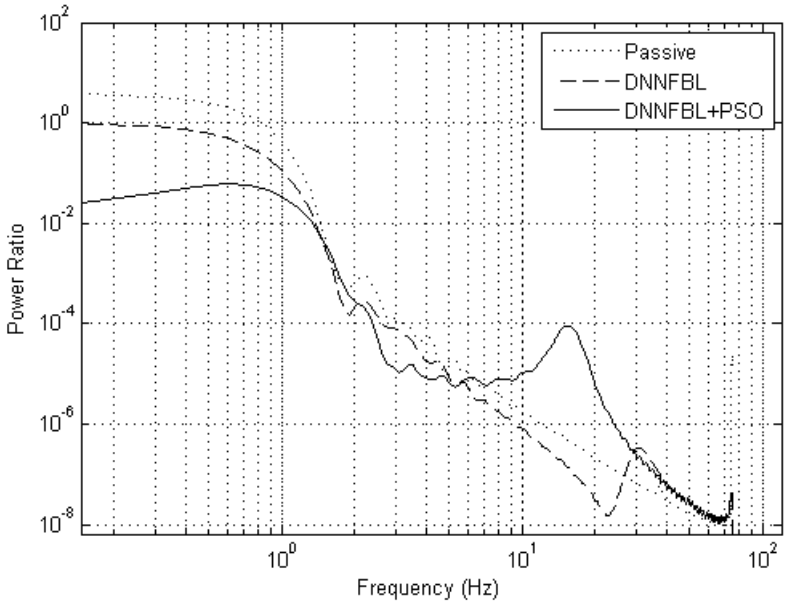

Figure 4.25: Ride comfort frequency response of the proposed intelligent controllers

The frequency responses of the system in terms of ride comfort and road holding are presented in Figures 4.25 and 4.26 respectively. As in the case of the quarter-car PID-controlled system, the intelligent controller exhibited its worst behaviour when subjected to low frequencies ranging from 0.1Hz to 0.8Hz. Both the optimized and non-optimized controllers improved upon the passive system in this range with the optimal-based controller producing considerably lower body-heave accelerations. At higher frequencies all signals were attenuated to a desirable degree with the non-optimal intelligent controller producing better results than the passive system up until 20Hz, after which it displayed a resonant peak. In contrast, the optimal controller experienced a resonance peak earlier at 8Hz and behaved the weakest at these high frequencies.

The road holding properties shown in frequency-domain bear similar resemblance to a high-pass filter, where the weakest road holding characteristics were observed at low frequencies. The proposed intelligent controllers indicated better road holding properties than that of the passive system at lower frequencies with the optimal controller being slightly better. At higher frequencies each system performed more or less similary and were each able to drastically attenuate high frequency signals. The fact that the proposed controller schemes generated both improved road holding and ride comfort than that of the passive system in the more sensitive low frequency range implies that the intelligent controllers were successful in finding a better compromise to these conflicting performance criteria than that of the passive system. Moreover, the improved response of the optimal intelligent controller concludes that

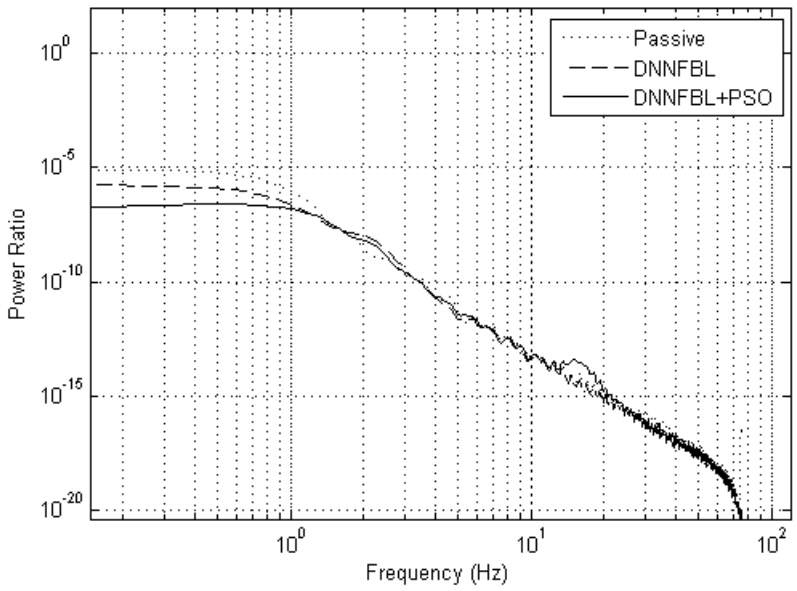

Figure 4.26: Road holding frequency response of the proposed intelligent controllers

optimization algorithms such as DE, GA and PSO does indeed play a significant role in improving the AVSS overall performance.

4.9 Comparison Study on PID and Intelligent Controllers

Comparison of the best intelligent controller to that of the best optimal linear controller (PID+DE) presented in section 3.1, shows that both controllers have an edge over the other each other in various aspects. Firstly, the linear control law produced quicker settling time and consequently better RMS values for suspension travel and actuation force. This behaviour is anticipated as the intelligent control is adaptive by nature and transmits control inputs that is function of the neural network output, which is always greater than zero until the system comes to rest. This neuro-control contribution remains considerably high for a significant period after the disturbance is removed and this tends to increase the settling time of the system.

However, the intelligent controller contained a much lower degree of chattering than the linear control law and this consequently gave it superior ride comfort where it fell in a much more comfortable region of the International Organization for Standardization 2631 (2003) standards. The road holding and control input voltage was better as well. The intelligent controller maintained a lower degree of chattering,

which is desirable as less chattering is less likely to cause actuator and motor failure, will produce better forward acceleration if the tyre deflection does not oscillate extensively [Gillespie (1992)] and provide a more comfortable ride as the system dampens out more smoothly. Additionally, the suspension travel output for variations in selected vehicle parameters generated a significantly lower steady-state error that its counterpart with less chattering. This infers that the intelligent controller contained a superior sensitivity to parameter variations than that of the PID controller.

The degree of the steady-state error was better for the intelligent controller, where an increase in speed did not result in further oscillations as in the case of the PID+DE case. Furthermore, lower steady-state errors were reported for the case of the intelligent controller. These results highlight that intelligent controllers have an improved sensitivity to parameter variations than linear controllers such as PID. Such behaviour is in agreement with literature and this further justifies the effectiveness of the proposed intelligent controller.

4.10 Summary

The proposed method of training dynamic neural networks through heuristic search algorithms was successful when implementing PSO and DE, but was ineffective when using CRS, GA and PS. The indirect adaptive DNNFBL control methodology proved more challenging to tune manually and hence as a result produced weaker results than the benchmark manually-tuned PID case. However, the implementation of random search methods such as PSO and DE overcame this drawback with both producing better response than the PID in all aspects of the AVSS performance and was able to find a better compromise in conflicting performance criteria than the passive and PID cases. The intelligent controller remained BIBO stable for a range of parameter variations. It possessed better signal attenuation properties than those of the passive system within aspects of road holding and ride comfort.

5 Dynamic Neural Network-Based Feedback Linearization Control of a Nonlinear Full-Car Electrohydraulic Vehicle Suspension System

Intelligent control of the full-car model is considerably complex as compared to the quarter-car model because the system is now a multi-input multi-output system (MIMO) as opposed to the single-input single-output (SISO) configuration of the quarter-car model. Additionally, there is coupling between system inputs and outputs, and this increases the difficultly in both learning the system dynamics as well as deriving a suitable control law. Nevertheless, an indirect adaptive DNN-based feedback linearization technique that was performed for the quarter-car model will be employed here as well as it has proven to be successful for MIMO systems [Garces et al. (2003)].

The controller basically works by primarily creating a linear mapping between the virtual inputs $\boldsymbol{v}$ and the system outputs $\mathbf{y}$. This linear relationship is created by an intelligent dynamic neural network based feedback linearizing controller DNNFBL. This controller operates by training a dynamic neural network (DNN) to learn the nonlinear mapping between the actual control inputs $\mathbf{u}$ and the output $\mathbf{y}$ of the AVSS. Thereafter, a feedback linearization law is applied to the DNN to determine a feedback law that will approximate a linear mapping between the virtual control input $\boldsymbol{v}$ and the system outputs y, and to simultaneously decouple the system. The DNNFBL control is combined with the multi-loop PID control scheme previously utilized in PID-based AVSS with the intention of attaining superior performance. Furthermore, the performance index is computed and fed into an optimization algorithm which computes the optimal controller gains. A schematic of the proposed control system is shown in Figure 5.1. The aim of the proposed controller is twofold. The first is to learn the dynamics of the plant with a DNN model through a global

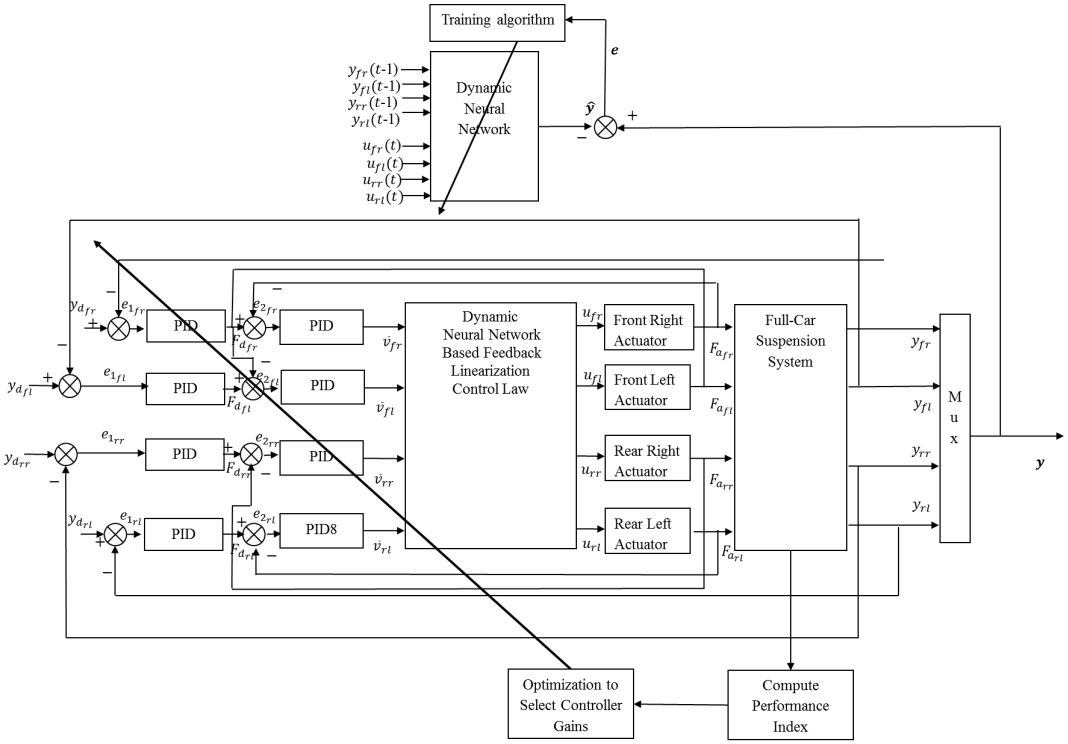

Figure 5.1: Schematic of the proposed full-car indirect adaptive intelligent controller

optimization-based learning algorithm. Subsequently, the second objective is to create a control based on the DNN model that creates a decoupled system and a linear mapping between the virtual system inputs **V** and the system outputs **O**. With this achieved, linear controllers such as PID controllers can be incorporated to acquire desired system performance.

This section begins with an analysis of the system to verify that it is indeed input-output feedback linearizable as well as stable under such a control method. Later, a detailed development of the DNN is presented, followed by the formulation of the control law. Thereafter, methods for controller tuning are explained, and afterwards the simulation results and discussion are drawn up. This chapter concludes with a comparative analysis between the intelligent controller and the best optimal PID controller, and a brief summary is given at the end of the chapter.

5.1 Input-output Linearization of Full-car AVSS

Before DNN-based feedback linearization may be performed, it is necessary to ensure that the full-car system is both input-output feedback linearizable and input-state

stable. To perform these tests, the relative degree r_{ij} of each suspension system output y_{ij} needs to be computed, with subscripts i, j denoting the longitudanal (front f or rear r) and lateral (left l and right r) positions of each suspension system respectively. To recap, relative degree basically indicates how many times the output y_{ij} needs to be differentiated with respect to time to have at least one of the systems inputs u_{ij} explicitly appearing. Conversely, it may be also interpreted as the number of times the control input u_{ij} to the i, j^{th} suspension system has to be integrated to reach the output y_{ij}. For the system to be input-output feedback linearizable, the following condition must be satisfied:

- The relative degree r_{ij} of each output y_{ij} must be less than the number of system states P. i.e.: $r_{ij} \leq P$.

Before the stability study is performed, the system inputs and outputs need to be defined. The control inputs are the voltages supplied into the front right, front left, rear right and rear left hydraulic actuators $(u_{fr}, u_{fl}, u_{rr}, u_{rl})$. Suspension travels at each wheel are chosen as the system outputs as suspension travel is the fundamental property that governs suspension dynamics. Hence, the outputs y_{fr}, y_{fl}, y_{rr} and y_{rl} are given by:

$$h_{fr}(\mathbf{x}) = y_{fr} = x_1 - (x_{17} - l_f \sin x_{19} + a_f/2 \sin x_{21}) \tag{5.1}$$

$$h_{fl}(\mathbf{x}) = y_{fl} = x_5 - (x_{17} - l_f \sin x_{19} - a_f/2 \sin x_{21}) \tag{5.2}$$

$$h_{rr}(\mathbf{x}) = y_{rr} = x_9 - (x_{17} + l_f \sin x_{19} + a_f/2 \sin x_{21}) \tag{5.3}$$

$$h_{rl}(\mathbf{x}) = y_{rl} = x_{13} - (x_{17} + l_f \sin x_{19} - a_f/2 \sin x_{21}) \tag{5.4}$$

As the definition explains, the relative degree of the system is determined by continuously taking the time derivative of the output y_{ij} until a corresponding r^{th} derivative of that output y_{ij}^r is explicitly a function of at least one of the system inputs u_{ij} such that:

$$y_{ij}^r = a_{ij}(\mathbf{x}) + b_{ij}(\mathbf{x}) u_{ij} \tag{5.5}$$

where $a_{ij}(\mathbf{x})$ and $b_{ij}(\mathbf{x})$ are nonlinear functions that have been produced as a consequence of the above computation. Moreover, the resulting dynamics of the coupled nonlinear system may be expressed in matrix form as [Ha and Gilbert (1986)]:

$$\mathbf{y}_{ij}^r = f(\mathbf{x}, \mathbf{u}) = \mathbf{A}(\mathbf{x}) + \mathbf{B}(\mathbf{x})\mathbf{u} \tag{5.6}$$

where $\mathbf{A}(\mathbf{x})$ is the characteristic matrix, vector $\mathbf{y}^r$ is the respective derivative of the outputs at which one of the system input explicitly appears, $\mathbf{u}$ is the input vector containing all the system inputs, and $\mathbf{B}(\mathbf{x})$ is the coupling between system states

and system inputs.

The first derivative of the system outputs $y_{ij}^{(1)}$ which are described through state-space form given in Eqs. (2.51) to (2.86) is determined as follows:

$$\begin{aligned} y_{ij}^{(1)} &= \frac{\partial y_{ij}}{\partial t} = \frac{\partial y_{ij}}{\partial \mathbf{x}} \frac{\partial \mathbf{x}}{\partial t} = \frac{\partial h_{ij}(\mathbf{x})}{\partial x} \dot{\mathbf{x}} \\ &= \frac{\partial h_{ij}}{\partial \mathbf{x}} \left[f(\mathbf{x}) + g_{fr}(\mathbf{x}) u_{fr} + g_{fl}(\mathbf{x}) u_{fl} + g_{rr}(\mathbf{x}) u_{rr} + g_{rl}(\mathbf{x}) u_{rl} \right] \\ &= \mathfrak{L}_f h_{ij}(\mathbf{x}) + \mathfrak{L}_{g_{fr}} h_{fr}(\mathbf{x}) u_{fr} + \mathfrak{L}_{g_{fl}} h_{fl}(\mathbf{x}) u_{fl} \\ &\quad + \mathfrak{L}_{g_{rr}} h_{rr}(\mathbf{x}) u_{rr} + \mathfrak{L}_{g_{rl}} h_{rl}(\mathbf{x}) u_{rl} \end{aligned} \tag{5.7}$$

Therefore:

$$\begin{aligned} y_{fr}^{(1)} &= \mathfrak{L}_f h_{fr}(\mathbf{x}) + \sum \mathfrak{L}_{g_{ij}} h_{fr}(\mathbf{x}) u_{ij} = x_2 - (x_{18} - l_f x_{20} \cos x_{19} + a_f/2 x_{22} \cos x_{21}) \\ &= \mathfrak{L}_f h_{fr}(\mathbf{x}) \end{aligned} \tag{5.8}$$

$$\begin{aligned} y_{fl}^{(1)} &= \mathfrak{L}_f h_{fl}(\mathbf{x}) + \sum \mathfrak{L}_{g_{ij}} h_{fl}(\mathbf{x}) u_{ij} = x_6 - (x_{18} - l_f x_{20} \cos x_{19} - a_f/2 x_{22} \cos x_{21}) \\ &= \mathfrak{L}_f h_{fl}(\mathbf{x}) \end{aligned} \tag{5.9}$$

$$\begin{aligned} y_{rr}^{(1)} &= \mathfrak{L}_f h_{rr}(\mathbf{x}) + \sum \mathfrak{L}_{g_k} h_{rr}(\mathbf{x}) u_{ij} = x_{10} - (x_{18} + l_f x_{20} \cos x_{19} + a_f/2 x_{22} \cos x_{21}) \\ &= \mathfrak{L}_f h_{rr}(\mathbf{x}) \end{aligned} \tag{5.10}$$

$$\begin{aligned} y_{rl}^{(1)} &= \mathfrak{L}_f h_{rl}(\mathbf{x}) + \sum \mathfrak{L}_{g_{ij}} h_{rl}(\mathbf{x}) u_{ij} = x_{14} - (x_{18} + l_f x_{20} \cos x_{19} - a_f/2 x_{22} \cos x_{21}) \\ &= \mathfrak{L}_f h_{rl}(\mathbf{x}) y_{ij} \end{aligned} \tag{5.11}$$

where $\mathbf{f}(\mathbf{x})$, $\mathbf{g}(\mathbf{x})$ and $\mathbf{u}$ are the full-car system matrices described in Eq. (2.51) to (2.86).$\frac{\partial h_{ij}}{\partial x} f(\mathbf{x})$ is defined as $\mathfrak{L}_f h_{ij}(\mathbf{x})$, which is referred to as the Lie derivative of output h_{ij} along $\mathbf{f}$. For the first derivative of the outputs, $\mathfrak{L}_g h_{ij}(\mathbf{x})$ (x) was zero, which subsequently infers that $y_{fr}^{(1)}$, $y_{fl}^{(1)}$, $y_{rr}^{(1)}$, and $y_{rl}^{(1)}$ are not explicitly dependent on any of the system inputs u_{fr}, u_{fl}, u_{rr} or u_{rl}.

Therefore, computation of the latter derivative is carried out and this yields:

$$\begin{aligned} y_{ij}^{(2)} &= \frac{\partial^2 y_{ij}}{\partial t^2} = \frac{\partial \frac{\partial y_{ij}}{\partial t}}{\partial \mathbf{x}} \frac{\partial \mathbf{x}}{\partial t} = \frac{\partial \mathfrak{L}_f h_{ij}(\mathbf{x})}{\partial x} \dot{\mathbf{x}} \\ &= \frac{\partial \mathfrak{L}_f h_{ij}(\mathbf{x})}{\partial \mathbf{x}} \left[f(\mathbf{x}) + g_{fr}(\mathbf{x}) u_{fr} + g_{fl}(\mathbf{x}) u_{fl} + g_{rr}(\mathbf{x}) u_{rr} + g_{rl}(\mathbf{x}) u_{rl} \right] \\ &= \mathfrak{L}_f^2 h_{ij}(\mathbf{x}) + \mathfrak{L}_{g_{fr}} \mathfrak{L}_f h_{fr}(\mathbf{x}) u_{fr} + \mathfrak{L}_{g_{fl}} \mathfrak{L}_f h_{fl}(\mathbf{x}) u_{fl} \\ &\quad + \mathfrak{L}_{g_{rr}} \mathfrak{L}_f h_{rr}(\mathbf{x}) u_{rr} + \mathfrak{L}_{g_{rl}} \mathfrak{L}_f h_{rl}(\mathbf{x}) u_{rl} \end{aligned} \tag{5.12}$$

$$
\begin{aligned}
y_{fr}^{(2)} &= \mathfrak{L}_f^2 h_{fr}(\mathbf{x}) + \sum \mathfrak{L}_{g_{ij}} \mathfrak{L}_f h_{fr}(\mathbf{x}) u_{ij} \\
&= \frac{\partial x_2 - (x_{18} - l_f x_{20} \cos x_{19} + a_f/2 x_{22} \cos x_{21})}{\partial t} \\
&= \mathfrak{L}_f^2 h_{fr}(\mathbf{x}) \qquad (5.13)
\end{aligned}
$$

$$
\begin{aligned}
y_{fl}^{(2)} &= \mathfrak{L}_f^2 h_{fl}(\mathbf{x}) + \sum \mathfrak{L}_{g_{ij}} \mathfrak{L}_f h_{fl}(\mathbf{x}) u_{ij} \\
&= \frac{\partial x_6 - (x_{18} - l_f x_{20} \cos x_{19} - a_f/2 x_{22} \cos x_{21})}{\partial t} \\
&= \mathfrak{L}_f^2 h_{fl}(\mathbf{x}) \qquad (5.14)
\end{aligned}
$$

$$
\begin{aligned}
y_{rr}^{(2)} &= \mathfrak{L}_f^2 h_{rr}(\mathbf{x}) + \sum \mathfrak{L}_{g_{ij}} \mathfrak{L}_f h_{rr}(\mathbf{x}) u_{ij} \\
&= \frac{\partial x_{10} - (x_{18} + l_f x_{20} \cos x_{19} + a_f/2 x_{22} \cos x_{21})}{\partial t} \\
&= \mathfrak{L}_f^2 h_{rr}(\mathbf{x}) \qquad (5.15)
\end{aligned}
$$

$$
\begin{aligned}
y_{rl}^{(2)} &= \mathfrak{L}_f^2 h_{rl}(\mathbf{x}) + \sum \mathfrak{L}_{g_{ij}} \mathfrak{L}_f h_{rl}(\mathbf{x}) u_{ij} \\
&= \frac{\partial x_{14} - (x_{18} + l_f x_{20} \cos x_{19} - a_f/2 x_{22} \cos x_{21})}{\partial t} \\
&= \mathfrak{L}_f^2 h_{rl}(\mathbf{x}) \qquad (5.16)
\end{aligned}
$$

Again, the second derivative of each output $y_{ij}^{(2)}$ is not explicitly dependent on any of the control inputs u_{fr}, u_{fl}, u_{rr} or u_{rl}. Computation of the succeeding derivative produces:

$$
\begin{aligned}
y_{ij}^{(3)} &= \frac{\partial^3 y_{ij}}{\partial t^3} = \frac{\partial \frac{\partial^2 y_{ij}}{\partial t^2}}{\partial \mathbf{x}} \frac{\partial \mathbf{x}}{\partial t} = \frac{\partial \mathfrak{L}_f^2 h_{ij}(\mathbf{x})}{\partial x} \dot{\mathbf{x}} \\
&= \frac{\partial \mathfrak{L}_f^2 h_{ij}(\mathbf{x})}{\partial \mathbf{x}} \left[f(\mathbf{x}) + g_{fr}(\mathbf{x}) u_{fr} + g_{fl}(\mathbf{x}) u_{fl} + g_{rr}(\mathbf{x}) u_{rr} + g_{rl}(\mathbf{x}) u_{rl} \right] \\
&= \mathfrak{L}_f^3 h_{ij}(\mathbf{x}) + \mathfrak{L}_{g_{fr}} \mathfrak{L}_f^2 h_{fr}(\mathbf{x}) u_{fr} + \mathfrak{L}_{g_{fl}} \mathfrak{L}_f^2 h_{fl}(\mathbf{x}) u_{fl} \\
&\quad + \mathfrak{L}_{g_{rr}} \mathfrak{L}_f^2 h_{rr}(\mathbf{x}) u_{rr} + \mathfrak{L}_{g_{rl}} \mathfrak{L}_f^2 h_{rl}(\mathbf{x}) u_{rl} \qquad (5.17)
\end{aligned}
$$

$$
\begin{aligned}
y_{fr}^{(3)} &= \mathfrak{L}_f^3 h_{fr}(\mathbf{x}) + \sum \mathfrak{L}_{g_{ij}} \mathfrak{L}_f^2 h_{fr}(\mathbf{x}) u_{ij} \\
&= \frac{\partial^3 x_2 - (x_{18} - l_f x_{20} \cos x_{19} + a_f/2 x_{22} \cos x_{21})}{\partial t^3} \\
&= \mathfrak{L}_f^3 h_{fr}(\mathbf{x}) \qquad (5.18)
\end{aligned}
$$

$$
\begin{aligned}
y_{fl}^{(3)} &= \mathfrak{L}_f^3 h_{fl}(\mathbf{x}) + \sum \mathfrak{L}_{g_{ij}} \mathfrak{L}_f^2 h_{rr}(\mathbf{x}) u_{ij} \\
&= \frac{\partial^3 x_6 - (x_{18} - l_f x_{20} \cos x_{19} - a_f/2 x_{22} \cos x_{21})}{\partial t^3} \\
&= \mathfrak{L}_f^3 h_{fl}(\mathbf{x}) \qquad (5.19)
\end{aligned}
$$

$$
\begin{aligned}
y_{rr}^{(3)} &= \mathfrak{L}_f^3 h_{rr}(\mathbf{x}) + \sum \mathfrak{L}_{g_{ij}} \mathfrak{L}_f^2 h_{rr}(\mathbf{x}) u_{ij} \\
&= \frac{\partial^3 x_{10} - (x_{18} + l_f x_{20} \cos x_{19} + a_f/2 x_{22} \cos x_{21})}{\partial t^3} \\
&= \mathfrak{L}_f^3 h_{rr}(\mathbf{x}) \qquad (5.20)
\end{aligned}
$$

$$
\begin{aligned}
y_{rl}^{(3)} &= \mathfrak{L}_f^3 h_{rl}(\mathbf{x}) + \sum \mathfrak{L}_{g_{ij}} \mathfrak{L}_f^2 h_{rl}(\mathbf{x}) u_{ij} \\
&= \frac{\partial^3 x_{14} - (x_{18} + l_f x_{20} \cos x_{19} - a_f/2 x_{22} \cos x_{21})}{\partial t^3} \\
&= \mathfrak{L}_f^3 h_{rl}(\mathbf{x}) \qquad (5.21)
\end{aligned}
$$

Once more, the third derivative of each of the system outputs $y_{fr}^{(3)}$, $y_{fl}^{(3)}$, $y_{rr}^{(3)}$ and $y_{rl}^{(3)}$ is also independent of any of the system inputs u_{fr}, u_{fl}, u_{rr} and u_{rl} as $\mathfrak{L}_{g_j} \mathfrak{L}_f^2 h_j(\mathbf{x}) u_j = 0$. The subsequent derivative of the outputs generates:

$$
\begin{aligned}
y_{ij}^{(4)} &= \frac{\partial^4 y_{ij}}{\partial t^4} = \frac{\partial \frac{\partial^3 y_{ij}}{\partial t^3}}{\partial \mathbf{x}} \frac{\partial \mathbf{x}}{\partial t} = \frac{\partial \mathfrak{L}_f^3 h_{ij}(\mathbf{x})}{\partial x} \dot{\mathbf{x}} \\
&= \frac{\partial \mathfrak{L}_f^3 h_{ij}(\mathbf{x})}{\partial \mathbf{x}} \left[f(\mathbf{x}) + g_{fr}(\mathbf{x}) u_{fr} + g_{fl}(\mathbf{x}) u_{fl} + g_{rr}(\mathbf{x}) u_{rr} + g_{rl}(\mathbf{x}) u_{rl} \right] \\
&= \mathfrak{L}_f^4 h_{ij}(\mathbf{x}) + \mathfrak{L}_{g_{fr}} \mathfrak{L}_f^4 h_{fr}(\mathbf{x}) u_{fr} + \mathfrak{L}_{g_{fl}} \mathfrak{L}_f^3 h_{fl}(\mathbf{x}) u_{fl} \\
&+ \mathfrak{L}_{g_{rr}} \mathfrak{L}_f^3 h_{rr}(\mathbf{x}) u_{rr} + \mathfrak{L}_{g_{rl}} \mathfrak{L}_f^3 h_{rl}(\mathbf{x}) u_{rl} \qquad (5.22)
\end{aligned}
$$

$$y_{fr}^{(4)} = \mathfrak{L}_f^4 h_{fr}(\mathbf{x}) + \sum \mathfrak{L}_{g_{ij}} \mathfrak{L}_f^3 h_{fr}(\mathbf{x}) u_{ij} \qquad (5.23)$$

$$y_{fl}^{(4)} = \mathfrak{L}_f^4 h_{fl}(\mathbf{x}) + \sum \mathfrak{L}_{g_{ij}} \mathfrak{L}_f^3 h_{fl}(\mathbf{x}) u_{ij} \qquad (5.24)$$

$$y_{rr}^{(4)} = \mathfrak{L}_f^4 h_{rr}(\mathbf{x}) + \sum \mathfrak{L}_{g_{ij}} \mathfrak{L}_f^3 h_{rr}(\mathbf{x}) u_{ij} \qquad (5.25)$$

$$y_{rl}^{(4)} = \mathfrak{L}_f^4 h_{rl}(\mathbf{x}) + \sum \mathfrak{L}_{g_{ij}} \mathfrak{L}_f^3 h_{rl}(\mathbf{x}) u_{ij} \qquad (5.26)$$

However, the fourth derivatives of the system outputs $y_{fr}^{(4)}$, $y_{fl}^{(4)}$, $y_{rr}^{(4)}$, and $y_{rl}^{(4)}$ are explicitly a function of one of the system inputs u_{ij}. Thus, the nonlinear dynamics of the full-car system may be expressed in terms of the control inputs and the characteristic matrix $\mathbf{A}(\mathbf{x})$ as follows [Ha and Gilbert (1986) and Garces et al. (2003)]:

$$\mathbf{y}^4 = f(\mathbf{x}, \mathbf{u}) = \mathbf{A}(\mathbf{x}) + \mathbf{B}(\mathbf{x})\mathbf{u} \qquad (5.27)$$

with:

$$
\mathbf{A}(\mathbf{x}) = \begin{bmatrix}
\mathfrak{L}_f^4 h_{fr}(\mathbf{x}) & \mathfrak{L}_f^4 h_{fr}(\mathbf{x}) & \mathfrak{L}_f^4 h_{fr}(\mathbf{x}) & \mathfrak{L}_f^4 h_{fr}(\mathbf{x}) \\
\mathfrak{L}_f^4 h_{fl}(\mathbf{x}) & \mathfrak{L}_f^4 h_{fl}(\mathbf{x}) & \mathfrak{L}_f^4 h_{fl}(\mathbf{x}) & \mathfrak{L}_f^4 h_{fl}(\mathbf{x}) \\
\mathfrak{L}_f^4 h_{rr}(\mathbf{x}) & \mathfrak{L}_f^4 h_{rr}(\mathbf{x}) & \mathfrak{L}_f^4 h_{rr}(\mathbf{x}) & \mathfrak{L}_f^4 h_{rr}(\mathbf{x}) \\
\mathfrak{L}_f^4 h_{rl}(\mathbf{x}) & \mathfrak{L}_f^4 h_{rl}(\mathbf{x}) & \mathfrak{L}_f^4 h_{rl}(\mathbf{x}) & \mathfrak{L}_f^4 h_{rl}(\mathbf{x})
\end{bmatrix} \qquad (5.28)
$$

$$
\mathbf{B}(\mathbf{x}) = \begin{bmatrix} y_{fr}^{(4)} \\ y_{fl}^{(4)} \\ y_{rr}^{(4)} \\ y_{rl}^{(4)} \\ r_{fl} \end{bmatrix} == \begin{bmatrix}
\mathfrak{L}_f^4 h1(\mathbf{x}) + \sum \mathfrak{L}_{g_{ij}} \mathfrak{L}_f^3 h_{fr}(\mathbf{x}) \\
\mathfrak{L}_f^4 h2(\mathbf{x}) + \sum \mathfrak{L}_{g_{ij}} \mathfrak{L}_f^3 h_{fl}(\mathbf{x}) \\
\mathfrak{L}_f^4 h3(\mathbf{x}) + \sum \mathfrak{L}_{g_{ij}} \mathfrak{L}_f^3 h_{rr}(\mathbf{x}) \\
\mathfrak{L}_f^4 h4(\mathbf{x}) + \sum \mathfrak{L}_{g_{ij}} \mathfrak{L}_f^3 h_{rl}(\mathbf{x})
\end{bmatrix} \qquad (5.29)
$$

Moreover, the vector of relative degrees is given as:

$$\mathbf{r} = \begin{bmatrix} r_{fr} & r_{fl} & r_{rr} & r_{rl} \end{bmatrix} = \begin{bmatrix} 4 & 4 & 4 & 4 \end{bmatrix} \qquad (5.30)$$

where r_{fr}, r_{fl}, r_{rr}, and r_{rl} are the relative degrees of output y_{fr}, y_{fl}, y_{rr}, and y_{rl} respectively. Since the relative degree of system is less than the number of system states ($r \leq P$), the system is input-output linearizable. As in the case of intelligent quarter-car control, the system coordinate system may be transformed into a new differential homeomorphic coordinate system which is described by Eq. (5.31). This co-ordinate system basically expresses the system in terms of its observable and unobservable dynamics with the intent of simplifying the stability study. In relation to this new coordinate system, the relative degree indicates the number of observable dynamics that lie within this control system. Furthermore, the difference between the system states and the relative degree corresponds to the number of unobservable dynamics present in the system.

$$z = \Psi(\mathbf{x}) = \begin{bmatrix} \boldsymbol{\xi} & \boldsymbol{\eta}^T \end{bmatrix} \tag{5.31}$$

where $\boldsymbol{\xi}$ is the observable dynamics with $(total\ system\ states - r_{ij}) = (22 - 4) = 18$ states as the relative degree r_{ij} of output y_{ij} is 4 with $\boldsymbol{\xi}_{ij} = \begin{bmatrix} z_{ij_1} & z_{ij_2} & z_{ij_3} & z_{ij_4} \end{bmatrix}^T$, and $\boldsymbol{\eta}_{ij}$ is the unobservable or zero dynamics of the system which contains 18 states since the difference between the number of states and relative degree r_{ij} is 18, and hence: $\boldsymbol{\eta}_{ij} = \begin{bmatrix} \psi_{ij_1}(\mathbf{x}) & \psi_{ij_2}(\mathbf{x}) & ..... & \psi_{ij_{18}}(\mathbf{x}) \end{bmatrix}^T$. In accordance with Eq. (5.31), observable system states are thus defined as: $z_{ij_1} = y_{ij}$, $z_{ij_2} = y_{ij}^{(1)}$, $z_{ij_3} = y_{ij}^{(2)}$, $z_{ij_4} = y_{ij}^{(3)}$ and the zero dynamics are demarcated as: $z_{ij_5} = \psi_{ij_1}(\mathbf{x})$,$z_{ij_6} = \psi_{ij_2}(\mathbf{x})$,, $z_{ij_{22}} = \psi_{ij_{18}}(\mathbf{x})$ The new differential homeomorphic coordinate system may also be expressed in state-space form in terms of a virtual control input υ as follows:

$$\dot{\boldsymbol{\xi}}_{ij} = \mathbf{A}_{c_{ij}}\boldsymbol{\xi}_{ij} + \mathbf{B}_{c_{ij}}\upsilon_{ij} + \bar{\mathbf{p}}_{ij}(w) \tag{5.32}$$

$$y_{ij} = \mathbf{C}_{c_{ij}}\boldsymbol{\xi}_{ij} \tag{5.33}$$

In order to create a linear mapping between the virtual control input υ_{ij} and the system outputs y_{ij}, and a decoupled system such that:

$$\mathbf{A}_{c_{ij}} = \begin{bmatrix} 0 & 1 & 0 & 0 \\ 0 & 0 & 1 & 0 \\ 0 & 0 & 0 & 1 \\ \lambda_{0_{r_{ij}}} & \lambda_{1_{r_{ij}}} & \lambda_{2_{r_{ij}}} & \lambda_{3_{r_{ij}}} \end{bmatrix} \mathbf{B}_{c_{ij}} = \begin{bmatrix} 0 \\ 0 \\ 0 \\ 1 \end{bmatrix} \mathbf{C}_c = \begin{bmatrix} 1 & 0 & 0 & 0 \end{bmatrix}^T$$

$$\bar{\mathbf{p}}_{ij}(w) = \begin{bmatrix} 0 & 0 & 0 & 1 \end{bmatrix}^T$$

The virtual control vector υ and hence the individual virtual control inputs υ_{ij}must be determined through the subsequent relation which is essence computes the a linearizing decoupling law based the systems untransformed characteristic matrix $\mathbf{A}(\mathbf{x})$ presented in Eq. (5.27).

$$\mathbf{u} = \mathbf{P}(\mathbf{x}) + \mathbf{Q}(\mathbf{x})\upsilon \tag{5.34}$$

where $\mathbf{u} = \begin{bmatrix} u_{fr} & u_{fl} & u_{rr} & u_{rl} \end{bmatrix}$, $\upsilon = \begin{bmatrix} \upsilon_{fr} & \upsilon_{fl} & \upsilon_{rr} & \upsilon_{rl} \end{bmatrix}$, $\mathbf{P}(\mathbf{x}) = -\mathbf{A}(\mathbf{x})^{-\mathbf{1}}\mathbf{B}(\mathbf{x})$, and $\mathbf{Q}(\mathbf{x}) = -\mathbf{A}(\mathbf{x})^{-\mathbf{1}}$. When applying control, the characteristic matrix may implore design parameters $\lambda_{0_{r_{ij}}}$, $\lambda_{1_{r_{ij}}}$, $\lambda_{2_{r_{ij}}}$, $\lambda_{3_{r_{ij}}}$, and $\lambda_{4_{r_{ij}}}$ to augment and stabilise system performance [Garces et al. (2003)]. Hence, $\mathbf{A}(\mathbf{x})$, and $\mathbf{B}(\mathbf{x})$ take the ensuing forms:

$$\mathbf{A}(\mathbf{x}) = \begin{bmatrix} \lambda_{4_{r1}} L_f^4 h_{fr}(\mathbf{x}) & \lambda_{4_{r1}} \mathfrak{L}_f^4 h_{fr}(\mathbf{x}) & \lambda_{4_{r1}} \mathfrak{L}_f^4 h_{fr}(\mathbf{x}) & \lambda_{4_{r1}} \mathfrak{L}_f^4 h_{fr}(\mathbf{x}) \\ \lambda_{4_{r2}} \mathfrak{L}_f^4 h_{fl}(\mathbf{x}) & \lambda_{4_{r2}} \mathfrak{L}_f^4 h_{fl}(\mathbf{x}) & \lambda_{4_{r2}} \mathfrak{L}_f^4 h_{fl}(\mathbf{x}) & \lambda_{4_{r2}} \mathfrak{L}_f^4 h_{fl}(\mathbf{x}) \\ \lambda_{4_{r3}} \mathfrak{L}_f^4 h_{rr}(\mathbf{x}) & \lambda_{4_{r3}} \mathfrak{L}_f^4 h_{rr}(\mathbf{x}) & \lambda_{4_{r3}} \mathfrak{L}_f^4 h_{rr}(\mathbf{x}) & \lambda_{4_{r3}} \mathfrak{L}_f^4 h_{rr}(\mathbf{x}) \\ \lambda_{4_{r4}} \mathfrak{L}_f^4 h_{rl}(\mathbf{x}) & \lambda_{4_{r4}} \mathfrak{L}_f^4 h_{rl}(\mathbf{x}) & \lambda_{4_{r4}} \mathfrak{L}_f^4 h_{rl}(\mathbf{x}) & \lambda_{4_{r4}} \mathfrak{L}_f^4 h_{rl}(\mathbf{x}) \end{bmatrix} \tag{5.35}$$

$$\mathbf{B}(\mathbf{x}) = \begin{bmatrix} y_{fr}^{(4)} \\ y_{fl}^{(4)} \\ y_{rr}^{(4)} \\ y_{rl}^{(4)} \end{bmatrix} == \begin{bmatrix} \lambda_{4_{r_{fr}}} \mathfrak{L}_f^4 h1(\mathbf{x}) + \sum \lambda_{jr_{fr}} \mathfrak{L}_{g_{ij}} \mathfrak{L}_f^3 h_{fr}(\mathbf{x}) \\ \lambda_{4_{r_{fl}}} \mathfrak{L}_f^4 h2(\mathbf{x}) + \sum \lambda_{jr_{fl}} \mathfrak{L}_{g_{ij}} \mathfrak{L}_f^3 h_{fl}(\mathbf{x}) \\ \lambda_{4_{r_{rr}}} \mathfrak{L}_f^4 h3(\mathbf{x}) + \sum \lambda_{jr_{rr}} \mathfrak{L}_{g_{ij}} \mathfrak{L}_f^3 h_{rr}(\mathbf{x}) \\ \lambda_{4_{r_{rl}}} \mathfrak{L}_f^4 h4(\mathbf{x}) + \sum \lambda_{jr_{rl}} \mathfrak{L}_{g_{ij}} \mathfrak{L}_f^3 h_{rl}(\mathbf{x}) \end{bmatrix} \tag{5.36}$$

where $\lambda_{0_{r_{ij}}}$, $\lambda_{1_{r_{ij}}}$, $\lambda_{2_{r_{ij}}}$, $\lambda_{3_{r_{ij}}}$, and $\lambda_{4_{r_{ij}}}$ are design parameters. However, in order for the diffeomorphism to successfully produce differential homeomorphic coordinate system, the following condition must be guaranteed [Shi et al. (2010),Garces et al. (2003)]:

Ψ be invertible which infers that:

$$\mathfrak{L}_g \psi_{ij} = \frac{d\psi_{ij}}{dx} g(\mathbf{x}), \quad r_{ij} + 1 \leq i \leq n_s \tag{5.37}$$

After this feedback linearizing control law is applied to the system, the linearized decoupled system may be described as follows:

$$\sum_{k=0}^{r_{ij}} \lambda_{kr_{ij}} \frac{d^k y_{ij}}{dt^k} = \upsilon_{ij} \tag{5.38}$$

with a closed-loop transfer function given as:

$$G_{ij}(s) = \frac{Y_{ij}(s)}{V_i(s)} = \frac{1}{\lambda_{4r_{ij}} s^4 + \lambda_{3r_{ij}} s^3 \lambda_{2r_{ij}} s^2 \lambda_{1r_{ij}} s + \lambda_{0r_{ij}}} \tag{5.39}$$

The proposed transformation is valid if the relative vector $\mathbf{r}$ is well defined, $\mathbf{A}(\mathbf{x})$ is defined such that Eq. (5.34) is solvable and design parameters must be selected such that:

$$det \left[diag \begin{pmatrix} \lambda_{1_{r_{fr}}} & \lambda_{1_{r_{fl}}} & \lambda_{1_{r_{rr}}} & \lambda_{1_{r_{rl}}} \end{pmatrix} \right] \neq 0 \tag{5.40}$$

To ensure system stability, both the observable $\boldsymbol{\xi}_{ij}$ and zero $\boldsymbol{\eta}_{ij}$ system dynamics must be stable. Asymptotic stability of the system is ensured if the origin of the transformed system ($\boldsymbol{\xi}_{ij} = 0, \boldsymbol{\eta}_{ij} = 0$) is an equilibrium point. Careful study of the linearized decoupled system modelled according to Eq. (5.39) bears similar resemblance to pole placement control. Therefore, to guarantee global system stability

Routh-Hurwitz criterion is applied to the characteristic polynomial. This principle requires that all poles of the system described by Eq. (5.39) to lie in the negative half plane. Hence, the design parameters $\lambda_{0_{r_{ij}}}$, $\lambda_{1_{r_{ij}}}$, $\lambda_{2_{r_{ij}}}$, $\lambda_{3_{r_{ij}}}$ and $\lambda_{4_{r_{ij}}}$ are specifically chosen to meet this condition and guarantee stability.

This feedback linearizing law may be augmented with any control method with the aim of attaining better system performance. As there is a linear mapping between the virtual controls υ_{ij} and their respective system outputs y_{ij}, the virtual input υ_{ij} may be computed using linear control laws. The virtual control υ_{ij} may be designed around a linear control law as the system has now been linearized. The resulting hybrid control method will significantly improve system performance with satisfactory parameter sensitivity and disturbance attenuation. Hence, the virtual input υ_{ij} may be chosen:

$$\upsilon_{ij} = -\sum_{k=0}^{r_{ij}} \lambda_{kr_{ij}} \frac{d^k y_{ij}}{dt^k} + \bar{\upsilon}_{ij} \tag{5.41}$$

where $\bar{\upsilon_{ij}}$ is the new external input for the i, j^{th} output y_{ij}, which may be based on any linear control law. In this investigation, it is set to be a function of the reference signal $y_{d_{ij}}$ and the output signal y_{ij} and hence the control error e. Therefore, the new virtual control input $y_{d_{ij}}$ may be determined with a PID output feedback controller as follows:

$$\bar{\upsilon}_{ij} = K_P e + K_I \int_0^T e.dt + K_D \frac{de}{dt} \tag{5.42}$$

5.2 System Identification

The next step in the controller design involves system identification. System identification begins by capturing a relevant input-output data set which best captures most of the expected dynamics of the plant. As in the case of quarter-car model White-Band-Limited noise (WBL) that is bounded to $\pm 10V$ is used for each of the input data. However, the settings of each WBL are slightly varied so that the system's coupling is captured. From Figures 3.47 and 3.50, it is evident that both the PVSS and AVSS are sensitive in the frequency range of $0.5Hz$ to $80Hz$, and it is thus paramount that the system identification input data covers these frequencies [Dahunsi and Pedro (2010)]. Thus the settings of the WBL are listed in Table 5.1 and the corresponding input data is shown in Figures 5.2 to 5.5. The suspension travel at each of the wheels is chosen as the system outputs to be learnt. This is because these outputs are the primary factor upon which the model is based. The

Table 5.1: Configuration setting of input data for system identification for the full-car model

Input	**WBL Configuration**	**Input**	**WBL Configuration**
u_{fr}	Bounds of $\pm 10V$ Seed strength of 23341 Sampling Time of $0.001s$ Noise Power of 0.1	u_{fl}	Bounds of $\pm 10V$ Seed strength of 22641 Sampling Time of $0.001s$ Noise Power of 0.08
u_{rr}	Bounds of $\pm 10V$ Seed strength of 22641 Sampling Time of $0.001s$ Noise Power of 0.07	u_{rl}	Bounds of $\pm 10V$ Seed strength of 22641 Sampling Time of $0.001s$ Noise Power of 0.05

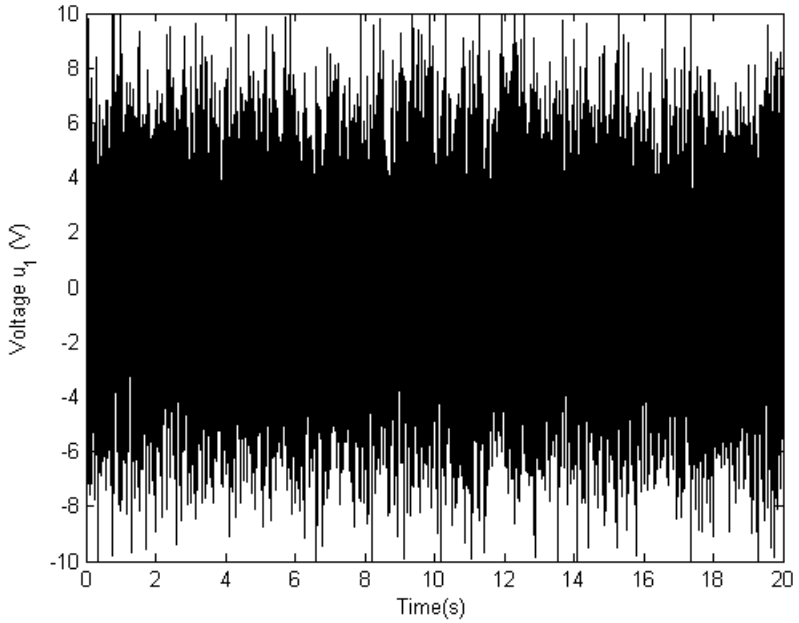

Figure 5.2: Front right actuator input data used for system identification

respective output data are shown in Figures 5.6 to 5.9. The output data is bounded to $\pm 0.01m$, which is acceptable as the suspension travel was limited to this range in the case of the full-car PID-based AVSS.

In contrast to the quarter-car intelligent AVSS, this DNN is a MIMO system. In the proposed controller four neural networks will be trained to learn the dynamics

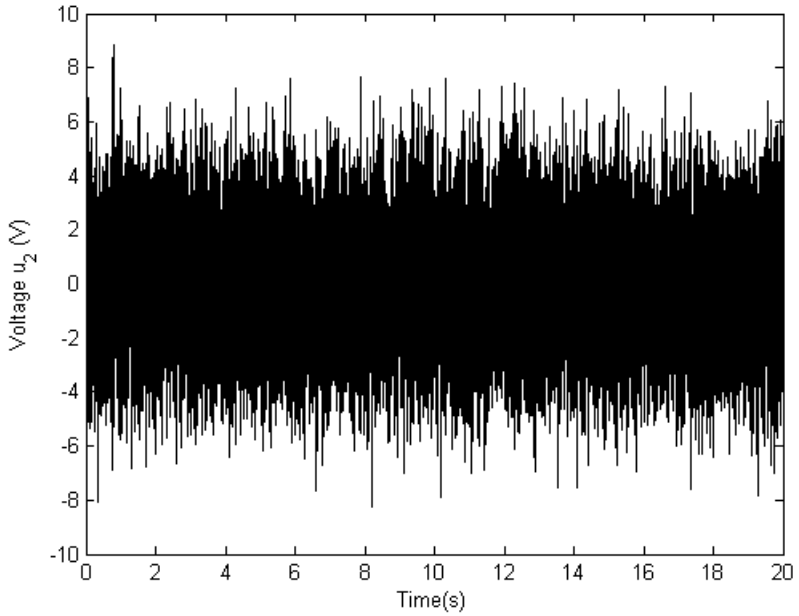

Figure 5.3: Front left actuator input data used for system identification

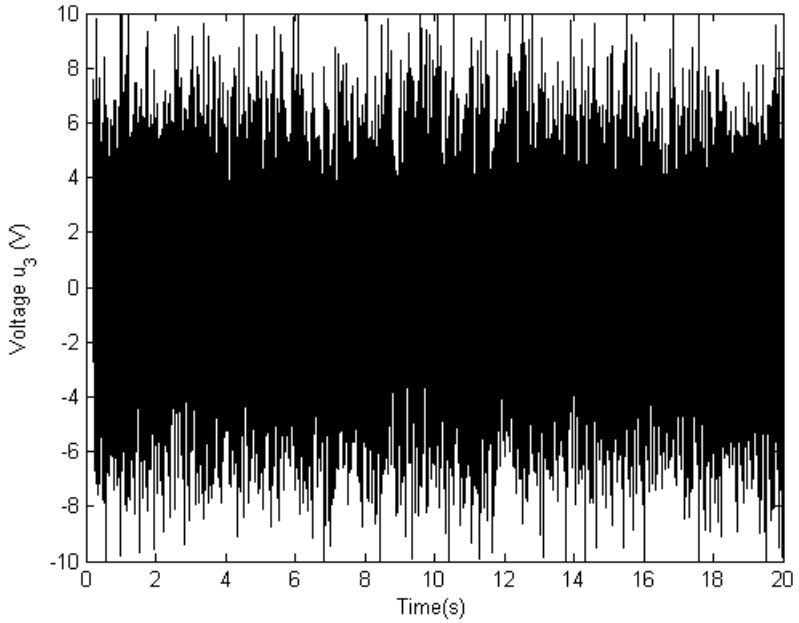

Figure 5.4: Rear right actuator input data used for system identification

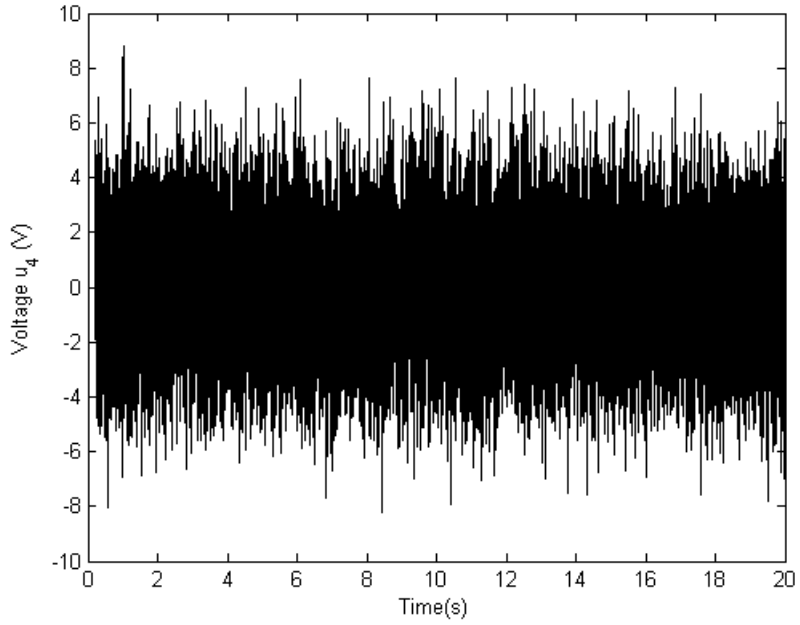

Figure 5.5: Rear left actuator input data used for system identification

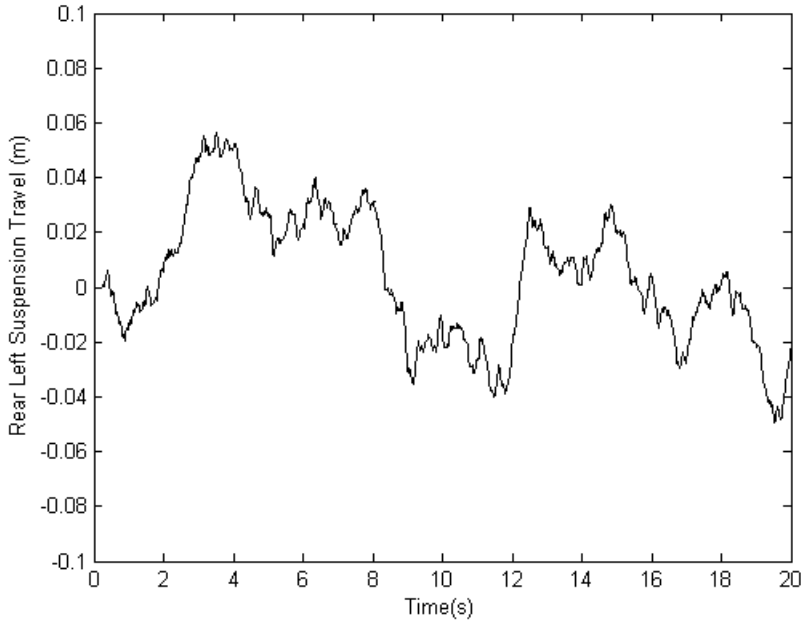

Figure 5.6: Front right suspension travel output data used for system identification

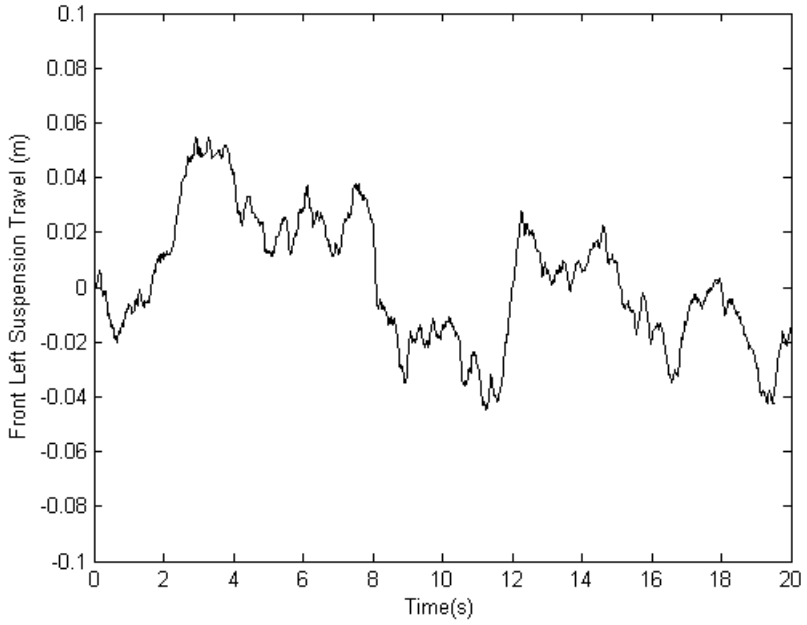

Figure 5.7: Front left suspension travel output data used for system identification

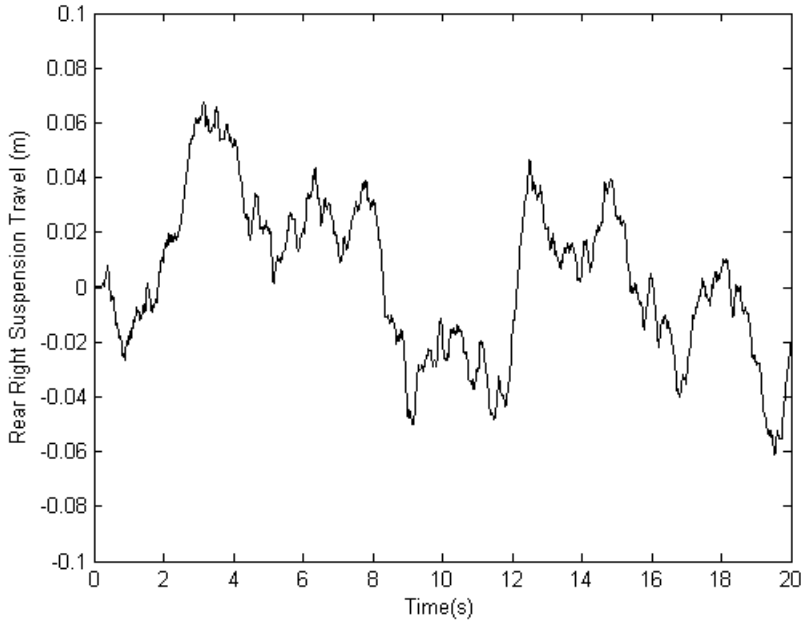

Figure 5.8: Rear right suspension travel output data used for system identification

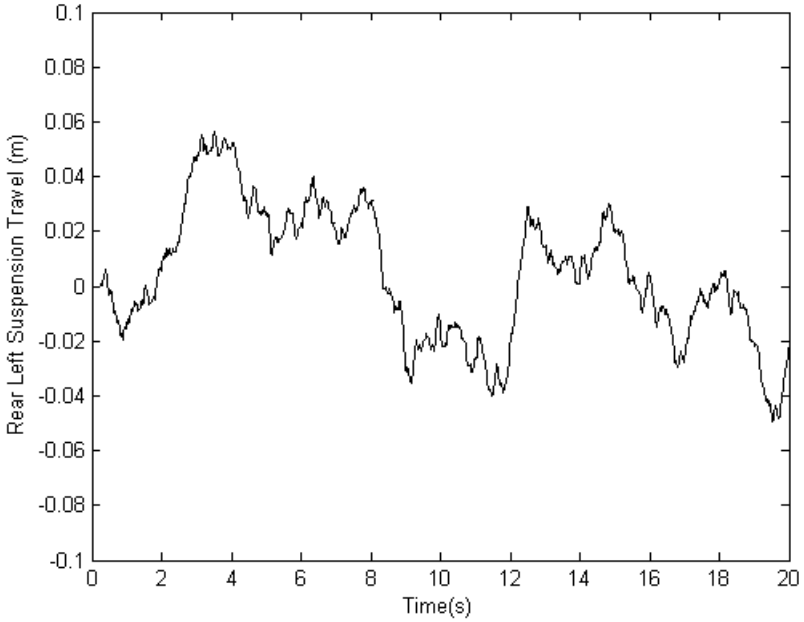

Figure 5.9: Rear left suspension travel output data used for system identification

of the four system outputs. Each DNN has the following form:

$$\begin{aligned}\dot{x}_{ij} &= -\boldsymbol{\beta}_{ij}\mathbf{x} + \mathbf{W}_{ij}\sigma(\mathbf{x_{ij}}) + \mathbf{g}_{1_{ij}}(\mathbf{x})u_{fr} + \mathbf{g}_{2_{ij}}(\mathbf{x})u_{fl} + \mathbf{g}_{3_{ij}}(\mathbf{x})u_{rr} + \mathbf{g}_{4_{ij}}(\mathbf{x})u_{rl} \\ &\quad + \boldsymbol{\gamma}_{1_{ij}}(\mathbf{x})y_{fr}(t-1) + \boldsymbol{\gamma}_{2_{ij}}(\mathbf{x})y_{fl}(t-1) + \boldsymbol{\gamma}_{3_{ij}}(\mathbf{x})y_{rr}(t-1) \\ &\quad + \boldsymbol{\gamma}_{4_{ij}}(\mathbf{x})y_{rl}(t-1) \qquad (5.43)\end{aligned}$$

$$\hat{y}_{ij} = h_{ij}(\mathbf{x}) = \sum_{L=1}^{n_n} \mathbf{w_{ij_L}}\mathbf{x_{ij_1}} \qquad (5.44)$$

where subscript denotes the i,j^{th} dynamic neural network at the i,j^{th} suspension system with i denoting the longitudanal position (front f or rear r) and j signifying the lateral position (right r or left l) of the suspension system, $\mathbf{x}$ is a vector denoting the outputs of each neuron, $\boldsymbol{\beta}$ designates the matrix containing the time constants of each neuron in the hidden layer, $\sigma(\mathbf{x})$ is the vector containing the neuron outputs after it had been passed through the activation function, $\mathbf{W}_{ij}$ is the inter-connecting neuron weights, u_{ij} are the various control input signals that are being passed into the real system, $\mathbf{g}_{k_{ij}}$ is a matrix which holds the weighting contributions that the k^{th} control input u_{ij} has on each neuron, $y_{ij}(t-1)$ holds the system outputs at the previous time step, and $\boldsymbol{\gamma}_{\mathbf{k_{ij}}}$ is the contribution of these aforementioned outputs on each neuron. $\mathbf{w}_{ij}$ is a vector containing the associating weighting contribution of each neuron in the hidden layer, n_n is the number of neurons in the hidden layer. The i,j^{th} DNN may be also described in terms of a pseudo function $\mathbf{f_{ij}}$ such that

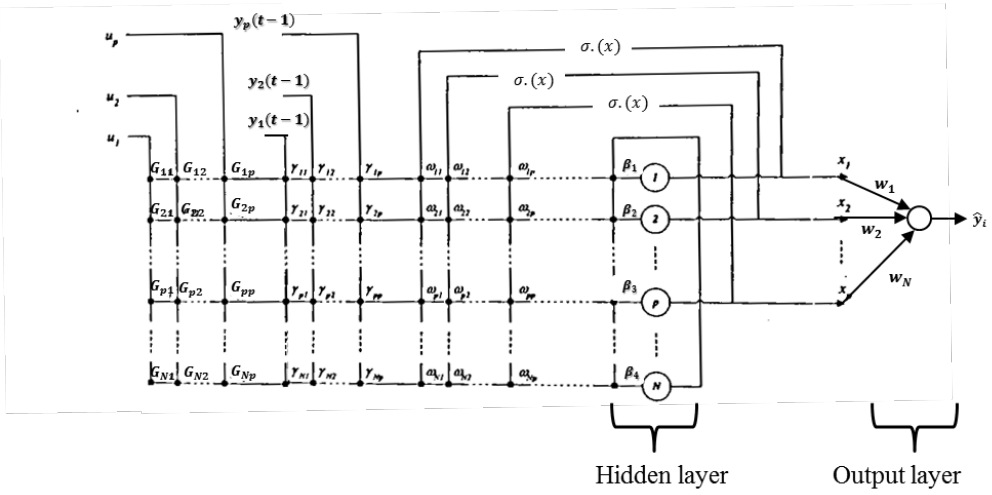

Figure 5.10: Schematic of the applied MIMO DNN

feedback linearization may be employed. The ensuing form is given as:

$$\begin{aligned}\dot{\mathbf{x}}_{\mathbf{ij}} &= \mathbf{f}_{\mathbf{ij}} + \mathbf{g}_{1_{ij}}(\mathbf{x})u_{fr} + \mathbf{g}_{2_{ij}}(\mathbf{x})u_{fl} + \mathbf{g}_{3_{ij}}(\mathbf{x})u_{rr} + \mathbf{g}_{2_{ij}}(\mathbf{x})u_{rl} + \\ &\quad \boldsymbol{\gamma}_{1_{ij}}(\mathbf{x})y_{fr}(t-1) + \boldsymbol{\gamma}_{2_{ij}}(\mathbf{x})y_{fl}(t-1) + \boldsymbol{\gamma}_{3_{ij}}(\mathbf{x})y_{rr}(t-1) \\ &\quad + \boldsymbol{\gamma}_{4_{ij}}(\mathbf{x})y_{rl}(t-1) \end{aligned} \tag{5.45}$$

with:

$$\mathbf{f}_{\mathbf{ij}} = -\boldsymbol{\beta}_{\mathbf{ij}}\mathbf{x}_{\mathbf{ij}} + \mathbf{W}_{ij}\sigma(\mathbf{x}) \tag{5.46}$$

A schematic of the DNN is shown in Figure 5.10 and the configuration of the applied DNN is summarized below.

1. Number of hidden layers is 2.
2. Number of neurons in the first hidden layer n_n is 13.
3. 4 delayed state inputs.
4. 4 delayed control inputs.
5. Number of neurons in the second hidden layer is 1.

This specific configuration was selected using pruning such as was done for the quarter-car model. This was achieved using the method of pruning which operates by comparing the topology of the output data obtained by DNN for various hidden layer configurations and subsequently selecting the best configuration [Nϕrgaard et al. (2000)]. Each of the DNN models were set to have similar network parameter values so that the comparison would be credible. The results for the various configurations are plotted in Figure 5.11. Figure 5.11 indicates that the output data of the

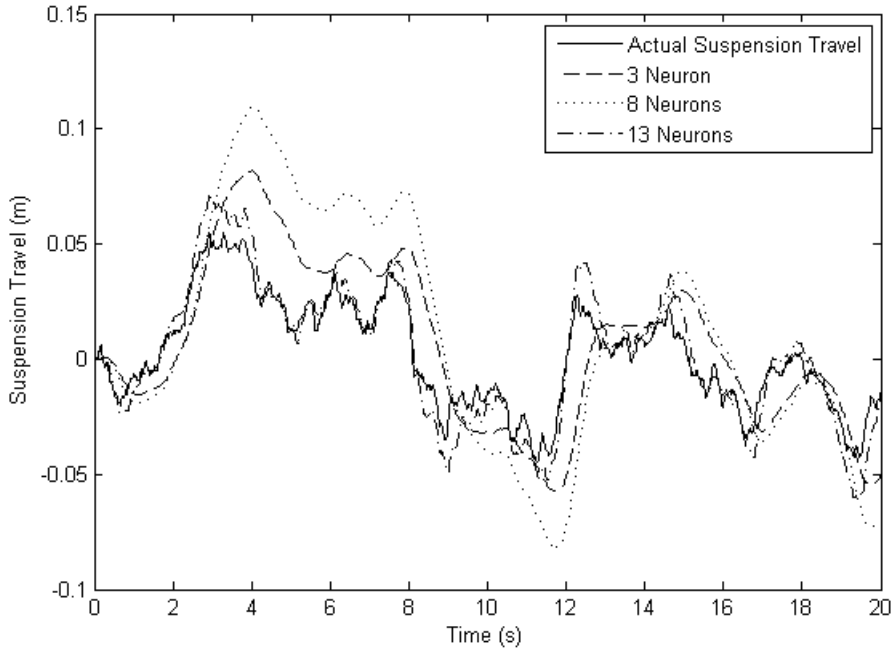

Figure 5.11: Network output data for various DNN configurations

3 neuron and 8 neuron configurations are relatively poor and are unable to capture the rate of change of the output data. The 13 neuron configuration is however able to perform effectively. Hence, a DNN with 13 neurons in the first hidden layer was selected for this investigation.

The dynamic neural network is trained using the PSO learning algorithm that was used in quarter-car intelligent control. PSO-based system identification will only be performed as it achieved the best results for the quarter-car intelligent controller. However, there are only two variations in this learning algorithm, which is required so that the DNN may be adapted to the full-car model. Firstly, the number of control variables to be computed by the PSO routine has now increased due to the greater number of neurons and the additional neural network inputs. Secondly, there are now four objective function J_{ij} which is the MSE value for each suspension travel output y_{ij}. Hence, the objective function has the following form:

$$J_{ij} = MSE = \frac{1}{2N}\sum_{i=0}^{N}(y_{ij} - \hat{y}_{ij})^2 \tag{5.47}$$

where $\hat{y}_{ij}$ is the predicted DNN suspension output for the y_{ij}. The configuration settings of the PSO learning routine are listed in Table 5.2. The convergence history of the training algorithm is plotted in Figure 5.12 and the identification results are

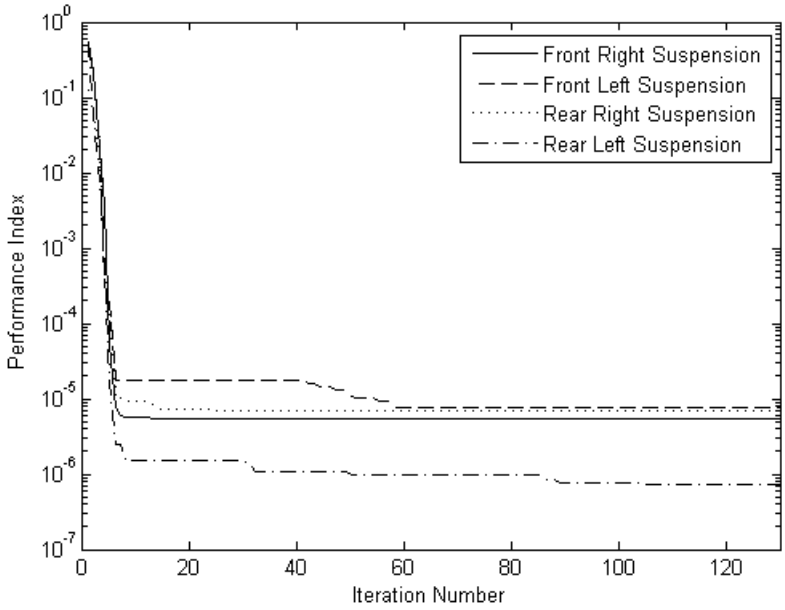

Figure 5.12: DNN training results obtained through PSO learning

superimposed with the output data in Figures 5.13 to 5.16 respectively. The corresponding validation results are plotted in Figures 5.17 to 5.20 respectively. The MSE values obtained were as good as those reported by Dahunsi et al. (2011) who controlled quarter-car nonlinear electrohydraulic AVSS using static neural networks. Hence, this system identification results are acceptable and have performed comparatively efficient.

Table 5.2: PSO settings for the full-car system identification

Routine	**PSO**
Population Size	100
Stopping Criteria	50 Iterations
Optimization	w_1 =0.5, w_2 =2
Parameters	w_3 =2

It is worth noting that formulation of the control law may only be possible if the dynamic neural network itself is stable. To ensure this stability the following conditions must be satisfied: [Garces et al. (2003)]

Step i. The activation function $\sigma(\mathbf{x})$ is continuously differentiable.

Step ii. $\sigma(\mathbf{x})$ is bounded to $0 \leq \sigma(\mathbf{x}) \leq 1$

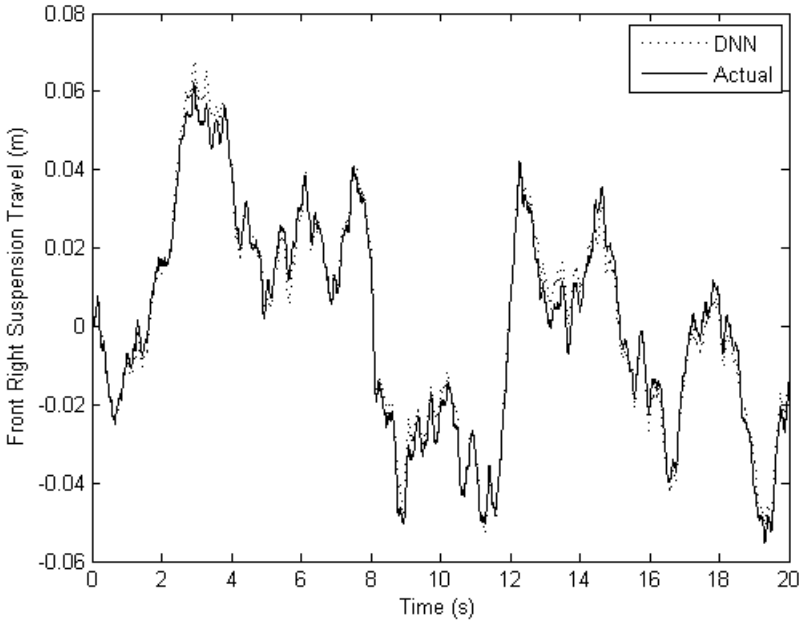

Figure 5.13: Identification results obtained for the front right suspension system

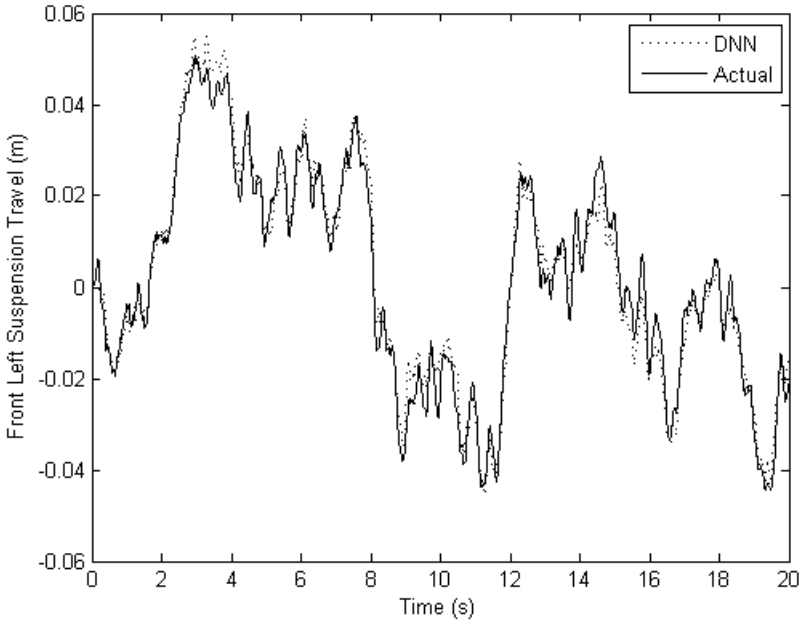

Figure 5.14: Identification results obtained for the front left suspension system

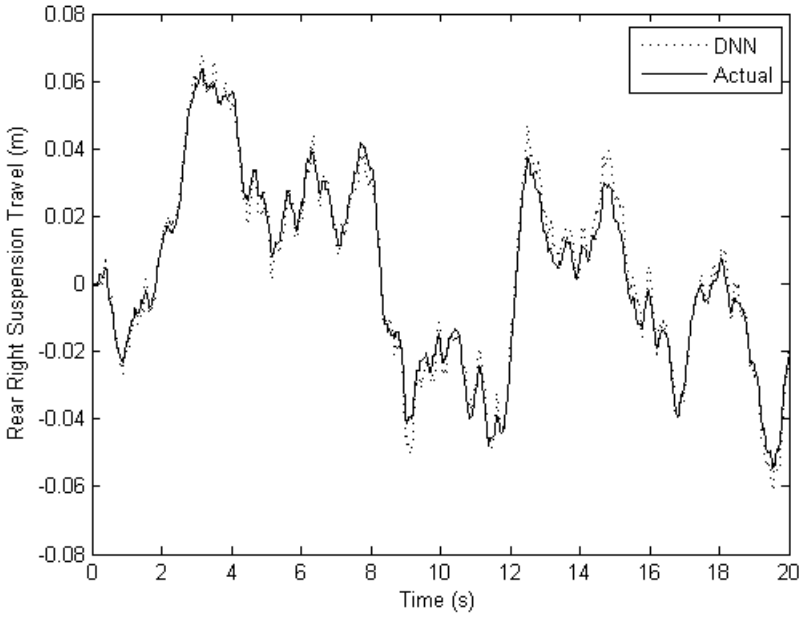

Figure 5.15: Identification results obtained for the rear right suspension system

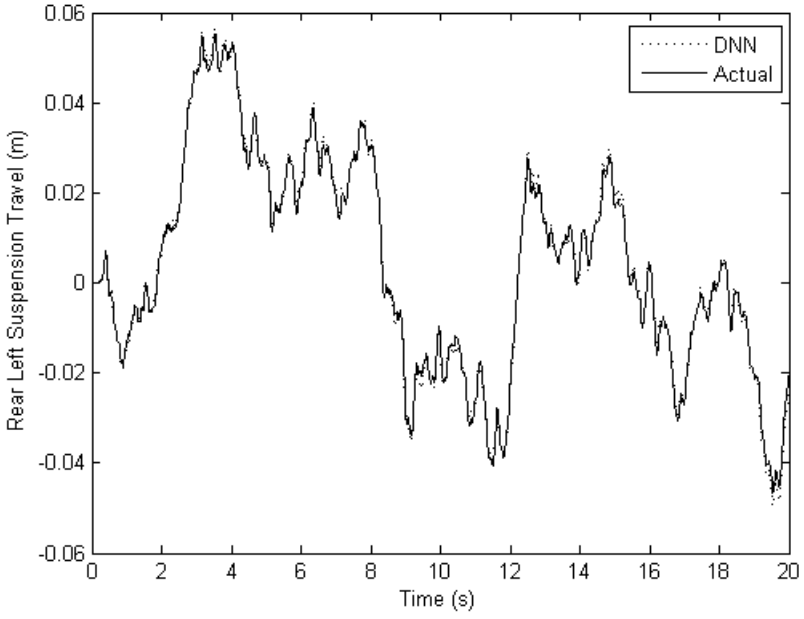

Figure 5.16: Identification results obtained for the rear left suspension system

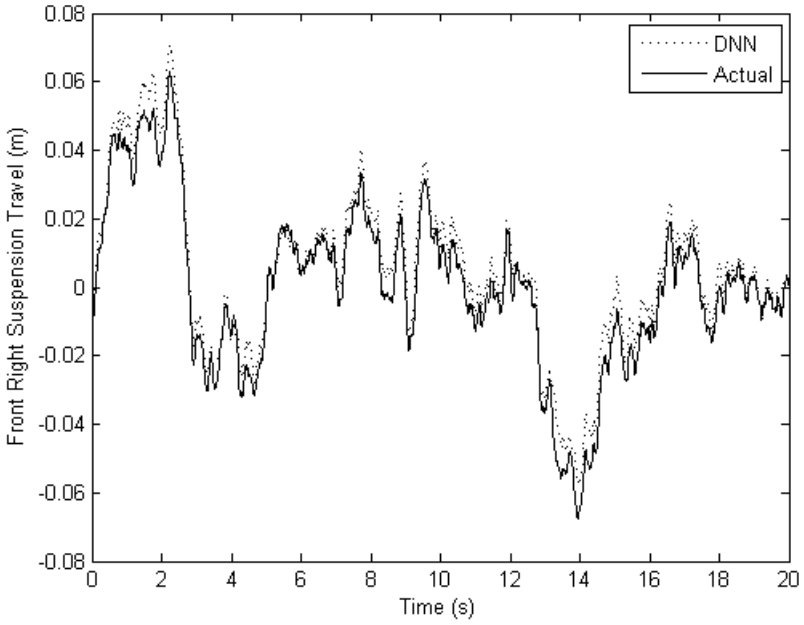

Figure 5.17: DNN validation results for the front right suspension system

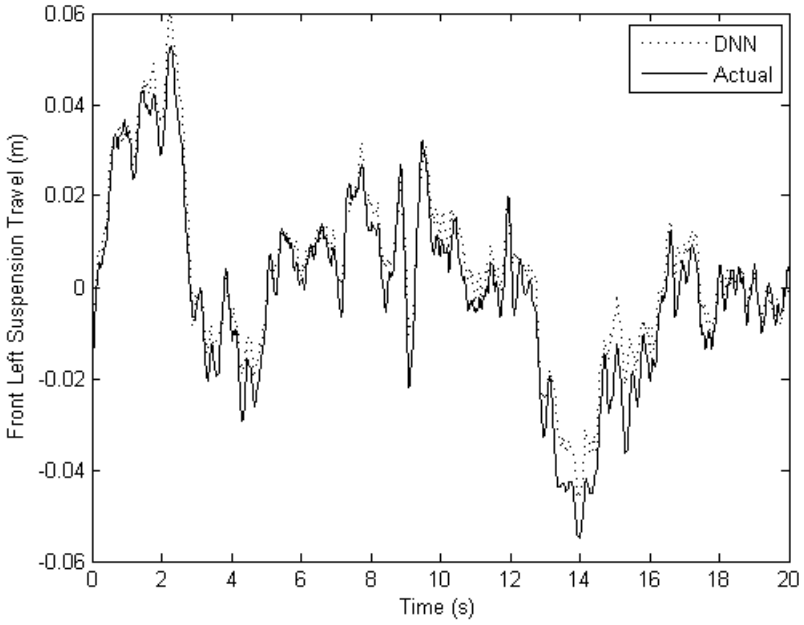

Figure 5.18: DNN validation results for the front left suspension system

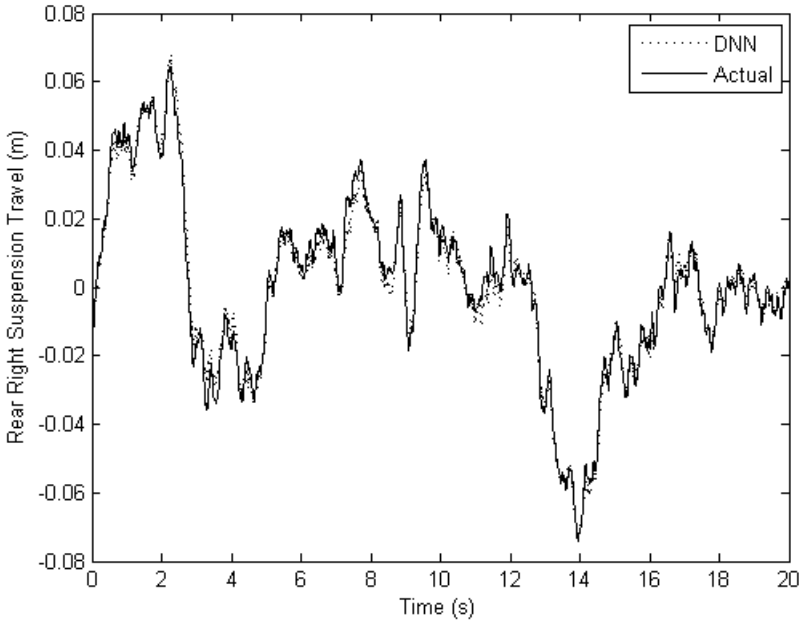

Figure 5.19: DNN validation results for the rear right suspension system

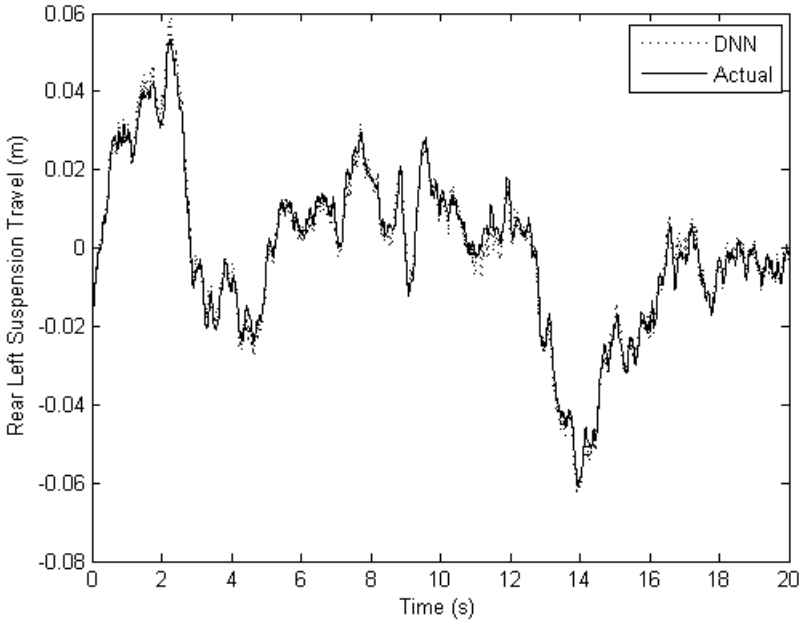

Figure 5.20: DNN validation results for the rear left suspension system

Step iii. Given $u_t \epsilon \mathbb{R}_+$, there is a symmetric and positive solution P to Eq. (5.48)

$$\boldsymbol{\beta}^{\mathbf{T}}\mathbf{P_{ij}} - \mathbf{P_{ij}}\boldsymbol{\beta} = -\mu \mathbf{I}_{ij} \tag{5.48}$$

where $\mathbf{I}$ is an identity matrix and μ is a scaling factor, which Garces et al. (2003) argued should have a value of 1.

Step iv. the inequality of Eq. (5.49) must be satisfied:

$$||\mathbf{W}_{ij}||^2 \leq \frac{\mu - 2||\mathbf{P_{ij}}||}{||\mathbf{P_{ij}}||} \tag{5.49}$$

where $||.||$ signifies the Euclidean norm of the specified matrix.

where $||.||$ signifies the Euclidean norm of the specified matrix. As the activation function $\sigma(\mathbf{x})$ is the hyperbolic tangent function, conditions i. and ii. are fulfilled. Every DNN model satisfied both Eq. (5.48) and the inequality of Eq. (5.49). Hence, it may be concluded that the DNNs attained through training are indeed stable.

5.3 Controller Development and Tuning

Before, the controller is developed, a specific condition must be guaranteed. A feedback linearizing law can only be developed if the DNN is input-output feedback linearizable. This requires the relative degree r_{ij} of each output y_{ij} to be less than the number of system states $r_{ij} < n$. The respective relative degrees are computed in the same manner as done for the actual full-car model as presented in section 5.1. The only difference is that it is now applied to the trained DNN models instead of the full-car model. The system outputs based on each dynamic neural network are given as follows:

$$\hat{y}_{fr} = h_{fr}(\mathbf{x}) \tag{5.50}$$

$$\hat{y}_{fl} = h_{fl}(\mathbf{x}) \tag{5.51}$$

$$\hat{y}_{rr} = h_{rr}(\mathbf{x}) \tag{5.52}$$

$$\hat{y}_{rl} = h_{rl}(\mathbf{x}) \tag{5.53}$$

with $\hat{y}_{ij}$ denoting the output from the i, j^{th} DNN which learns the suspension travel dynamics at the i, j^{th} wheel. The relative degree of the system is determined by continuously taking the time derivative of the output h_{ij} until a corresponding the r^{th} derivative of that output $y_{ij}^{(r)}$ is explicitly a function of at least one of the system inputs u_{ij} such that:

$$\hat{y}_{ij}^{(r)} = a_{ij}(\mathbf{x}_{ij}) + b_{ij}(\mathbf{x}_{ij})u_{ij} \tag{5.54}$$

where $a_{ij}(\mathbf{x}_{ij})$ and $b_{ij}(\mathbf{x}_{ij})$ are any nonlinear functions that have been produced as a consequence of the above computation. Moreover, the resulting dynamics of the coupled nonlinear system may be expressed in matrix form as [Ha and Gilbert (1986)]:

$$\hat{\mathbf{y}}^{(r)} = f(\mathbf{x}, \mathbf{u}) = \mathbf{A}(\mathbf{x}) + \mathbf{B}(\mathbf{x})\mathbf{u} \tag{5.55}$$

where $\mathbf{A}(\mathbf{x})$ is the characteristic matrix, vector $\mathbf{y}^{(r)}$ is the respective derivative of the outputs at which one of the system input explicitly appears, $\mathbf{u}$ in the input vector containing all the system inputs, and $\mathbf{B}(\mathbf{x})$ is the coupling between system states and system inputs.

The first derivative of the system DNN outputs $\hat{y}_{ij}^{(1)}$ which are described using Eq. (5.43) and (5.44) is determined as follows:

$$\begin{aligned}
\hat{y}_{ij}^{(1)} &= \frac{\partial \hat{y}_{ij}}{\partial t} = \frac{\partial \hat{y}_{ij}}{\partial \mathbf{x}_{ij}} \frac{\partial \mathbf{x}_{ij}}{\partial t} = \frac{\partial h_{ij}(\mathbf{x})}{\partial \mathbf{x}} \dot{\mathbf{x}}_{ij} \\
&= \frac{\partial h_{ij}}{\partial \mathbf{x}_{ij}} \left[\mathbf{f}_{ij}(\mathbf{x}) + g_{1_{ij}}(\mathbf{x}) u_{fr} + g_{2_{ij}}(\mathbf{x}) u_{fl} + g_{3_{ij}}(\mathbf{x}) u_{rr} + g_{4_{ij}}(\mathbf{x}) u_{rl} \right] \\
&= \left[\begin{array}{ccccc} \frac{\partial h_{fr}}{\partial x_{ij_1}} & \frac{\partial h_{fr}}{\partial x_{ij_2}} & \ldots & \ldots & \frac{\partial h_{fr}}{\partial x_{ij_8}} \end{array} \right] \left[\mathbf{f}_{ij}(\mathbf{x}) + \mathbf{g}(\mathbf{x}) \mathbf{u} \mathbf{f}_{ij}(\mathbf{x}) + g_{1_{ij}}(\mathbf{x}) u_{fr} + \right. \\
&\quad \left. g_{2_{ij}}(\mathbf{x}) u_{fl} + g_{3_{ij}}(\mathbf{x}) u_{rr} + g_{4_{ij}}(\mathbf{x}) u_{rl} \right]^T \\
&= w_{ij_1} \left[-\beta_{ij_1} x_1 + \sum_{k=1}^{13} W_{ij_{1k}} \sigma(x_k) \right] = \mathfrak{L}_{f_{ij}} h_{ij}(\mathbf{x})
\end{aligned} \tag{5.56}$$

where $\frac{\partial h_{ij}}{\partial \mathbf{x}} \mathbf{f_{ij}}(\mathbf{x})$ is defined as $\mathfrak{L}_{f_{ij}} h_{ij}(\mathbf{x})$, which is referred to as the Lie derivative of h_{ij} along $\mathbf{f}_{ij}$. For each of the DNN's at each suspension system, $\mathfrak{L}_{g_k} h_{ij}(\mathbf{x})$ is zero, which subsequently infers that $\hat{y}_{ij}^{(1)}$, $\hat{y}_{ij}^{(1)}$, $\hat{y}_{ij}^{(1)}$, and $\hat{y}_{ij}^{(1)}$ of the i, j^{th} suspension systems are not explicitly dependent on any of the system inputs u_{ij}. Therefore, computation of the latter derivative is carried out and this yields:

$$\begin{aligned}
\hat{y}_{ij}^{(2)} &= \frac{\partial^2 \hat{y}_{ij}}{\partial t^2} = \frac{\partial \frac{\partial \hat{y}_{ij}}{\partial t}}{\partial \mathbf{x}_{ij}} \frac{\partial \mathbf{x}_{ij}}{\partial t} = \frac{\partial \mathfrak{L}_f h_{ij}(\mathbf{x}_{ij})}{\partial x} \dot{\mathbf{x}}_{ij} \\
&= \frac{\partial \mathfrak{L}_{f_{ij}} h_{ij}(\mathbf{x}_{ij})}{\partial \mathbf{x}_{ij}} \left[f_{ij}(\mathbf{x}) + g_{1_{ij}}(\mathbf{x}) u_{fr} + g_{2_{ij}}(\mathbf{x}) u_{fl} + g_{3_{ij}}(\mathbf{x}) u_{rr} + g_{4_{ij}}(\mathbf{x}) u_{rl} \right] \\
&= \mathfrak{L}^2_{f_{ij}} h_{ij}(\mathbf{x}_{ij}) + \mathfrak{L}_{g_{1_{ij}}} \mathfrak{L}_{f_{ij}} h_{fr}(\mathbf{x}) u_{fr} + \mathfrak{L}_{g_{2_{ij}}} \mathfrak{L}_{f_{ij}} h_{fl}(\mathbf{x}_{ij}) \\
&= u_{fl} + \mathfrak{L}_{g_{3_{ij}}} \mathfrak{L}_{f_{ij}} h_{rr}(\mathbf{x}_{ij}) u_{rr} + \mathfrak{L}_{g_{4_{ij}}} \mathfrak{L}_{f_{ij}} h_{rl}(\mathbf{x}_{ij}) u_{rl} \\
&= w_{ij_{k1}} [-\beta_{ij_1} x_1 + W_{ij_{11}} (1 - \sigma(\mathbf{x_{ij_1}})^2) + W_{ij_{12}} (1 - \sigma(\mathbf{x_{ij_2}})^2) \ldots\ldots\ldots \\
&= + W_{ij_{13}} (1 - \sigma(\mathbf{x_{ij_{13}}})^2)] \left[\mathbf{f}_{ij}(\mathbf{x}) + \mathbf{g}_{k_{ij}}(\mathbf{x}) u_{ij} \right] \\
&= d_{ij}(\mathbf{x}) + e_{ij}(\mathbf{x}) u_{ij} \\
&= \mathfrak{L}^2_{f_{ij}} h_{ij}(\mathbf{x}) + \mathfrak{L}_{g_{ij}} \mathfrak{L}_{f_{ij}} h_{ij}(\mathbf{x}) u_{ij}
\end{aligned} \tag{5.57}$$

where $d_{ij}(\mathbf{x})$ or $\mathfrak{L}^2_{f_{ij}} h_{fr}(\mathbf{x})$ is the free response of the system and $e_{ij}(\mathbf{x})u_{ij}$ or $\mathfrak{L}_{g_{k_{ij}}} \mathfrak{L}_{f_{ij}} h_{ij}(\mathbf{x})u_{ij}$ is the free response of the system. Hence, for each DNN, the second derivative of the output is thus:

$$\hat{y}^{(2)}_{fr} = \mathfrak{L}^2_{f_{fr}} h_{fr}(\mathbf{x}) + \mathfrak{L}_{g_{1_{fr}}} \mathfrak{L}_{f_{fr}} h_{fr}(\mathbf{x}) u_{fr} \tag{5.58}$$

$$\hat{y}^{(2)}_{fl} = \mathfrak{L}^2_{f_{fl}} h_{fl}(\mathbf{x}) + \mathfrak{L}_{g_{2_{fl}}} \mathfrak{L}_{f_{fl}} h_{fl}(\mathbf{x}) u_{fl} \tag{5.59}$$

$$\hat{y}^{(2)}_{rr} = \mathfrak{L}^2_{f_{rr}} h_{rr}(\mathbf{x}) + \mathfrak{L}_{g_{3_{rr}}} \mathfrak{L}_{f_{rr}} hrr(\mathbf{x}) u_{rr} \tag{5.60}$$

$$\hat{y}^{(2)}_{rl} = \mathfrak{L}^2_{f_{rl}} h_{rl}(\mathbf{x}) + \mathfrak{L}_{g_{4_{rl}}} \mathfrak{L}_{f_{rl}} h_{rl}(\mathbf{x}) u_{rl} \tag{5.61}$$

In the preceding computations, the each of the four DNN models generated a matrix where $g_{1_{fr}}(\mathbf{x})$, $g_{2_{fl}}(\mathbf{x})$, $g_{3_{rr}}(\mathbf{x})$, and $g_{4_{rl}}(\mathbf{x})$ were considerably large constants. Thus, the second time derivative of the network output $\hat{y}^{(2)}_{ij}$ produced a solution which was explicitly dependent on at least one of the control input u_{ij}. Hence, the relative degree of each DNN model is two. This is less than the 13 states of the DNN models. Hence the vector of relative degree $\mathbf{r}$ is:

$$\mathbf{r} = \begin{bmatrix} r_{fr} & r_{fl} & r_{rr} & r_{rl} \end{bmatrix}^T = \begin{bmatrix} 2 & 2 & 2 & 2 \end{bmatrix}^T \tag{5.62}$$

The resulting nonlinear dynamics of the DNN configurations may be expressed in terms of its characteristic matrix $\mathbf{A}(\mathbf{x})$ as follows:

$$\mathbf{y}^2 = f(\mathbf{x}, \mathbf{u}) = \mathbf{A}(\mathbf{x}) + \mathbf{B}(\mathbf{x})\mathbf{u} \tag{5.63}$$

with:

$$\mathbf{A}(\mathbf{x}) = \begin{bmatrix} \mathfrak{L}_{g_{1_{fr}}} \mathfrak{L}^2_{f_{fr}} h_{fr}(\mathbf{x}) & \mathfrak{L}_{g_{2_{fr}}} \mathfrak{L}^2_{f_{fr}} h_{fr}(\mathbf{x}) & \mathfrak{L}_{g_{3_{fr}}} \mathfrak{L}^2_{f_{fr}} h_{fr}(\mathbf{x}) & \mathfrak{L}_{g_{4_{fr}}} \mathfrak{L}^2_{f_{fr}} h_{fr}(\mathbf{x}) \\ \mathfrak{L}_{g_{1_{fl}}} \mathfrak{L}^2_{f_{fl}} h_{fl}(\mathbf{x}) & \mathfrak{L}_{g_{2_{fl}}} \mathfrak{L}^2_{f_{fl}} h_{fl}(\mathbf{x}) & \mathfrak{L}_{g_{3_{fl}}} \mathfrak{L}^2_{f_{fl}} h_{fl}(\mathbf{x}) & \mathfrak{L}_{g_{4_{fl}}} \mathfrak{L}^2_{f_{fl}} h_{fl}(\mathbf{x}) \\ \mathfrak{L}_{g_{1_{rr}}} \mathfrak{L}^2_{f_{rr}} h_{rr}(\mathbf{x}) & \mathfrak{L}_{g_{2_{rr}}} \mathfrak{L}^2_{f_{rr}} h_{rr}(\mathbf{x}) & \mathfrak{L}_{g_{3_{rr}}} \mathfrak{L}^2_{f_{rr}} h_{rr}(\mathbf{x}) & \mathfrak{L}_{g_{4_{rr}}} \mathfrak{L}^2_{f_{rr}} h_{rr}(\mathbf{x}) \\ \mathfrak{L}_{g_{1_{rl}}} \mathfrak{L}^2_{f_{rl}} h_{rl}(\mathbf{x}) & \mathfrak{L}_{g_{2_{rl}}} \mathfrak{L}^2_{f_{rl}} h_{rl}(\mathbf{x}) & \mathfrak{L}_{g_{3_{rl}}} \mathfrak{L}^2_{f_{rl}} h_{rl}(\mathbf{x}) & \mathfrak{L}_{g_{4_{rl}}} \mathfrak{L}^2_{f_{rl}} h_{rl}(\mathbf{x}) \end{bmatrix} \tag{5.64}$$

$$\mathbf{B}(\mathbf{x}) = \begin{bmatrix} \hat{y}^{(2)}_{fr} \\ \hat{y}^{(2)}_{fl} \\ \hat{y}^{(2)}_{rr} \\ \hat{y}^{(2)}_{rl} \end{bmatrix} = \begin{bmatrix} \mathfrak{L}^2_{f_{fr}} h_{fr}(\mathbf{x}) + \sum \mathfrak{L}_{g_{ij}} \mathfrak{L}^1_{f_{fr}} h_{fr}(\mathbf{x}) \\ \mathfrak{L}^2_{f_{fl}} h_{fl}(\mathbf{x}) + \sum \mathfrak{L}_{g_{ij}} \mathfrak{L}^1_{f_{fl}} h_{fl}(\mathbf{x}) \\ \mathfrak{L}^2_{f_{rr}} h_{rr}(\mathbf{x}) + \sum \mathfrak{L}_{g_{ij}} \mathfrak{L}^1_{f_{rr}} h_{rr}(\mathbf{x}) \\ \mathfrak{L}^2_{f_{rl}} h_{rl}(\mathbf{x}) + \sum \mathfrak{L}_{g_{ij}} \mathfrak{L}^1_{f_{rl}} h_{rl}(\mathbf{x}) \end{bmatrix} \tag{5.65}$$

As the relative degree of system is less than the number of system states ($r_{ij} \leq n$), the system is thus input-output linearizable. The system coordinates can be transformed into a more friendly differential homeomorphic coordinate system which is described by Eq. (5.66). This co-ordinate breaks down the system dynamics into its observable $\boldsymbol{\xi}$ and unobservable $\boldsymbol{\eta}$. This new co-ordinate system is as follows:

$$z = \Psi(\mathbf{x}) = \begin{bmatrix} \boldsymbol{\xi} & \boldsymbol{\eta}^T \end{bmatrix} \tag{5.66}$$

where $\boldsymbol{\xi}$ is the observable dynamics with $(N - r_{ij}) = (13 - 2) = 11$ states as the relative degree r_{ij} of DNN output $\hat{y}_{ij}$ is 2 with $\boldsymbol{\xi}_{ij} = \begin{bmatrix} z_{ij_1} & z_{ij_2} \end{bmatrix}^T$, and $\boldsymbol{\eta}_{ij}$ is the unobservable or zero dynamics of the system which contains 11 states since the difference between the number of states and relative degree of each DNN model is 11, and hence: $\boldsymbol{\eta}_{ij} = \begin{bmatrix} \psi_{ij_1}(\mathbf{x}) & \psi_{ij_2}(\mathbf{x}) & ..... & \psi_{ij_{11}}(\mathbf{x}) \end{bmatrix}^T$. In accordance with Eq. (5.31), observable system states are thus defined as: $z_{ij_1} = \hat{y}_{ij}$, $z_{ij_2} = \hat{y}_{ij}^{(1)}$ and the zero dynamics are demarcated as: $z_{ij_5} = \psi_{ij_1}(\mathbf{x})$,$z_{ij_6} = \psi_{ij_2}(\mathbf{x})$,, $z_{ij_{13}} = \psi_{ij_{11}}(\mathbf{x})$ The new differential homeomorphic coordinate system may also be expressed in state-space form in terms of a virtual control input υ as follows:

$$\dot{\boldsymbol{\xi}}_{ij} = \mathbf{A}_{c_{ij}}\boldsymbol{\xi}_{ij} + \mathbf{B}_{c_{ij}}\upsilon_i + \bar{\mathbf{p}}_{ij}(w) \tag{5.67}$$

$$y_{ij} = \mathbf{C}_{c_{ij}}\boldsymbol{\xi}_{ij} \tag{5.68}$$

In order to create a linear mapping between the virtual control input υ_{ij} and the system outputs y_{ij}, and a decoupled system such that:

$$\mathbf{A}_c = \begin{bmatrix} 0 & 1 \\ \lambda_{0_{r_{ij}}} & \lambda_{1_{r_{ij}}} \end{bmatrix} \mathbf{B}_c = \begin{bmatrix} 0 \\ 1 \end{bmatrix} \mathbf{C}_c = \begin{bmatrix} 1 & 0 \end{bmatrix}^T \bar{\mathbf{p}}(w) = \begin{bmatrix} 0 & 1 \end{bmatrix}^T \tag{5.69}$$

The virtual control vector υ must be determined through the following computation which generates a linearizing decoupling law by solving the control law that removes the linearities present in Eq. (5.63). This gives rise to the following linearizing control signal

$$\mathbf{u} = \mathbf{P}(\mathbf{x}) + \mathbf{Q}(\mathbf{x})\upsilon \tag{5.70}$$

where $\mathbf{u} = \begin{bmatrix} u_{fr} & u_{fl} & u_{rr} & u_{rl} \end{bmatrix}$, $\upsilon = \begin{bmatrix} \upsilon_{fr} & \upsilon_{fl} & \upsilon_{rr} & \upsilon_{rl} \end{bmatrix}$, $\mathbf{P}(\mathbf{x}) = -\mathbf{A}(\mathbf{x})^{-1}\mathbf{B}(\mathbf{x})$, and $\mathbf{Q}(\mathbf{x}) = -\mathbf{A}(\mathbf{x})^{-1}$. When applying control, the characteristic matrix may implore design parameters $\lambda_{0_{r_{ij}}}$, $\lambda_{1_{r_{ij}}}$, and $\lambda_{2_{r_{ij}}}$ to augment and stabilise system performance[Garces et al. (2003)]. Hence, $\mathbf{A}(\mathbf{x})$, and $\mathbf{B}(\mathbf{x})$ take the ensuing forms:

$$\mathbf{A}(\mathbf{x}) = \begin{bmatrix} \lambda_{2_{r_{fr}}}\mathfrak{L}_{g_{1_{fr}}}\mathfrak{L}_{f_{fr}}^2 h_{fr}(\mathbf{x}) & \lambda_{2_{r_{fr}}}\mathfrak{L}_{g_{2_{fr}}}\mathfrak{L}_{f_{fr}}^2 h_{fr}(\mathbf{x}) & \lambda_{2_{r_{fr}}}\mathfrak{L}_{g_{3_{fr}}}\mathfrak{L}_{f_{fr}}^2 h_{fr}(\mathbf{x}) \\ \lambda_{2_{r_{fl}}}\mathfrak{L}_{g_{1_{fl}}}\mathfrak{L}_{f_{fl}}^2 h_{fl}(\mathbf{x}) & \lambda_{2_{r_{fl}}}\mathfrak{L}_{g_{2_{fl}}}\mathfrak{L}_{f_{fl}}^2 h_{fl}(\mathbf{x}) & \lambda_{2_{r_{fl}}}\mathfrak{L}_{g_{3_{fl}}}\mathfrak{L}_{f_{fl}}^2 h_{fl}(\mathbf{x}) \\ \lambda_{2_{r_{rr}}}\mathfrak{L}_{g_{1_{rr}}}\mathfrak{L}_{f_{rr}}^2 h_{rr}(\mathbf{x}) & \lambda_{2_{r_{rr}}}\mathfrak{L}_{g_{2_{rr}}}\mathfrak{L}_{f_{rr}}^2 h_{rr}(\mathbf{x}) & \lambda_{2_{r_{rr}}}\mathfrak{L}_{g_{3_{rr}}}\mathfrak{L}_{f_{rr}}^2 h_{rr}(\mathbf{x}) \\ \lambda_{2_{r_{rl}}}\mathfrak{L}_{g_{1_{rl}}}\mathfrak{L}_{f_{rl}}^2 h_{rl}(\mathbf{x}) & \lambda_{2_{r_{rl}}}\mathfrak{L}_{g_{2_{rl}}}\mathfrak{L}_{f_{rl}}^2 h_{rl}(\mathbf{x}) & \lambda_{2_{r_{rl}}}\mathfrak{L}_{g_{3_{rl}}}\mathfrak{L}_{f_{rl}}^2 h_{rl}(\mathbf{x}) \end{bmatrix}$$

$$\begin{bmatrix} .. & \lambda_{2_{r_{fr}}}\mathfrak{L}_{g_{4_{fr}}}\mathfrak{L}_{f_{fr}}^2 h_{fr}(\mathbf{x}) \\ .. & \lambda_{2_{r_{fl}}}\mathfrak{L}_{g_{4_{fl}}}\mathfrak{L}_{f_{fl}}^2 h_{fl}(\mathbf{x}) \\ .. & \lambda_{2_{r_{rr}}}\mathfrak{L}_{g_{4_{rr}}}\mathfrak{L}_{f_{rr}}^2 h_{rr}(\mathbf{x}) \\ .. & \lambda_{2_{r_{rl}}}\mathfrak{L}_{g_{4_{rl}}}\mathfrak{L}_{f_{rl}}^2 h_{rl}(\mathbf{x}) \end{bmatrix} \tag{5.71}$$

$$\mathbf{B}(\mathbf{x}) = \begin{bmatrix} \hat{y}_{fr}^{(2)} \\ \hat{y}_{fl}^{(2)} \\ \hat{y}_{rr}^{(2)} \\ \hat{y}_{rl}^{(2)} \end{bmatrix} = \begin{bmatrix} \lambda_{2_{r_{fr}}}\mathfrak{L}_f^2 h1(\mathbf{x}) + \sum_{j=1}^{1}\lambda_{jr_{fr}}\mathfrak{L}_{g_j}\mathfrak{L}_f^3 h_{fr}(\mathbf{x}) \\ \lambda_{2_{r_{fl}}}\mathfrak{L}_f^2 h2(\mathbf{x}) + \sum_{j=1}^{1}\lambda_{jr_{fl}}\mathfrak{L}_{g_j}\mathfrak{L}_f^3 h_{fl}(\mathbf{x}) \\ \lambda_{2_{r_{rr}}}\mathfrak{L}_f^2 h3(\mathbf{x}) + \sum_{j=1}^{1}\lambda_{jr_{rr}}\mathfrak{L}_{g_j}\mathfrak{L}_f^3 h_{rr}(\mathbf{x}) \\ \lambda_{2_{r_{rl}}}\mathfrak{L}_f^2 h4(\mathbf{x}) + \sum_{j=1}^{1}\lambda_{jr_{rl}}\mathfrak{L}_{g_j}\mathfrak{L}_f^3 h_{rl}(\mathbf{x}) \end{bmatrix} \tag{5.72}$$

where $\lambda_{0_{r_{ij}}}$, $\lambda_{1_{r_{ij}}}$, and $\lambda_{2_{r_{ij}}}$, are design parameters or controller gains which are tuned with the aim of improving system performance. However, in order for the diffeomorphism to successfully produce differential homeomorphic coordinate system, the following condition must be ensured [Shi et al. (2010),Garces et al. (2003)]: Ψ be invertible which infers that:

$$\mathfrak{L}_g \psi_i = \frac{d\psi_i}{dx} g(\mathbf{x}), \quad r+1 \leq i \leq n_s \tag{5.73}$$

The resulting decoupled linear system now has the ensuing form:

$$\sum_{k=0}^{r_{ij}} \lambda + k_{r_{ij}} \frac{d^k y_{ij}}{dt^k} = \upsilon_{ij} \tag{5.74}$$

and its resulting close loop transfer function of each DNN controller is given as:

$$G_{ij}(s) = \frac{Y_{ij}(s)}{V_i(s)} = \frac{1}{\lambda_{2_{r_{ij}}} s^2 \lambda_{1_{r_{ij}}} s + \lambda_{0_{r_{ij}}}} \tag{5.75}$$

The proposed transformation is valid if the relative vector $\mathbf{r}$ is well defined, $\mathbf{A}(\mathbf{x})$ is defined such that Eq. (5.34) is solvable and design parameters must be selected such that:

$$det \left[diag \begin{pmatrix} \lambda_{2_{r_{fr}}} & \lambda_{2_{r_{fl}}} & \lambda_{2_{r_{rr}}} & \lambda_{2_{r_{rl}}} \end{pmatrix} \right] \neq 0 \tag{5.76}$$

To ensure system stability, both the observable $\boldsymbol{\xi}_{ij}$ and zero $\boldsymbol{\eta}_{ij}$ system dynamics must be stable. Asymptotic stability of the system is ensured if the origin of the transformed system ($\boldsymbol{\xi}_{ij} = 0, \boldsymbol{\eta}_{ij} = 0$) is an equilibrium point. Careful study of the linearized decoupled system modelled according to Eq. (5.75) bears similar resemblance to pole placement control. Therefore, to guarantee global system stability Routh-Hurwitz stability criterion is applied to the characteristic polynomial. This principle requires all poles of the system described by Eq. (5.39) to lie in the negative half plane. Hence, the design parameters $\lambda_{0_{r_{ij}}}$, $\lambda_{1_{r_{ij}}}$, $\lambda_{2_{r_{ij}}}$, are specifically chosen to meet this condition and guarantee stability.

This feedback linearizing law may be augmented with any control method with the aim of attaining better system performance. As there is a linear mapping between the virtual controls υ_{ij} and the predicted system outputs $\hat{y}_{ij}$, the virtual input υ may be computed using linear control laws. Linear control laws can be successfully incorporated to any linear system will significantly improve system performance with satisfactory parameter sensitivity and disturbance attenuation. Hence, the virtual input υ_{ij} may be chosen:

$$\upsilon_{ij} = -\sum_{k=0}^{r_{ij}} \lambda_{k_{r_{ij}}} \frac{d^k y_{ij}}{dt^k} \bar{v}_{ij} \tag{5.77}$$

where $\bar{v_{ij}}$ is the new external input for the i, j^{th} DNN predicted output $\hat{y}_{ij}$, which may be based on any linear control law. This control law will be the multi-loop PID control scheme that was implemented in full-car PID-based AVSS in section 3.2. A schematic of the control structure is shown in Figure 5.1. The inner loop aims to stabilise the actuator and the outer loop manipulates the control variable, which as in the case of the PID-based AVSS is the suspension travel at the respective wheels.

In this figure, $y_{d_{ij}}$ signifies the equilibrium set point of the i, j^{th} wheel, which is set to zero to address the regulation problem; numbers 1 to 4 are representative of the front right, front left, rear right and rear left wheels respectively; $e_{1_{ij}}$ are the outer loop control error of the i, j^{th} outer loop, whereas $e_{2_{ij}}$ denotes that of the respective inner loops; $F_{a_{ij}}$ is the actuator forces supplied at the i, j^{th} actuator with $F_{d_{ij}}$ signifying its respective desired force which is being tracked using the inner PID controllers. y_{fr}, y_{fl}, y_{rr}, and y_{rl} are the suspension travels that are manipulated through the outer control loops; and $\bar{v}_{fr}$, $\bar{v}_{fl}$, $\bar{v}_{rr}$ and $\bar{v}_{rl}$ are the respective control signals that are passed into the FBL portion of the DNNFBL law. The PID controllers operate as follows:

$$e_{1_{ij}} = y_{ij} - y_{d_{ij}} \tag{5.78}$$

$$F_{d_n} = K_{P_{ij}} e_{1_{ij}} + K_{D_{ij}} \frac{de_{1_{ij}}}{dt} + K_{I_{ij}} \int_0^T e_{1_{ij}}.dt \tag{5.79}$$

$$e_{2_{ij}} = F_{a_{ij}} - F_{d_{ij}} \tag{5.80}$$

$$\bar{v}_{ij} = k_{p_{ij}} e_{2_{ij}} + k_{d_{ij}} \frac{de_{2_{ij}}}{dt} + k_{i_{ij}} \int_0^T e_{2_{ij}}.dt \tag{5.81}$$

with y_{ij} is the suspension travel experienced at the i^{th} forward longitudinal position and j^{th} lateral position of vehicle, where i may take either f(front) or r(rear), and j is either r(right) or l(left); are the $K_{P_{ij}}$ and $k_{p_{ij}}$ are the proportional gains of the controllers manipulating the i, j^{th} wheel and they correspond to the outer and inner loops respectively; similary $K_{I_{ij}}$ and $k_{i_{ij}}$ are the corresponding integral gains of the controllers; $K_{D_{ij}}$ and $k_{d_{ij}}$ are the derivative gains of the respective control loops; and T is the simulation time. In retrospect, the dynamics of each suspension is controlled by 6 PID controller gains and 4 feedback linearization gains. This gives a total of 40 controller gains or problem variables.

The FBL is augmented with same multi-loop PID controllers used in PID-based AVSS design with the objective of meeting the design specifications and performance index listed for full-car PID control (see section 3.2.3). As in the case of PID-based

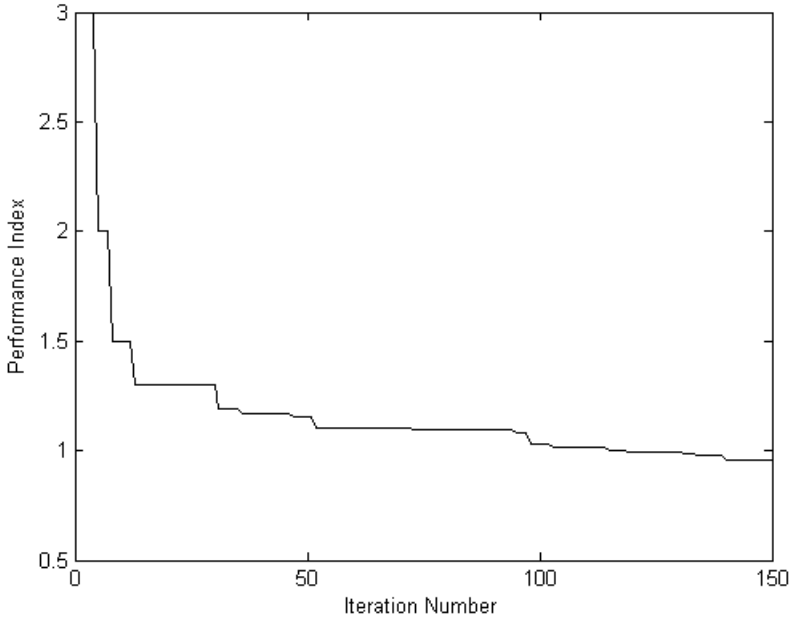

Figure 5.21: Convergence of performance index through PSO-based optimization for full-car intelligent controller

AVSS, the controller gains may be selected manually or through an optimization policy. In this control architecture, PSO-based controller tuning is performed as it produced the most consistent results in this research study as a whole. The algorithm steps are summarized in section 3.1.5.3. The only variation in this application is the number of control variables are now 40 and the cost function corresponds to the performance index of the full car model presented in Eq. (3.28) to (3.33): The controller gains are tuned manually and with the aid of PSO-based optimization. The configuration settings of the PSO algorithm are given in Table 5.3. The

Table 5.3: Optimization parameters for the PSO routine for the full-car intelligent controller

Routine	**PSO**
Population Size	100
Stopping Criteria	150 Iterations
Optimization	w_1 =0.5, w_2 =2
Parameters	w_3 =2

convergence history of the performance index through the implementation of PSO is presented in Figure 5.21. The initial condition for this routine corresponds to the set of gains attained through manual tuning. Figure 5.21 clearly indicates that

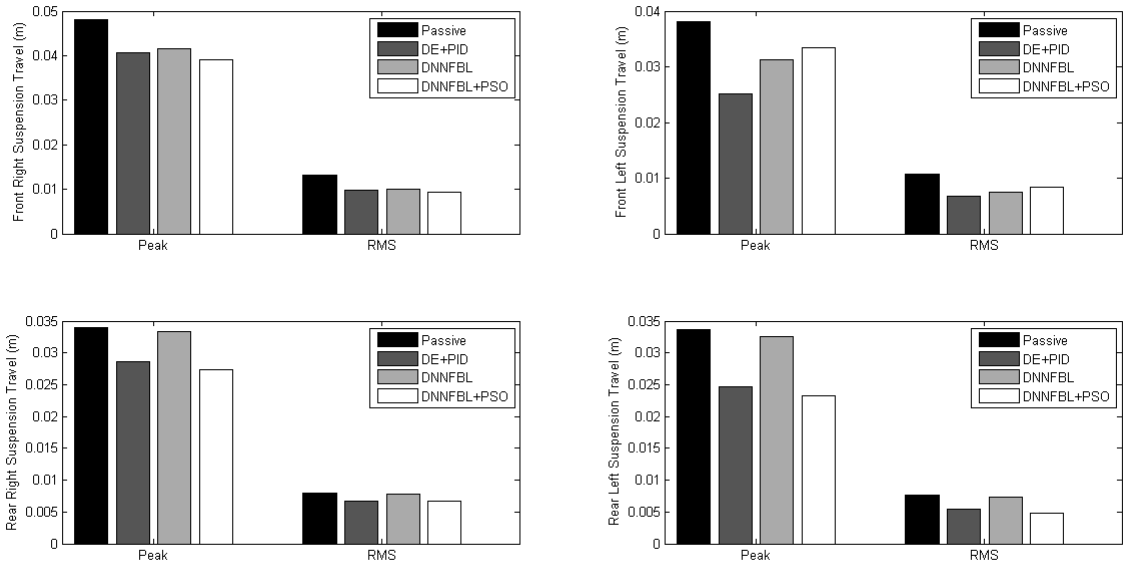

Figure 5.22: Bar graphs depicting the variation in suspension travel for each control law

optimization through PSO was successful in lowering the performance index by approximately 40%. However, careful study of each performance criterion must be studied to examine if the conflicting performance criteria have been resolved. The controller gains attained through both manual tuning and feedback linearization are listed in Table 5.4.

5.4 Simulation Results

This analysis conducts a study on the system response to a deterministic road bump disturbance with a profile described by Eqs. (2.90) to (2.93). A summary of the system performance through intelligent control is presented in Tables 5.5 and 5.6 as well as the bar graphs in Figures 5.22 to 5.25. As in the case of the full-car PID-based controller, suspension performance including suspension travel, tyre dynamic load and control input voltage are graphically reported in Figures 5.26 to 5.28 respectively for the rear right wheel as the system response was the worst at this wheel.

The suspension travel response for both the intelligent and optimal augmented intelligent controller produced a significant improvement to that of the PVSS. In both these cases the peak and RMS suspension travel was reduced substantially with the optimal case showing the best results with a further improvement of 10% in suspension travel RMS value and displayed noticeable lower peaks in the third and fourth oscillations. Additionally, the intelligent controller exhibited quicker settling

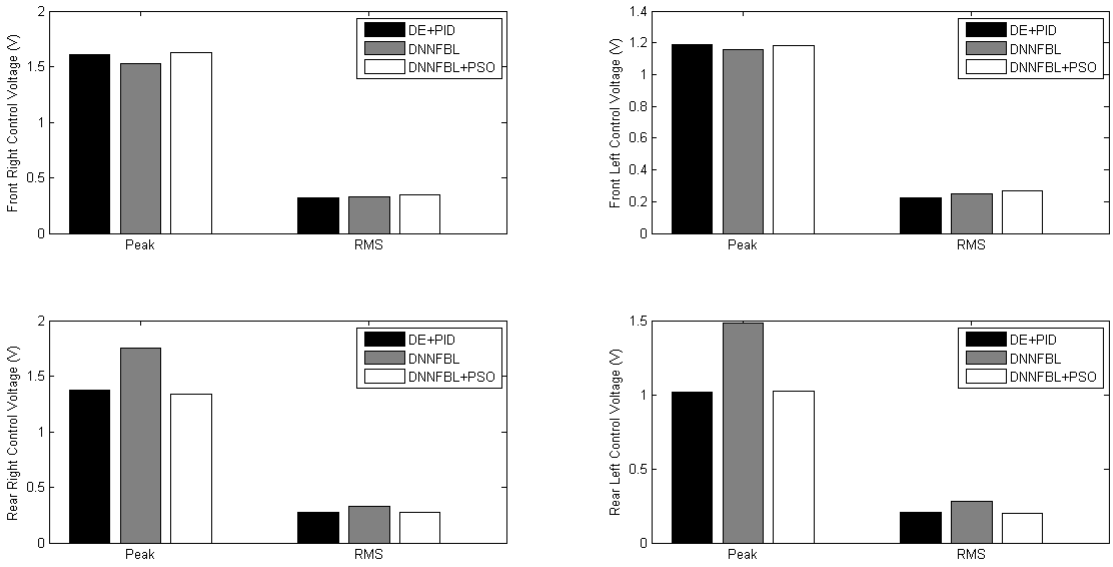

Figure 5.23: Bar graphs illustrating the difference in control input voltage for the proposed controllers

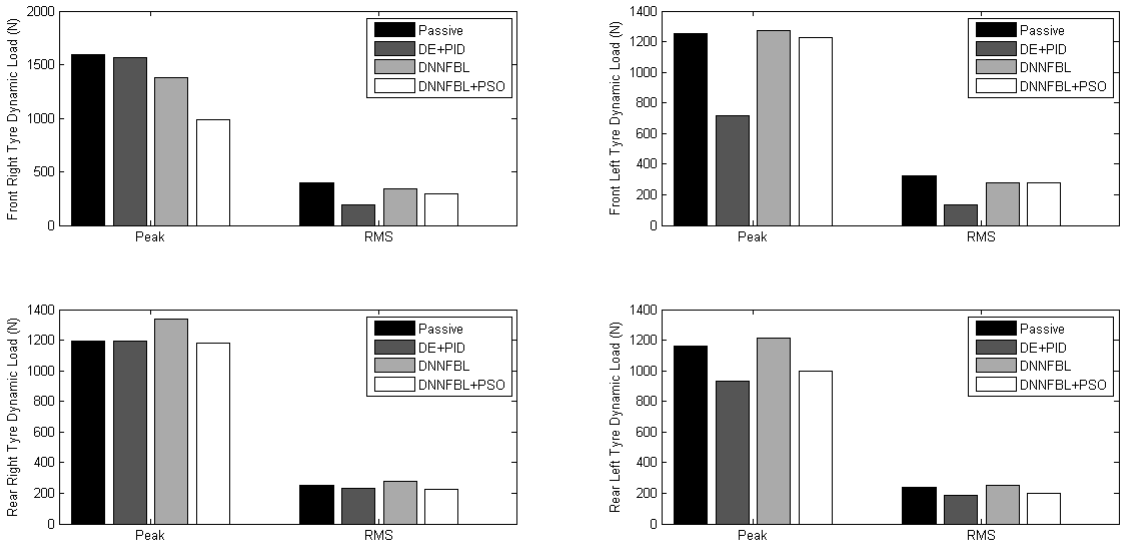

Figure 5.24: Bar graphs summarizing the road holding aspect for each control case

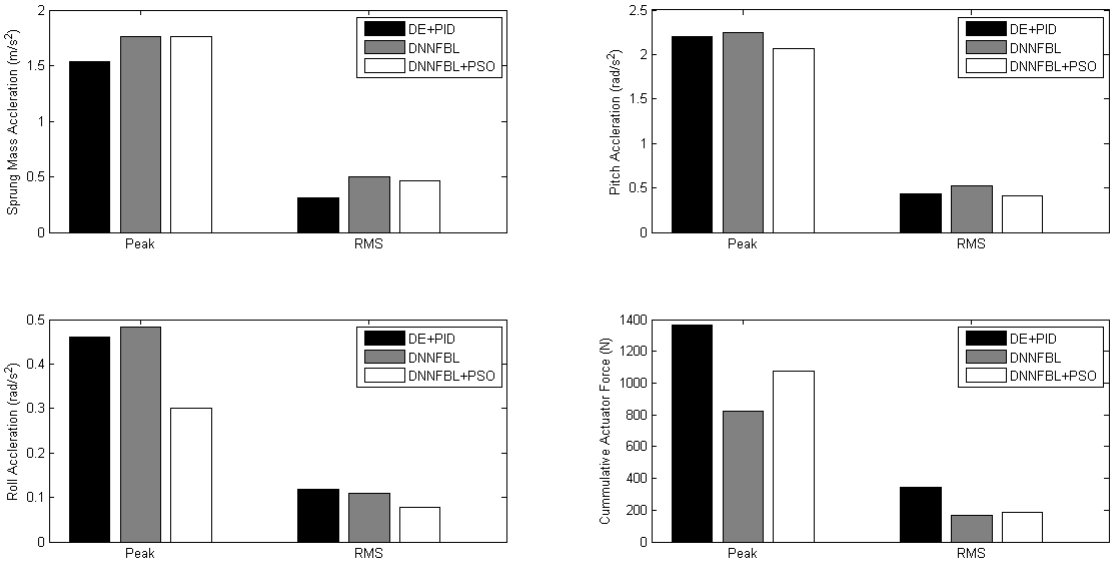

Figure 5.25: Quantitative information pertaining to the vehicle handling, ride comfort and actuator force

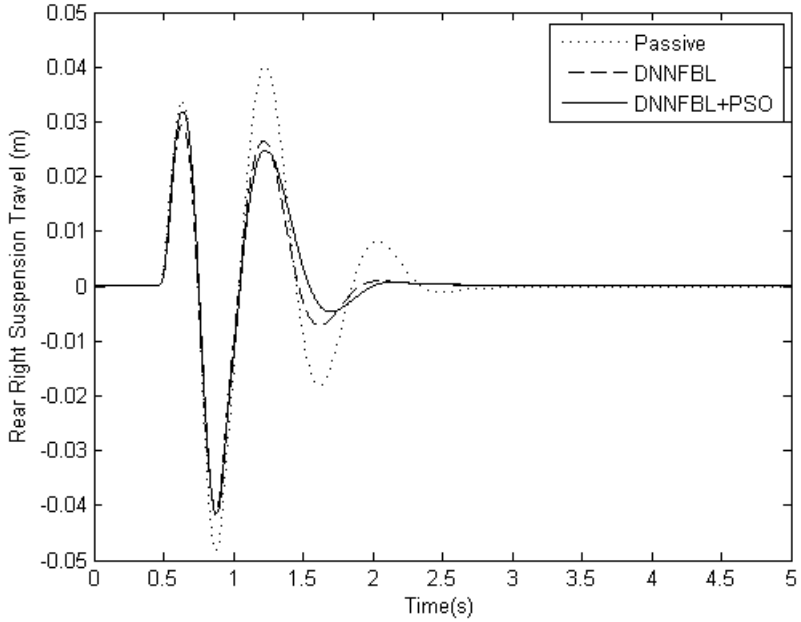

Figure 5.26: Suspension travel response through the implementation of intelligent control

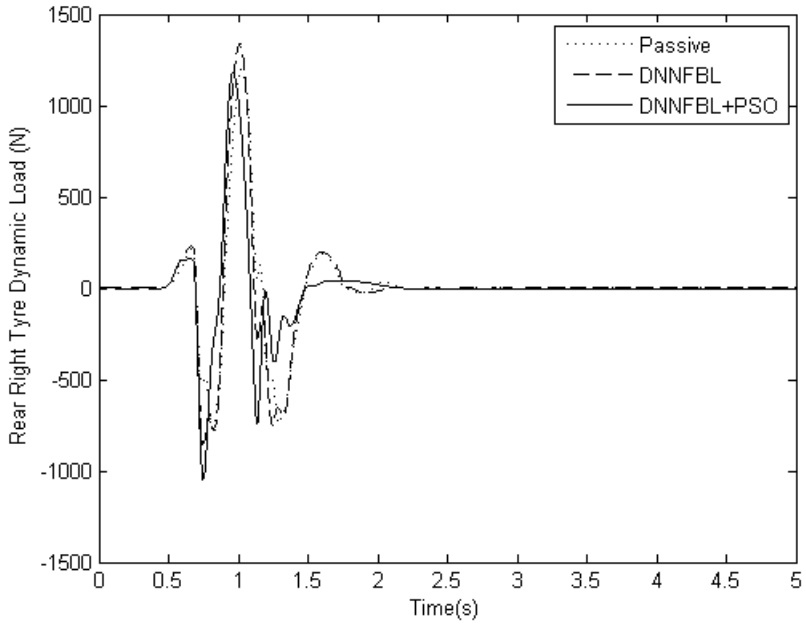

Figure 5.27: Comparative plot of the tyre dynamic load response for the proposed intelligent control schemes

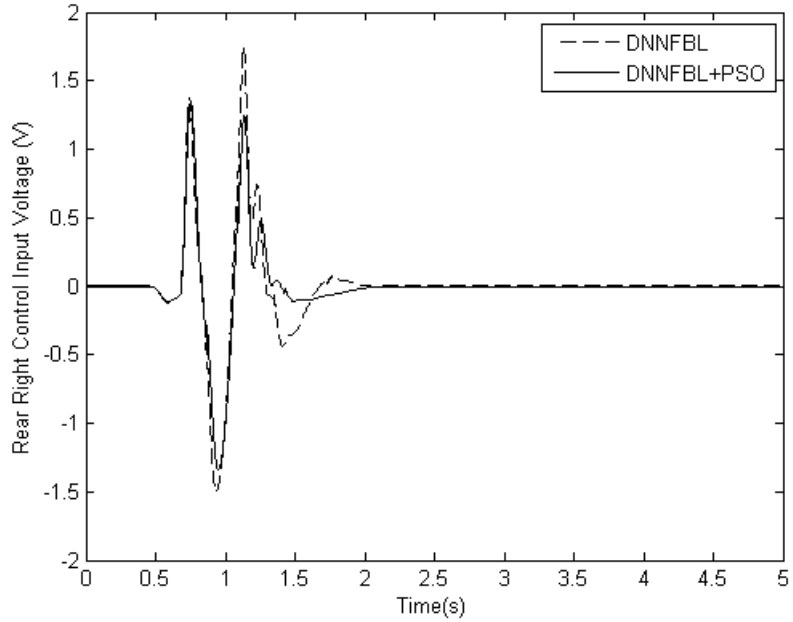

Figure 5.28: Ride comfort observed through the use of intelligent control and optimized intelligent control

Table 5.4: List of controller gains selected for full-car intelligent control

	Front Right Suspension System					
	Outer PID Loop Gains			Inner PID Loop Gains		
Technique	K_P	K_I	K_D	k_p	k_i	k_d
Manual	1114	205	-694	0.0025	0.00179	0
PSO	2540	103	-1051	0.0034	0.01102	3×10^{-9}
	Feedback Linerization Controller Gains					
Gains	$\lambda_{0_{r1}}$		$\lambda_{1_{r1}}$		$\lambda_{2_{r1}}$	
Manual	0		0		0.24	
PSO	0.001		0.001		0.24	
	Front Left Suspension System					
	Outer PID Loop Gains			Inner PID Loop Gains		
Technique	K_P	K_I	K_D	k_p	k_i	k_d
Manual	3071	21	769	0.0045	0.00334	0
PSO	2293	441	1421	0.0050	-0.00104	3×10^{-9}
	Feedback Linerization Controller Gains					
Gains	$\lambda_{0_{r2}}$		$\lambda_{1_{r2}}$		$\lambda_{2_{r2}}$	
Manual	0		0		0.24	
PSO	0.031		0.021		0.239	
	Rear Right Suspension System					
	Outer PID Loop Gains			Inner PID Loop Gains		
Technique	K_P	K_I	K_D	k_p	k_i	k_d
Manual	662	171	-650	0.0042	0.00252	0
PSO	11091	-1123	-606	0.0023	0.00818	3×10^{-9}
	Feedback Linerization Controller Gains					
Gains	$\lambda_{0_{r3}}$		$\lambda_{1_{r3}}$		$\lambda_{2_{r3}}$	
Manual	0		0		0.24	
PSO	0.003		0.001		0.0241	
	Rear left Suspension System					
	Outer PID Loop Gains			Inner PID Loop Gains		
Technique	K_P	K_I	K_D	k_p	k_i	k_d
Manual	7393	356	142	0.0043	0.00474	0
PSO	9211	229	1213	0.0009	0.00487	1×10^{-9}
	Feedback Linerization Controller Gains					
Gains	$\lambda_{0_{r4}}$		$\lambda_{1_{r4}}$		$\lambda_{2_{r4}}$	
Manual	0		0		0.24	
PSO	0.025		0.037		0.24	

Table 5.5: Summary of selected suspension performance incorporating the proposed intelligent controller

Technique	**Front Right Suspension Travel**(m)		**Front Left Suspension Travel**(m)	
	RMS	**Peak**	**RMS**	**Peak**
Passive	0.038	0.0107	0.048	0.0131
DNNFBL	0.040	0.0097	0.031	0.0075
DNNFBL+PSO	0.041	0.0100	0.033	0.0083
PID+DE	0.039	0.0094	0.025	0.0067
Technique	**Rear Right Suspension Travel**(m)		**Rear Left Suspension Travel**(m)	
	RMS	**Peak**	**RMS**	**Peak**
Passive	0.033	0.0079	0.033	0.0076
DNNFBL	0.033	0.0077	0.032	0.0072
DNNFBL+PSO	0.027	0.0066	0.023	0.0048
PID+DE	0.028	0.0067	0.024	0.0054
Technique	**Front Right Tyre Dynamic Load**(N)		**Front Left Tyre Dynamic Load**(N)	
	RMS	**Peak**	**RMS**	**Peak**
Passive	1594	395	1254	321
DNNFBL	1562	340	1271	280
DNNFBL+PSO	1374	292	1227	279
PID+DE	984	189	713	132
Technique	**Rear Right Tyre Dynamic Load**(N)		**Rear Left Tyre Dynamic Load**(N)	
Passive	1194	248	81158	240
DNNFBL	1335	279	1211	249
DNNFBL+PSO	1182	226	1000	201
PID+DE	1196	229	930	185

time than the PVSS. Moreover, the proposed intelligent controllers improved the system's transient response with fewer oscillations where it was observed that the response dampened out as soon as the disturbance was removed. Similar responses were observed at each of the wheels and this infers that the intelligent controllers were successful in improving suspension travel. These results are anticipated as the performance index used in both optimization and manual tuning placed large emphasis on suspension travel and hence as a consequence of lowering the performance

Table 5.6: Summary of selected suspension performance incorporating the proposed intelligent controller

Technique	**Front Right Control Input Voltage**(V)		**Front Left Control Input Voltage**(V)	
	RMS	**Peak**	**RMS**	**Peak**
DNNFBL	1.52	0.333	1.15	0.248
DNNFBL+PSO	1.62	0.345	1.18	0.267
PID+DE	1.61	0.318	1.18	0.225
Technique	**Rear Right Control Input Voltage**(V)		**Rear Left Control Input Voltage**(V)	
	RMS	**Peak**	**RMS**	**Peak**
DNNFBL	1.75	0.329	1.48	0.279
DNNFBL+PSO	1.34	0.276	1.02	0.197
PID+DE	1.37	0.278	1.01	0.204
Technique	**Pitch Acceleration** (rad/s^2)		**Roll Acceleration** (rad/s^2)	
	RMS	**Peak**	**RMS**	**Peak**
Passive	2.36	0.516	0.588	0.130
DNNFBL	2.24	0.523	0.483	0.108
DNNFBL+PSO	2.06	0.414	0.301	0.0784
PID+DE	1.62	0.314	0.328	0.0668
Technique	**Heave Acceleration** (m/s^2)		**Effective Hydraulic Force**(N)	
	RMS	**Peak**	**RMS**	**Peak**
Passive	2.44	0.648	N/A	N/A
DNNFBL	1.75	0.499	820	167
DNNFBL+PSO	1.75	0.466	1074	185
PID+DE	1.72	0.306	1363	342

Performance Index J			
Passive	DNNFBL	DNNFBL+PSO	PID+DE
5	3.2	0.98	1.1

index meant a reduction in suspension travel.

In relation to the tyre dynamic load, the non-optimized intelligent control scheme was unsuccessful in improving upon the PVSS in both RMS and peak values. The optimal-based intelligent controller did however produce a slight improvement in

peak tyre dynamic load. On the other hand, it did manage to substantially improve the RMS value and transient behaviour where its latter peaks were considerably lower than its counterparts. It also possessed a significantly less degree of chattering. At the front wheels, the tyre dynamic load of both intelligent control methods produced a noticeable augmentation from the PVSS. However, the rear left wheel produced the same outcome as the rear right wheel where the non-optimized case had not enhanced the PVSS. Even though the performance index has a considerable weighting on peak tyre dynamic load and other performance criterion, it does not necessarily imply that lowering the performance index would reduce that criterion. This is because these criteria are in conflict with one other and substantially lowering one criterion such as suspension travel might limit the degree of reduction in another criterion such as tyre dynamic load. However, the marginally positive results obtained for the optimized case infers that optimization was more successful in resolving the conflicting suspension performance criteria than the conventional manual tuning approach.

The control input voltage required to manipulate the output variables for the optimized case contained a marginally superior peak, RMS value and damping rate. A similar trend was detected at each wheel and this suggests that optimization was successful in both improving suspension performance and resolving the inherent conflicts associated with them. In contrast to control input voltage, the cumulative input force presented in Figure 5.29 was greater for the optimized case. In a sense, this is anticipated as larger control forces are required to inherently cancel out the detrimental effects of disturbances.

In relation to ride comfort, Figure 5.30 indicates that both intelligent controllers performed desirably well in this aspect with a considerable reduction in RMS and peak acceleration values. The the optimal intelligent controller outperformed the non-optimal controller by a sizeable extent. Additionally, the transient behaviour pertaining to the latter peaks, system damping rate and settling time of the implemented intelligent methodologies was superior to the passive case with the optimal scheme producing the best results in these aspects.

With regards to vehicle handling, Figure 5.31 illustrates that the non-optimized intelligent controller performed marginally better than the passive case with a slight decrease in peak and RMS values for pitch acceleration. Furthermore, no substantial enhancement in transient response was observed. Conversely, the optimized case

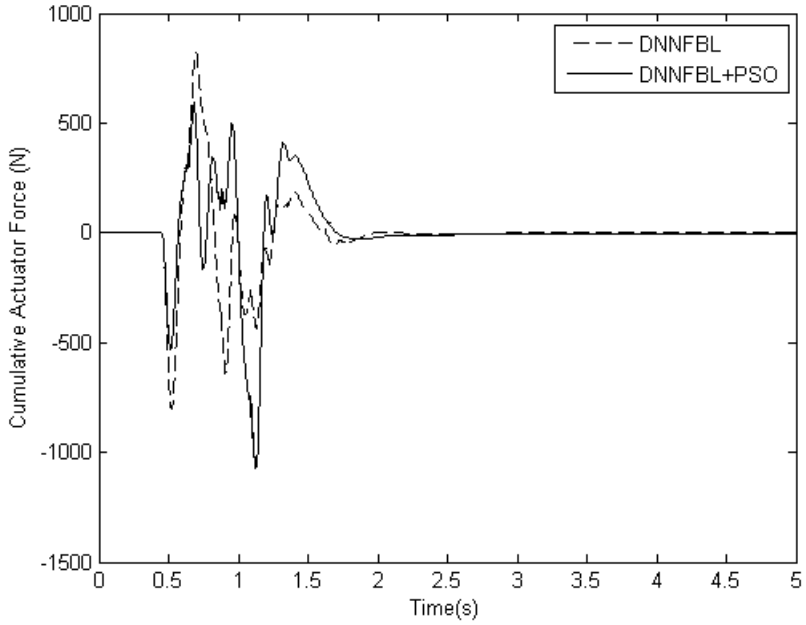

Figure 5.29: Cumulative actuator force produced in the employment of intelligent control

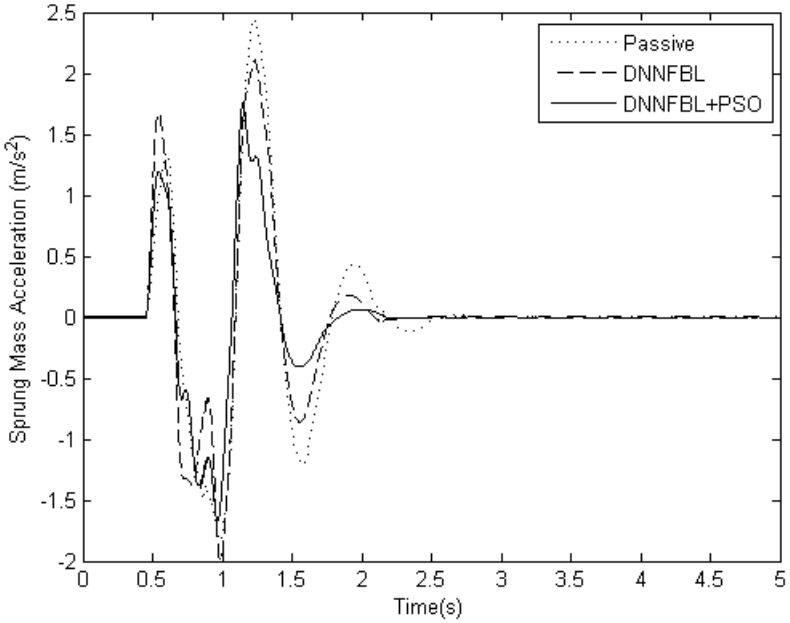

Figure 5.30: Ride comfort observed through the use of intelligent control and optimized intelligent control

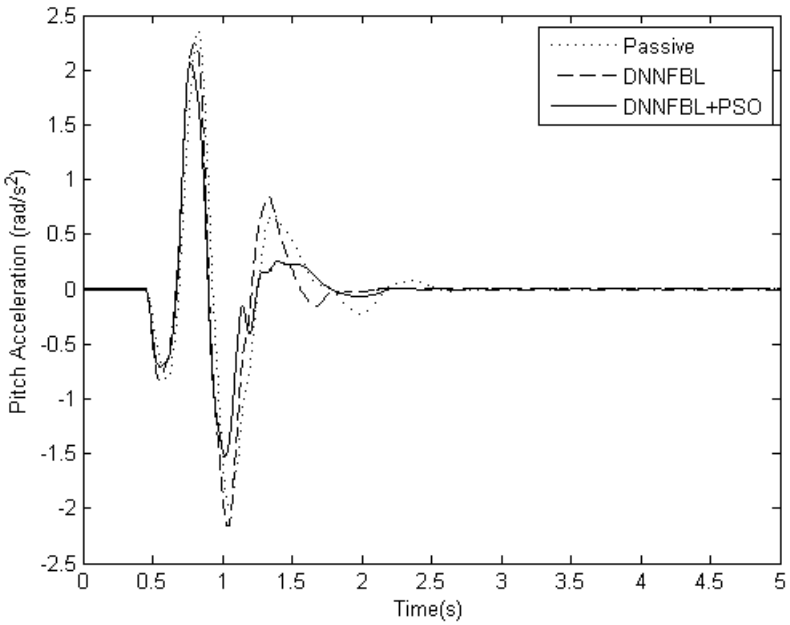

Figure 5.31: Vehicle handling characteristics as captured by pitch acceleration for the intelligent control scheme

was successful in lowering the peak and RMS values of pitch acceleration extensively. In addition, the implementation of optimality saw improved transient performance with a quicker settling time, less chattering and lower secondary peaks.

Pertaining to roll acceleration, Figure 5.32 shows the intelligent controller generated a significant improvement to that of the passive case with lower peaks, reduced RMS and improved transient characteristics. Furthermore, the application of optimization appreciably minimized the roll acceleration with a lower degree of chattering. The successful reduction in ride comfort and vehicle handling was projected as each of these criteria had significant weightings in the performance index. Moreover, the improvements of each suspension system performance criterion with optimization, infers that PSO and intelligent control was successful in resolving the trade-offs associated with suspension systems.

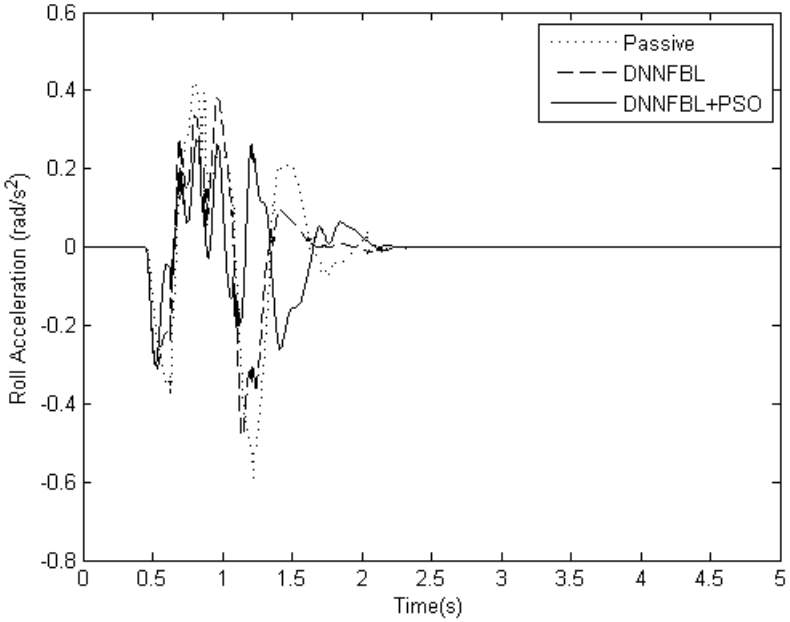

Figure 5.32: Vehicle handling features observed through roll acceleration for the intelligent control techniques

5.5 Sensitivity to Parameter Variations and Frequency-Domain Analysis

The response observed for the sinusoidal bump road profile was BIBO stable as all steady-state values ranged below 0.0001% of the peak values. One of the fundamental purposes of invoking intelligent control is to produce a system with a low sensitivity to parameter variations. Hence, it is vital that proposed intelligent control scheme be examined in relation to parameter variations. For a typical vehicle; inertia, tyre stiffness and damping, and vehicle speed are expected to change with variations in fuel, passenger numbers, tyre pressure and horizontal speed. These parameters tend to change by $\pm 20\%$.

Figures 5.33 and 5.34 show the response of the rear right suspension travel when the vehicle is subjected to the same road disturbance but with a variation of $\pm 20\%$ in mass, pitch inertia, roll inertia, tyre damping and stiffness coefficients and vehicle speed. These results clearly depict a BIBO stable system with steady-state values ranging below 0.0001% of peak values. For all variations except that of increased vehicle speed, transient behaviour was comparatively good with quicker settling times, damping rate and minimal oscillations. The poor transient response observed for

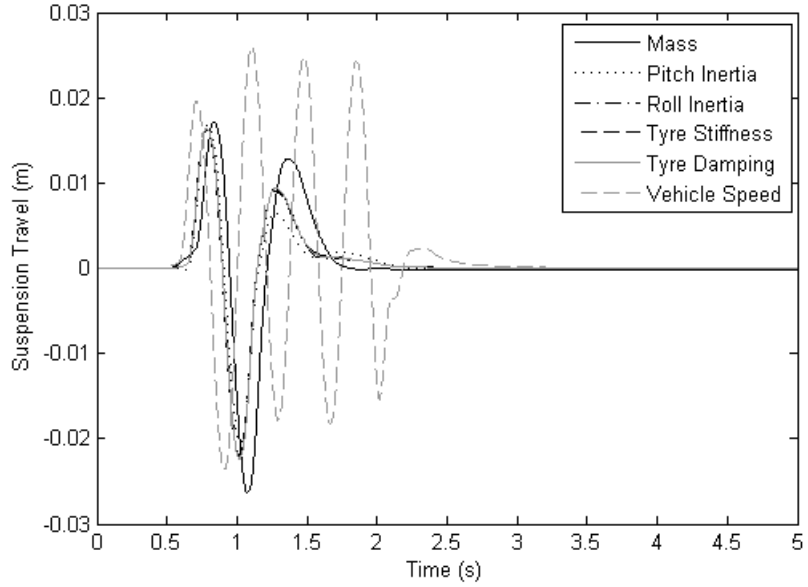

Figure 5.33: Suspension travel response for +20% variations in selected parameter

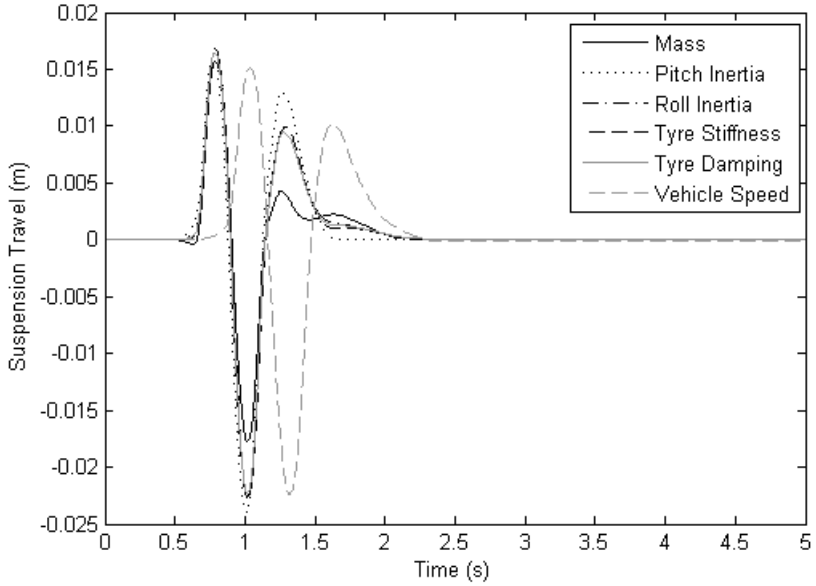

Figure 5.34: Suspension travel response for −20% variations in selected parameters

the 20% increase in vehicle speed may be resolved by implementing gain scheduling. It is also worth mentioning that the DNNFBL AVSS indicated quicker settling times than that of the PID-based AVSS case presented in section 3.2.6.

As in the case of full-car PID control (see section 3.2.6), frequency-domain analysis is performed in the range of $0.5Hz$ to $80Hz$ for ride comfort, vehicle handling and

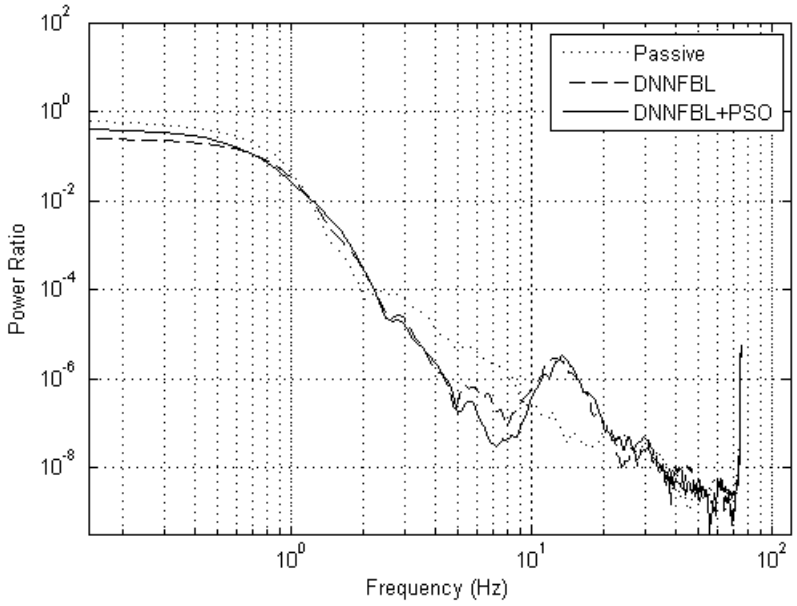

Figure 5.35: Frequency response of ride comfort for the full-car intelligent system in the region of anticipated sensitive frequencies

road holding. These cases are presented in Figures 5.35 to 5.38. The relevant parameter settings are summarized in Table 5.7.

Table 5.7: PSD frequency configuration for full-car intelligent controllers

Parameter	**Setting**
Computation	Algorithm Welch
Windowing Function	Hanning
Number of points included in fourier transform (NNFT)	1024
Length of Window (NWind)	256
Sampling Frequency	80Hz

Each of the frequency-domain plots indicated the 0-1Hz frequency range as the most sensitive as it contained the greatest power ratios. A sharp fall in power ratios were observed which indicated that the signals were almost completely attenuated in the high frequency range. However, a resonance peak did occur for ride comfort and vehicle handling in the vicinity of $10Hz$. Nevertheless, the power ratios were still low enough not to create any significant impact.

In the low-frequency region, which has the most significant impact; intelligent control showed the best improvement from PVSS. It achieved considerably better vehicle

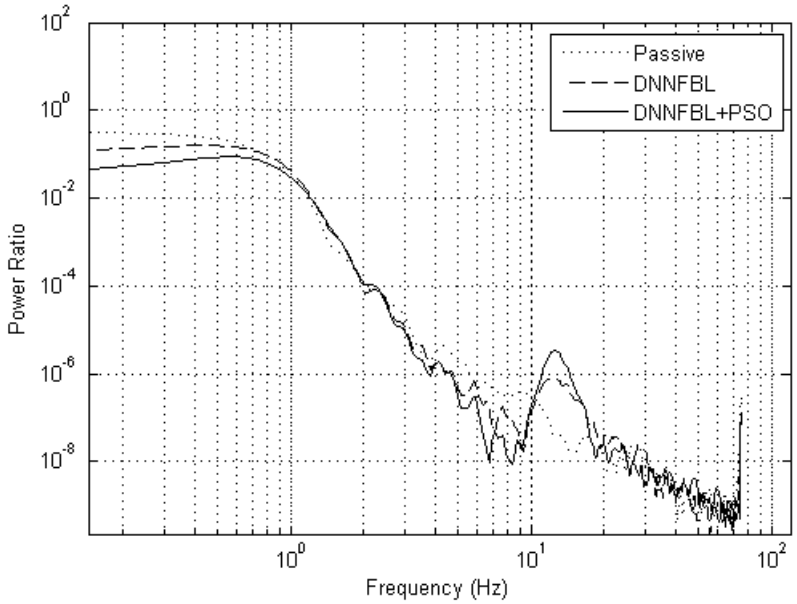

Figure 5.36: Frequency-domain analyses of vehicle handling for the full-car intelligent system with respect to pitch acceleration

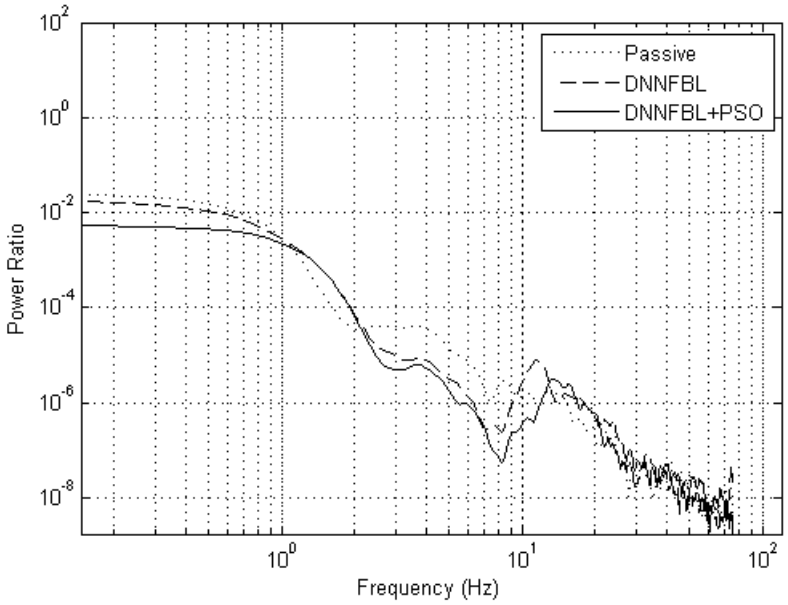

Figure 5.37: Examination of frequency response for roll acceleration for the full-car intelligent system

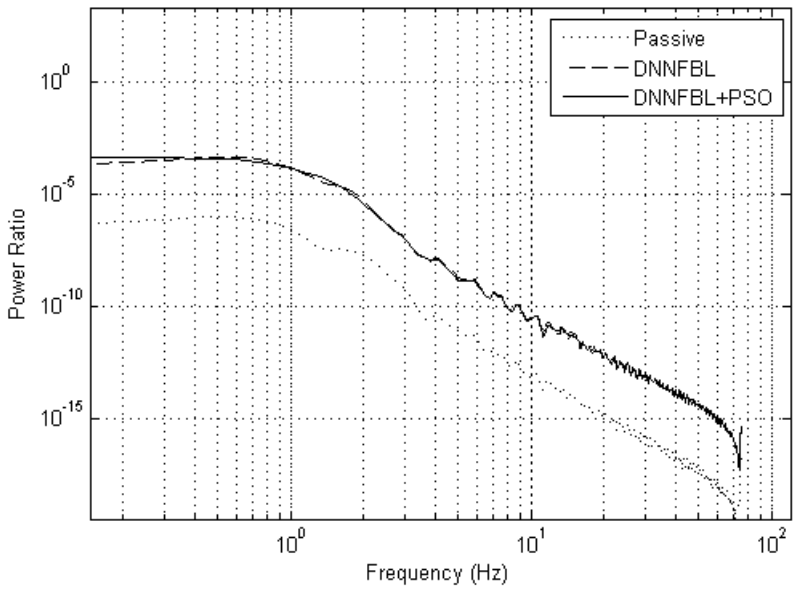

Figure 5.38: Road holding frequency-domain analyses

handling and road holding, whereas the non-intelligent case performed marginally better than it in ride comfort. Moreover, the optimal intelligent controller maintained a strong compromise between these conflicting criteria for this sensitive region.

5.6 Assessment in Relation to Benchmark PID Design

The proposed optimal intelligent controller outperformed each of the PID-based controllers in certain aspects of AVSS performance whilst performing marginally weaker in other. Its positive features include enhanced roll acceleration and suspension travel, and a lower degree of system chattering. With the intelligent control scheme, the suspension travel transient behaviour and settling time are considerably superior to that of all the PID-based controllers. Intelligent control produced a significant improvement in peak and RMS values of the roll acceleration and thus possessed better vehicle handling capabilities. Although the pitch acceleration of the intelligent control scheme had a similar peak as the best PID controller (the DE-based PID), it possessed improved transient behaviour with reduced settling times, quicker damping and smaller subsequent peaks. Thus, it may be concluded that the optimal intelligent controller was more successful in resolving the trade-offs between suspension travel, vehicle handling and ride comfort as opposed to all the

PID-based controllers.

The drawbacks of the proposed intelligent controller include a higher peak for body-heave acceleration than the PID, PID+MPSO and PID+CRS cases. It is however worth mentioning that this peak was marginally better than the PID+DE case, which was the best PID-based controller as it not only had the lowest overall performance index but was able to best resolve the AVSS trade-offs. However, even though the optimal intelligent control performed marginally better than the PID, PID+MPSO and PID+CRS in road holding at each wheel, it was still completely surpassed by the PID+DE case. Hence, the optimal intelligent controller was not able to resolve the AVSS trade-off between road holding and ride comfort to the extent to which the best PID-based controller (PID+DE) did. Nevertheless, it did perform marginally better than the other PID controllers in this respect.

In relation to control input voltage and cumulative actuator force, the optimal intelligent controller achieved marginally better results as compared to the PID, PID+MPSO and PID+MCRS cases. It had lower RMS and peak values with a lesser degree of chattering as compared to the best PID+DE case. This infers that the intelligent controller attained a better resolve between power consumption terms and other AVSS performance criteria. With regards to parameter sensitivity, the optimal intelligent controller showed a better sensitivity to parameter variations, lower settling time, RMS and peak values of suspension travels for both +20% and -20% change in selected suspension parameters.

The overall better characteristics of the intelligent controller may be attributed to several reasons. Firstly, the cancellation of system nonlinearities through the process of feedback linearization could have played a major role in improving system behaviour. Secondly, the nature of the optimization routine used for controller tuning is solely based on randomness and hence the results may be purely random and based on the nature of the problem. The latter reason does hold strong ground as the non-optimized intelligent controller produced poor road holding and ride comfort as compared to the PID cases. It did however contain superior suspension travel, and power consumption characteristics which may be credited to the first reason suggested. In addition, the adaptive nature of the controller gives it the ability to adapt based on the nature of the disturbance, system response and input frequencies. As a result, this inherent characteristic provides a major improvement in system robustness and performance.

5.7 Summary

The intelligent-based controller design was deemed successful in improving AVSS performance from that of the passive case. Implementation of the optimization algorithms saw a considerable improvement in system response with a better resolve between conflicting performance criteria than its non-optimal counterpart. The best intelligent controller was proven to be superior to the best PID-based controller as it produced better settling time, less chattering and enhanced roll acceleration with similar control input voltage and actuator force produced. Sensitivity to parameter variations was kept low and the system remained BIBO stable for a wide range of changes in inertia, tyre pressure and vehicle speed. The system performed adequately and maintained a good compromise between the conflicting performance criteria in the low frequency ranges.

6 Conclusions and Recommendations

6.1 Conclusions

The study of this research involves developing a nonlinear electrohydraulic AVSS which aims to resolve the conflicts in performance criteria (i.e. ride comfort, road holing, vehicle handling, suspension travel, and power consumption). Two controllers have been proposed for this task and analysis was performed on both quarter-car and full-car models. The quarter-car model was investigated as it serves as a foundation for the development and implementation of the more realistic full-car model. Moreover, numerous studies have been performed on the quarter-car AVSS as hence it will provide an adequate basis of comparison. The models include nonlinear components and incorporate actuator dynamics such that realism, which is lacking in most research studies is achieved.

The first control scheme involves the most widely implemented PID controller, which is now tuned using global optimization methods which is based on a performance index that addresses all the vehicle conflicting performance criteria. Optimization algorithms implemented and later compared include CRS, DE, GA, PSO, and PS; of which DE performed the best in addressing suspension design trade-offs. These algorithms operate by randomly searching a defined space where a potentially good solution might exist. In each iterations the new solutions are generated and older ones are discarded according to certain criteria. To account for stability and chatter of the actuator, multiple control loops are formulated to both regulate the control variable and maintain actuator integrity. For full-car analysis modified versions of PSO and CRS were implemented with successful improvements over their predecessors. However, DE still achieved superior performance over all the proposed optimization methods with both superior performance index and better compromise between suspension trade-offs.

The second control technique involved an intelligent control method that follows an indirect adaptive approach, where dynamic neural networks are set to learn the dynamics of the plant. Network training was achieved through global optimization approaches. Thereafter, the feedback linearization nonlinear control law is applied to the trained dynamic neural network in conjunction with conventional PID control. The resulting hybrid controller is tuned through global optimization technique with the intent of improving system performance and finding a suitable compromise between design criteria.

Application of the second control law achieved certain improvements over the PID control systems, whilst suffering drawbacks in others. Similar performance indices were attained through both methods, but the manner in which inherent conflicts were addressed, and the system's response in terms of transient behaviour varied substantially.

6.2 PID Control through Global Optimization-Based Tuning

The application of global optimization strategies to a multi-loop PID controller produced improved performance index and yielded a better compromise between conflicting suspension performance criteria for both the quarter-car and full-car models as compared to the its uncontrolled and manually-tuned counterparts. DE in particular proved to be the best optimization procedure for improving system performance and resolving design trade-offs as compared to other proposed optimization algorithms for quarter-car and full-car AVSS. The performance of GA, PSO and CRS followed marginally close with slightly weaker performance indices and notably larger peak and RMS values in each performance aspect. PS on the other hand produced a solution with improved ride comfort, but poorer transient behaviour with increased settling times and chattering. In each algorithms enhanced ride comfort, road holding, transient behaviour and settling time from those of the manual and PVSS was achieved at the cost of larger control input voltage and applied force, which is anticipated as larger control inputs and controller forces are required to increasingly cancel out the effects of disturbance signals. System performance through optimization achieved comparatively superior results for more severe disturbance as those that were reported in previous studies. In the frequency domain, the DE still

manage to maintain an edge in ride comfort and road holding over its manual and PVSS counterparts. System response also showed consistency in transient behaviour and performance for variations in parameters that occur due to the influx of fuel, payload, tyre pressure and vehicle speed.

In the full-car configuration, DE still proved to be the most consistent as it was the only algorithm that maintained a desirable compromise and satisfactory performance in ride comfort, vehicle handling, suspension travel, road holding and power consumption. Even though the modified variants of PSO and MCRS outperformed their predecessors with considerably better performance index. They did not however achieve the effectiveness of the DE algorithm. Like the manually-tuned case, they displayed the inability to resolve all conflicting performance criteria, but only managed an improvement over the manually-tuned and PVSS in aspects of ride comfort, vehicle handling and suspension travel, whilst suffering a major drawback in road holding. Nevertheless, their positive output was as a result of greater flexibility in searching the solution space, where regions around the best solution in each iteration was efficiently explored. The successful performance of DE was attributed to the structure of its algorithm; which permits efficient exploration of the search space, and through certain acceptance conditions only replaces weaker solutions if and only if better solutions are found. In contrast the other algorithms lack these properties and replace and add new solutions according to weaker formulations without any conditions for these tasks.

6.3 Intelligent Control

DNN were able to successfully learn the quarter-car's system dynamics through PSO and DE-based learning algorithms. The training results were close to those achieved for static neural networks that were reported in the literature. GA, CRS and PS could not train these algorithms to sufficient level and were discarded. As opposed to quarter-car and full-car controller tuning, DNN training involves significantly larger degree of variables that are to be computed and the scope proved too challenging for GA, CRS and PS to manage. This was inherently due to the nature of these algorithms, which poses limited exploration capabilities, where solution are not necessarily generated to directly move closer to the regions of better solutions. The PSO performed noticeably better than the DE in this aspect and this was

attributed to the nature of the DNN model and the random nature of the algorithm.

Controller tuning of the hybrid DNNFBL with PID control proved rather cumbersome and did not produce a significant improvement to the uncontrolled system. Augmentation of the hybrid neuro-PID controller with global optimization-based tuning enhanced system performance and better resolved the conflicting performance criteria as compared to its manually-tuned counterparts for both quarter-car and full-car models. PSO performed better and this was attributed to the randomness of these algorithms and the better performance of PSO in system identification, which had a more pronounced impact on the indirect adaptive control law than that of the DE-trained DNN. As the PSO performed the best it was solely incorporated in the full-car intelligent controller, of which system identification matched that of the quarter-car system and intelligent control yielded a suitable compromise between conflicting performance criteria, which was substantially better than PVSS.

In relation to PID control, the quarter-car intelligent controller attained smoother response with minimal chattering. The system response in each aspect remained marginally similar to that of PID control, but the settling time of the intelligent controller was considerably better than the PID-controlled case. In full-car configuration the intelligent controller performed better in certain aspects such as vehicle handling, suspension travel, control force, transient behaviour and settling time; and lacked over the PID in terms of road holding. Moreover, in terms of parameter variations, the intelligent controller produced lower steady-state errors in parameter variations in the case of the quarter-car systems, and maintained better transient performance over the PID-based controllers. In the frequency domain, they also reported a better compromise between vehicle handling, ride comfort and road holding over that of the PID controller. These results indicate that the adaptive characteristic of the DNNFBL controller as well as its task of cancelling system nonlinearities are a pivotal properties that improve AVSS performance.

6.4 Recommendations

The proposed improvements and further research that is essential to see this work implemented in real life systems involves:

1. Creating an experimental rig to validate the results of the computational solutions. A single wheel rig could be used to validate quarter-car control laws, but full-car models that included vital coupling, pitch and roll dynamics would be more realistic.

2. Implementing gain scheduling to resolve the steady-state errors and transient behaviour associated with variations in vehicle speed.

3. Testing the controllers for various types of disturbances included rough road disturbance inputs, potholes, multiple bumps and high speed cornering.

4. Designing a fault-tolerant control that accounts for system uncertainties, deteriorations and failed components that can be implemented as it addresses the most troubling issues in implementation of AVSS.

5. The entire research may be re-conducted to simultaneously handle various types of disturbances including a variety of bumps, rough roads and pot holes. In this case, the performance index will contain additional terms which measure the systems performance subjected to various disturbances as opposed to just a single disturbance.

6. As an alternative to using PID after feedback linearization is complete, linear control methods that includes multiple feedback terms such as H_∞ and H_2 control may be used to improve system performance. Optimal control policies such as LQG and LQR may be also applied after feedback linearization to find the best compromise between conflicting performance criteria.

References

Akcay, H. and Turkay, S. (2011). "Influence of Tire Damping on Actively Controller Quarter-Car Suspensions." ASME Journal of Vibration. Acoustics. vol. 133, no. 5.

Al-Holou, N., Lahdhiri, T., Weaver, J., and Al-Abbas, F. (2002). "Sliding Mode Neural Network inference Fuzzy Logic Control for Active Suspension System." IEEE Transactions on Fuzzy Systems, vol. 10, no. 2, pp. 234–246.

Al Seyab, R. and Cao, Y. (2008). "Differential Recurrent Neural Network Based Predictive Control." Computers & Chemical Engineering, vol. 32, no. 7, pp. 1533–1545.

Aldair, A.A. and Wang, W.J. (2011). "Neural Controller Based Full Vehicle Nonlinear Active Suspension Systems with Hydraulic Actuators." International Journal on Control and Automation, vol. 4, no. 2, pp. 79–94.

Alfi, A. and Fateh, M.M. (2011). "Identification of Nonlinear Systems Using Modified Particle Swarm Optimization: A Hydraulic Suspension System." Vehicle System Dynamics: International Journal of Vehicle Mechanics and Mobility, vol. 49, no. 6, pp. 871–887.

Ali, M. (1994). "Some Modified Global Optimization Algorithm with Applications." UK: PhD Dissertation Loughborough University.

Ali, M.M., Storey, C. and Törn, A. (1997). "Application of Stochastic Global Optimization Algorithms to Practical Problems 1." Journal of Optimization Theory and Applications, vol. 95, no. 3, pp. 545–563.

Aly, A.A. (2011). "PID Parameters Optimization Using Genetic Algorithm Technique for Electrohydraulic Servo Control System." Intelligent Control and Automation, vol. 2, no. 1, pp. 69–76.

Amani, A.M., Sedigh, A.K. and Yazdanpanah, M.J. (2004). "A QFT Approach to Robust Control of Automobile Active Suspension." Proceedings of the 5th Asian

Control Conference (*ASCC'04*), Melbourne, Australia, 20-23 July 2004, vol. 1, no. 1, pp. 604–610.

Becerikli, Y., Konar, A.F. and Samad, T. (2003). "Intelligent Optimal Control with Dynamic Neural Networks." Neural Networks: The Official Journal of the International Neural Network Society, vol. 16, no. 2, pp. 251–259.

Behera, L and Kar, B (2003) "Intelligent Systems and Control, Principles and Applications." USA: Oxford Higher Education.

Chamseddine, A., Raharijaona, T. and Noura, H. (2006). "Sliding Mode Control Applied to Active Suspension Using Nonlinear Full Vehicle and Actuator Dynamics." Proceedings of the 45^{th} IEEE Conference on Decision and Control, San Diego, CA, USA, 13-15 Dec. 2006 pp. 3597–3602.

Chen, H. and Guo, K.H. (2005). "Contrained H_∞ Control of Active Suspensions: An LMI Approach." IEEE Transactions Control System Technology, vol. 13, no. 3, pp. 414-421.

Chen, S., Zhou, H., Liu, H. and Yao, M. (2011). "Optimal Design of Active Suspension Based on LQG Control without Road Input Signal." Proceedings of the 4^{th} International Conference on Intelligent Computation Technology and Automation, (*ICICTA'11*), Shenzhen, Guangdong 28-29 March 2011, no. 1, pp. 456–459.

Chiou, J.S., Tsai, S.H. and Liu, M.T. (2012). ""A PSO-based Adaptive Fuzzy PID-Controllers." Simulation Modelling Practice and Theory, vol. 26, pp. 49–59.

Corona, D., Giua, A. and Seatzu, C. (2004). "Optimal Control of Hybrid Automata: Design of a Semiactive Suspension." Control Engineering Practice, vol. 12, no. 10, pp. 1305–1318.

Crews, J.H., Mattson, M.G. and Buckner, G.D. (2011). "Multi-objective Control Optimization for Semi-active Vehicle Suspensions." Journal of Sound and Vibration, vol. 330, no. 23, pp. 5502–5516.

Dahunsi, O.A. and Pedro, J.O. (2010). "Neural Network-Based Identification and Approximate Predictive Control of a Servo-Hydraulic Vehicle Suspension System." Engineering Letters, vol. 18, no. 4.

Dahunsi, O.A. and Pedro, J.O. (2011). "System Identification and Neural Network based PID Control of Servo Hydraulic Vehicle Suspension System." SAIEE Africa Research Journal, vol. 101, no.3, pp. 93-105.

Du, H. and Zhang, N. (2007). "Control of Active Vehicle Suspensions with Actuator Time Delay." Journal of Sound and Vibration, vol. 301, no. 1-2, pp. 236–252.

Ekoru, J.E.D. and Pedro, J.O. (2013). "Proportional-Integral-Derivative Control of Nonlinear Half-car Electro-hydraulic Suspension Systems ." Journal of Zhejiang University-SCIENCE A(Applied Physics and Engineering), vol. 14, no. 6, pp. 401–416.

Ekoru, J.E.D., Dahunsi, O.A., and Pedro, J.O. (2011). "PID Control of a Nonlinear Half-Car Active Suspension System via Force Feedback." Proceedings of the $10th$ IEEE International Control Conference (*Africon 2011*), Livingstone, Zambia, 13-15 September 2011, pp. 1–6.

Elbayomy, K.M., Zongxia, J. and Huaqing, Z. (2008). "PID Controller Optimization by GA and Its Performance on the Electro-hydraulic Servo Control System." Chinese Journal of Aeronautics, vol. 21, no. 1, pp. 378–384.

ElMadany, M.M., Abduljabbar, Z. and Arabia, S. (1990). "Design and Evaluation of Advanced Suspension Systems for Truck Ride Comfort." Computers & Structures, vol. 36, no. 2, pp. 321–331.

Eski, I. and Yildirim, S. (2009) "Vibration Control of Vehicle Active Suspension System using a New Robust Neural Network Control System." Simulation Modelling Practice and Theory, vol. 17, no. 5, pp. 778–793.

European Commission. (2002). "Directive 2002/44/EC of the European Parliament and the Council of 25 June 2002 on the Minimum Health and Safety Requirements Regarding the Exposure of Workers to the Risk Arising From Physical Agents (Vibration)." Official Journal of the European Communities, Luxembourg.

Fallah, M., Bhat, R. and Xie, W.F. (2009). "H_∞ Robust Control of Active Suspensions: A Practical Point Of View ." Proceedings of the 2009 American Control Conference (*ACC'09*), St Louis, MO, USA pp. 1385–1390.

Fateh, M. and Zirkohi, M. (2011). "Adaptive Impedance Control of a Hydraulic Suspension System using Particle Swarm Optimization ." Vehicle System Dynamics: International Journal of Vehicle Mechanics and Mobility, vol. 49, no. 12, pp. 1951–1965.

Garces, F.R., B, V.M., Kambhampati, C. and Warwick, K. (2003). "Strategies for Feedback Linearization A Dynamic Neural Network Approach." London: Oxford Higher Education.

Gillespie, T.G. (1992). "Fundamentals of Vehicle Dynamics." Warrendale: Society of Automotive Engineers.

Griffin, M.J. (2007) "Discomfort from Feeling Vehicle Vibration." Vehicle System Dynamics, vol. 45, no. 7-8, pp. 679–698.

Guclu, R and Gulez, K (2008) "Neural Network Control of Seat Vibrations of a Non-linear Full Vehicle Model using PMSM." Mathematical and Computer Modelling, vol. 47, no. 11-12, pp. 1356–1371.

Guclu, R. and Gulez, K. (2010). "Neural Network Control of Non-linear Full Vehicle Model Vibrations." Vibration Control, Edited by Mickael Lallart, Publisher: Sciyo, Chapters, Published August 18, 2010, no. September.

Gupta, M.M., Jin, L. and Homma, N. (2003). "Static and Dynamic Neural Networks, From Fundmamentals to Advanced Theory." Hoboken, New Jersey, USA: John Wiley & Sons, Inc.

Ha, I.J. and Gilbert, E.G. (1986) "A Complete Characterization of Decoupling Control Laws for a General Class of Nonlinear Systems." IEEE Transactions on Automatic Control, vol. 31, no. 9, pp. 823–830.

Hayakawa, K., Matsumoto, K., Yamashita, K., Suzuki, Y., Fujimori, K. and Kimura, H. (1999). "Robust H_∞ Feedback Control of Decoupled Automobile Active Suspension Systems." Automat. Contr, vol. 44, no. 1, pp. 392-396.

He, Y. and McPhee, J. (2005). "Multidisciplinary Design Optimization of Mechatronic Vehicles with Active Suspensions." Journal of Sound and Vibration, vol. 283, no. 1-2, pp. 217–241.

Hrovat, D. (1997). "Survey of Advanced Suspension Developments and Related Optimal Control Applications ." Automatica, vol. 33, no. 10, pp. 1781–1817.

Huang, C.M., Yen, J.Y. and Chen, M.S. (2000). "Adaptive Nonlinear Control of Repulsive Maglev Suspension Systems." Control Engineering Practice, vol. 8, no. 12, pp. 1357–1367.

ISO2631. (2003). "Mechanical Vibration and Shock - Evaluation of Human Exposure to Whole-Body Vibration - Part 1: General Requirements ." Geneva, Switzerland: International Organization for Standardization.

ISO8608. (1995). "Mechanical Vibration - Road Surface Profiles -Reporting of Meansured Data." Geneva, Switzerland: International Organization for Standardization.

Isidori, A. (1989). "Nonlinear Control System." Springer-Verlag, Berlin.

Jelali, M. and Kroll, A. (2003). "Hydraulic Servo-Systems: Modelling, Identification and Control." Springer-Verlag, Londom.

Jeżowski, J., Bochenek, R. and Ziomek, G. (2005). "Random Search Optimization Approach for Highly Multi-Modal Nonlinear Problems." Advances in Engineering Software, vol. 36, no. 8, pp. 504–517.

Kaddissi, C., Saad, M. and Kenne, J.P. (2009). "Interlaced Backstepping and Integrator Forwarding for Nonlinear Control of an Electrohydraulic Active Suspension." Journal of Vibration and Control, vol. 15, no. 1, pp. 101–131.

Kaelo, P. and Ali, M.M. (2007)."Differential Evolution Algorithms using Hybrid Mutation, Computational Optimization and Application."Computational Optimization and Application, vol. 4, no. 2, pp. 231–246.

Kim, M.Y. and Lee, C-O. (2008). "An Experimental Study on the Optimization of Controller Gains for an Electrohydraulic Servo System Using Evolution Strategies." Control Engineering Practice, vol. 14, no. 1, pp. 137–147.

Kloiber, T., Koch, G. and Lohmann, B. (2010). "Modified Optimal Control of a Nonlinear Active Suspension System." 49^{th} IEEE Conference on Decision and Control (*CDC*), pp. 5572–5577.

Kolda, T. and Lewis, R.M. and Torczon, V. (2003). "Optimization by Direct Search: New Perspective on Classical and Modern Methods ." SIAM Review, vol. 45, no. 3, pp. 385–482.

Koshkouei, A.J. and Burnham, K.J. (2008). "Sliding Mode Controllers for Active Suspensions." Proceedings of the 17^{th} IFAC World Congress: The International Federation of Automatic Control (*IFAC'08*), COEX, Seoul, Korea, 6-11 July 2008, vol. 17, pp. 3416–3421.

Kumar, M.S. and Vijayarangan, S. (2007). "Analytical and Experimental Studies of Active Suspension Systems of Light Passenger Vehicle Base on Ride Comfort." Mechanika, vol. 65, no. 3, pp. 34–41.

Li, F. (2011) "Dynamic Neural Network Based Nonlinear Control of a Distillation Column." Intelligent Control and Automation, vol. 2, no. 3, pp. 383–387.

Lian, R.J. (2013) "Enhanced Adaptive Self-Organizing Fuzzy Sliding-Mode Controller for Active Suspension Systems." IEEE Transactions on Industrial Electronics, vol. 60, no. 3, pp. 958–968.

Lin, J., Lian, R.J., Huang, C.N. and Sie, W.T. (2009). "Enhanced Fuzzy Sliding Mode Controller for Active Suspension Systems." Mechatronics, vol. 19, no. 7, pp. 1178–1190.

Lin, J.S. and Huang, C.J. (2004). "Nonlinear Backstepping Active Suspension Design Applied to a Half-Car Model." Vehicle System Dynamics, vol. 42, no. 6, pp. 373–393.

Lu, S., Ximing, C. and Jun, Y. (2007). "Genetic Algorithm-based Optimal Vehicle Suspension Design using Minimum Dynamic Pavement Load as a Design Criterion." Journal of Sound and Vibration, vol. 301, no. 1-2, pp. 18–27.

Marzbanrad, J., Ahmadi, G., Zohoor, H. and Hojjat, Y. (2004). "Stochastic Preview Control of a Vehicle Suspension." Journal of Sound and Vibration, vol. 275, no. 3-5, pp. 973–990.

Menon, P.P., Bates, D.G., Postlethwaite, I., Marcos, A., Fernandez, V. and Bennani, S. (2008). "Worst Case Analysis of Control Law for Re-entry Vehicles Using Hybrid Differential Evolution." Berlin: Advances in Differential Evolution: Studies in Computational Intelligence, Springer, vol. 143.

Merritt, H.E. (1967). "Hydraulic Control Systems." Technology and Engineering, John Wiley and Sons, New York.

Metered, H., Bonello, P. and Oyadiji, S.O. (2010). "An Investigation into the use of Neural Networks for the Semi-Active Control of a Magnetorheologically Damped Vehicle Suspension." Proceedings of the Institution of Mechanical Engineers, Part D: Journal of Automobile Engineering, vol. 224, no. 7, pp. 829–848.

Minsta, H.A., Venugopal, R., Kenné, J-P. and Belleau, C. (2012) "Feedback Linearization-Based Position Control of an Electrohydraulic Servo System With Supply Pressure Uncertainty." IEEE Transactions of Control Systems and Technonlogy, vol. 20, no. 4, pp. 1092–1099.

Moon, SY and Kwon, WH (1998) "Genetic-based Fuzzy Control for Half-car Active Suspension Systems." International Journal of Systems Science, vol. 29, no. 7, pp. 699–710.

Nagaraj, B. and Vijayakumar, P. (2011). "A Comparative Study of PID Controller Tunning using GA, PSO, EP and ACO." Journal of Automation, Mobile Robotics and Intelligent Systems, vol. 5, no. 2 pp. 305–313.

Nanayakkara, V.K., Ikegami, Y. and Uehara, H. (2002). "Evolutionary Design of Dynamic Neural Networks for Evaporator Control." vol. 25, pp. 813–826.

Nϕrgaard, M., Ravn, O., Poulsen, N.K. and Hansen, L.K. (2000). "Neural Networks for Modelling and Control of Dynamic Systems." London: Springer.

Noura, H., Theilliol, D., Ponsart, J-C. and Chamseddine, A. (2009). "Fault-tolerant Control Systems, Design and Practical Applications." Advances in Industrial Control, Chapter 5, Sensor Fault-tolerant Control Method for Active Suspension System, pp. 157-209, 1st Edition, Springer, London.

O'Dwyer, A. (2006). "Handbook of PI and PID Controller Tuning Rules." London: London: Imperial College Press.

Pedro, J.O. and Mgwenya, T. (2004). "LQR Control of a Full-car Active Suspension with Actuator Dynamics ." Proceedings of the 4^{th} South African Conference on Applied Mechanics (*SACAM'04*), Johannesburg, South Africa, pp. 1–9.

Pedro, J.O., Dahunsi, O.A. and Baloyi, N. (2011). "Direct Adaptive Neural Control of a Quarter-Car Active Suspension System." Proceedings of the 10^{th} IEEE International Control Conference (*Africon 2011*), Livingstone, Zambia, 13-15 September 2011, pp. 1–6.

Pedro, J.O. and Dahunsi, O.A. (2011). "Neural Network Based Feedback Linearization Control of a Servo-Hydraulic Vehicle Suspension System." International Journal of Applied Mathematics and Computer Science, vol. 21, no. 1, pp. 137–147.

Pedro, J.O., Dangor, M., Dahunsi, O.A. and Ali, M.M. (2013a). "Differential Evolution-Based PID Control of Nonlinear Full-Car Electrohydraulic Suspensions." Mathematical Problems in Engineering, vol. 2013, pp. 1-13.

Pedro, J.O., Dangor, M., Dahunsi, O.A. and Ali, M.M. (2013b). "CRS and PS-Optimised PID Controller for Nonlinear, Electrohydraulic Suspension Systems." Proceedings of the 9thAsian Control Conference (*ASCC2013*), Istanbul, Turkey, 23-26 June 2013.

Pekgökgöz, R., Gürel, M, Bilgehan, M. and Kisa, M. (2010). "Active Suspension of Cars using Fuzzy Logic Controller Optimized by Genetic Algorithm ." International Journal of Engineering and Applied Sciences, vol. 2, no. 4, pp. 27–37.

Poussot-Vassal, C., Sename, O., Dugard, P., Gaspar, P., Szabo, Z. and Bokor, J. (2006). "Multi-objective qLPV h_∞/h_2 Control of a Half Vehicle." In Proceedings of the 10^{th} MINI Conference on Vehicle System Dynamics, Identification and Anomalies (*VSDIA'06*), Budapest, Hungary, November 2006, pp. 1–6.

Price, W.L. (1983). "Global Optimization by Controlled Random Search ." Journal of Optimization Theory and Applications, vol. 40, no. 3, pp. 333–348.

Rajeswari, K. and Lakshmi, P. (2010). "PSO Optimized Fuzzy Logic Controller for Active Suspension System." Proceedings of the 2^{nd} International Conference on

Advances in Recent Technologies in Communication and Computing (*ARTCom 2010*), Kottayam, India, 15-16 Oct 2010, pp. 278–283.

Rodriguez, R.C. and Yu, W. (2012). "Robust Adaptive Control via Neural Linearization and Compensation." Journal of Control Science and Engineering, vol. 1, no. 1, pp. 604–610.

Ryu, S., Kim, Y. and Park, Y. (2008). "Robust H_∞ Preview Control of an Active Suspension System with Norm-Bounded Uncertainties." International Journal of Automotive Technology, vol. 9, no. 5, pp. 585–592.

Sam, Y. and Hudha, K. (2006) "Modelling and Force Tracking Control of Hydraulic Actuator for an Active Suspension System." Proceedings of the 1^{st} IEEE Conference on Industrial Electronics and Applications(*ICIEA 2006*), Singapore, 24-26 May 2006, pp. 1–6.

Sapinski, B. and Rosol, M. (2008).) "Autonomous Control System for a 3 DOF Pitch-Plane Suspension Model with MR Shock Absorbers." Computers & Structures vol. 86, no. 3-5, pp. 379–385.

Sarkar, B.K., Mandal, P., Saha, R., Mookherjee, S.m Sanyal, D. (2013). "GA-optimized Feedforward-PID Tracking Control for a Rugged Electrohydraulic System Design." ISA Transactions, vol. 52, no. 6, pp. 853-861.

Shi, J., Li, X. and Zhang, J. (2010). "Feedback Linearization and Sliding Mode Control for Active Hydro Pneumatic Suspension of a Special-Purpose Vehicle ." Institute of Mechanical Engineers, Part D: Journal of Automobile Engineering, vol. 211, no. 3, pp. 171–181.

Spentzas, K. and Kanarachos, A. (2002). "Design of a Non-Linear Hybrid Car Suspension System Using Neural Networks." Mathematics and Computers in Simulation, vol. 60, no. 3-5, pp. 369–378.

Tang, C., Zhaq, G., Li, H. and Zhuo, S. (2009). "Research on Suspension System based on Genetic Algorithm and Neural Network Control." Proceedings of the 2^{nd} International Conference on Intelligent Computation Technology and Automation Volume (*ICICTA '09*), Changsha, Hunan, 16 October 2009, vol. 1, pp. 468–471. .

Tian, L. and Collins, C. (2004). "A Dynamic Recurrent Neural Network-Based Controller for a Rigid-Flexible Manipulator System." Mechatronics, vol. 14, no. 5, pp. 471–490.

Tuan, H.D., Ono, E. and Apkarian, P. (2001). "Nonliear H_∞ Control for an Integrated Suspension System via Parameterized Linear Matrix Inequality Characterizations." IEEE Transactions Control System Technology, vol.9, no. 1, pp. 175-185.

Turkay, S. and Ackay, H. (2011). "Multi-Objective Control of Full-Vehicle Suspensions: A Case Study." In Proceedings of the 18^{th} IFAC World Congress, Milan, Italy, 28 August - 2 September 2011, pp. 1826.1831.

Wai, R.J., Lee, J.D. and Chuang, K.L. (2011). "Real-Time PID Control Strategy for Maglev Transportation System via Particle Swarm Optimization." IEEE Transactions on Industrial Electronics, vol. 58, no. 2, pp. 629–646.

Wang, D., Lin, X. and Zhang, Y. (2011). "Fuzzy Logic Control for a Parallel Hybrid Hydraulic Excavator Using Genetic Algorithm." Automation in Contruction, vol. 20, no. 1, pp. 581–587.

Wang, Y-C. and Chien, C-J. (2012). "An Output-Recurrent-Neural-Network-Based Iterative Learning Control for Unknown Nonlinear Dynamic Plants." Journal of Control Science and Engineering, vol. 58, no. 2, pp. 629–646.

Wu, Z. Wang, W and Bai, Z. (2012). "Improved Genetic Algorithm Optimizing PID Parameters for Electro-hydraulic Servo System." Communications in Computer and Information Science, Revised Selected Papers from: International Conference Communications and Information Processing (ICCIP2012), 7-11 March 2012, Part I, Springer-Verlag, Berlin, pp. 386–393.

Yagiz, N. and Hacioglu, Y. (2008). "Backstepping Control of a Vehicle with Active Suspension." Control Engineering Practice, vol. 16, no. 12, pp. 1457–1467.

Yagiz, N., Hacioglu, Y. and Taskin, Y. (2008). "Fuzzy Sliding-Mode Control of Active Suspensions." IEEE Transactions on Industrial Electronics, vol. 55, no. 11, pp. 3883–3890.

Yagiz, N. and Sakman, L. (2005). "Robust Sliding Mode Control of a Full Vehicle Without Suspension Gap Loss ." Journal of Vibration and Control, vol. 11, no. 11, pp. 1357–1374.

Yahaya, M., Sama, H., Johari, H., Osman, M., Ruddin, M. and Ghanib, A. (2004). "A Class of Proportional-Integral Sliding Mode Control with Application to Active Suspension System ." Systems and Control Letters, vol. 51, no. 3-4, pp. 217–223.

Yamashita, M., Fujimor, K., Hayakawa, K. and Kimura, H. (2004). "Application of H_∞ Control of Active Suspension Systems ." Automatica, vol. 30, no. 1, pp. 1717–1729.

Yao, J., Jiang, G., Yan, H. and Di, D. (2013). "Particle Swarm Optimization-Based Neural Network Control for an Electro-hydraulic Servo System." Journal of Vibration and Control, vol. 51, no. 3-4, pp. 1–9.

Yildirim, S. (2004). "Vibration Control of Suspension Systems Using a Proposed Neural Network." Journal of Sound and Vibration, vol. 277, no. 4-5, pp. 1059–1069.

Zapateiro, M., Luo, N., Karimi, H.R. and Vehi, J. (2009). "Vibration Control of a Class of Semi-active Suspension System using Neural Network and Backstepping Techniques." Mechanical Systems and Signal Processing, vol. 23, no. 1, pp. 1946–1953.